ANKARA YILDIRIM BEYAZIT UNIVERSITY

GRADUATE SCHOOL OF NATURAL AND APPLIED SCIENCES

NOVEL SEMICONDUCTOR NANO-STRUCTURES FOR PHOTOCATALYTIC APPLICATIONS

Ph.D. Thesis by

Fatih ARLI

Department of Energy Systems Engineering

September 2022

ANKARA

NOVEL SEMICONDUCTOR NANO-STRUCTURES FOR PHOTOCATALYTIC APPLICATIONS

A Thesis Submitted to

The Graduate School of Natural and Applied Sciences of

Ankara Yıldırım Beyazıt University

In Partial Fulfillment of the Requirements for the Degree of Philosophy of Doctorate in Energy System Engineering, Department of Energy System Engineering

by

Fatih ARLI

Sep, 2022

ANKARA

Ph.D. THESIS EXAMINATION RESULT FORM

We have read the thesis entitled **"NOVEL SEMICONDUCTOR NANO-STRUCTURES FOR PHOTOCATALYTIC APPLICATIONS"** completed by **FATIH ARLI** under the supervision of **ASSOC. PROF. DR. KUROŞ SALIMI** and we certify that in our opinion it is fully adequate, in scope and in quality, as a thesis for the degree of Philosophy of Doctorate.

Assoc. Prof. Dr. Kuroş SALİMİ

Supervisor

Assoc. Prof. Dr. Nuray ÇELEBİ

Jury Member

Prof. Dr. Nuray YILDIZ

Jury Member

Prof. Dr. Afife GÜVENÇ

Jury Member

Asst. Prof. Dr. Furkan SOYSAL

Jury Member

Prof. Dr. Sadettin ORHAN

Director

Graduate School of Natural and Applied Sciences

ETHICAL DECLARATION

I hereby declare that, in this thesis which has been prepared in accordance with the Thesis Writing Manual of Graduate School of Natural and Applied Sciences,

- All data, information and documents are obtained in the framework of academic and ethical rules,
- All information, documents and assessments are presented in accordance with scientific ethics and morals,
- All the materials that have been utilized are fully cited and referenced,
- No change has been made on the utilized materials,
- All the works presented are original,

and in any contrary case of above statements, I accept to renounce all my legal rights.

Date: **Signature:**

……..

Name & Surname:…….

CONTENTS

Ph.D. THESIS EXAMINATION RESULT FORM ii
ETHICAL DECLARATION iii
ACKNOWLEDGMENTS vii
ABSTRACT viii
ÖZ ix
NOMENCLATURE x
LIST OF TABLES xiv
LIST OF FIGURES xv
CHAPTER 1-INTRODUCTION 1
CHAPTER 2-SOLAR WATER SPLITTING (PC AND PEC WS) 9
2.1 Photocatalytic Water Splitting 10
2.4.1 Cocatalyst Loading 11
2.4.1 Single Photocatalyst Water Splitting Systems 13
2.4.2 Type II Photocatalyst Water Splitting Systems 14
2.4.3 Z-scheme Water Splitting Systems 15
2.3 Photoelectrochemical Water Splitting 16
2.4 Material Selections for PC, (PEC) Water Splitting, and Some Definitions 19
2.4 Photoanodes for Photocatalytic Water Splitting 25
2.4.1 Titanium dioxide (TiO_2) 26
2.4.2 Hematite (α-Fe_2O_3) 27
2.4.3 Bismuth Vanadate ($BiVO_4$) 29
2.4.4 Zinc Oxide (ZnO) 31
2.5 Semiconductor for Photoelectrochemical Water Splitting 34
2.5.1 Cerium Oxide (Ce_2O) 34
2.5.2 Metal-Organic Framework (MOFs) 36
CHAPTER 3-MATERIALS and METHODS 39
3.1 ZnO@PDA/CeO_2 NPs PEC Hydrogen Generation 39
3.1.1 Material 39
3.1.2 Fabrication Methods 39
3.1.3 Photocatalytic Dye Degradation and Trapping Experiments for ZnO@PDA/CeO_2 NPs 41
3.2 ZnO@MOF-5-C NPs for PEC Hydrogen Evolution 42

3.2.1 Material 42
3.2.2 Synthesis Methods 42
3.2.3 Trapping Experiment for ZnO@MOF-5-C NPs 44
CHAPTER 4-PHYSICAL AND CHEMICAL CHARACTERIZATION OF PHOTOANODES 46
4.1 Uv-Vis Spectroscopy 46
4.2 X-Ray Diffraction (XRD) 47
4.3 Scanning Electron Microscopy (SEM) 49
4.4 Transmission Electron Microscopy (TEM) 49
4.5 X-Ray Photoelectron Spectroscopy (XPS) 50
4.6 Brenauer-Emmett-Teller Spectroscopy (BET) 51
4.7 Photoluminescence Spectroscopy (PL) 52
CHAPTER 5-PHOTOELECTROCHEMICAL MEASUREMENTS 53
5.1 Photoelectrochemical Reactor Design 53
5.2 Linear Sweep Voltammetry (LSV) Measurements 55
5.3 Tafel Slope Measurements 56
5.4 Incident Photon to Current Efficiency (IPCE) Measurements 58
5.5 Applied Bias Photon to Current Efficiency (ABPE) Measurements 58
5.6 Electrochemical Impedance Spectroscopy (EIS) Measurements 59
5.6.1 Mott-Schottky Analysis 60
5.6.2 Nyquist Plot Analysis 62
5.6.3 Bode Plot Analysis 63
CHAPTER 6-RESULTS and DISCUSSION 64
6.1 Physical and Chemical Characterization of Z-scheme ZnO@PDA/CeO_2 Photoanodes 64
6.6.1 XRD Pattern of ZnO and Z-scheme ZnO@PDA/CeO_2 NPs 64
6.1.2 SEM Images of ZnO, ZnO@PDA and ZnO@PDA/CeO_2 NPs 65
6.1.3 TEM Images of ZnO, ZnO@PDA and ZnO@PDA/CeO_2 NPs 66
6.1.4 Uv-Vis Specta of ZnO, ZnO@PDA and ZnO@PDA/CeO_2 heterostructures 67
6.1.5 XPS Images ZnO, and ZnO@PDA/CeO_2 NPs 69
6.1.6 Brunauer-Emmett-Teller (BET) analaysis of ZnO and ZnO@PDA/CeO_2 NPs 71
6.1.7 Photoluminescence Spectroscopy (PL) Analysis of ZnO, ZnO@PDA/CeO_2 NPs 73

6.1.8 LSV Results of ZnO, and ZnO@PDA/CeO_2 NPs 74
6.1.9 Tafel slope of ZnO and ZnO@PDA/CeO_2 NPs 75
6.1.10 IPCE Results of ZnO and ZnO@PDA/CeO_2 heterostructures 76
6.1.11 ABPE Results of ZnO and ZnO@PDA/CeO_2 NPs 77
6.1.12 Mott-Schottky Results of ZnO and CeO_2 NPs 78
6.1.13 Nyquist Plot Results of ZnO and ZnO@PDA/CeO_2 heterostructures .. 81
6.1.14 Z-Scheme Charge Transfer Mechanism for ZnO@PDA/CeO_2 NPs 82
6.2 Physical and Chemical Characterization of Z-scheme ZnO@MOF-5 NPs 86
6.2.1 XRD Pattern of ZnO, ZnO@MOF-5 and ZnO@MOF-5-C heterostructures 86
6.2.2 SEM Images of ZnO, ZnO@MOF-5, and ZnO@MOF-5-C heterostructures 89
6.2.3 UV-Vis Spectra Images of ZnO, ZnO@MOF-5 and, ZnO@MOF-5-C heterostructures 91
6.2.4 XPS Results of ZnO, ZnO@MOF-5-C heterostructures 92
6.2.5 Brunauer-Emmett-Teller (BET) analysis of ZnO and ZnO@MOF-5-C heterostructures 94
6.2.6 Photoluminescence Spectroscopy (PL) Analysis of ZnO and ZnO@MOF-5-C heterostructures 96
6.2.7 LSV Images of ZnO, ZnO@MOF-5 and ZnO@MOF-5-C heterostructures 97
6.2.8 Tafel slope of ZnO, ZnO@MOF-5 and ZnO@MOF-5-C NPs 98
6.2.9 IPCE Results of ZnO, ZnO@MOF-5, and ZnO@MOF-5-C heterostructures 99
6.2.10 ABPE Results of ZnO, ZnO@MOF-5 and ZnO@MOF-5-C heterostructures 100
6.2.11 Mott-Schottky Results of ZnO and MOF-5 heterostructures 101
6.2.12 Nyquist Plot Results of ZnO, ZnO@MOF-5, and ZnO@MOF-5-C heterostructures 103
6.2.13 Bode Plot Results of ZnO, ZnO@MOF-5, and ZnO@MOF-5-C heterostructures 106
6.2.14 Z-Scheme charger transfer mechanism for ZnO@MOF-5-C heterostructures 107
CHAPTER 7-CONCLUSIONS 110
REFERENCES 114
CURRICULUM VITAE 148

ACKNOWLEDGMENTS

First and foremost, I would like to express my deep gratitude to my advisor, Assoc. Prof. Dr. Kuroş SALİMİ, for his supervision and direction throughout my Ph.D. studies. My advisor's knowledge, support, availability, and patience helped me a lot in developing this thesis.

Besides my advisor, I'd like to express my gratitude to the members of my thesis committee: Prof. Dr. Nuray YILDIZ, Prof. Dr. Afife GÜVENÇ, Assoc. Prof. Dr. Nuray ÇELEBİ, and Asst. Prof. Dr. Furkan SOYSAL for their insightful advice and recommendations, which significantly improved this thesis. I would also like to thank the Ankara Yıldırım Beyazıt University Institute of Science staff and the faculty members of the Energy Systems Engineering Department for their support.

Moreover, I would like to thank the University of Ankara, particularly the Chemical Engineering Laboratory. The lab doors were always open to me, and all the researchers in the lab gave me all kinds of support during my thesis work. They were always very friendly and hospitable to me.

Finally, I would like to present my greatest gratitude to my parents, my wife, and my children for their dedication and support throughout the writing of this thesis and the unconditional love that they gave me all my life.

To all of you, thank you.

2022, September **Fatih ARLI**

NOVEL SEMICONDUCTOR NANO-STRUCTURES FOR PHOTOCATALYTIC APPLICATIONS

ABSTRACT

The rapid decrease in fossil energy sources and the increase in carbon emissions in the world has led to the search for renewable, cheap, and environmentally friendly energy sources. Solar energy is the most researched energy source because it is clean, abundant, and sustainable. Photoelectrochemical (PEC) water splitting studies, which convert solar energy directly into electrical energy using semiconductor photocatalysts have been continuously researched since 1972. Recently, zinc oxide (ZnO) has emerged as one of the most promising semiconductors for photocatalytic applications among various metal oxides. In this study, two zinc-based photoanodes were fabricated in a star shape, and the PEC water splitting performance was investigated. Initially, PDA bridged ZnO@PDA/CeO_2 Z-scheme ternary heterojunction were rationally synthesized. PDA was utilized as an electron transfer mediator, and its PEC performance was investigated under LED illumination. A low photocurrent density for ZnO@PDA/CeO_2 heterostructures was obtained due to the low separation of electron-hole pairs under dark conditions (24 μA/cm^2). However, thanks to the novel Z-scheme system, this rate has been increased by approximately ten times (251 μA cm^2) under LED (30 mW/cm^2) irradiation. In the second study, carbon-incorporated ZnO@MOF-5-C Z-scheme ternary heterostructures were fabricated. These novel synthesized nanoparticles PEC water splitting efficiency was investigated under Xenon (300mW/cm^2) irradiation. The photocurrent density for the ZnO@MOF-5-C nanoparticle was measured under dark (0.27 mA/cm^2) and light conditions (3.49 mA/cm^2) at 2.50 V vs. RHE respectively. Moreover, the Z-scheme charge transfer mechanism within ZnO@PDA/CeO_2 and ZnO@MOF-5-C ternary heterojunctions was verified using radical scavengers and trapping experiments as well as X-ray photoelectron spectroscopy methods. According to this thesis, the PDA and an N-doped carbon layer facilitated the separation and also pumping of photogenerated charge carriers for enhanced PEC H_2 generation.

Keywords: Z-scheme heterojunction, Electron transfer layer, PDA, ZnO/CeO_2, N-doped carbon layer, ZnO@MOF-5, Water splitting, H_2 generation

FOTOKATALİTİK UYGULAMALAR İÇİN YENİ YARI İLETKEN NANO YAPILAR

ÖZ

Dünyada fosil enerji kaynaklarının hızla azalması ve karbon emisyonlarının artması, yenilenebilir, ucuz ve çevre dostu enerji kaynakları arayışlarına yol açmıştır. Güneş enerjisi, temiz, bol ve sürdürülebilir olması nedeniyle en çok araştırılan enerji kaynağıdır. Güneş enerjisini yarı iletken fotokatalizörler kullanarak doğrudan elektrik enerjisine dönüştüren fotoelektrokimyasal su bölme çalışmaları 1972 yılından beri sürekli olarak araştırılmaktadır. Son zamanlarda, Çinko oksit (ZnO), çeşitli metal oksitler arasında fotokatalitik uygulamalar için en umut verici yarı iletkenlerden biri olarak ortaya çıkmıştır. Bu çalışmada, yıldız şeklinde iki çinko bazlı fotoanot üretildi ve fotoelektrokimyasal (PEC) su ayırma performansı araştırıldı. Başlangıçta, PDA köprülü ZnO@PDA/CeO_2 Z-şeması üçlü heteroeklem rasyonel olarak sentezlendi. Elektron transfer aracısı olarak PDA kullanıldı ve LED aydınlatma altında fotoelektrokimyasal performansı araştırılmıştır. ZnO@PDA/CeO_2 üçlü heteroyapı yoğunluğu için fotoakım, karanlık koşullar altında (24 $\mu A/cm^2$) elektron-delik çiftlerinin düşük ayrılması nedeniyle elde edildi. Ancak yeni Z-şema sistemi sayesinde bu oran LED (30 mW/cm^2) ışınlaması altında yaklaşık on kat (251 $\mu A\ cm^2$) artırılmıştır. İkinci çalışmada karbon içeren ZnO@MOF-5-C Z-şeması üçlü heteroyapılar üretildi. Bu yeni sentezlenmiş nanoparçacıkların fotoelektrokimyasal su ayırma verimi Xe ($300mW/cm^2$) ışınlaması altında incelenmiştir. ZnO@MOF-5-C nanoparçacığı için fotoakım yoğunluğu, sırasıyla 2.50 V RHE'de (0.27 mA/cm^2, 3.49 mA/cm^2) karanlık ve aydınlık koşullar altında ölçülmüştür. Ayrıca, ZnO@PDA/CeO_2 ve ZnO@MOF-5-C üçlü heteroeklemler içindeki Z-şeması yük transfer mekanizması, radikal süpürücüler ve yakalama deneyleri, X-ışını fotoelektron spektroskopi yöntemleri kullanılarak doğrulandı. Sonuçlarımıza göre, PDA ve N katkılı bir karbon tabakası, geliştirilmiş PEC hidrojen üretimi için fotojenere yük taşıyıcıların ayrılmasını ve pompalanmasını kolaylaştırdı.

Anahtar Kelimeler Z-şeması heteroeklem, Elektron transfer katmanı, PDA, ZnO/ CeO_2, N katkılı karbon tabakası, ZnO@MOF-5, Su ayırma, H_2 üretimi

NOMENCLATURE

Greek Letter Symbols

f_{max}	Maximum frequency
ι_n	Electron lifetime
C	Capacitance
C	Capacitance per unit area of space charge layer.
e	Fundamental charge constant (1.602×10^{-19} C)
e^-	Electron
h^+	Hole
G	Gibbs free energy
J_{ph}	Photocurrent density
k_B	Boltzmann's constant (1.381×10^{-23}J K^{-1})
mA	Milliampere
mW	Milliwatt
n_{abs}	Ligh absorption efficiency
n_{inj}	Surface charge injection efficiency
n_{sep}	Charge separation efficiency
P	Power density
P_{mono}	Monochromatic illumination power intensity
T	Temperature (K)
t	Time, (s)
V	Volts, Volume (m^3)
V_b	Potential applied between working and counter electrode
V_{fb}	Flat-band potential
W	Watts
W	Warburg impedance
Z_{ima}	Imaginary part of the impedance
Z_{real}	Resistance part of the impedance
Z_w	Impedance
ΔG	Gibbs free energy, (kJ mol^{-1})
ε	Dielectric constant of the semiconductor
ε_0	Permittivity of vacuum (8.85×10^{-14} F/cm)
E_{rev}	Reversible potential

I	Current
K	Kelvin
R	Universal gas constant
V	Potential
b	Tafel slope (mV/dec^{-1})
j	Current density
j_o	Exchange current density
α	Absorption coefficient
η	Overpotential
v	Frequency of the wave
θ	Bragg's angle
λ	Wavelength, (nm)

Acronyms

ABPE	Applied Bias Photon to Current Efficiency
Ag/AgCl	Silver Silver Chloride Electrode
BET	Brunauer-Emmett-Teller
BQ	Benzoquinone
Ar	Argon
C	Carbon
CB	Conduction Band of Semiconductor
DI	Deionized Water
DMF	Dimethylformamide
EDS	Energy Disperse Spectroscopy
EtOH	Ethanol
EDTA	Ethylene Diamine Tetra Acetic Acid
FTO	Fluorinated Tin Oxide
HCl	Hydrochloric Acid
HER	Hydrogen Evolution Reaction
HOP	Hydrogen Evolution Photocatalyst
JCPDS	Powder Breakdown Standard Card No
J-V	Current Density-Voltage Measurement
KCI	Potassium Chloride
LED	Light Emitting Diode
LSV	Linear Sweep Voltammetry

M	Molality
MOF	Metal-Organic Framework
TPA	Terephthalic Acid
cm	Centimeter
mL	Milliliter
mg	Milligram
IPA	Isopropyl Alcohol
IPCE	Incident Photon to Current Efficiency
IR	Infrared Spectroscopy
NHE	Normal Hydrogen Electrode
NA_2SO_4	Sodium Hydroxide
NaOH	Sodium Sulfate
Nm	Nanometer
NPs	Nanoparticles
NS	Nanosphere
RE	Reference Electrode
O_2	Oxygen
OEP	Oxygen Evolution Photocatalyst
OER	Oxygen Evolution Reaction
OCP	Open-circuit potential
PDA	Polydopamine
PEC	Photoelectrochemical
PEMFC	Proton Exchange Membrane Fuel Cell
PC	Photocatalytic
PL	Photoluminescence Spectroscopy
p-type	Positive type semiconductor
Pd	Palladium
pH	Power of Hydrogen
Pt	Platinum
RE	Reference Electrode
RHE	Reversible Hydrogen Electrode
Ru	Ruthenium
SCE	Saturated Calomel Electrode
SEM	Scanning Electron Microscopy

SHE	Standart Hydrogen Electrode
SHE	Solar to Hydrogen Efficiency
SSA	Specific Surface Area
TEM	Transmission Electron Microscopy
UV	Ultraviolet Spectroscopy
UV-vis	Ultraviolet-Visible Spectroscopy
VB	Valence Band of Semiconductor
$(Zn(acac))_2$	Zinc acetylacetonate
WE	Working Electrode
Xe	Xenon Light
XRD	X-Ray Diffraction
XPS	X-ray Photoelectron Spectroscopy
µM	Micrometer
µL	Microliter

LIST OF TABLES

Tablo 5. 1 EIS data circuit elements summary 62

Table 6. 1 Experimentally obtained specific surface area (SSA), pore volume, and mean pore size value of ZnO star and ZnO@PDA/CeO_2 NPs 73

Table 6. 2 Values of circuit elements for Z-scheme ZnO@PDA/CeO_2 heterostructures calculated from Nyquist plots. 82

Table 6. 3 Experimentally obtained specific surface area (SSA), pore-volume, and mean pore size value of ZnO star and ZnO@MOF-5-C heterostructures 94

Table 6. 4 Values of circuit elements for ZnO, ZnO@MOF-5, and ZnO-MOF-5-C heterostructures calculated from Nyquist plots 104

Table 6. 5 Electron lifetimes and corresponding frequencies, obtained by EIS 107

Table 7. 1 Comparison of current density values at specific potentials, IPCE, ABPE,Tafel plot, light source, and power values of various Z-scheme and Type II heterojunction with ZnO@PDA/CeO_2 photoanodes. 111

Table 7. 2 Comparison of current density values at specific potentials, IPCE, ABPE,Tafel plot, light source, and power values of various Z-scheme and Type II heterojunction with ZnO@MOF-5-C photoanodes. 113

LIST OF FIGURES

Figure 1. 1 Hydrogen generation methods; (a) Current hydrogen generation (b) Global production percentages 2

Figure 2. 1 Schematic mechanism of photocatalytic water splitting; (a) semiconductor photocatalyst (b) one-step excitation 11

Figure 2. 2 Process of overall water splitting: (a) single cocatalyst (b) dual-cocatalyst (c) Functions of cocatalysts in photocatalytic H_2 production 12

Figure 2. 3 Schematic illustrations of single component photocatalysts 14

Figure 2. 4 Schematic illustrations of type-II heterojunction photocatalysts 15

Figure 2. 5 Z-scheme photocatalytic system 16

Figure 2. 6 PEC water splitting using; (a) a photoanode, (b) a photocathode, and (c) a photoanode and a photocathode in tandem configuration. Schematic representation of n-type photoelectrochemical (PEC) water splitting system (d) Photocatalytic water splitting energy diagrams based on;(f) one-step excitation and (g) two-step excitation (Z-scheme) 18

Figure 2. 7 Schematic representation of an irradiated photocatalyst 20

Figure 2. 8 Record count of publications on photocatalysis since 1995 21

Figure 2. 9 Classification of solids according to their electronic structure: (a) conductor, (b) semiconductor, (c) insulator 22

Figure 2. 10 Band gaps and band edge positions of some semiconductors associated with redox potentials for water splitting 23

Figure 2. 11 The visual representations of direct and indirect bandgap materials: (a) Direct, (b) Indirect 24

Figure 2. 12 Valence and conduction band edge for n-type metal oxide-based photoanodes. The blue dash lines show potential levels for water oxidation (1.23 VRHE) and reduction (0.0 VRHE) 26

Figure 2. 13 Crystal structures of the TiO_2: (a) anatase, (b) brookite, and (c) rutile phase 27

Figure 2. 14 The main strategies for improving hematite PEC performance for water splitting 28

Figure 2. 15 Methods applied to improve PEC performance of $BiVO_4$ 30

Figure 2. 16 The crystal structures of the ZnO; blue spheres represent zinc, whereas pink spheres represent oxygen 31

Figure 2. 17 Energy potentials of ZnO and redox potentials for PEC water splitting at pH = 7, relative to NHE 32

Figure 2. 18 Crystal structures of the CeO_2 34

Figure 2. 19 Modification pathway to improve the CeO_2 photocatalytic performance 36

Figure 2. 20 (a) The structure of IRMOF-1 (MOF-5) with the Zn_4O tetrahedra indicated in blue and the cavity indicated by a yellow sphere (O, red; C, black) (b) Chemical structure of terephthalic acid 37

Figure 2. 21 Several research groups produced porous MOFs to accommodate/retain chemical species in their pores/channels [171] 38

Figure 3. 1 Schematic synthesis pathway of ZnO@PDA/CeO_2 NPs 40

Figure 3. 2 (a) Schematic representation of the home-made visible LED photo-reactor, and (b) plausible degradation pathway using visible LED light array and reduction of O^{-}_{2} 41

Figure 3. 3 Schematic fabrication route of the ZnO@MOF-5-C NPs 43

Figure 3. 4 300W Arc Xenon Light 45

Figure 4. 1 (a) A simplified setup of the primary parts of a UV-Vis spectrophotometer (b) UV-1601 Shimadzu spectrophotometer setup 46

Figure 4. 2 Bragg's law 47

Figure 4. 3 Rigaku Miniflex 600 Powder X-ray Diffractometer 48

Figure 4. 4 Hitachi SU5000 scanning electron microscopy setup 49

Figure 4. 5 JEOL-2100 F Transmission Electron Microscopy setup 50

Figure 4. 6 Thermo-K-Alpha-Monochromator Spectrometer setup 51

Figure 4. 7 Nova 2200E BET setup 52

Figure 4. 8 Horiba Jobin Yvon instrument (PL) setup 52

Figure 5. 1 CorrTest Electrochemical Workstation Potentiostat/Galvanostat setup . 54

Figure 5. 2 Prepared working electrodes: (a) ZnOstar, ZnO@PDA, and ZnO@PDA/CeO_2 NPs, (b) ZnO star, ZnO@MOF-5, and ZnO@MOF-5-C NPs 55

Figure 5. 3 Illustration of Linear Potential Sweep in LSV 56

Figure 5. 4 Tafel plots for anodic and cathodic branches of the current-overpotential curve, with $\alpha = 0.5$, T = 298 K, and $i_0 = 10^{-6}$ A cm^{-2} 57

Figure 5. 5 Mott-Schottky plot of ZnO photoanode for correct V_{fb} determination .. 61

Figure 5. 6 Representation of Impedance in a Nyquist plot (a) Randles equivalent circuit (b), Randles circuit with Warburg elements (c) 63

Figure 6. 1 XRD pattern of ZnO and ZnO@PDA/CeO_2 heterostructures. 65

Figure 6. 2 SEM images of (a) ZnO star, (b) ZnO@PDA, and (c) ZnO@PDA/CeO_2 heterostructures, (d) corresponding SEM elemental mapping images of Zn, Ce, and O 66

Figure 6. 3 TEM images of ZnO@PDA/CeO_2 heterostructures 67

Figure 6. 4 (a) UV-Vis spectra of ZnO, CeO_2, and ZnO@PDA/CeO_2 heterostructures ; (b) Tauc plot of ZnO; (c) Tauc plot of CeO_2 NPs 68

Figure 6. 5 (a) X-ray photoelectron spectroscopy survey spectra of: (a) pristine ZnO and ZnO@PDA/CeO_2 NPs ; (b) high-resolution Zn 2p core level for ZnO and

$ZnO@PDA/CeO_2$ NPs ;(c) high-resolution O 1s core level for ZnO and $ZnO@PDA/CeO_2$ NPs; (d) high-resolution 3d for $ZnO@PDA/CeO_2$ NPs 70

Figure 6. 6 (a) Nitrogen adsorption-desorption diagram and, (b) Pore size distribution of ZnO and Z-scheme $ZnO@PDA/CeO_2$ NPs..... 72

Figure 6. 7 Photoluminescence of pristine ZnO and Z-scheme $ZnO@PDA/CeO_2$ NPs. 74

Figure 6. 8 J-V results of pristine ZnO and Z-scheme $ZnO@PDA/CeO_2$ heterostructures (under dark and light) 75

Figure 6. 9 Tafel plots of ZnO, $ZnO@PDA/CeO_2$ heterostructures 76

Figure 6. 10 IPCE spectra of ZnO and $ZnO@PDA/CeO_2$ heterostructures..... 77

Figure 6. 11 ABPE value of ZnO and $ZnO@PDA/CeO_2$ heterostructures (inset: PEC stability of the $ZnO@PDA/CeO_2$ NPs under 0.16 V (vs. reversible hydrogen electrode) for 1200 s) 78

Figure 6. 12 Mott-Schottky plots for (a) ZnO, (b) CeO_2, and (c) $ZnO@PDA/CeO_2$ heterostructures 80

Figure 6. 13 Schematic representation of the PEC reaction mechanism of Z-scheme $ZnO@PDA/CeO_2$ heterojunctions..... 81

Figure 6. 14 Nyquist plots of Z-scheme $ZnO@PDA/CeO_2$ heterostructures in dark and light..... 82

Figure 6. 15 Schematic representation of photoinduced charge transfer prosses for $ZnO@PDA/CeO_2$ NPs: (a) Type II heterojunction and (b) Z-scheme heterojunctions, (c) The change of MB concentration with time using pristine ZnO and Z-scheme $ZnO@PDA/CeO_2$ NPs (reaction conditions: concentration of MB: 3.125×10^{-5} M; photocatalyst amount: 10 mg); (d) Photocatalytic performance of Z-scheme $ZnO@PDA/CeO_2$ NPs using IPA, BQ, and Na-EDTA scavengers (the error bars were calculated according to three replicate experiments); PL spectra belong to (e) the $\cdot O_2^-$ and (f) the $\cdot OH$ trapping experiments using Z-scheme $ZnO@PDA/CeO_2$ NPs (reaction conditions: photocatalyst amount: 10 mg; the concentration of BQ and TPA: 0.5 mM) (the error bars were calculated according to three replicate experiments). 85

Figure 6. 16 XRD pattern of (a) ZnO, ZnO@MOF-5 , and ZnO@MOF-5-C NPs (b) Bare MOF-5 NPs 88

Figure 6. 17 SEM images of (a) ZnO star, (b) ZnO@MOF-5, and (c) ZnO@MOF-5-C heterostructures; (d) corresponding SEM elemental mapping images of Zn, O, C, and N 90

Figure 6. 18 (a) UV-Vis spectra of ZnO, MOF-5, ZnO@MOF-5 and ZnO@MOF-5-C heterostructures; (b) Tauc plot of ZnO; (c) Tauc plot of MOF-5 and (d) Tauc plot of ZnO@MOF-5-C heterostructures 91

Figure 6. 19 XPS survey spectra of (a) bare ZnO and ZnO@MOF-5-C heterostructures; (b) high-resolution Zn 2p core level for ZnO and ZnO@MOF-5-C NPs; (c) high-resolution O 1s core level for ZnO and ZnO@MOF-5-C

heterostructures; (d) high-resolution N 1s for ZnO@MOF-5-C heterostructures (e) C1s of ZnO@MOF-5 sample (f) C1s of ZnO@MOF-5-C heterostructures. 93

Figure 6. 20 (a) Nitrogen adsorption-desorption diagram ZnO, ZnO@MOF-5, and ZnO@MOF-5-C heterostructures, and (b) pore size distribution of ZnO, ZnO@MOF-5, and ZnO@MOF-5-C heterostructures 95

Figure 6. 21 Photoluminescence of pristine ZnO and ZnO@MOF-5-C heterostructures 96

Figure 6. 22 J-V results of pristine ZnO, ZnO@MOF-5, and Z-scheme ZnO@MOF-5-C NPs (under dark and light) 97

Figure 6. 23 Tafel plots of ZnO, ZnO@MOF-5 and ZnO@MOF-5-C heterostructures 98

Figure 6. 24 IPCE spectra of ZnO, ZnO@MOF-5, and ZnO@MOF-5-C heterostructures 99

Figure 6. 25 ABPE value of ZnO, ZnO@MOF-5, and ZnO@MOF-5-C heterostructures 101

Figure 6. 26 Mott-Schottky plots for (a) Pristine ZnO, (b) Pristine MOF-5 NPs ... 102

Figure 6. 27 Schematic representation of the PEC reaction mechanism of Z-scheme ZnO@MOF-5-C heterojunctions 103

Figure 6. 28 Nyquist plots of ZnO, ZnO@MOF-5, and ZnO-MOF-5-C heterostructures (a) light, (b) dark 105

Figure 6. 29 Nyquist plots of ZnO, ZnO@MOF-5, and ZnO-MOF-5-C heterostructures in dark 106

Figure 6. 30 Schematic representation of photoinduced charge transfer prosses for ZnO@PDA/CeO_2 NPs: (a) Type II heterojunction and (b) Z-scheme heterojunctions, (c) the $^{\cdot}OH$ (d) $^{\cdot}O_2^-$ the trapping experiments using Z-scheme ZnO@MOF-5-C heterostructures (reaction conditions: photocatalyst amount:4 mg; the concentration of TPA and BQ: 0.5 mM) (the error bars were added based on three replicate experiments). 108

CHAPTER 1

INTRODUCTION

An increasing world population and industrial development have significantly increased energy consumption. Currently, fossil energy sources such as coal, natural gas, and oil are used to meet the world's energy needs [1–3]. Furthermore, more than 90% of hydrogen production is met by fossil fuels. The most widely used hydrogen production techniques are partial methane oxidation, coal gasification, and steam methane reformation [2]. This rate means approximately 830 million tons of CO_2 emissions per year [4]. Moreover, these sources are unfortunately non-renewable. Also, due to the restricted availability of fossil fuels and their ability to regenerate in a short time, the currently discovered reserves are estimated to be less than 60, 40, and 250 years for natural gas, oil, and coal, respectively [5]. Moreover, environmental damage, such as the emission of carbon dioxide and greenhouse gases due to the use of fossil fuels and global warming, has attracted the attention of researchers to the new sources of energies. Therefore, interest and research in environmentally friendly, safe, cheap, alternative, and renewable energy sources have rapidly intensified to meet countries energy needs worldwide. Researchers consider hydrogen as most promising energy to replace fossil fuel use in future energy systems to provide a high level of energy security and better price control using different material sources [6–8]. In addition, the use of hydrogen can contribute to the solution of some of the adverse environmental and social problems such as climate change and local air pollution caused by fossil fuels [6]. Hydrogen is the most abundant element in the universe, naturally found in water, fossil fuels, and organic compounds with a high energy content [8,9]. Moreover, hydrogen is an environmentally friendly fuel that does not emit polluting emissions when combustion [10,11]. Hydrogen can be produced with different resources and technologies (Figure 1.1). The technologies used to produce hydrogen from various materials are shown in Figure 1.1a [12]. Figure 1.1b shows that a considerable portion of the hydrogen produced is derived from fossil fuels [3,13].

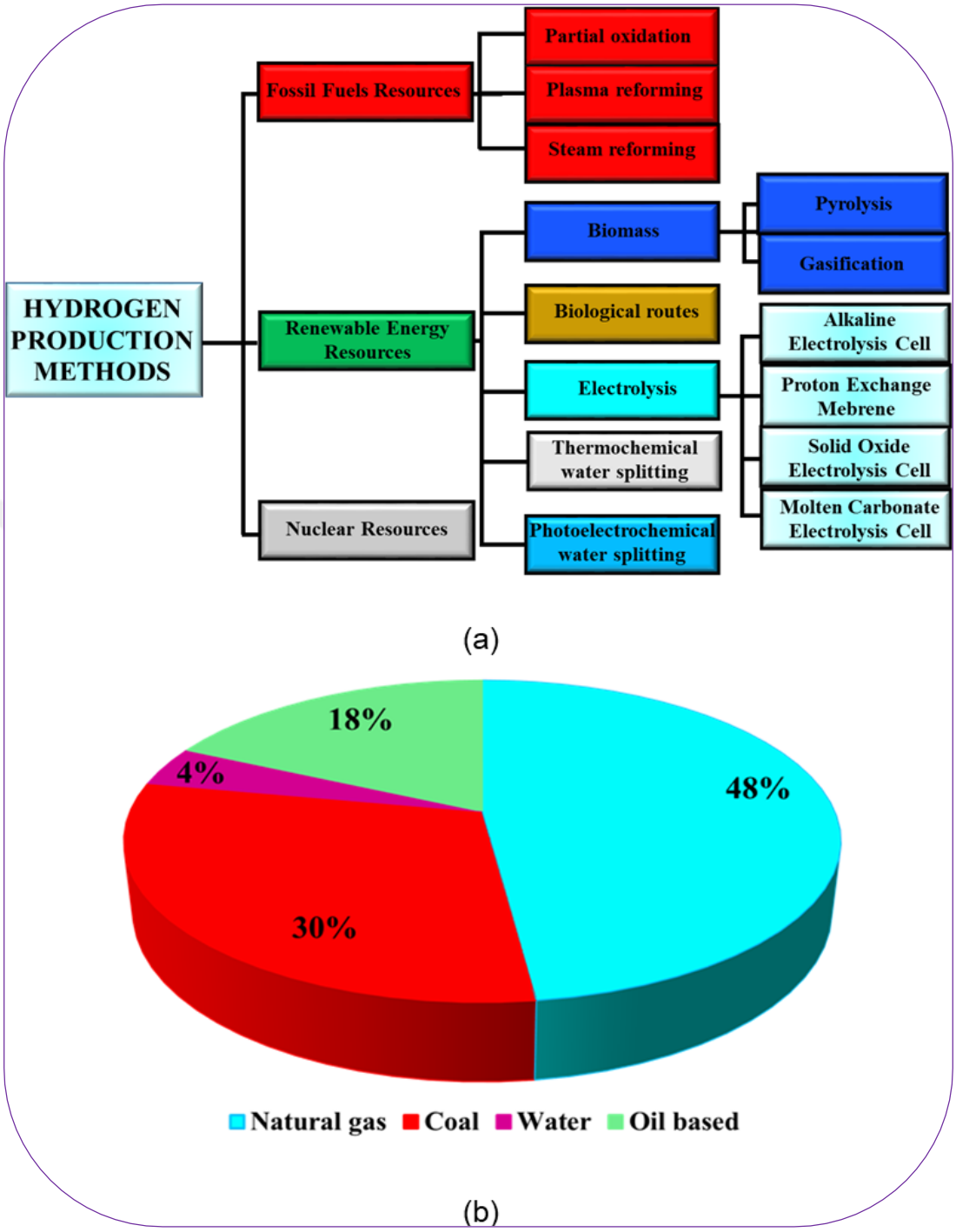

Figure 1. 1 Hydrogen generation methods; (a) Current hydrogen generation (b) Global production percentages

Recently, photocatalysts based on semiconductor metal oxides have indicated great promise for energy and environmental applications (e.g., wastewater treatment, water splitting, and etc.) [14–17]. Advanced oxidation processes (AOPs), such as photocatalysis, are crucial for water treatment because of their high efficiency,

reproducibility, and simplicity [18]. The efficiency of AOPs depends on photocatalyst, which is activated using a small amount of catalyst and minimal energy for electron-hole generation, therefore producing free radicals to attack organic pollutants [19]. Zinc oxide (ZnO) is one of the most promising semiconductors for photocatalytic applications among numerous metal oxides [14,15,20–27]. However, the photocatalytic activity of ZnO in the visible region is reduced due to a large band gap (E_g = 3.37 eV), which causes the use of a small portion of the solar spectrum, lowering catalytic efficiency [14,16,19,21,28]. It is crucial to absorb sunlight for water splitting and dye degradation properly. Scientists have developed numerous approaches to solve the abovementioned issues, resulting in improved ZnO photocatalytic performance with reduced band gap and visible light photoresponsivity [16,29–32]. Constructing a suitable heterojunction between two semiconductors with an appropriate band gap has been regarded as an effective way of enhancing charge separation efficiency [33–35]. Recently, Z-scheme heterojunctions have been more efficient than type II heterojunctions, owing to their special band positions and accelerated electron-hole separation [29,36]. In the Z-scheme approach, electrons on the less negative conduction band (CB) potential of one semiconductor moves to the lower positive valance band (VB) potential of another semiconductor resulting in electrons in more negative CB and holes in more positive VB potentials. This phenomenon provided strong redox ability as high as possible with higher photocatalytic performance [34–40]. In direct Z-scheme heterojunctions, electrons of one semiconductor transfer directly to holes of other semiconductors. In Z-scheme heterojunctions, electrons move from one semiconductor to another through an electron mediator to facilitate electron transport and inhibit electron-hole recombination, thereby enhancing photocatalytic performance [34]. Cerium oxide (CeO_2) has shown decent photocatalytic performance under UV-vis light illumination thanks to its abundant oxygen vacancies, good electron acceptor, good redox ability, and low cost [29,41–43]. Owing to the suitable band gap positions, Z-scheme heterojunction between CeO_2 and ZnO has been constructed. The effective photoinduced charge separation causes an enhancement in the redox capacity of ZnO/CeO_2 heterostructures compared with pristine ZnO and CeO_2 catalysts [29]. Engineering heterojunction between semiconductors with electron mediator has

emerged as an efficient way to obtain high photocatalytic efficiency owing to improved charge separation. However, the direct Z-scheme could not be enough due to weak electron transport between semiconductors [36]. Noble metals (such as Au or Ag) have usually been used as electron/charge-transfer mediators in Z-scheme heterojunctions [44–48]. These nanoparticles (NPs) facilitate the movement of charge carriers between semiconductors, leading to strong reducing/oxidizing power of electrons and holes, respectively [44–48]. Furthermore, in Z-scheme heterostructures, some low-cost metal oxides and carbon-based materials (reduced graphene oxides, carbon nanotubes, and etc.) have been utilized as electron transfer layers to enhance photocatalytic performance by improving light responsivity and charge carrier separation [35,36]. More recently, researchers have focused on biomimetic polydopamine (PDA) due to its binding ability with catechol groups, good electron transport capability, photoconductivity, and biocompatibility to enhance the photocatalytic performance of photocatalysts [36,49–51]. Guo et al. reported the first attempt at constructing PDA as an electron transfer mediator in g-C_3N_4@PDA/BiOBr Z-scheme heterostructures and investigated the photocatalytic applications [36]. Up to now, several investigations have been reported to investigate the photocatalytic activity of ZnO-CeO_2 catalyst in Z-scheme heterojunction. Murali et al. fabricated a novel Type II ZnO-CeO_2-rGO (ZCG) ternary heterostructure by hydrothermal methods and investigated PEC performance under Xenon light illumination of 100 mW/cm^2. They reported the highest photocurrent density value of 0.69 mA/cm^2 at 1.5V vs. RHE [14]. Hezam et al. fabricated plasmonic Z-scheme Ag-ZnO-CeO_2 using a sunlight-driven combustion approach and investigated the photocatalytic performance as well. They obtained the highest photocurrent density of 16 µA/cm^2 by using a 300 W Xenon (AM 1.5 G)/100 mW/cm^2 light source [52]. Celebi et al. synthesized the ZnO@C-CeO_2 Z-scheme photoanodes by adding the PDA layer between ZnO (as the starting template) and CeO_2 (as the shell layer). The highest photocurrent efficiency measured was achieved (7.43 mA/cm^2) at 1.18 V vs. RHE, under Xenon light conditions, with no remarkable response under dark conditions [53]. Yousefi et al. fabricated Ce-doped ZnO and pure ZnO nanocomposite thin films with different Ce/Zn ratios using the sol-gel method, and the PEC performance was measured. The highest photon current performance was obtained at 2µA/cm^2 at 1.2 V

vs. Ag/AgCl under Xenon (0.1 W/cm^2) light. When they compared the results to undoped ZnO, they found that the photocurrent density was doubled at 0.6 V potential [54]. Xiao et al. reported type II CeO_2/ZnO structure using a hydrothermal method and investigated the PEC hydrogen evolution properties. Their findings indicated that the highest photocurrent density was 0.3 mA/cm^2 at 0.5 V under Xenon irradiation (200W/cm^2) [30]. Although the photocatalytic activity of ZnO-CeO_2 catalyst in Z-scheme heterojunction was investigated [28]. However, there is no report in the literature on the PDA-bridged Z-scheme ZnO/CeO_2 heterostructures for enhanced PEC H_2 generation until now. In the first part of this thesis, a novel ZnO@PDA/CeO_2 Z-scheme heterojunctions were rationally designed for the first time, and the effect of the PDA electron transfer mediator was investigated on the PEC water splitting performance under visible LED irradiation. Additionally, the mechanism and plausible photocatalytic pathway of novel designed ternary Z-scheme ZnO@PDA/CeO_2 photocatalysts were elucidated. In PEC water splitting systems, MOF structures have been used by research communities for the past ten years because they satisfy the majority of photoelectrode requirements thanks to their large specific surface area, uniform and tunable pores, low cost, simplicity of synthesis, and open pore structure [55–58]. Apart from the advantages mentioned earlier, they improve the catalytic activity by enabling the easy incorporation of heteroatoms (C, N, P, and O) [55,58]. Moreover, the band gaps of MOFs can be easily controlled by changing their components. Furthermore, their highly crystalline structure has a high charge separation efficiency by suppressing electron-hole recombination [55,58,59]. So far, MOFs have been widely applied in the fields of catalysts, hydrogen storage, drug delivery, gas storage, chemical catalysis, and sensing [60–63]. Furthermore, MOF structures have recently received attention from researchers, particularly in the fields of photocatalytic water splitting, CO_2 reduction, and organic dye decolorization [61]. Up to now, many studies describing photocatalytic and PEC hydrogen production studies using MOF-based nanoparticles and various light sources have been reported in the literature. Celebi et al. investigated the PEC performance under LED light by fabricating a new core/shell polydopamine@Ni-MOF (pDA@Ni-MOF) heterogeneous photoanode and obtained that the highest photocurrent density was 8.61 mA/cm^2 at 0.77 V vs. RHE. This ratio was calculated under the same conditions for

Ni-MOF and bare pDA (0.008 V vs. RHE) and (0.011 V vs. RHE), respectively [59]. Zhou et al. fabricated a CoNi-MOF/$BiVO_4$ photoanode using a hydrothermal deposition technique to investigate PEC performance under AM 1.5 G light irradiation. The photocurrent density of CoNi-MOFs/$BiVO_4$ was measured as 3.2 mA cm^{-2} at 1.23 V vs. RHE for water oxidation [64]. Hao Xuqiang et al. synthesized Z-scheme CdS/MOF-5 heterojunctions using the hydrothermal method. They utilized an aqueous solution of Na_2S and Na_2SO_3 and a 300 W Xenon lamp to measure the photocatalytic H_2 generation. The maximum photocatalytic hydrogen production for the CdS/MOF-5 photoanode was calculated as (11.62 mmol h^{-1} g^{-1}). When compared to pure MOF-5 and CdS, the ratio increased by approximately 89.38 and 31.4 times, respectively. As a result, the importance of Z-scheme photocatalyst development in solar energy conversion of producing Zn-vacancy ZnS from MOF-5 was emphasized [65]. Yang et al. fabricated the C-ZnO photocatalyst constructed from Cu-decorated MOF-5 by calcination and photo-reduction method and investigated the photocatalytic hydrogen evolution using a 300W Xenon lamp as a light source. Cu/C–ZnO photocatalysts showed excellent results for photocatalytic hydrogen production under visible light. The hydrogen production rate increased approximately 9663-fold (5.363 mmol/g/h) compared to ZnO [66]. Celebi et al. synthesized the zirconium-based MOF (UiO-66, PDA@MOF) core/shell heteronanostructures using PDA NPs as the starting template by one-pot nucleation growth method and investigated the PEC water splitting performance and photocatalytic performance under LED light. They obtained that 99% of the MB was decolored in 80 minutes with a significant photocatalytic performance value using PDA@MOF. Besides this, the highest photocurrent density was measured at 1.53 mA/cm^2 at low potential (0.28 V vs. RHE). This value increased about 20-fold compared to the PDA@MOF value under dark conditions. They clarified that MOF-based structures might be appropriate for solar energy conversion applications like industrial water splitting and peroxide solar cells [67]. Bai et al. synthesized the $BiVO_4$/Zn-MOF photoanode with a simple soaking technique and measured the PEC properties it under 300 W of Xenon irradiation using a 0.5 M Na_2SO_3 solution as the electrolyte. For $BiVO_4$/Zn-MOF, the photocurrent density under dark and light conditions was 0.47 mA/cm^{-2} and 1.46 mA/cm^{-2} (1.23 V vs. RHE), respectively. Finally, they reported that Zn-MOF particles play an important role in charge carrier

transport and separation [68]. Although the photocatalytic performance of ZnO and MOF-based nanoparticles in the Z-scheme heterojunction has been investigated in the literature, so far, no reports on ZnO@MOF-5-C ternary heterostructures for improved PEC H_2 production have been published in the literature. In the second part of this thesis, new ZnO@MOF-5-C ternary heterojunctions were fabricated and the effect of the N-doped electron transfer layer on PEC hydrogen evolution performance under visible Xenon light illumination was investigated. In addition, the mechanism and photocatalytic mechanism of the newly synthesized ternary Z-scheme ZnO@MOF-5-C photocatalysts were explained.

Thesis scope and outline

This thesis study aims to increase PEC efficiency by fabricating, characterisation, and optimizing novel photoanodes for PEC water splitting, which is one of the solar hydrogen generation methods. This thesis is divided into seven main chapters.

Chapter 1 describes fossil fuels that make up a large part of the energy used in the world and the harmful effects of this energy. Hydrogen production methods are shown schematically, and hydrogen production from solar energy using semiconductors (ZnO, CeO_2, and MOF) is briefly explained. In addition, brief information about the electron mediator role of the Z-scheme mechanism, which has recently attracted the scientific community attention, is given, and detailed literature research related to the thesis is explained in this section.

Chapter 2 explains the details of hydrogen generation from photocatalytic and PEC water splitting systems, as well as investigations to improve the performance of semiconductors in these systems.

Chapter 3 demonstrates the raw materials and devices which utilized in fabricated Z-scheme ZnO@PDA/CeO_2 and ZnO@MOF-5-C photoanodes and experimental methods (schematically).

Chapter 4 explains the characterization techniques (XRD, SEM, EDX, TEM, PL, BET, and XPS) in order to physical and structural analysis of photoanodes.

Chapter 5 explains the fabrication procedures of photoanodes as well as photocatalytic measurement techniques such as linear sweep voltammetry (LSV), applied bias photon

to current efficiency (ABPE), incident photon to current efficiency (IPCE), Tafel slope, Mott-Schottky, Nyquist, and Bode plot.

Chapter 6 demonstrates the results and discussion section of the ZnO@PDA/CeO_2 and ZnO@MOF-5-C photoanodes (physico-chemical, optical, and PEC properties).

Chapter 7, the results of the novel ZnO@PDA/CeO_2 and ZnO@MOF-5-C photoanodes are elucidated in detail. The findings were interpreted in all aspects, and the thesis was completed by offering future-oriented explanations for improving its performance in semiconductor-based hydrogen production.

CHAPTER 2

SOLAR WATER SPLITTING (PC AND PEC WS)

Solar water splitting is a system that converts solar energy into chemical energy based on the photosynthesis of green plants [69]. From the thermodynamic perspective, the overall water splitting reaction is an uphill reaction requiring a minimum Gibbs free energy of ΔG^0 = + 237 kJ/mol. According to the Nernst equation, this value corresponds to ΔE^0 = 1.23 V. This is explained as the semiconductor's ability to absorb light with photon energy greater than 1.23eV (λ∼1000 nm and shorter) to drive the water splitting reaction [70]. The general water-splitting reaction is given in equation (1.1) [71].

$$2H_2O \rightarrow 2H_2 + O_2 \qquad (\mathbf{1.1})$$

In an acidic electrolyte, the oxidation and reduction reactions can be written as in equations (1.2) and (1.3):

$$2H_2O + 4h^+ \rightleftharpoons O_2 + 4H^+ \quad E^0_{ox} = -1.299 \text{ V vs NHE} \qquad (\mathbf{1.2})$$

$$2H^+ + 4e^- \rightleftharpoons H_2 \quad E^0_{red} = +0.000 \text{ V vs NHE} \qquad (\mathbf{1.3})$$

For an alkaline electrolyte, the oxidation and reduction reactions can be written as given in equations (1.4) and (1.5):

$$4OH^- + 4h^+ \rightleftharpoons 2H_2O + O_2 \quad E^0_{ox} = -0.401 \text{ V vs NHE} \qquad (\mathbf{1.4})$$

$$4H_2O + 4e^- \rightleftharpoons 2H_2 + 4OH^- \quad E^0_{red} = -0.828 \text{ V vs NHE} \qquad (\mathbf{1.5})$$

The photocatalytic (PC) and photoelectrochemical (PEC) systems that use solar energy to produce hydrogen will be described in this section. Additionally, a brief description of the materials used in the operation of these systems will be explained.

2.1 Photocatalytic Water Splitting

A photocatalytic water splitting system is described as an efficient system for converting water into hydrogen and oxygen using semiconductor catalysts in order to produce environmentally friendly and sustainable hydrogen fuel by utilizing solar energy [72]. Also, photocatalytic water splitting is considered artificial photosynthesis, which is the same as solar-powered photosynthesis in green plants [73–75]. The photocatalytic process of light-induced water splitting can be created with an easy technology by utilizing semiconductor materials as photocatalysts. Light energy is converted into chemical energy during this process. Simultaneously, the water-splitting reaction is accelerated to generate Gibbs free energy (GE) [73]. In the literature, photocatalytic hydrogen production is schematically reported in three steps as shown in Figure 2.1 [4,70,75–77]. In the first step, photon of desirable energy i.e., hν equal to or greater than E_g of photocatalytic semiconductor strikes on the photocatalytic surface and is absorbed by the photocatalytic semiconductor. Then electrons in the semiconductor migrate from the filled valence band to the empty conduction band. As a result, electrons (e^-) and holes (h^+) are formed (Step 2). For example, the reaction can be expressed as in equation 2.1.

$$\text{Semiconductor} + h\nu \rightarrow e^-_{(CB)} + h^+_{(VB)} \qquad (\mathbf{2.1})$$

In the second step, electrons, and holes excited by the photon start to circulate freely on the surface of the semiconductor and collect in the active sites on the surface. Finally, the successfully separated electrons and holes will move towards the surface of the semiconductor and react with protons (H^+) to produce H_2 and with H_2O to produce O_2, respectively [75,78]. The reactions that take place during photocatalytic water separation are given in equations (2.2-2.4) [4,75,78,79].

$$\text{Reduction: } 2H^+ + 2e^- \rightarrow H_2 \qquad (\mathbf{2.2})$$

$$\text{Oxidation: } H_2O + h^+ \rightarrow 2H^+ + \frac{1}{2}O_2 \qquad (\mathbf{2.3})$$

$$\text{Overall reaction: } H_2O \rightarrow H_2 + \frac{1}{2}O_2 \qquad (\mathbf{2.4})$$

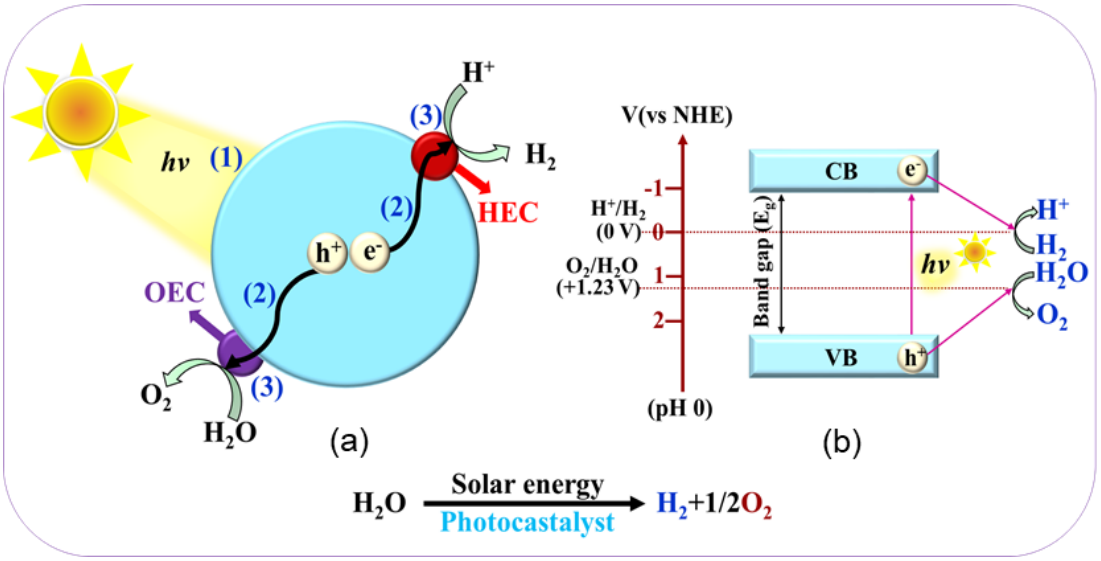

Figure 2. 1 Schematic mechanism of photocatalytic water splitting; (a) semiconductor photocatalyst (b) one-step excitation

2.4.1 Cocatalyst Loading

There are various methods to increase the efficiency of semiconductor photocatalysts. One of these methods is cocatalyst loading. Cocatalysts are substances that are deposited as nanoparticles or occasionally as layers on the photocatalyst surface [80–82]. They enhance the performance of at least one of the water splitting half reactions, such as the oxygen evolution reaction (OER) or the hydrogen evolution reaction (HER) [80,83]. The cocatalysts play four crucial roles in boosting the activity of the semiconductor photocatalysts in a photocatalytic H_2 evolution system (Figure 2.2a) [83,84]. First, cocatalysts can improve the harvesting of light. The localized surface plasmon resonance (LSPR) effect, which occurs in some plasmon metals (including Au and Cu), can increase the absorption of visible light. Second, cocatalysts can be influential in facilitating the separation of electron-hole pairs. When a cocatalyst is loaded onto the surface of the photocatalysts, the cocatalyst can attract electrons; consequently, the separation and transfer of the charge carriers can be enhanced [83,84]. Third, cocatalysts can suppress photo-corrosion and thereby increase the stability of semiconductor photocatalysts [83,85]. Visible light-sensitive semiconductors are susceptible to oxidation by photogenerated holes. This sensitivity predisposes them to self-separation, such as (oxy)sulfides and (oxy)-nitrides. The loading of cocatalysts on these semiconductors can prevent their decomposition by

removing photogenerated holes for O_2 formation and consequently increasing the stability of the semiconductors.

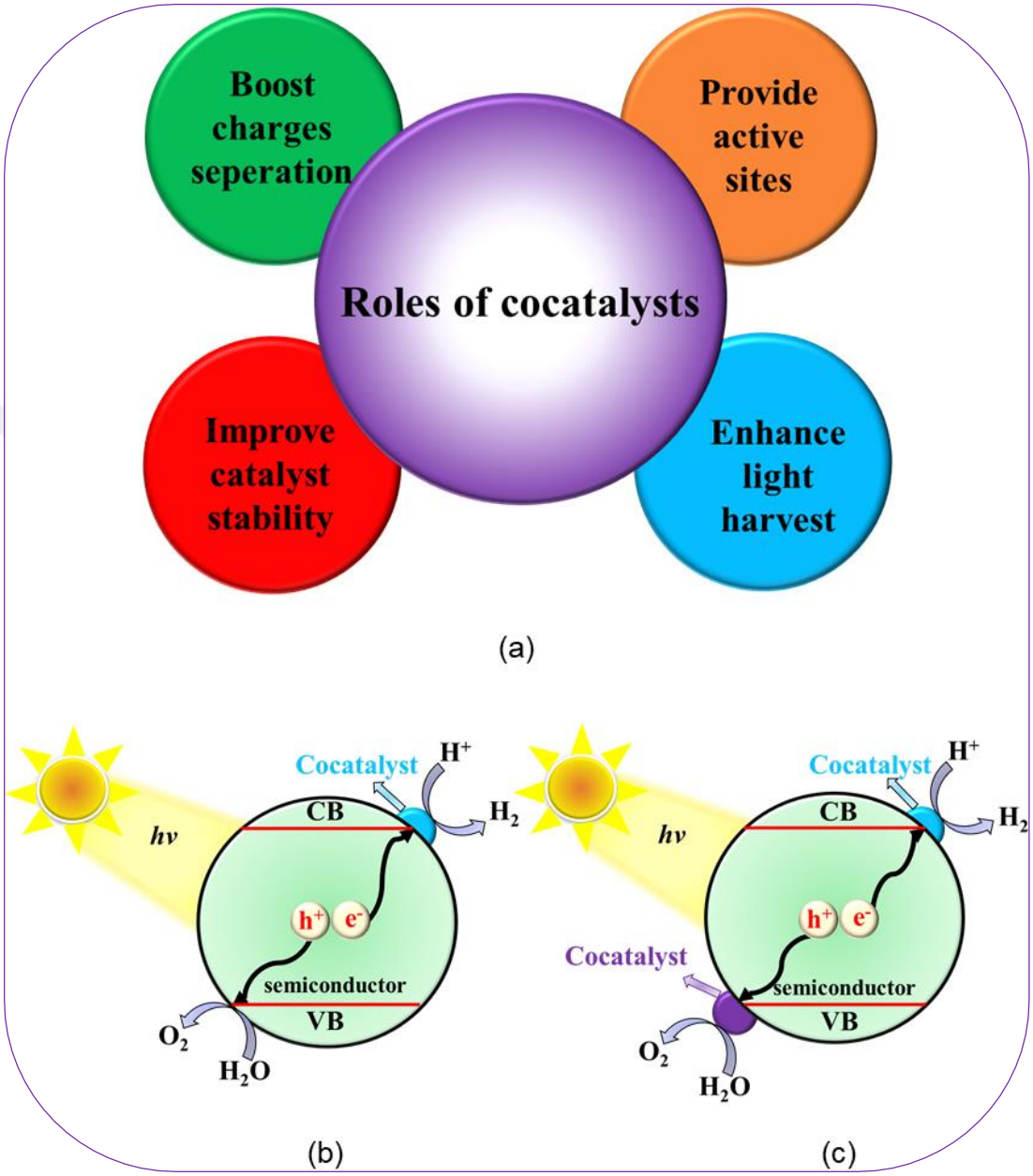

Figure 2. 2 Process of overall water splitting: (a) single cocatalyst (b) dual-cocatalyst (c) Functions of cocatalysts in photocatalytic H_2 production

Lastly, cocatalysts can provide active sites for photocatalytic reactions. Most cocatalysts can act as electron sinks and supply proton reduction sites [83,86]. Figures 2.2 (b) and (c) shows the charge transfer steps between the catalyst, the single-cocatalyst, and the two-cocatalyst. For instance, when the cocatalyst used as a noble

metal is loaded onto the surface of the photocatalyst, the photon-excited electrons begin to migrate to the surface of the cocatalyst. With this migration process, the noble metal is retained by the cocatalyst. Because the Fermi energy level of the noble metal is always smaller than the energy level of the semiconductor photocatalyst, photogenerated holes stay in the main photocatalyst and migrate to its surface, where electrons and holes are efficiently separated. Consequently, electrons and holes located separately in the photocatalytic reaction take part in reducing and oxidizing functions, respectively. Photocatalysts distributed on the surface play an important role in accelerating chemical reactions on the surface by suppressing back reactions and reducing electron-hole charge separation [83,86,87]. In the literature, it has been reported that the use of noble metals (Pt, Au, Pd, and Rh) is very effective in improving the photocatalysis efficiency of materials [88–90]. Conclusively, it should be noted that some of the co-catalysts give better efficiency in H_2 evolution reactions, whereas some have higher performance in O_2 evolution reactions. In the literature, Pt and Ru have been reported as H_2 evolution cocatalysts, while IrO_2 and RuO_2 have been reported as O_2 evolution cocatalysts. [91,92].

2.4.1 Single Photocatalyst Water Splitting Systems

Currently, photocatalytic overall water splitting is carried out using two main methods. The first of these approaches is to split water by one-step photoexcitation using single-component photocatalysts [93,94]. The schematic representation of the charge transfer mechanism in water splitting of single component photocatalysis is depicted in (Figure 2.3). Studies show that the material used has a narrow bandgap and also has a significantly high overpotential, which are desirable properties to facilitate photoactivation. This leads to better reduction and oxidation of the reactants due to a thermodynamically more negative CB potential, and a more positive VB potential level is thermodynamically applied. Thus, single-component photocatalysts should have a sufficiently small bandgap to be activated by light and suitable band-edge potentials to achieve total water splitting [95].

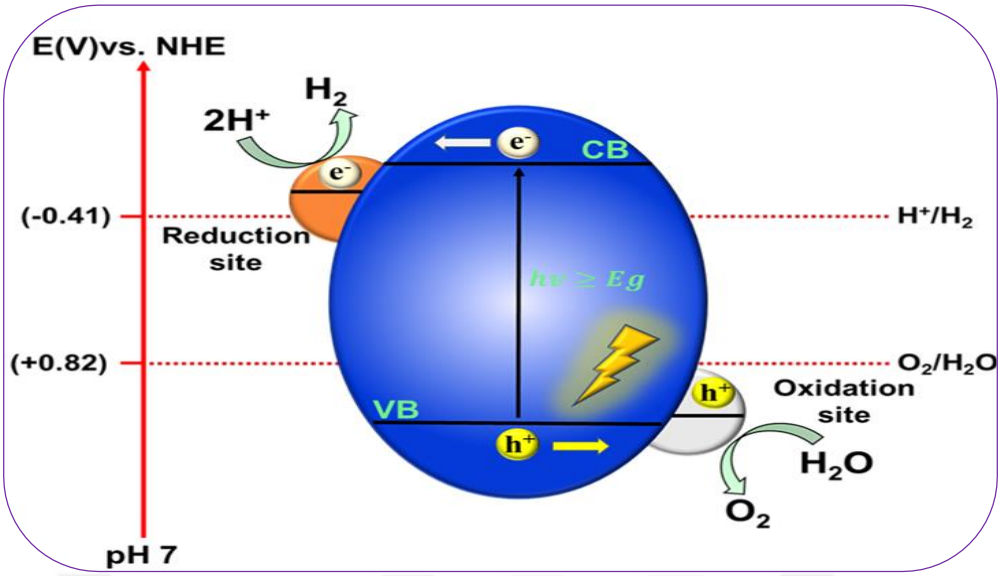

Figure 2. 3 Schematic illustrations of single component photocatalysts

In general, it is difficult for single-component photocatalysts to meet these extreme conditions [94,95]. For these reasons, the one-stage water splitting method has problems among photocatalyst candidates. Therefore, single-component photocatalysis can't have strong redox capability and a small band gap simultaneously. Moreover, single-component photocatalysts also suffer from rapid recombination of photogenerated electron-hole pairs [95–97].

2.4.2 Type II Photocatalyst Water Splitting Systems

Due to shortcomings in the single-component photocatalyst configuration, researchers have sought to adjust the configurations of photocatalysts [96]. For instance, using two semiconductors was aimed to increase the charge separation efficiency and photocatalytic performance, and they called such configurations type II heterojunction nanocomposites [94,96,98]. Designing a suitable heterojunction-type photocatalytic system can isolate electrons and holes in two distinct locations, thereby increasing the lifetime of photogenerated carriers. In type II heterojunction systems, gas formation occurs in two separate photocatalysts: HER on H_2 evolution photocatalysts and OER on O_2 evolution photocatalysts [94,98,99]. Despite the ability of heterojunction-type semiconductor nanocomposites to facilitate charge separation, the photocatalytic system's redox ability is weakened due to the migration of electrons and holes to more

electropositive CB and electronegative VB potentials due to the nature of charge transfer, as shown in Figure 2.4.

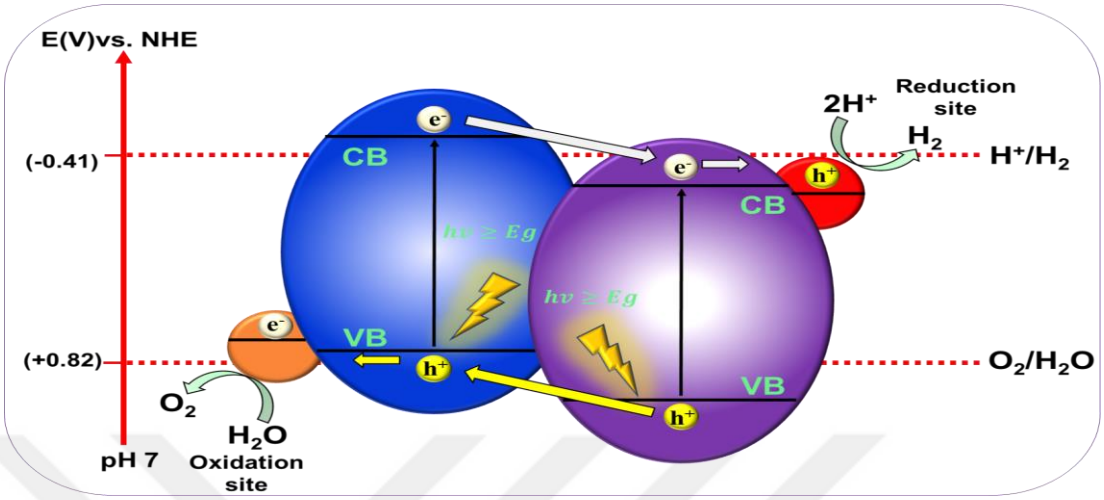

Figure 2. 4 Schematic illustrations of type-II heterojunction photocatalysts

2.4.3 Z-scheme Water Splitting Systems

To overcome the problems mentioned above, the investigators employed the second approach of the photocatalytic system, which is an anisotropic configuration. In this system, it consists of two photocatalysts and an electron mediator. This technique is known as the Z-scheme photocatalytic system, and it requires a two-step photo-excitation approach to achieve the water-splitting process. [89,99,100]. A biometric artificial Z-scheme photocatalytic system inspired by green plant photosynthesis can simultaneously demonstrate the following three requirements, which are shortcomings of other systems (both from one-component photocatalysts and heterojunction-type nanocomposites):1) small bandgap, 2) suitable band-edge position with considerable large overpotential, and 3) suppression in electron-hole pairs recombination [93,99]. The artificial Z-scheme photocatalytic system is also known as a two-stage photocatalytic system. The principle is that one serves as the reduction site and the other as the oxidation site (Figure 2.5). This system facilitates efficient water splitting.

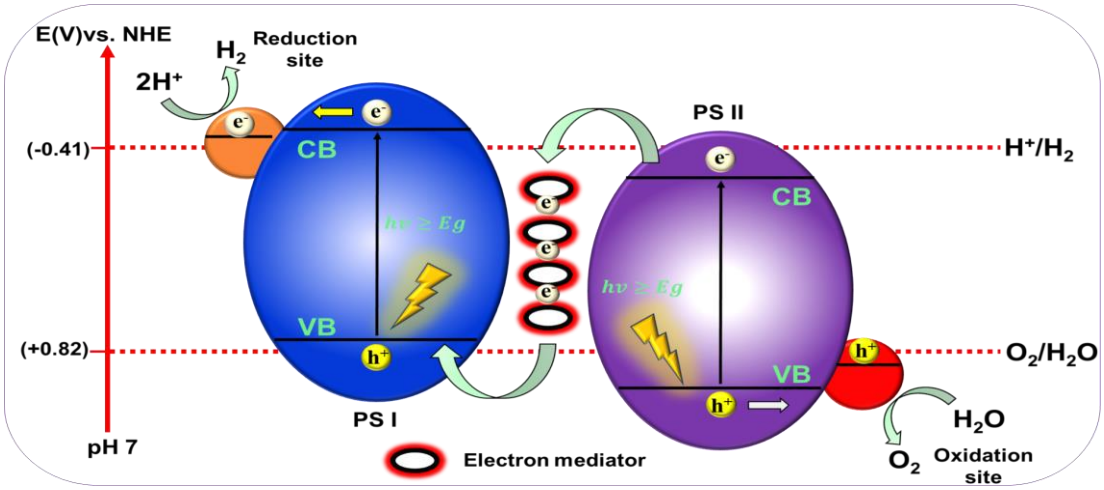

Figure 2. 5 Z-scheme photocatalytic system

In the Z-scheme system, an electron transport chain known as a mediator is used between the two photosystems. Also, the flow of electrons is facilitated by this electron transport. Unlike heterojunction-type semiconductor composites, Z-scheme allows for a distinct profile of electron flow due to incorporating an electron-hole channel. Electrons from the VB of both PS I and PS II will be excited to CB upon photoexcitation, leaving photogenerated holes in the VB. The electron mediator will then transport the photogenerated electrons in PS II to recombine with the holes from PS I's VB via Ohmic contact [99]. In this system, the transfer type of electrons allows the presence of electrons and holes in two different photocatalysis simultaneously while preserving their strong redox capabilities. Therefore, PS II forms a hole-rich photocatalyst for OER, while PS I accumulates electrons, providing HER with a suitable environment. Thus, when we compare the Z-scheme system with heterojunction type and single component photocatalysts, less change in Gibbs free energy is required to drive each photosystem. As shown in Figure 2.5, the rational design of the Z-scheme system bestows efficient charge isolation in a separated location with a relatively large overpotential sufficient to represent the excellent redox reaction.

2.3 Photoelectrochemical Water Splitting

Solar hydrogen production via PEC water splitting is a hopeful system for hydrogen production due to its sustainable, renewable, environmentally friendly, and low-cost

advantages. Water splitting relies on PEC technology, which can convert or store solar energy in chemical bonds. Scientists have reported numerous semiconductor materials in this field since the successful discovery of hydrogen production by PEC water splitting by Fujishima and Honda in 1972 [101,102]. Figure 2.6 shows the general design of a PEC system. In the PEC water splitting system, three different cell types are frequently used: n-type semiconductors as photoanodes, p-type semiconductors as photocathodes, and a tandem system with an n-type photoanode and a p-type photocathode [4,81,103]. In n-type photoanodes, photogenerated electrons are transferred to the counter electrode (cathode), producing an anodic photocurrent that converts the H^+ at the cathode to H_2 (Figure 2.6a). The p-type photocathode, on the other hand, transfers the photogenerated holes to the counter electrode (anode), resulting in a cathodic photocurrent and oxidizing water into O_2 and H^+ (Figure 2.6b). In the tandem cell system, not only the n-type photoanode but also the p-type photocathode works by absorbing light energy, which oxidizes water to O_2 and reduces H^+ to H_2, respectively (Figure 2.6c) [4,81,103]. As shown in Figure 2.6d, TiO_2 is a typical n-type semiconductor that is frequently used as a photoanode in an n-type PEC cell. An efficient PEC cell mechanism basically takes place in five main steps. These steps are given below, respectively [75].

1) absorption of light
2) charge generation
3) charge carrier separation and transportation
4) transfer charge carrier to the electrolyte
5) chemical reactions at the electron surfaces.

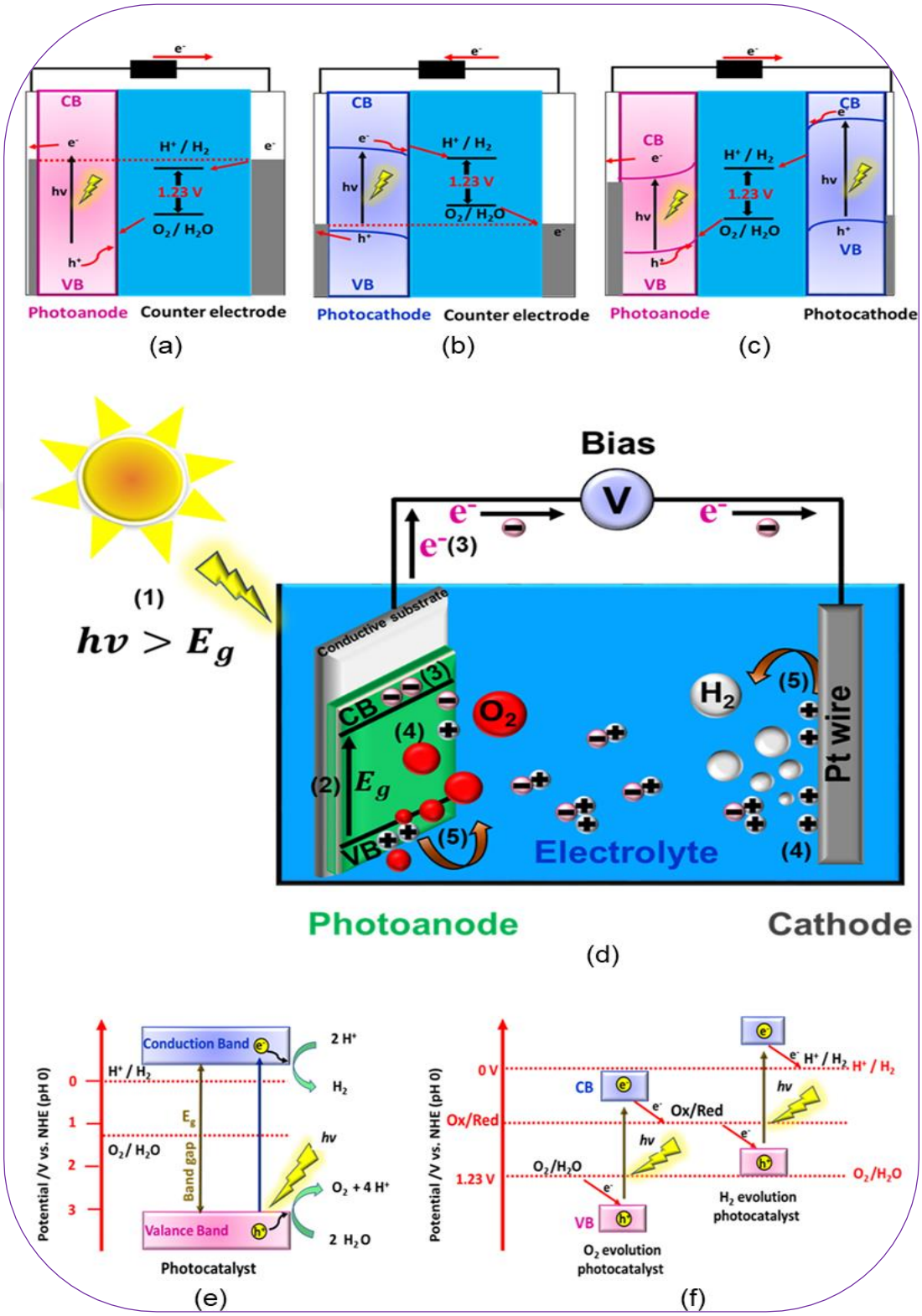

Figure 2. 6 PEC water splitting using; (a) a photoanode, (b) a photocathode, and (c) a photoanode and a photocathode in tandem configuration. Schematic representation of n-type photoelectrochemical (PEC) water splitting system (d) Photocatalytic water splitting energy diagrams based on;(f) one-step excitation and (g) two-step excitation (Z-scheme)

PEC water splitting consists of three crucial physiochemical steps. The first is light absorption by the semiconductor. The semiconductor naturally absorbs photons with energies greater than the band gap, and as a result, electrons are transferred to the CB, while holes are created in the VB. The charge carriers are separated and transported toward the surface in the second stage. Finally, redox reactions occur on the surface. The water splitting system using a single photocatalyst is shown schematically in (Figure 2.6e). This system should support some requirements. These can be explained as follows. The reduction and oxidation potentials of water, which are +0 and +1.23 V, respectively, against the normal hydrogen electrode (NHE) when the reactant solution is at pH=0, should provide. Moreover, as an alternative to the single component, two semiconductors can be connected in series with reversible redox shuttles, and this system is called the Z-scheme (Figure 2. 6f). It is explained in detail in section (2.4.3) [81,83].

2.4 Material Selections for PC, (PEC) Water Splitting, and Some Definitions

The materials used for water decomposition on particulate photocatalysts under visible light irradiation must meet certain basic requirements. First, let us briefly describe some concepts used in PC and PEC systems.

Photocatalyst or Semiconductor

Photocatalyst is a term commonly used to define the activation of a chemical process by a solid (known as a photocatalyst) exposed to a UV-visible light source [104,105]. The International Union of Pure and Applied Chemistry (IUPAC) defines photocatalysis as "a catalytic reaction involving light absorption by a substrate" [106]. As illustrated in Figure 2.7, incident light interacts with the photocatalyst, and electron-hole (e^-/h^+) pairs form if the energy is greater than or equal to the semiconductor's band gap (E_g). The term band gap is the energy difference between the conduction band (CB), the lowest energy band empty of electrons (LUMO), and the valence band (VB), the highest energy band occupied with electrons (HOMO) [104,105]. The steps of this process are as follows: First, as a result of the interaction

of the photocatalyst with the light, the electrons are excited, and they move from the VB to the CB, and holes are formed in the VB (Figure 2.7, steps 1 and 2). Second, these charges can initiate the reaction with the adsorbed species if they migrate from the bulk to the semiconductor surface and remain separate (Figure 2.7, steps 3 and 4). Finally, photoinduced electrons may participate in reduction processes, whereas photoinduced holes may initiate oxidation processes. Nevertheless, the CB and VB photogenerated charges recombine in bulk and on the semiconductor's surface, scattering energy as heat and returning to a non-excited state (Figure 2.7, steps 5 and 6) [104–106]. Notably, the relative occurrence of those stages (charge carrier's generation, recombination, and migration) depends on the intrinsic properties of the photocatalyst [104,107].

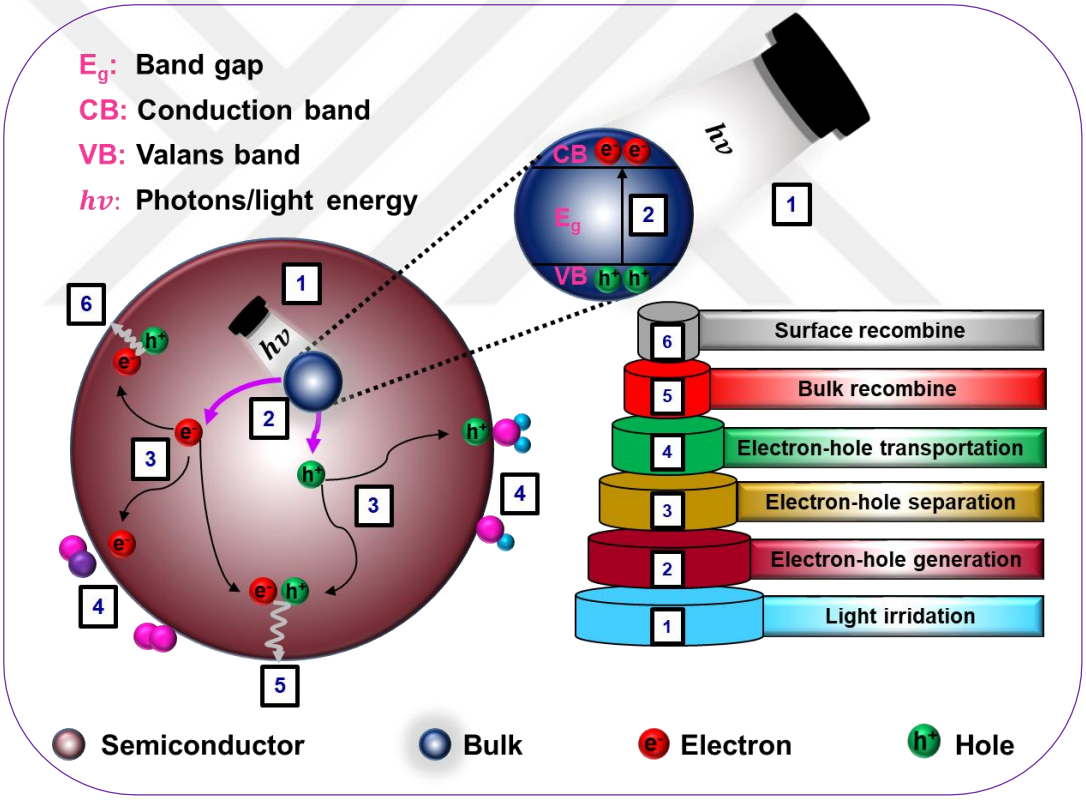

Figure 2. 7 Schematic representation of an irradiated photocatalyst

Since Fujishima and Honda performed the initial photocatalyst study, research on semiconductor photocatalysts has multiplied exponentially (Figure 2.8). This increase can be attributed to numerous applications, including environmental remediation and energy conversion to reduce carbon dioxide and water splitting [104,108].

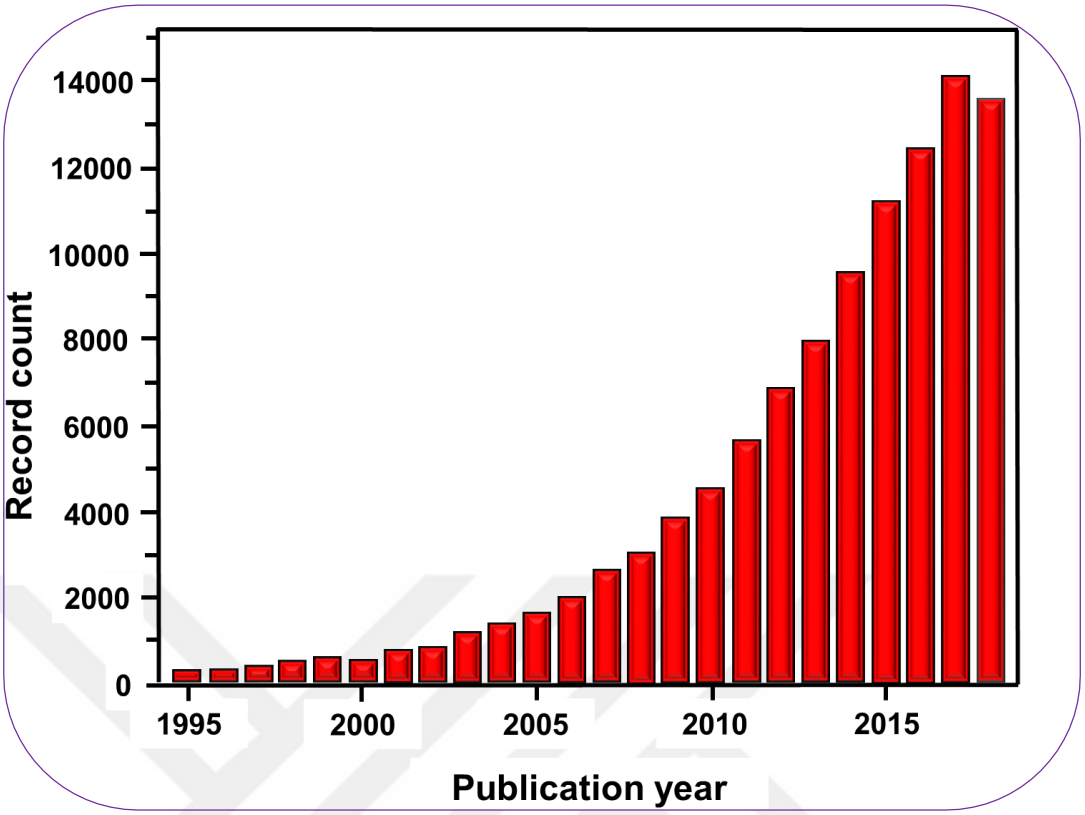

Figure 2. 8 Record count of publications on photocatalysis since 1995

They are semiconductors in photocatalytic applications (ZnO, TiO_2, Fe_2O_3, ZnS, CdS, CdSe, etc.). Photocatalysis is classified into two types based on the reaction medium: homogeneous and heterogeneous photocatalysis. Homogeneous photocatalysis occurs in a single phase, whereas heterogeneous photocatalysis occurs on the surface and at the interface. Semiconductor metal oxides are frequently used as heterogeneous photocatalysts. Semiconductor materials are characterized by electronic structures, defined by the "band theory." Band theory states that all matter is electronically called "band." It is a function of energy levels. Materials are classified based on the energy difference between these bands. The energy band diagrams for conductors, insulators, and semiconductors are shown in Figure 2.9 (a-c) [109]. The valence and conduction bands are adjacent in conductive materials, as illustrated in Figure 2.9a. On the other hand, the bandgap between the valence and conduction bands is usually equal to or greater than 10 eV in insulators. As a result, a significant amount of energy is required to move the electron into the conduction band (Figure 2.9b). The band gap in semiconductors is smaller than in insulators (Figure 2.9c) [109]. The transition of

electrons from the valence band to the conduction band occurs through an external factor such as thermal, electrical, or light.

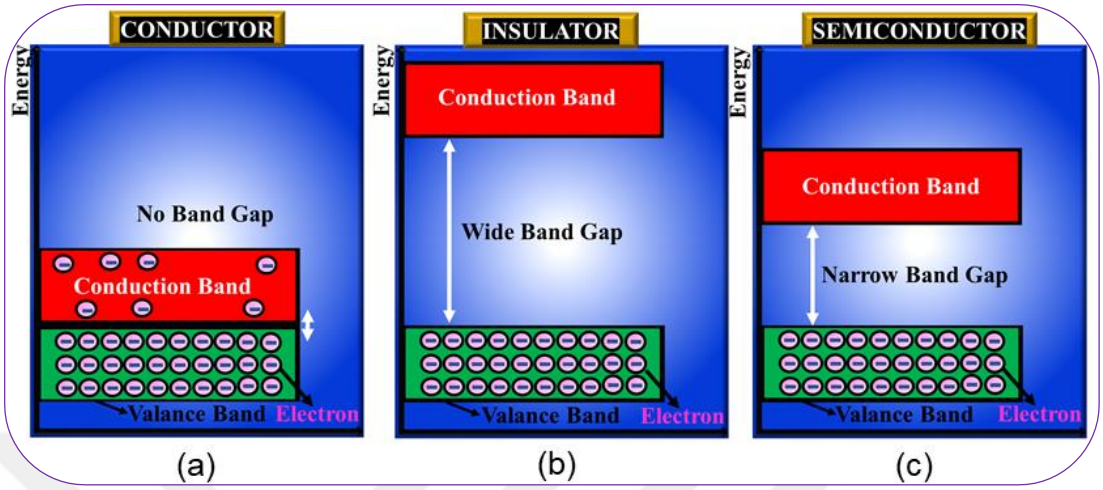

Figure 2. 9 Classification of solids according to their electronic structure: (a) conductor, (b) semiconductor, (c) insulator

Band Gap

The band gap is a term that describes the energy difference between the maximum valence band (VBM) and the minimum conduction band (CBM). The minimum band gap required for the light absorption properties of the semiconductor band gap is approximately equal to 1.6-2.2 eV [8]. Moreover, the valence band and conduction band edge locations should support water oxidation and reduction potentials for an ideal overall water-splitting semiconductor ($E_{CB} > E_{red,\ water}$ and $E_{VB} < E_{ox,\ water}$) [110–112]. The band-edge positions of representative semiconductors are shown in Figure 2.10, which can be utilized as a guideline when selecting suitable materials to act as photoelectrodes for water splitting. The ability of a semiconductor to pass photo-excited electron transfer to an absorbent particle depends on the band energy state of the semiconductor and the redox potential of the absorbates. From a thermodynamic point of view, pairs adsorbed by conduction band electrons can be photocatalytically reduced if the low redox potential is more negative than the conduction band. Furthermore, high redox potential can be more positive than the semiconductor valence band [110,112].

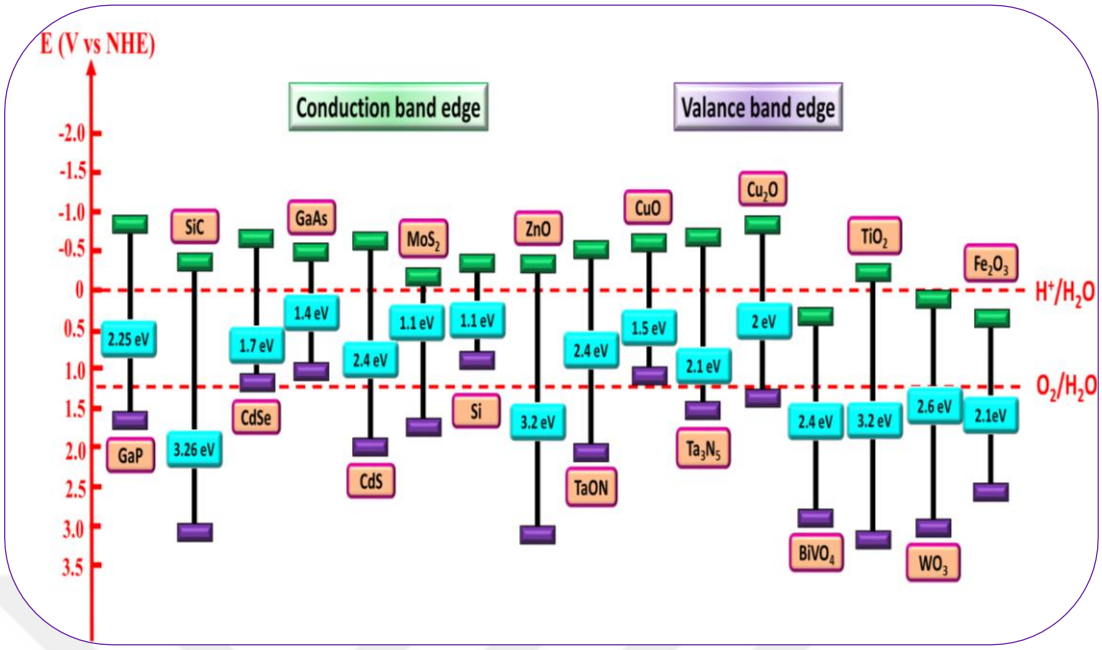

Figure 2. 10 Band gaps and band edge positions of some semiconductors associated with redox potentials for water splitting

The band position of the photocatalyst is the essential factor for modifying the redox potential of water. TiO_2, ZrO_2, $KTaO_3$, $SrTiO_3$, and $BiVO_4$ catalysts can perform the photocatalytic decomposition reaction of water [112]. However, some semiconductors cannot catalyze the reaction even though band gaps are consistent with the dissociation redox potential of water. For example, although CdS has a suitable band gap in the visible region, it is not active in decomposing water into H_2 and O_2. Because the holes formed by the light oxidize the S^{2-} ions in CdS instead of water, this phenomenon, which is generally seen in metal sulfide photocatalysts, is called photocorrosion [112]. On the other hand, some non-oxide compounds, such as phosphorus (GaP), and selenium (CdSe) compounds, both show good absorption properties in the visible region and have the necessary potential for water decomposition. However, these materials are unstable under irradiation and are degraded by photoanodic dissolution to form O_2 during water oxidation [112].

Direct and Indirect Bandgaps

The most important feature that affects and categorizes semiconductor's electronic transitions and optical stages are that the band structures are suitable for direct or

indirect transitions [113]. Momentum is conserved as the wave vector does not change as the electron passes from the valence band edge to the conduction band in direct bands (Figure 2.11a). The direct band coincides with the valence band's highest point and the conduction band's lowest point in the same wave vector [113,114]. An electron can move from the valence band to the conduction band through the absorption of a photon with an energy equal to the band gap in the crystal. On the other hand, in the indirect band gap, the wave vector of an electron that passes into the conduction band changes, so its momentum is not conserved (Figure 2.11b) [113,114]. A photon with higher energy than the band gap must be absorbed for an electron at the highest point of the valence band to enter the conduction band optically [114].

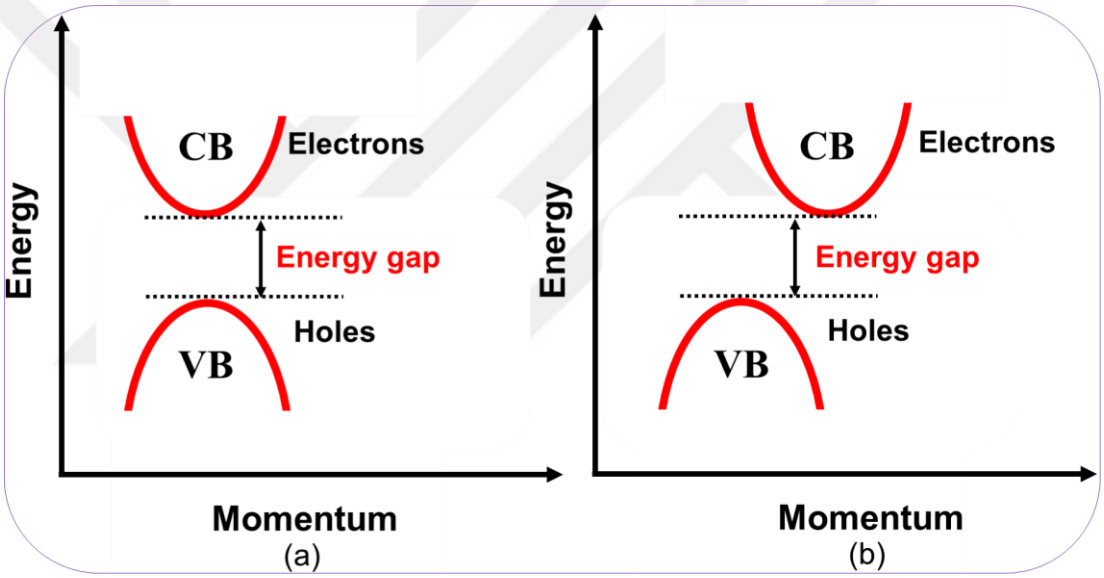

Figure 2. 11 The visual representations of direct and indirect bandgap materials: (a) Direct, (b) Indirect

The basic requirements for water splitting in the PC and PEC systems are described below.

- The band gap of semiconductor materials should be active in the visible region. Moreover, due to the potential and energy losses required for water separation, it is preferred that the band gap of the semiconductor is between 1.6-2.5 eV.
- The band edge position is essential to obtain good performance from hydrogen production. The valence band level should be more positive than the water

oxidation level (E_{O2}=H_2O), and the conduction band should be more negative than the H_2 production level (E_{H2}=H_2O).

- The material must be photochemically stable in an aqueous media to avoid photocorrosion during photoelectrolysis.
- Charge carriers must be transported from bulk oxide material to the counter electrode with minimal loss for highly efficient H_2 production.
- Low cost, easy accessibility, non-toxicity and high charge-carrier mobility [115].

2.4 Photoanodes for Photocatalytic Water Splitting

An n-type semiconductor is competent at producing oxygen at the photoanode-electrolyte interface. In an n-type semiconductor, photo-excited holes are formed. These holes then migrate to the interface. As a result, it converts water to oxygen. So, the photoanode's surface will likely be oxidized. [81]. Over the last 10-20 years, various photoanode materials for PEC hydrogen generation have been reported. Photoanode materials, also known as n-type semiconductors, are responsible for the formation of oxygen. These are some of the most researched and promising n-type semiconductors in the literature (TiO_2, ZnO, α-Fe_2O_3, $BiVO_4$, etc.) [116–119]. These n-type semiconductors must be suitable, environmentally friendly, and cost-effective in order to absorb the broadband spectrum. In addition, n-type semiconductors should be stable in an aqueous solution and have properties such as efficient charge collection. Figure 2.12 depicts the band properties of several n-type metal oxide semiconductors extensively studied as photoanodes for water oxidation. This section will describe some of the aforementioned n-type semiconductors most extensively investigated as photoanodes in PEC water splitting.

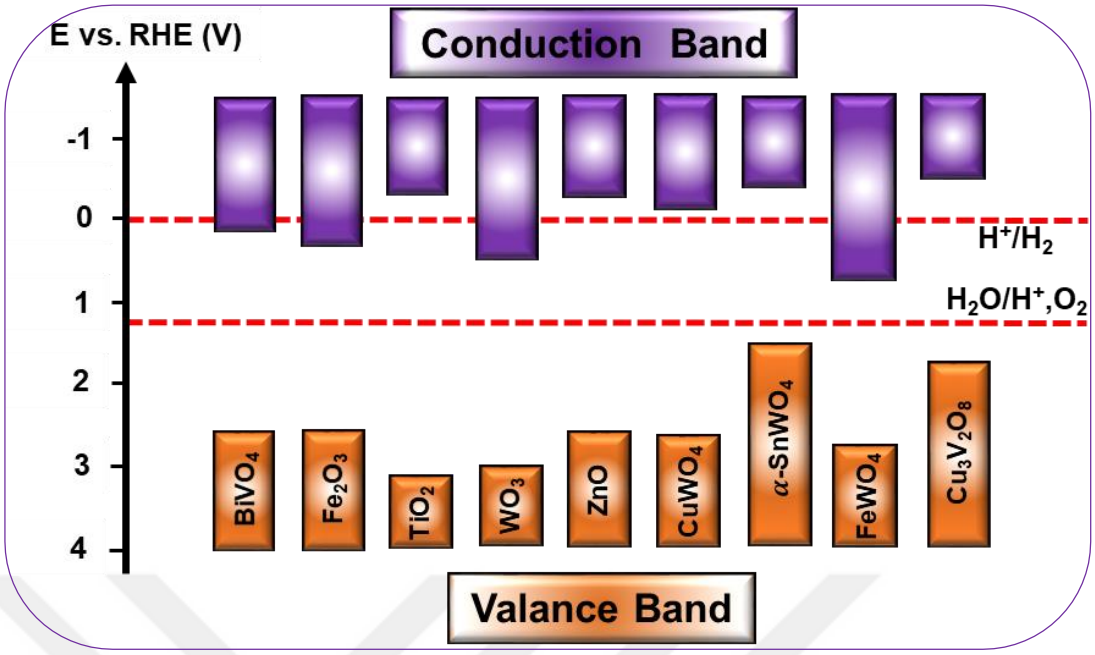

Figure 2. 12 Valence and conduction band edge for n-type metal oxide-based photoanodes. The blue dash lines show potential levels for water oxidation (1.23 VRHE) and reduction (0.0 VRHE)

2.4.1 Titanium dioxide (TiO_2)

TiO_2 has been one of the most widely reported n-type photoanodes among semiconductor materials since its use as PEC water splitting by Fujishima and Honda in 1972 [120–122]. Researchers have reported this photoanode many times because of its essential properties. These properties are primarily environmental friendliness, non-toxicity, economy, photocatalytic activity, corrosion resistance, and chemical stability [122,123]. Figure 2.13 demonstrates the researcher's three well-known TiO_2 crystal structures: rutile, anatase, and brookite. The band gap values of these crystal structures are 3.02 eV, 3.2 eV, and 2.96 eV, respectively [117,120]. TiO_2 can absorb only 5% of the solar spectrum due to its enormous band gap value, which corresponds predominantly to the UV region. Also, electron mobility is low. Therefore, STH hydrogen efficiency is very low (η= 2.2% for rutile and 1.3% for anatase TiO_2).Thus, a different method has been investigated to remove obstacles to high STH efficiency. As we know, researchers have studied increasing the surface area, reducing the band gap, and improving charge separation and electron transfer to improve TiO_2's photocatalytic activity [124,125].

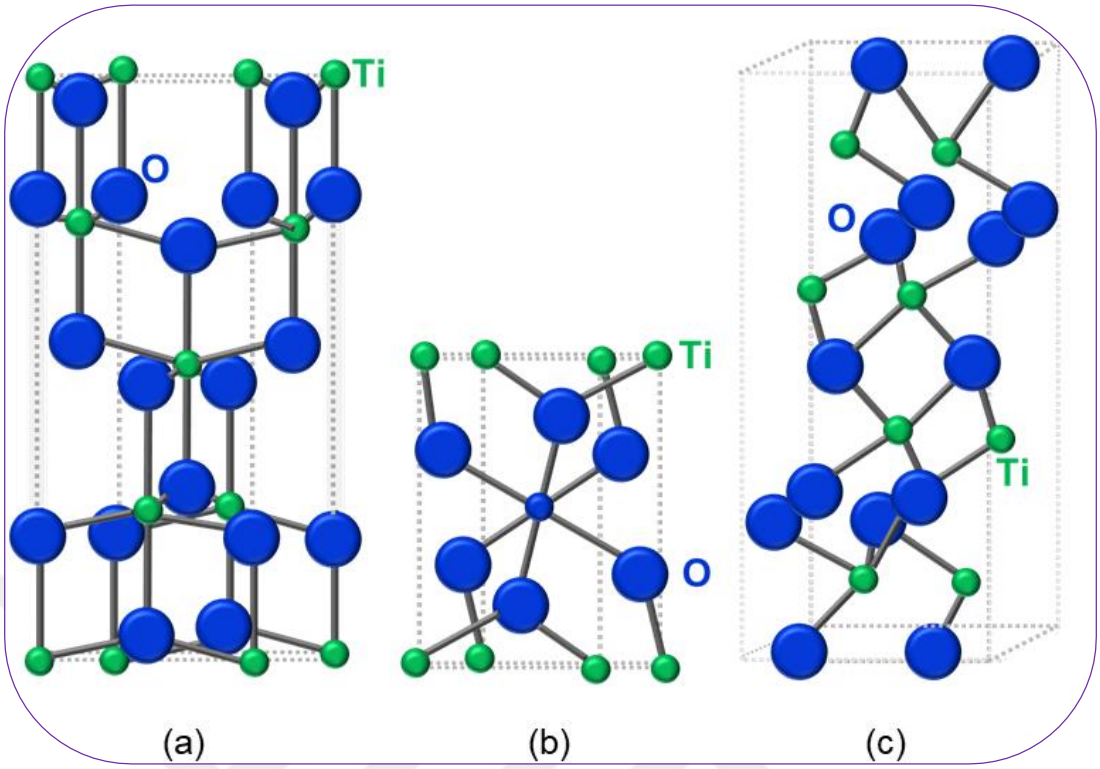

Figure 2. 13 Crystal structures of the TiO_2: (a) anatase, (b) brookite, and (c) rutile phase

Also, researchers have made many attempts to supplement the TiO_2 photoanode with anions and cations. They aimed to improve absorption by considering its stability and low cost while supplementing anions and cations, and they attempted to shift it to the visible range [125].

2.4.2 Hematite (α-Fe_2O_3)

In recent years, hematite (α-Fe_2O_3) has been one of the most promising photoanodes in PEC water splitting studies [118]. Because of its favourable band energy situation and a band gap of about 2-2.2 eV, it can absorb about 40% of sunlight. Besides, it has low cost, high stability, easy fabrication on a large scale, and non-toxicity properties [103,118,119,126]. Nevertheless, hematite has some disadvantages. These can be listed as follows.

1) The conduction band position of hematite is more positive than the proton reduction potential.
2) Due to rapid recombination, the charge carrier lifetime is short.

3) It has a relatively low absorption coefficient and requires a film with a minimum thickness of 400-500 nm for light absorption.
4) Hole mobility is slow due to a short diffusion length for holes. The diffusion length is 2-4 nm.
5) The accumulation of holes in the surface causes an increase in recombination, resulting in the water oxidation kinetics being very low [119].

Various studies have recently been reported to overcome the drawbacks of the hematite-based photoelectrodes mentioned above. The performance of hematite water splitting can be improved, as shown in Figure 2.14.

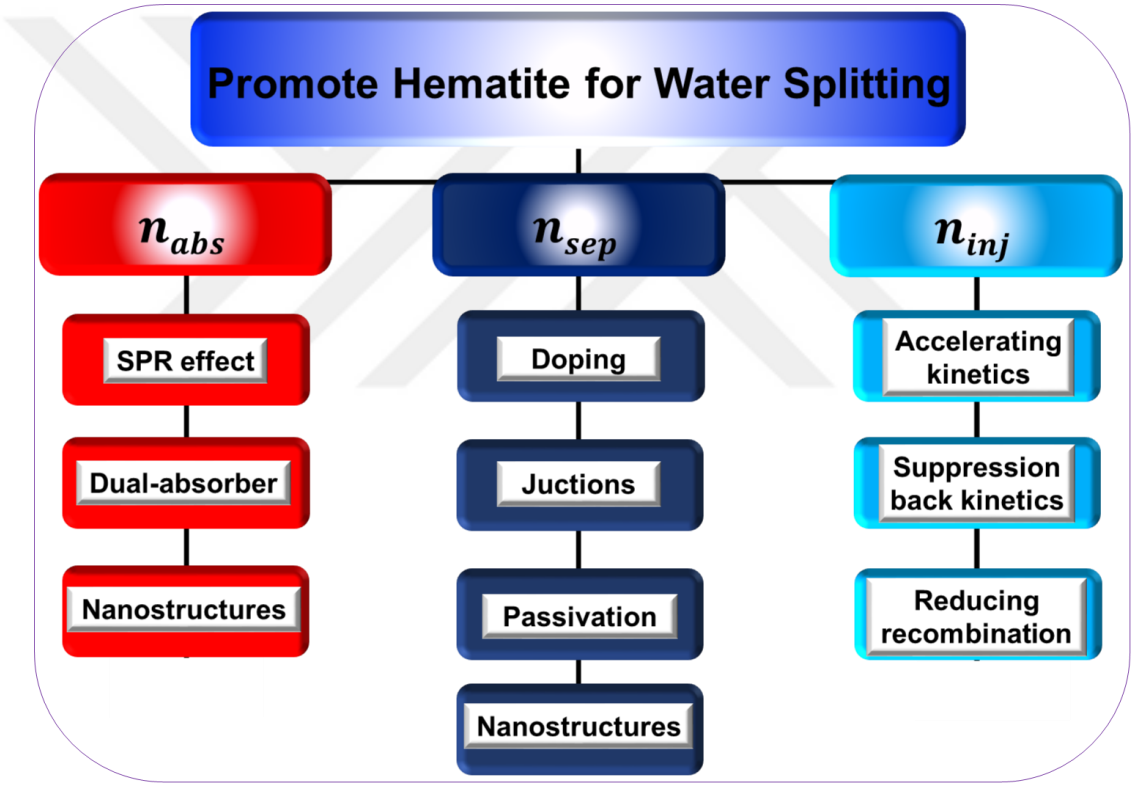

Figure 2. 14 The main strategies for improving hematite PEC performance for water splitting

In the first of these studies, doping was made using different elements such as Si, Ti, and P [119]. It was observed that this high concentration doping increased the conductivity of electrons in hematite. For instance, Si-doped nanocrystalline hematite films showed a significant increase in PEC performance with a photocurrent density of at least 2.7 mA cm^2 against RHE at 1.23V under solar irradiation. Second, it has

been reported that nanostructuring the semiconductor into branched nanorods or core–shells can overcome the short diffusion length of photo holes and facilitate efficient hole transportation to the surface. Thirdly, it has been demonstrated that co-photocatalysts like Co-Pi or FeOOH accelerate surface water oxidation. Finally, the addition of metal oxide under and upper layers on the ($\alpha - Fe_2O_3$) photoanode affects the passivation in the surface state, increasing the concentration and mobility of the charge carriers on the surface [119]. This process shows a remarkable increase in PEC performance [116].

2.4.3 Bismuth Vanadate ($BiVO_4$)

The bismuth vanadate ($BiVO_4$) photocatalyst was first studied by Kudo et al. in 1998 for solar oxidation. Bismuth vanadate ($BiVO_4$) is one of the most promising photoanodes among many investigated semiconductors for PEC water splitting [127]. Bismuth vanadate is an n-type semiconductor. It has a direct band gap and provides a significant visible light absorption of approximately 2.37-2.50 eV because of its very small band gap. Its positive valence band edge (2.4 V vs. RHE) provides enough overpotential for water and organic oxidation [127–129]. At the same time, it has attracted the attention of researchers due to its properties such as stability, neutrality, non-toxicity, and low cost [128]. $BiVO_4$ has a higher CB edge (0.02 V vs. RHE) than n-type photoanodes such as hematite ($\alpha - Fe_2O_3$) and tungsten trioxide (WO_3) which have been extensively studied in the literature [130]. As a result, relatively less bias potential (RHE vs. 0.0 V) is required to boost the photoelectrodes above the water reduction potential. However, although $BiVO_4$ is one of the most promising photoanodes, theoretically, the maximum current efficiency of $BiVO_4$, at 7.4 mA, corresponds to (1.23 V vs. RHE), and the STH value has been reported as approximately 9.1% in the literature [128,131]. In light of these results, its properties are still not fully exploited in PEC water splitting research due to some shortcomings [131–133]. As the disadvantages of $BiVO_4$, photogenerated electron-hole recombination, very poor electrical conductivity, and slow kinetic hole transfer for water oxidation are the most common limitations in the literature [128,130–132]. Various reported modification techniques have schematically demonstrated improved

hydrogen generation performance using PEC water splitting for $BiVO_4$ photoanodes (Figure 2.15).

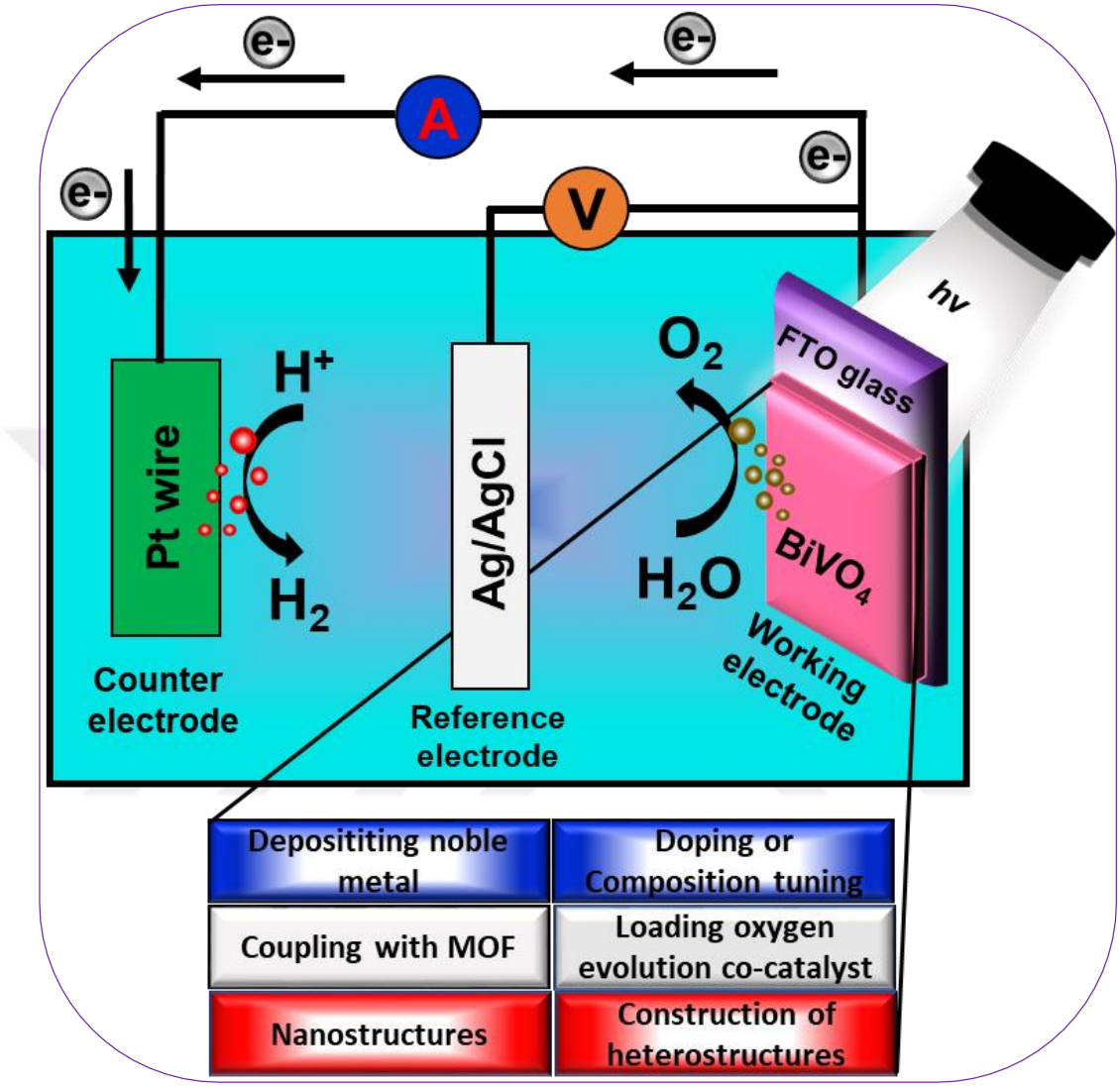

Figure 2. 15 Methods applied to improve PEC performance of $BiVO_4$

Doping methods to improve $BiVO_4$ electron transfer may be an excellent strategy to improve photocurrent and PEC performance. For example, Patil et al. reported that 2% Ag doping in pure BVO boosted the photocurrent density performance threefold compared to pure BVO [128,134]. In another study, Martin Rohloff et al. measured the photocurrent density of Mo-doped $BiVO_4$ photoanodes at 1.9 mA cm^{-2} at 1.23 V vs. RHE under solar light illumination (a 100 mW cm^{-2}) [128]. Surface modification of $BiVO_4$ with oxygen evolution cocatalysts such as cobalt phosphate (Co-Pi) is an

effective way to accelerate OER kinetics [128,135]. For W-doped $BiVO_4$ and Mo-doped $BiVO_4$, Co-Pi, and $BiVO_4$ semiconductors were modified, and their performance under 1sun (100mW/cm^2) light was investigated. Photocurrent densities at (1.23 V vs. RHE) have increased to 1.25 and 4.6 mA cm^2, respectively [128,136,137]. Tian et al. used tannic acid interact with Co ions (TACo) as an effective cocatalyst to suppress charge carrier recombination on $BiVO_4$ photoanodes, achieving a high photocurrent density of 4.8 mA cm^{-2} at 1.23 V (vs. RHE), (AM 1.5 G), which is about 3-fold higher than pure $BiVO_4$ [135].

2.4.4 Zinc Oxide (ZnO)

Zinc oxide is composed of zinc (2+) and oxygen (2-), both of which are abundant in the earth's crust. An essential reserve of approximately 230 million ZnO produces this metal oxide, which is advantageous compared to others [138]. Besides, it is odourless, has a bitter taste, and is insoluble in water. ZnO has been used in catalysis, ceramics, varistors, fertilizers, rubber and paint industries, and cosmetics as an essential semiconductor material [139]. Generally, ZnO can exist in three different crystal phases: rock salt, zinc blende, and hexagonal wurtzite (Figure 2.16) [138,139]. Among these, hexagonal wurtzite is the most stable in ambient conditions [138,140].

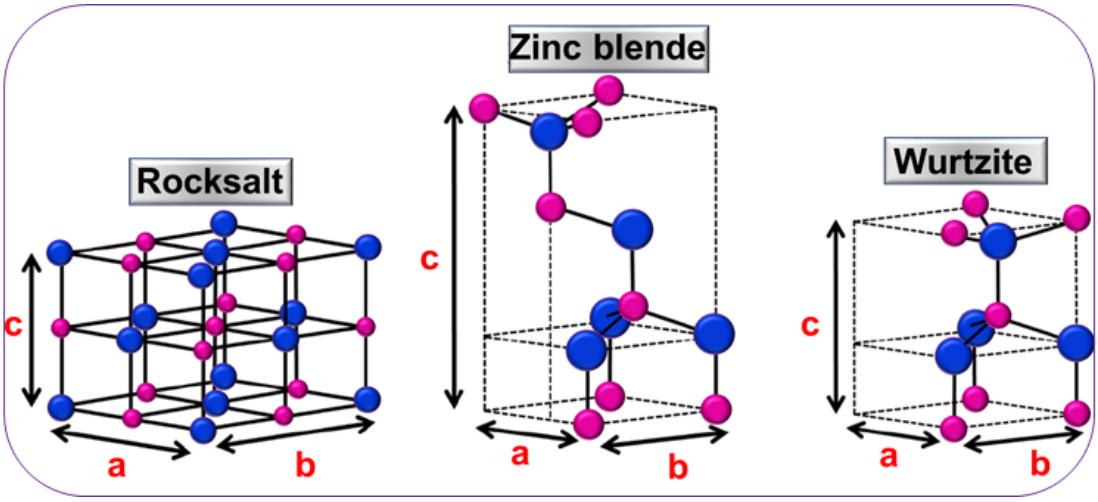

Figure 2. 16 The crystal structures of the ZnO; blue spheres represent zinc, whereas pink spheres represent oxygen

In the last ten years, there has been an increase in research on photoanodes using high-quality inorganic semiconductors (i.e., transition metal oxides such as TiO_2, ZnO,

Fe_2O_3, and SnO_2) for a PEC system [23]. Among the metal oxides mentioned above, ZnO is the most investigated photoanode after TiO_2 [141]. ZnO has been the most widely utilized photoanode due to considerable advantages, including low cost, environmentally friendly, easily adjustable morphology (including nanotrees, nanorods, nanosheets, nanowires, nanotubes, and so on), high electron mobility (bulk mobility: 200 $cm^2V^1s^1$), high catalytic activity [23,142–145]. Besides this, ZnO has been widely reported for PEC water splitting because of its performance comparable to TiO_2 in numerous catalytic reactions. The top of the ZnO photoanode VB is much more positive than water oxidation, while the bottom of CB is slightly more negative than the hydrogen reduction potential (Figure 2.17) [140]. These provide a significant advantage because ZnO conducts holes in water as the photoanode. Moreover, this advantage increases the PEC conversion efficiency by enhancing the separation of photogenerated electron-hole pairs in the photoanode [140].

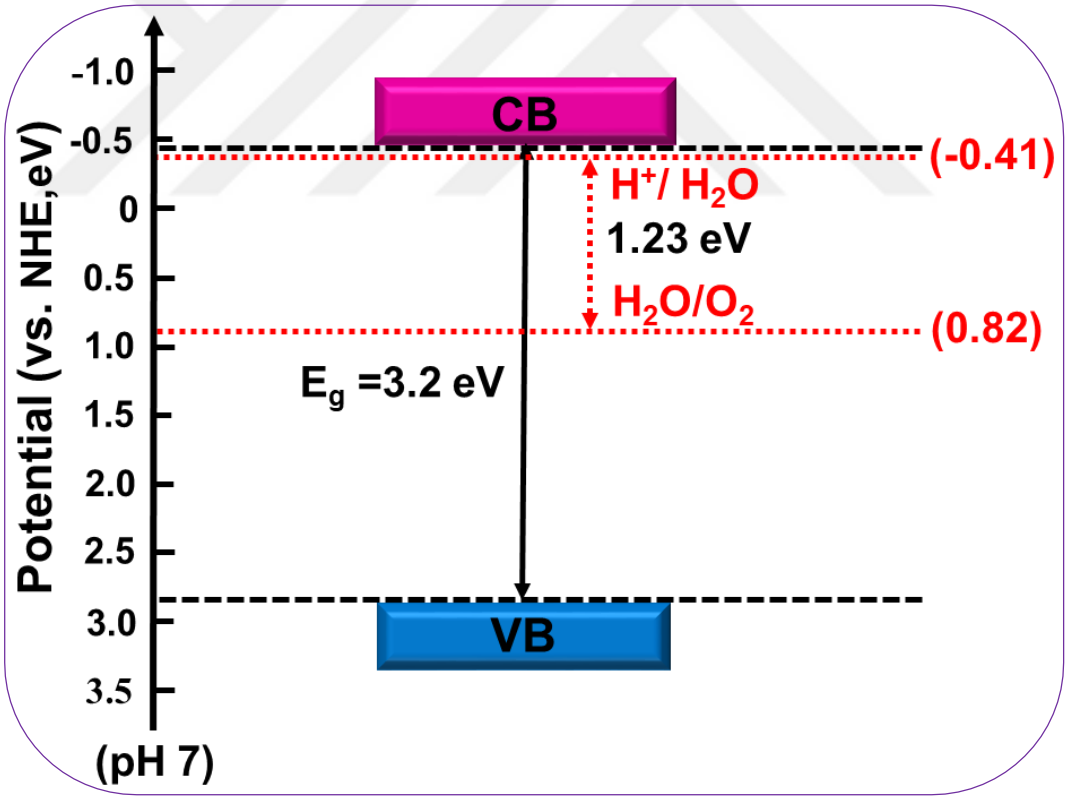

Figure 2. 17 Energy potentials of ZnO and redox potentials for PEC water splitting at pH = 7, relative to NHE

Despite these remarkable properties, ZnO-based photoanodes have not been commercialized on a large scale in PEC water splitting due to several limitations [142,146]. These restrictions are explained in the literature as follows: (i) The ZnO photoanode can benefit from UV light, which accounts for only 5% of the solar spectrum, due to its n-type direct wide band gap (Eg 3.1-3.37 eV) [23,138,140,142,145,147]; (ii) The rapid recombination of electrons and holes at the photoanode-electrolyte solution interface; (iii) Another severe limitation is ZnO decomposition when the pH of the solution is too low or too high, even in dark conditions [139,140,147]. Given the mentioned limitations, several effective methods exist to improve the photoelectrocatalytic activity of ZnO, including enhancing the separation efficiency of photogenerated electron-hole pairs, improving the surface reaction rate, and expanding the absorption spectrum to the visible light region [139,140,147]. Many studies have reported that constructing a heterojunction between ZnO and other semiconductors with a suitable band gap value effectively accelerates photogenerated electron-hole separation and increases the light absorption spectrum [148]. As a result, the conversion efficiency from solar to hydrogen is improved. For example, Bai et al. fabricated the ZnO NAs/RGO/Zn_2S_4 heterojunction, which was prepared by the solvothermal method using an aqueous Na_2SO_4 solution, and measured the PEC performance under Xenon (100mW/cm^2) illumination. As a result, NA_S/RGO/$ZnIn_2S_4$ heterojunctions outperformed pure ZnO NAs by more than 200% in photo-hydrogen conversion efficiency [148]. Celebi et al. reported the synthesis of carbon-incorporated yolk-shell ternary heterostructures of ZnO@C-CeO_2. Their research measured the highest photocurrent density of 7.43 mA/cm^2 at 1.18 V under light and found no remarkable response in dark conditions. According to the researchers, a conductive N-doped graphite carbon layer with mesoporous hollow morphologies improves PEC performance by facilitating charge transfer between the photoanode and electrolyte interfaces due to increased photon absorption and electron-hole separation efficiency [53].

2.5 Semiconductor for Photoelectrochemical Water Splitting

2.5.1 Cerium Oxide (Ce_2O)

The photocatalytic activity of a photocatalyst is highly dependent on some properties of that catalyst, such as its structure, morphology, and property. CeO_2 is one of the metal oxide semiconductors, and this semiconductor is the most frequently applied semiconductor after TiO_2 [149]. CeO_2 is an n-type semiconductor and an indirect semiconductor [150]. Figure 2.18 shows the cubic fluorite structure, the most stable crystal structure of CeO_2, and its strong adsorption capacity. Also, the theoretical band gap of pure CeO_2 is indicated as 6.0 eV in the literature. However, this bandgap varies between 2.6 and 3.4 eV, depending on the fabrication methods [149].

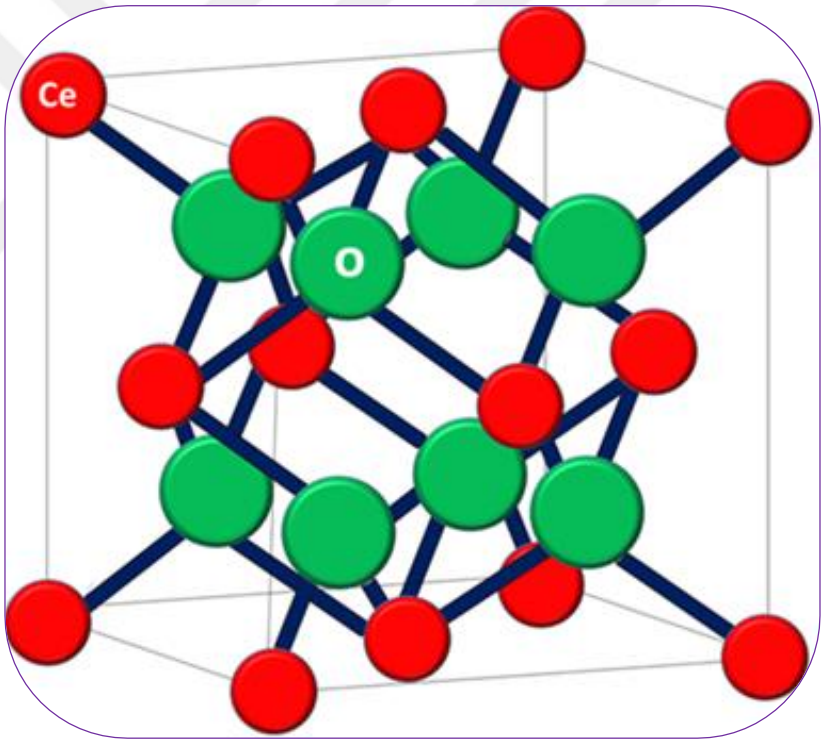

Figure 2. 18 Crystal structures of the CeO_2

Recently, rare earth oxide CeO_2 has been used as a promising semiconductor in catalysis studies, such as electrocatalysis, fuel cell, solar cell, photocatalyst, gas sensor, solid-state electrolytes, and water splitting for the generation of hydrogen, etc [151]. In addition to these application areas, the CeO_2 semiconductor performs well in the

UV region. So, it is utilized to protect against the sun in sunglasses lenses and cosmetic products. Moreover, CeO_2 has excellent properties, such as Ce^{+3} and Ce^{+4} redox couple, which are advantageous for low toxicity, cheap, high oxygen storage, chemical stability, and the formation of many oxygen vacancies [152,153]. Due to these advantages, it can reduce electron-hole recombination and increase its photocatalytic activity. Nonetheless, CeO_2 has disadvantages such as a wide bandgap (approximately 3.4 eV), low specific surface area, fast electron-hole recombination, and lower visible region absorption until 400 nm. The CeO_2 photoanode can only use 5% of the solar spectrum. To improve the shortcoming of the CeO_2 mentioned above, its performance has been significantly increased by making studies such as changing the electronic band alignment, restricting the electron-hole recombination, and boosting the electron-hole. Besides this, modifications to improve the CeO_2 photocatalytic performance are also shown in figure 2.19. In the literature, CeO_2 materials with different morphologies have been produced using other techniques. For example, thermal evaporation, co-precipitation, sol-gel, electrochemical, solvothermal synthesis, etc. The method of synthesis of the CeO_2 photocatalyst is very crucial because it has a direct impact on photocatalytic performance.

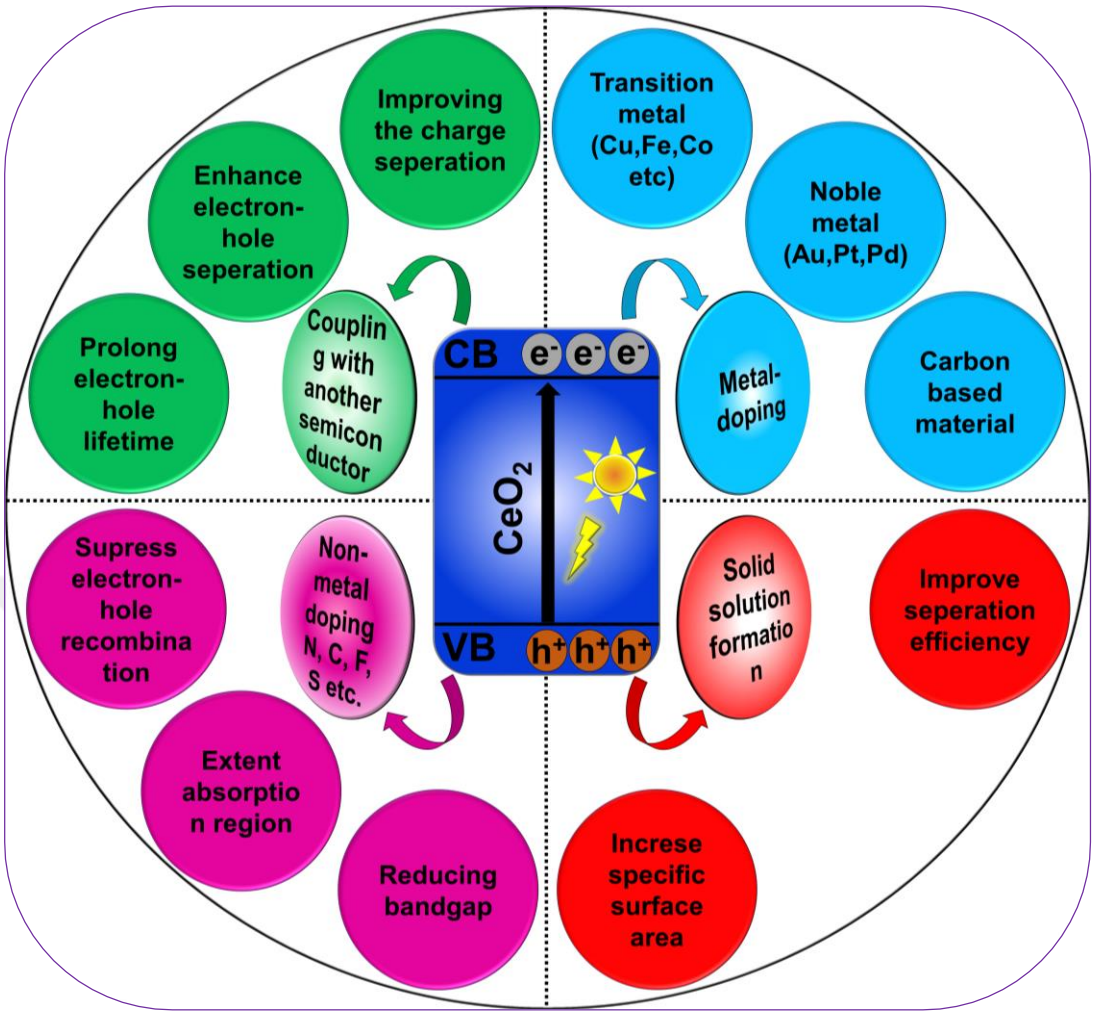

Figure 2. 19 Modification pathway to improve the CeO_2 photocatalytic performance

2.5.2 Metal-Organic Framework (MOFs)

Metal-organic framework MOFs are defined as crystalline materials with organic linkers and a metal oxide centre, with high porosity, large surface area, and unlimited network structures [154–157]. Porous coordination polymer or metal-organic frameworks (MOFs) have been over-reported over the past decade for their excellent properties. Information about structures and their importance in MOF studies was initiated by Robson, Moore, Yaghi, Kitagawa, and the Férey group in 1990. [55,155,158]. MOF structures are a new type of porous materials that have increased in importance in recent years with the combination of organic linkers and metal structures [155]. Thanks to its modular structure, it can be controlled chemically, structurally, and easily adjusted. Moreover, its synthetic design can be used in certain

areas due to its properties such as porosity, stability, conductivity, and particle morphology. Also, after the BET analysis, it has an extensive surface area of approximately 10000 $m^2 g^{-1}$ [155]. This value is considerably higher than their surface area compared to zeolite and carbon. More than 20000 MOF structures we know so far have been reported in the literature and are available in companies such as Sigma-Aldrich and Strem Chemical. Recently, studies of research groups to produce MOF-based photocatalysts have attracted attention due to some disadvantages of photocatalysts based on conventional semiconductors (such as recombination and solar photon utilization being about 5%) [155]. The essential properties of MOF have allowed it to be used in many fields such as CO_2 reduction [159,160], electrochemical and PEC water splitting [154,160], degradation of organic pollutants [161], catalysis [162,163], sensing [164], and adsorption [165]. Researchers have widely reported many MOFs for electrochemical and PEC hydrogen production as an active photocatalysts. An intrinsic property of MOFs is to keep their functionalities and structural properties intact; post-synthetic modification techniques make them suitable as the indispensable catalyst material for water-splitting. In addition, to continue and support water-splitting reactions, MOFs offer physical, chemical, and electronic versatility. The MOF-5 structure and the chemical formula of terephthalic acid used in this thesis are schematically below (Figure 2.20a-b) [166–168]. MOF-5 has the chemical formula $Zn_4O\ (BDC)_3(DMF)_8(C_6H_5Cl)$ and was first reported by Yagni et al. in 1999 [166,169].

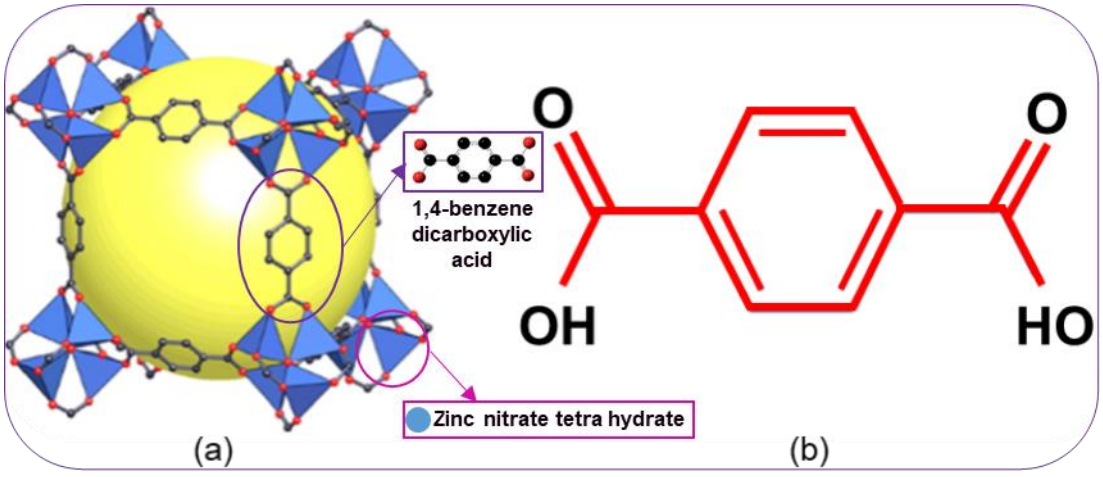

Figure 2. 20 (a) The structure of IRMOF-1 (MOF-5) with the Zn_4O tetrahedra indicated in blue and the cavity indicated by a yellow sphere (O, red; C, black) (b) Chemical structure of terephthalic acid

MOF-5, where DMF represents dimethylformamide and BDC represents terephthalic acid, comprise of Zn_4O clusters attached to ditopic linear BDC linkers [166]. MOF-5 molecules, with BET surface areas ranging from 260 to 4400 m^2g^{-1}, thermal stability up to 400°C, and 0.92-1.04 $cm^3\ g^{-1}$ micropores, aid in the resolution of problems encountered in materials used in biology, medicine, etc [168,170]. Figure 2.21 shows some of the MOF structures developed and widely used by the research communities [171].

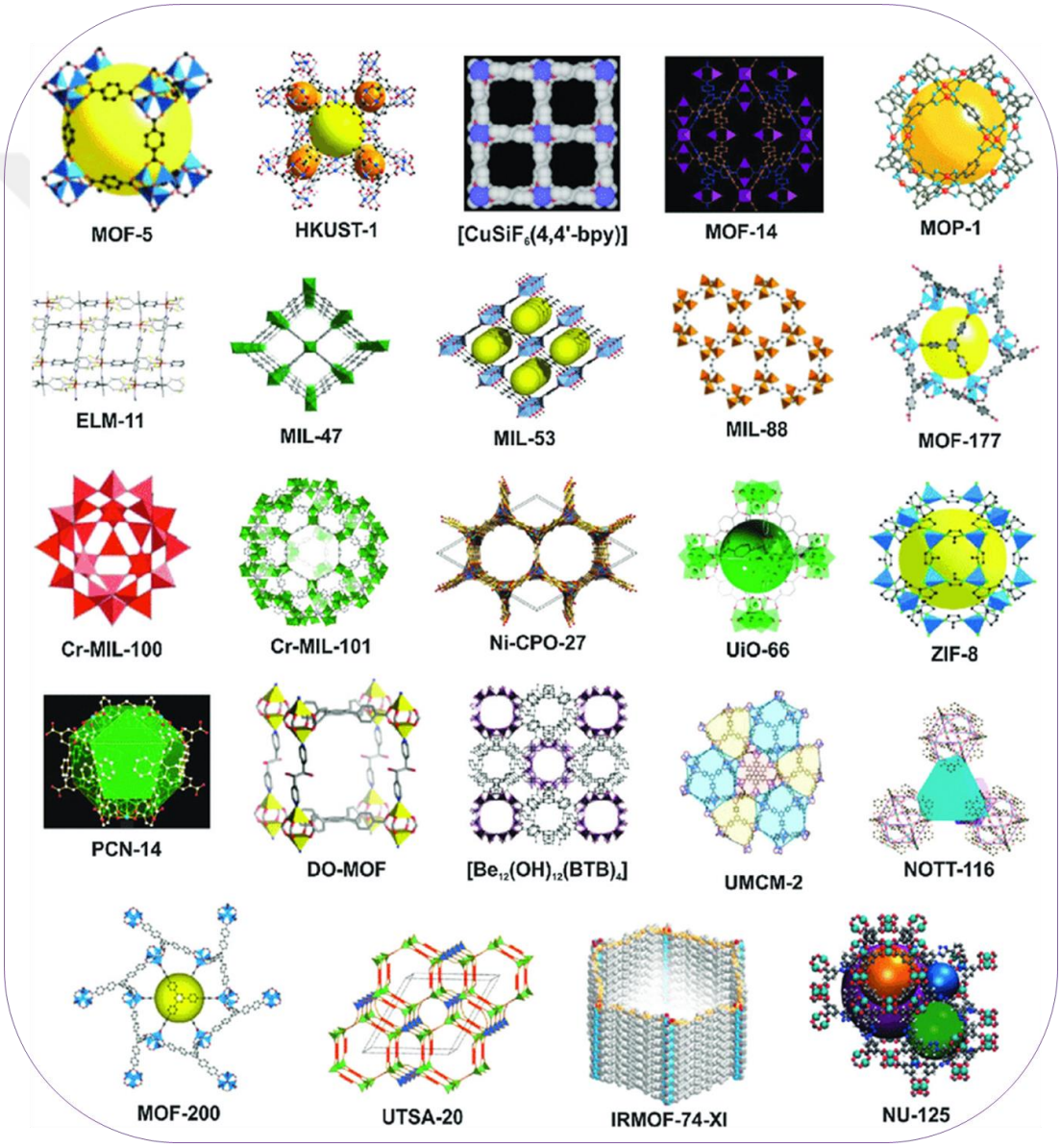

Figure 2. 21 Several research groups produced porous MOFs to accommodate/retain chemical species in their pores/channels [171]

CHAPTER 3

MATERIALS and METHODS

3.1 ZnO@PDA/CeO_2 NPs PEC Hydrogen Generation

3.1.1 Material

In this thesis, experimental studies were carried out with high purity chemicals. Zinc acetylacetonate ($Zn(acac)_2$), N, N-dimethylformamide (DMF), polyvinylpyrrolidone (PVP), sodium hydroxide (NaOH), cerium nitrate hexahydrate ($Ce(NO_3)_3.6H_2O$), dopamine hydrochloride and acetone (99,8%) were purchased from Sigma-Aldrich, USA. Absolute ethanol was received from Merck, Germany. Additionally, terephtalic acid (TPA), 2-propanol, ethylenediaminetetraacetic acid (EDTA), sodium sulfate (Na_2SO_4), nafion solution, 1,4-benzoquinone (BQ) and methylene blue (MB) were supplied from Sigma-Aldrich, USA. The cleaning of all glass materials used in the study was carried out using ultrapure water (≥18.2 M, Milli-Q, Millipore) in the experimental stages. In the PEC analysis, Fluorine-doped Tin oxide (FTO) was used as the working electrode, Pt wire was used as the counter electrode, and silver, silver chloride (Ag/AgCl) was used as the reference electrode. Also, a white COB LED (Light Emitting Diode), (Luminus XNova CMX-18, China) was used as the visible-light illumination source.

3.1.2 Fabrication Methods

In this thesis, ZnO@PDA/CeO_2 heterojunctions were fabricated using a systematic layer-by-layer approach (Figure 3.1). At first, star-shaped ZnO nanoparticles were synthesized by a hydrothermal method. Typically, zinc acetylacetonate ($Zn(acac)_2$, 60 mg) and PVP (0.1 g) were introduced into DMF/H_2O mixture (10 mL/2 mL). Subsequently, the pH of the medium was adjusted to 10 using an aqueous NaOH solution (0.25 M). Afterwards, the as-prepared solution was put into a stainless-steel Teflon-lined reactor and annealed at 140 °C for 90 min. After cooling down to room temperature, ZnO nanoparticles were precipitated by centrifugation at 5000 rpm for 3

min and washed with acetone and ethanol mixture several times [150,172]. In the second stage, ZnO nanoparticles were coated using polydopamine (PDA) according to the previously reported study with some modifications [150,173,174]. 13 mg ZnO was added into 10 mM Tris-HCl solution (20 mL, pH: 8.5) while mixing and sonicated for 10 min. Subsequently, 1 mg dopamine hydrochloride was introduced, and the obtained mixture was vigorously stirred at room temperature for 3 h. Afterwards, ZnO@PDA nanoparticles were separated from the medium using a centrifugation-decantation method and washed with water several times.

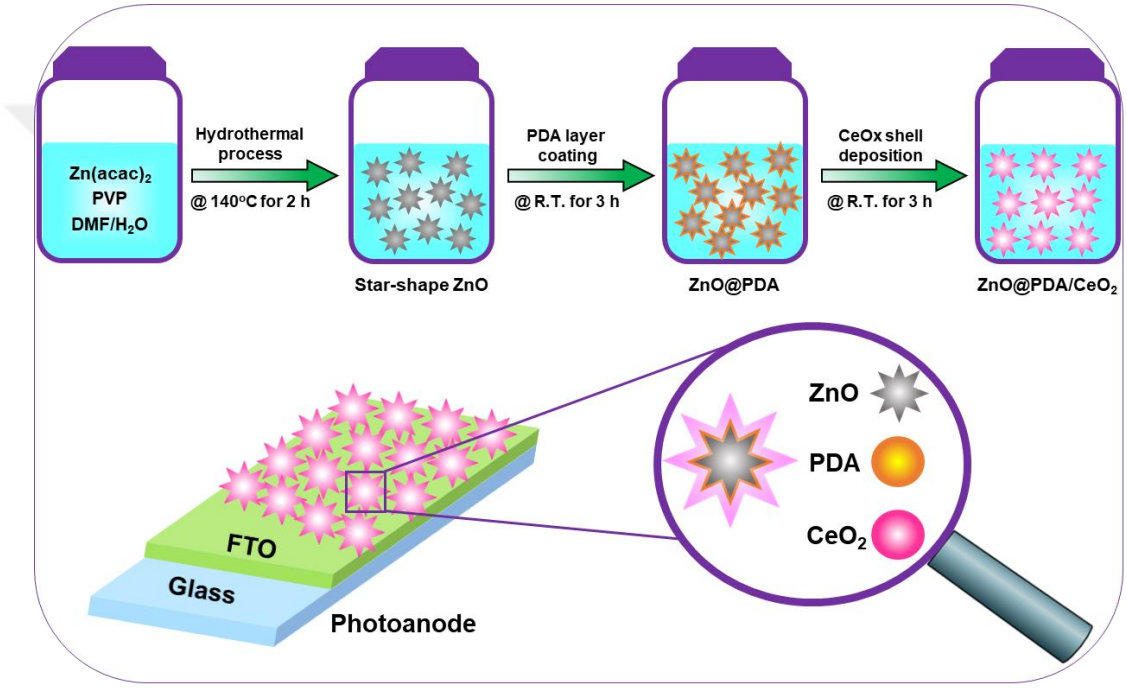

Figure 3. 1 Schematic synthesis pathway of ZnO@PDA/CeO_2 NPs

In the last stage, CeO_2 nanoparticles were coated onto ZnO@PDA nanoparticles thanks to the abundant catechol active sites as well as the redox activity of the catechol moieties. For this purpose, the as-prepared ZnO@PDA nanoparticles were introduced into an aqueous solution of $Ce(NO_3)_3.6H_2O$ (250 mg in 20 mL H_2O) and stirred at room temperature for 2 hr. Subsequently, 830 µL of NaOH solution (1.0 M) was added to the mixture, and the stirring continued for one h. Finally, the obtained ZnO@PDA/CeO_2 heterostructures were isolated from the reaction medium using a centrifugation-decantation procedure and washed with DI water several times

[150,175,176]. The obtained ZnO@PDA/CeO_2 heterostructures were re-dispersed in DI water and stored in the dark for further usage.

3.1.3 Photocatalytic Dye Degradation and Trapping Experiments for ZnO@PDA/CeO_2 NPs

The photocatalytic activity of ZnO@PDA/CeO_2 heterojunctions was determined using a homemade photo-reactor (Figure 3.2). The intensity of LED light was measured (30 mW/cm^2) by a Solar Power-meter (Mastech SM206, China). Briefly, 10 mg of ZnO@PDA/CeO_2 photocatalyst was added into an aqueous solution of MB (10 mL, 3.125×10^{-5} M) and stirred in the dark (@room temperature for 30 min), and the adsorption-desorption equilibrium was obtained.

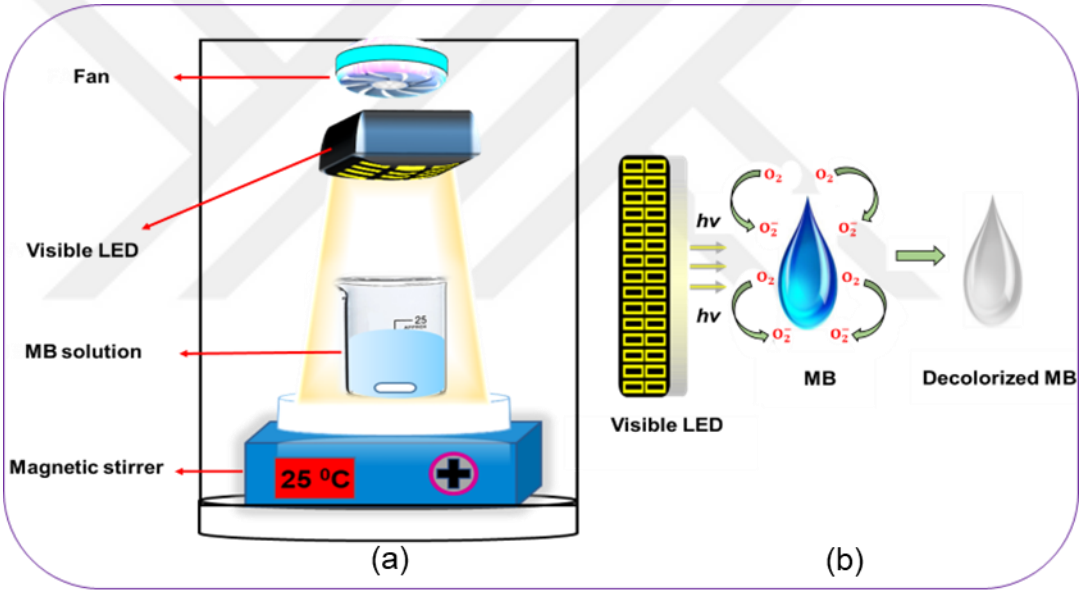

Figure 3. 2 (a) Schematic representation of the home-made visible LED photo-reactor, and (b) plausible degradation pathway using visible LED light array and reduction of O_2^-

Then, the dispersion was irradiated with the white LED light source, and the sampling was carried out to achieve the real-time concentration of MB dye solutions. Subsequently, the dispersion was centrifuged to separate the supernatant from the catalyst, and a UV-vis spectrometer determined concentrations at 610 nm with a calibration graph [150,177]. Moreover, different scavengers, isopropanol (IPA, $\cdot OH$), EDTA (h^+), and BQ, $\cdot O_2^-$ were used to test the effect of active species in photocatalytic reactions. The applied procedure was the same with MB photocatalytic degradation in

which the sampling was performed at 60 min to study MB real-time concentration. Moreover, generation of $\cdot OH$ and $\cdot O_2^-$ by photocatalyst were detected with fluorescence method. For this purpose, 10 mg catalyst was mixed with a 10 mL aqueous solution containing 0.5 mM TPA and 0.2 mM NaOH under the LED light. Samples were collected to specify hydroxyl radicals ($\cdot OH$) with photoluminescence (PL) measurements. Peroxide radicals ($\cdot O_2^-$) were identified with a similar procedure, except that 0.5 mM BQ solution was used instead of TPA and NaOH solution [67,150].

3.2 ZnO@MOF-5-C NPs for PEC Hydrogen Evolution

3.2.1 Material

In this thesis, experimental studies were carried out with high purity chemicals. Zinc acetylacetonate ($Zn(acac)_2$), cerium nitrate hexahydrate ($Ce(NO_3)_3.6H_2O$), N, N-dimethylformamide (DMF), sodium hydroxide (NaOH), polyvinylpyrrolidone (PVP), dopamine hydrochloride and acetone (99,8%) were purchased from Sigma-Aldrich, USA. Absolute ethanol was supplied by Merck, Germany. Additionally, Terephtalic acid (TPA), ethylenediaminetetraacetic acid (EDTA), sodium sulfate (Na_2SO_4), nafion solution, 1,4-benzoquinone (BQ), 2-propanol, and methylene blue (MB) were supplied from Sigma-Aldrich, USA. The cleaning of all glass materials used in the study was carried out using ultrapure water (≥18.2 M, Milli-Q, Millipore) in the synthesis stages. In the PEC measurements, Fluorine-doped Tin oxide (FTO) was used as the working electrode, Pt wire was used as the counter electrode, and silver, silver chloride (Ag/AgCl) was used as the reference electrode. In addition, the visible-light illumination source used 300 W Xe (Xenon Lamb).

3.2.2 Synthesis Methods

ZnO@MOF-5-C ternary heterojunctions were synthesized based on a systematic layer-by-layer approach (Figure 3.3). At first, star-shaped ZnO nanoparticles were synthesized using a hydrothermal method. The synthetic pathway of ZnO nanoparticles were described in Section 3.1.2 in detail.

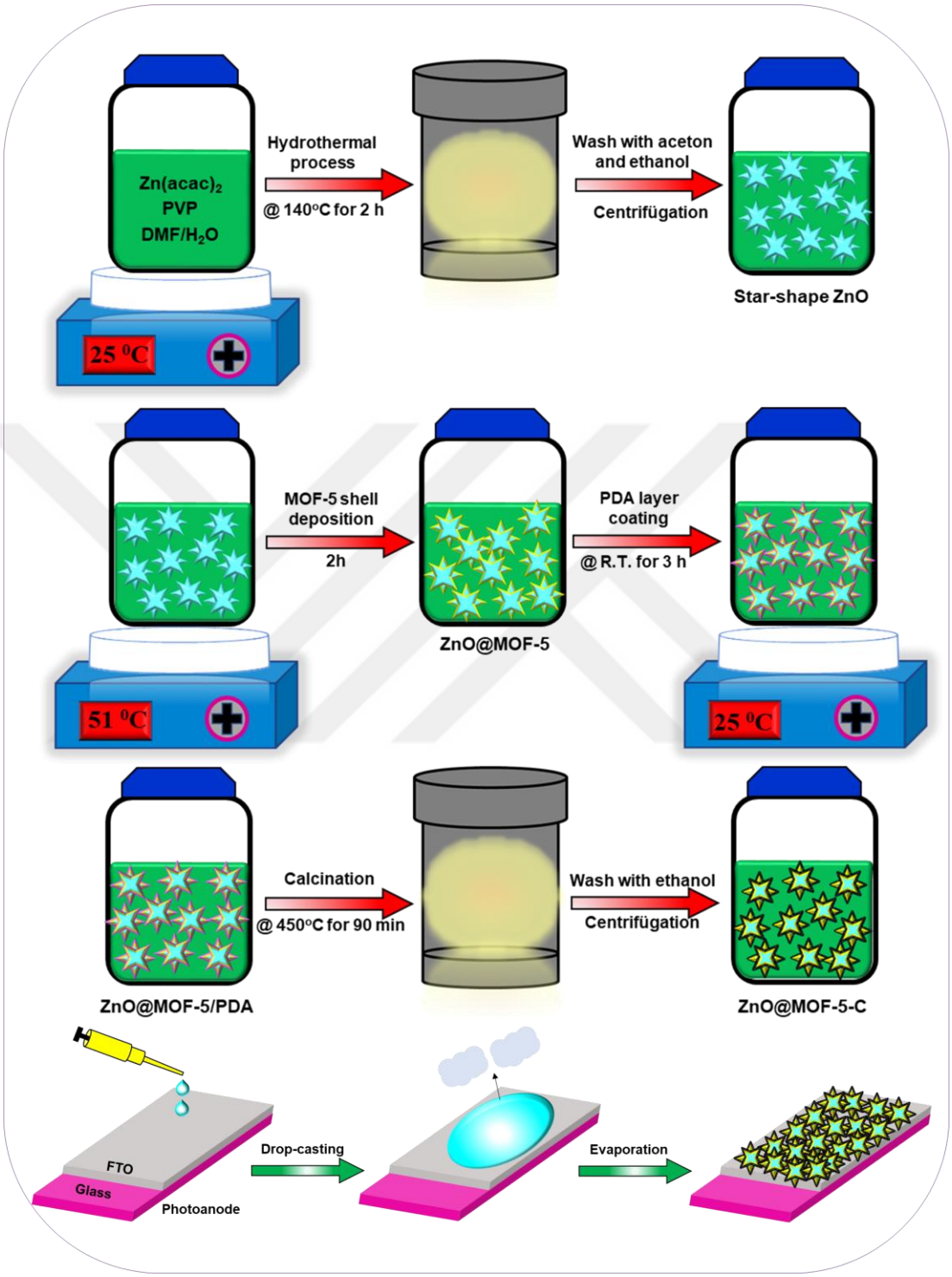

Figure 3. 3 Schematic fabrication route of the ZnO@MOF-5-C NPs

In the second step, MOF-5 nanoparticles were synthesized onto ZnO star nanoparticles. Briefly, the ethanol-terephthalic acid solution (10 mg in 10 mL EtOH) was added to the as-prepared ZnO (5 mg in 5 mL of EtOH) nanoparticles and stirred at 51 °C for 2 hours in a temperature-controlled magnetic stirrer [150,172]. Lastly, the resulting ZnO@MOF-5 core-shell heterostructures were isolated from the reaction medium using the centrifugation-decantation method and washed several times with ethanol [150,175,176]. Thirdly, ZnO@MOF-5 nanoparticles were coated with polydopamine (PDA) using previous techniques [173]. In other words, 5 mg ZnO@MOF-5 was added into 10 mM Tris-HCl solution (20 mL, pH: 8.5) while mixing and sonicated for 10 min. Subsequently, 1 mg dopamine hydrochloride was introduced, and the obtained mixture was vigorously stirred at room temperature for three hours. Then, ZnO@MOF-5-PDA nanoparticles were separated from the medium using the centrifugation-decantation method and washed with water several times. After this process, it was taken into the porcelain bowl and calcinated at 450 °C (3°C /min. heating) degrees for 45 minutes.

3.2.3 Trapping Experiment for ZnO@MOF-5-C NPs

In the trapping experiment, the effect of active species on the photocatalytic reaction was tested using different scavengers, terapterephthalic acid (TPA, ·OH), and (BQ, $\cdot O_2^-$). In this experiment, the Xenon light source shown in Figure 3.4 was used, and its light intensity (100 mW/cm^2) was measured using a solar energy meter (Mastech SM206, China). The trapping experiment steps were the same with MB photocatalytic degradation in section 3.1.3. The trapping experiment were performed for 60 minutes to examine the effect of active species on the photocatalytic reaction. Furthermore, the photocatalyst's production of ·OH and $\cdot O_2^-$ was determined using the fluorescence technique. For this purpose, firstly, 4-mg catalyst was mixed with 4 mL aqueous solution containing 0.75 mM TPA and 3 mM NaOH under Xe light. Photoluminescence (PL) measurements were performed to determine the presence of hydroxyl radicals (·OH). A similar procedure was carried out, except that 5 mM BQ solution was used to detect peroxide radicals as well ($\cdot O_2^-$) [53,150].



Figure 3. 4 300 W Arc Xenon Light

CHAPTER 4

PHYSICAL AND CHEMICAL CHARACTERIZATION OF PHOTOANODES

The optical and electrical properties of the photoanodes were examined in this part.

4.1 Uv-Vis Spectroscopy

A UV spectrophotometer is a tool for measuring absorbance, reflectance, and transmittance in materials. This technique can measure the optical properties of materials from the ultraviolet (UV) to the infrared (IR) spectrum. Each molecule emits different wavelengths of light within this broad range. It can be absorbed or reflected. Its spectrum shows the bands corresponding to the structural groups in the molecule. Pure barium sulfate was used as reference material. Figure 4.1 shows the spectrophotometer used in this thesis (UV-1601 Shimadzu spectrophotometer, Japan). The nanoparticles were measured between 200 and 800 nm in diameter.

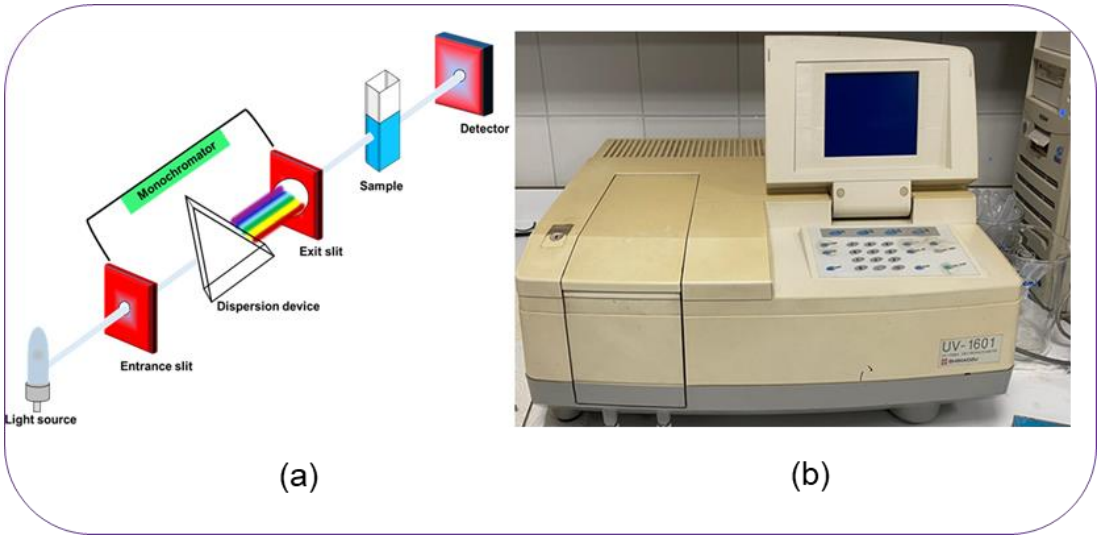

Figure 4. 1 (a) A simplified setup of the primary parts of a UV-Vis spectrophotometer (b) UV-1601 Shimadzu spectrophotometer setup

The band gap of the synthesized nanoparticles was calculated using the Kubelka-Munk function, which can be found in equation 4.1 [53,150,178].

$$(\alpha h\nu)^n = A(h\nu - E_g) \quad \textbf{(4.1)}$$

Where, h is the Planck constant, *v* is the photon's frequency, E_g is the band gap energy, and A is the constant value. The "n" factor depends on the nature of the electron transition and is equal to 2 or 1/2 for the direct and indirect transition band gaps, respectively.

4.2 X-Ray Diffraction (XRD)

X-ray diffraction (XRD) is a vital technique for determining material properties like crystal structure, crystal size, and strain [179]. Figure 4.2 illustrates the working principle of XRD. It operates based on the Bragg's law, which is expressed as the reflection of the incidence of a parallelized X-ray beam on a crystal plane of the sample to be characterized.

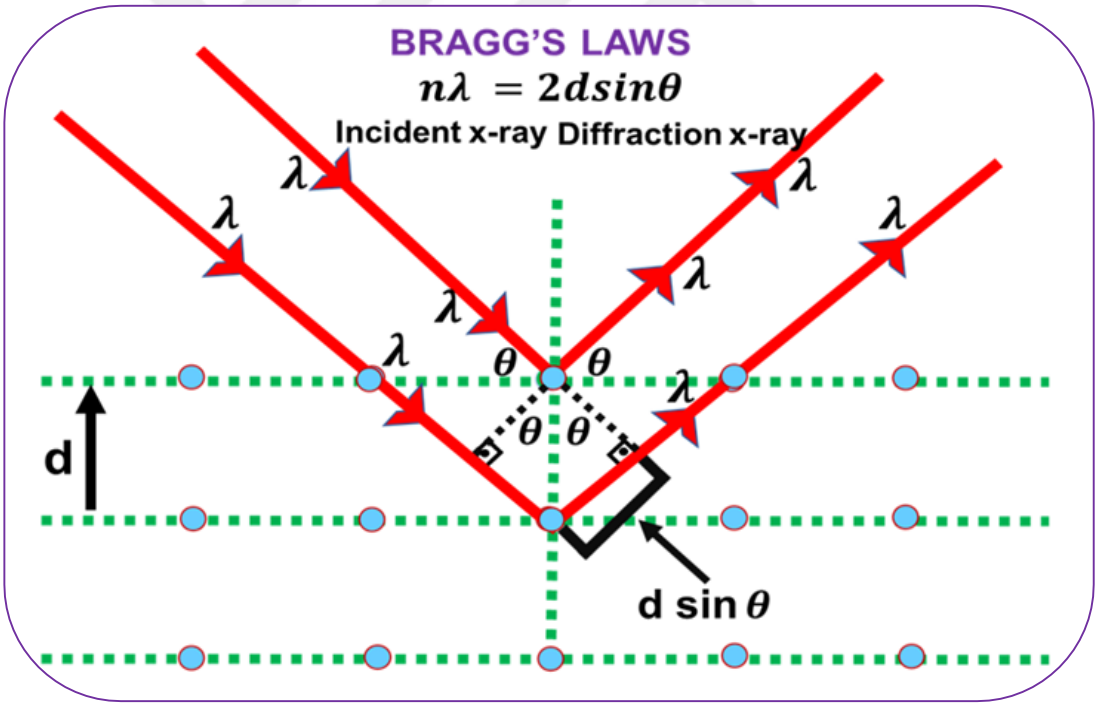

Figure 4. 2 Bragg's law



Figure 4. 3 Rigaku Miniflex 600 Powder X-ray Diffractometer

Diffraction is observed when light is scattered. The atoms are organized in a repetitive and sequential order in the crystal structure, known as the lattice structure. This method uses an electromagnetic beam with a wavelength such as the interatomic space between atoms in the crystal structure. The diffraction patterns produced by X-ray reflection are used to obtain information about the three-dimensional atomic packaging of the materials studied in the crystal structure. As shown in equation 4.2, Bragg's law defines the incident ray's diffraction condition [180].

$$n\lambda = 2d\sin\theta \quad \textbf{(4.2)}$$

Where, *d* denotes the distance between diffraction planes, *θ* is the Brag's diffraction angle, *λ* is the X-ray wavelength, and *n* is an integer. The crystal structure of the nanostructures produced in this thesis was investigated by Cu Ka ½ radiation and X-ray diffraction (XRD) using the Rigaku Miniflex 600 W device in Figure 4.3. In addition, the synthesized nanoparticles were scanned at a step size of 0.02 degrees in the range of 10-80 degrees. The results were compared with known phases (PDF diffraction data files) and analyzed using PDXL software.

4.3 Scanning Electron Microscopy (SEM)

SEM is a powerful characterization analysis method that describes nanoparticle morphology, composition, and structure. The working principle of the SEM device is to generate an electron beam and scan the surface of a sample with this generated electron beam. Varying signals in the form of electrons or energy resulting from interactions between the sample and incoming electrons can be captured by different detectors. Also, EDS is a micro-study of elements' chemical composition and other surface morphology characterization. EDS is determined from SEM images by the distribution of surface maps of elements [179]. In this thesis, nanoparticles' morphology, composition, and structure were investigated using a Scanning Electron Microscope (SEM: Hitachi SU5000, Japan) equipped with a field emission electron gun and coupled with an Energy Dispersion Spectrometer (EDS) (Figure 4.4).



Figure 4. 4 Hitachi SU5000 scanning electron microscopy setup

4.4 Transmission Electron Microscopy (TEM)

Transmission electron microscopy is undoubtedly one of the most important methods of nanoparticle characterization analysis [181]. Some of the basic components of TEM and SEM are electron guns, electromagnetic lenses, and electron apertures. In addition,

they are similar in terms of electron generation. However, in TEM, electrons are transmitted through the sample, and an image is formed with the captured electrons. Despite this, it provides a higher resolution (0.2 nm) than SEM analysis.

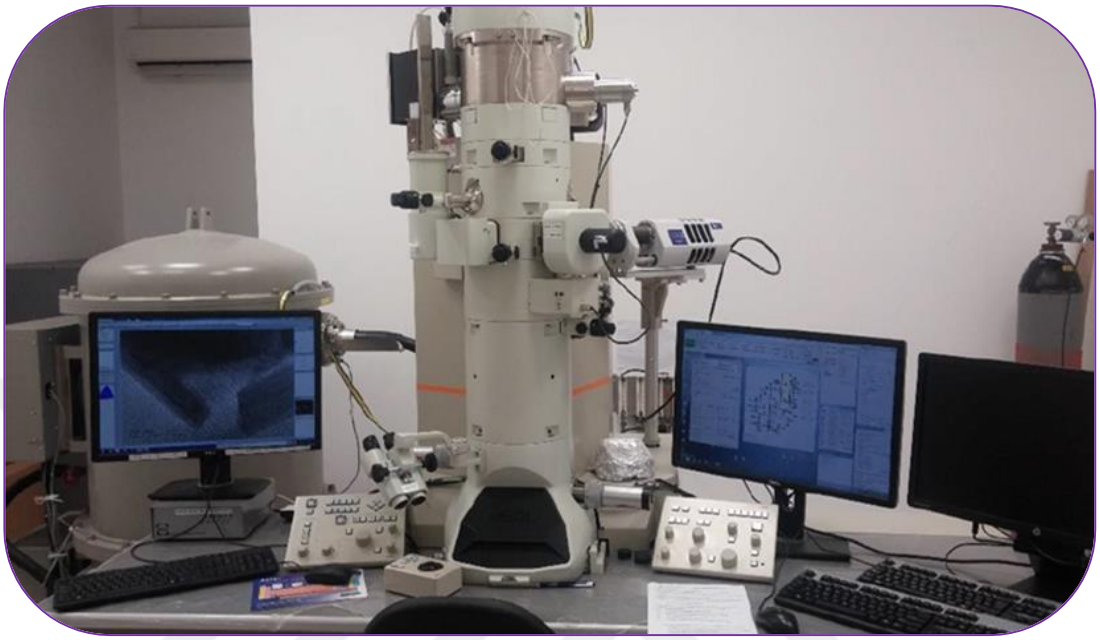

Figure 4. 5 JEOL-2100 F Transmission Electron Microscopy setup

We can learn about the crystal structure, element information, and morphology of material using TEM. Furthermore, TEM images differ depending on the materials density, thickness, and composition. The TEM images in this thesis study were obtained using the JEOL 2100F brand TEM device, as shown in Figure 4.5.

4.5 X-Ray Photoelectron Spectroscopy (XPS)

XPS is commonly used to provide information about a materials basic composition, experimental formula, chemical state, and electronic state. The XPS analyzer works on the principle of measuring the kinetic energy of electrons emitted from the first 1-10 nm of the material by first irradiating a sample with X-rays [182].

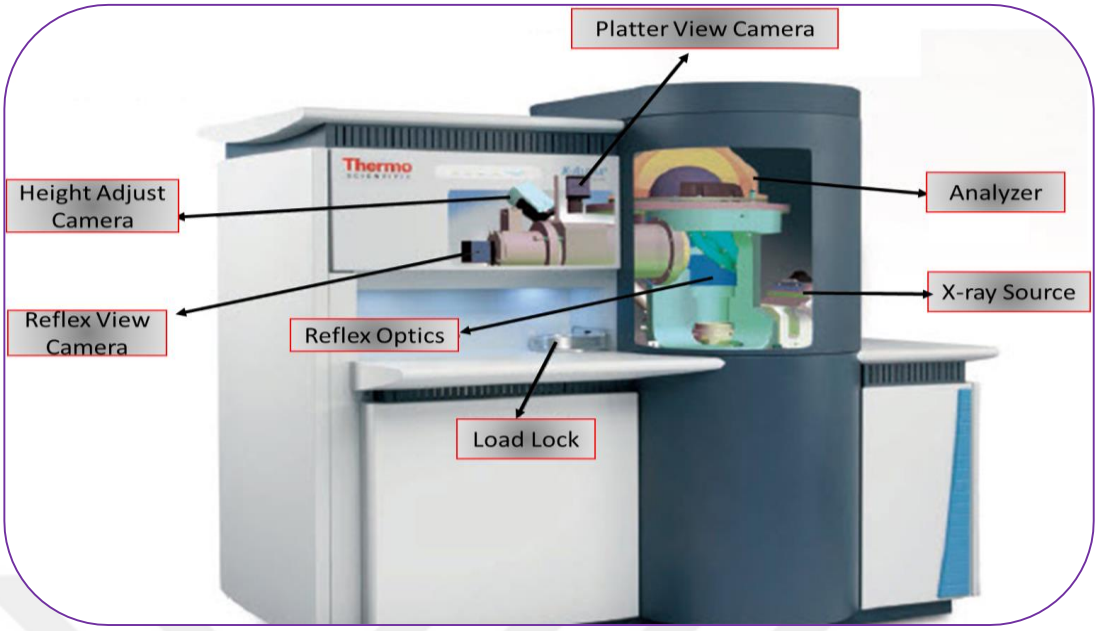

Figure 4. 6 Thermo-K-Alpha-Monochromator Spectrometer setup

Furthermore, XPS relies on basic spectroscopy criteria. In the typical XPS spectrum, the electrons' binding energy (eV) on the X-axis and the number of electrons on the Y-axis are obtained. In addition, each item has a fingerprint binding energy value, and peaks occur depending on this value [183]. Figure 4.6 displays the surface composition of the materials determined in this investigation using the Thermo-K-Alpha-Monochromator Spectrometer (USA) and X-ray photoelectron spectroscopy (XPS).

4.6 Brenauer-Emmett-Teller Spectroscopy (BET)

The Brunauer-Emmett-Teller (BET) analysis method is the widely preferred characterization technique for determining a powdered samples specific surface area (SSA) and pore sizes under high vacuum conditions [184]. The principle of the (BET) theory is that the surface area is determined by the volume of N_2 gas adsorbed on the materials surface [185]. As shown in Figure 4.7, the specific surface area of photocatalysts was measured using the N_2 sorption instrument (Quantachrome, Nova 2200E, U.K.).



Figure 4. 7 Nova 2200E BET setup

4.7 Photoluminescence Spectroscopy (PL)

The photoluminescence (PL) spectrum of novel nanoparticles was measured using a HORIBA Jobin Yvon instrument (USA) and a He-Cd pulsed laser radiation source (325 nm) (Figure 4.8).

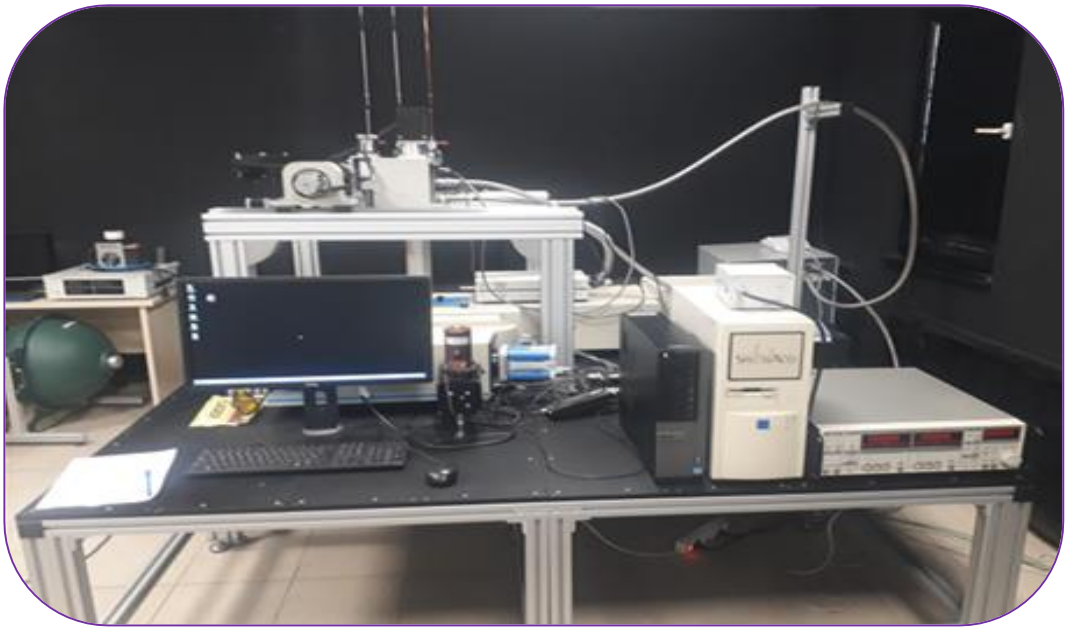

Figure 4. 8 Horiba Jobin Yvon instrument (PL) setup

CHAPTER 5

PHOTOELECTROCHEMICAL MEASUREMENTS

5.1 Photoelectrochemical Reactor Design

All PEC measurements in this thesis were performed using the CorrTest Electrochemical Workstation Potentiostat/ Galvanostat with a standard three electrochemical cell consisting of a working electrode, a platinum wire counter electrode, and a saturated Ag/AgCl electrode as a reference (Figure 5.1a) [186,187]. Figure 5.1b demonstrates the reactor used for PEC measurements of photoanodes. The dimensions of this reactor are as follow: a 3 cm diameter optical window made of quartz glass, a 10 mL electrolyte volume, and a light path distance of 2 cm from the working electrode. In this thesis, two photoanodes based on ZnO were fabricated. In the first case, the PEC properties of ZnO@PDA/CeO_2 photoanodes were measured under LED illumination at (30 mW/cm^2) in a 0.1 M Na_2SO_4 solution (pH: 7) (Figure 5.1c). As a working electrode, FTO glass was modified with the nanoparticles. For this purpose, 1 cm x 2 cm-sized FTO glasses cleaned in an ultrasonic bath with a mixture of ethanol and water (50:50 v/v). Next, the 0.3 cm^2 surface area of FTO glass was coated by the photocatalyst in DI water/ethanol/Nafion solution (5 wt%) mixture (25:25:1 volumetric ratio) followed by drying on a hot plate (100 ^oC) for 15 min at atmospheric conditions (Figure 5.2a) [53,61,67,150]. Secondly, the PEC performance of Z-scheme ZnO@MOF-5-C photoanodes were studied in a three-electrode configuration with 0.1 M Na_2SO_4 electrolyte and 300 W (100 mW/cm^2) Xeon Lamp illumination conditions (5.1d) [186,187]. FTO glass modified with ZnO@MOF-5-C, Ag/AgCl, and Pt wire were used as working, reference, and counter electrodes, respectively. In this case, 1 mg of catalyst was dispersed in a mixture of ethanol-water (20 mL) Nafion (5% by weight). For measurement, 10 μL of this dispersion was coated dropwise on a 0.5 cm^2 FTO glass and dried on a hot plate at 100 °C for 10 minutes (5.2b).

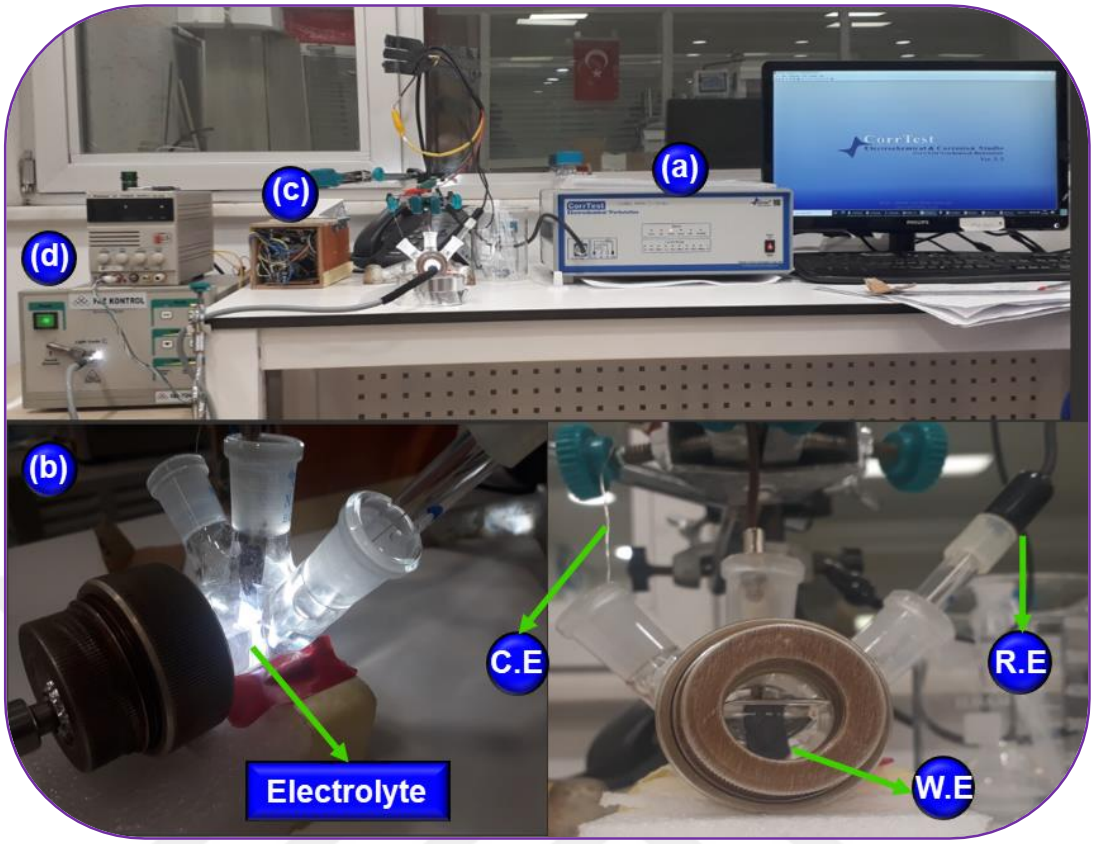

Figure 5. 1 CorrTest Electrochemical Workstation Potentiostat/Galvanostat setup

All PEC measurements were taken with reference to Ag/AgCl (reference electrode). The potential measured against the Ag/AgCl electrode was converted to RHE (reversible hydrogen electrode) using the Nernst equation (equation 5.1) [186,188,189]. The potential vs. Ag/AgCl relationship was converted to NHE using equation (5.2) [67].

$$E_{RHE} = E_{Ag/AgCl} + E^{o}_{Ag/AgCl} + 0.059\ X\ pH \quad \textbf{(5.1)}$$

$$E_{NHE} = E_{Ag/AgCl} + E^{o}_{Ag/AgCl} \quad \textbf{(5.2)}$$

Where, E_{RHE} stands for reversible hydrogen electrode and $E^{0}_{Ag/AgCl}$ stands for the standard electrode potential of the Ag/AgCl electrode. It equals 0.1976 V vs. NHE at 25 ^{0}C , and $E_{Ag/AgCl}$ stands for the external potential measured against the Ag/AgCl reference electrode [189].

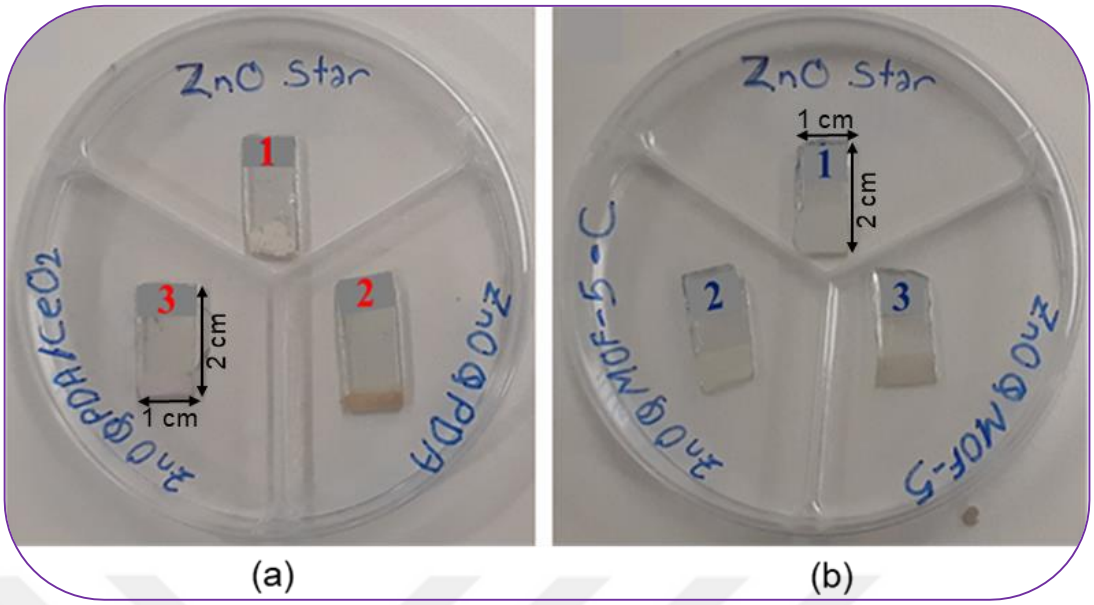

Figure 5. 2 Prepared working electrodes: (a) ZnOstar, ZnO@PDA, and ZnO@PDA/CeO_2 NPs, (b) ZnO star, ZnO@MOF-5, and ZnO@MOF-5-C NPs

5.2 Linear Sweep Voltammetry (LSV) Measurements

Linear Sweep Voltammetry (LSV) is an electrochemical measurement method in the field of fuel cells, hydrogen production technologies, and microbial electrochemical systems [190]. Figure 5.3 represents the LSV working principle. A linear voltage is applied between the measured working electrode and the auxiliary electrode in the LSV measurement technique, and the electrode potential changes linearly with this voltage [191]. This thesis study performed linear sweep voltammetry (LSV) measurements under dark and light conditions. Besides this, LSV measurements were taken at -1.0 V and +1.5 V scanning rates. The potential values of the data obtained in the measurements were converted to RHE using equation 5.1. The applied bias photon-to-current efficiency (ABPE), incident photon to current efficiency (IPCE), and Tafel Slope values were obtained with LSV curves.

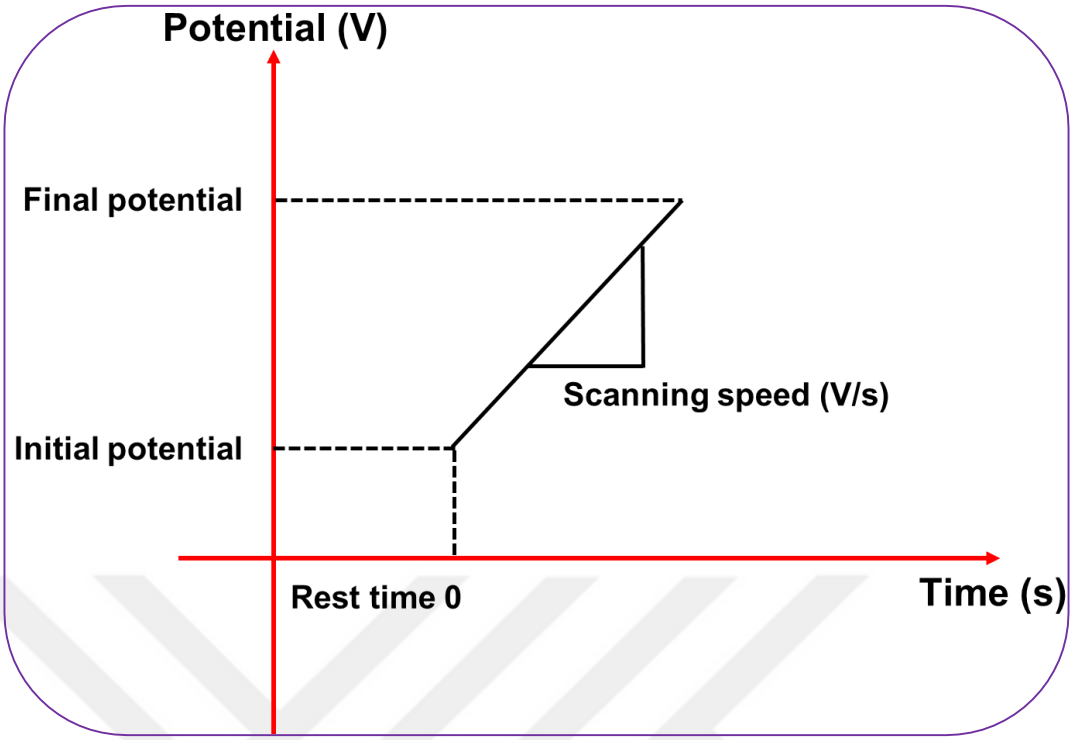

Figure 5. 3 Illustration of Linear Potential Sweep in LSV

5.3 Tafel Slope Measurements

The Tafel slope is a vital electrochemical parameter for evaluating and characterizing electrocatalysts that reflecting the sensitivity of the current response to overpotential [62,192]. The Tafel equation gives the experimental potential dependence of the current density and is widely utilized in hydrogen evolution reactions (equations 5.3) [62,67,193,194].

$$\eta = a + b \log(i) \quad \textbf{(5.3)}$$

In this equation, η is the overpotential (mV), b denotes the Tafel slope (mV/dec), "i" is the current density (mA/cm^2), i_0 is the exchange current density. Typically, there is a cathodic branch with a slope of – αF/2.3RT and an anodic branch with a slope of (1-α) F/2.3RT [194–196]. As illustrated in Figure 5.4, both linear parts are extrapolated to an intercept of logi_0. The plots obviously deviate from linear behavior as η approaches zero, as the backward reactions can no longer be considered as negligible. The Tafel slope demonstrates the potential difference in changing the current density

by 10-fold and is frequently used to investigate which pathway is involved during the HER process [194–196].

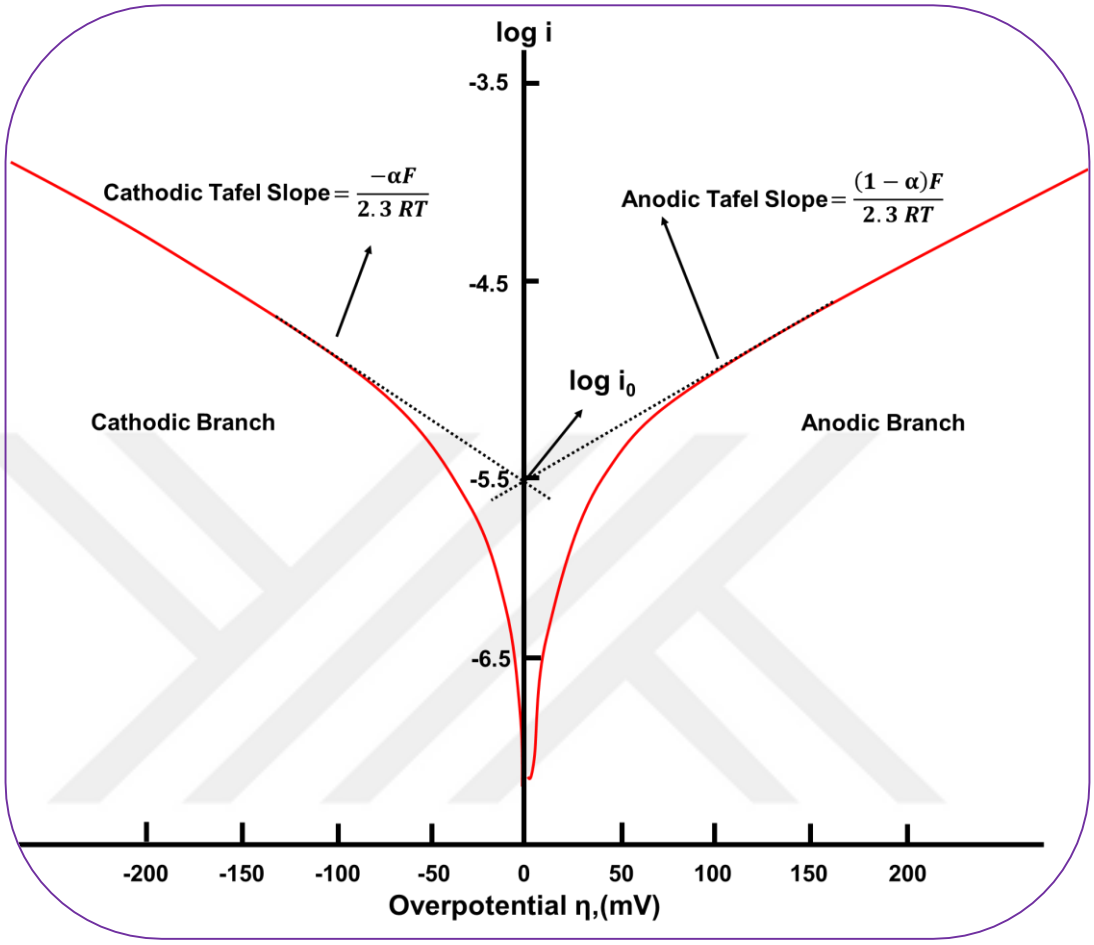

Figure 5. 4 Tafel plots for anodic and cathodic branches of the current-overpotential curve, with α = 0.5, T = 298 K, and $i_0 = 10^{-6}$ A cm^{-2}

Also, the Tafel slope is a significant parameter for assessing PEC performance in water splitting [197]. The smaller the Tafel slope, the higher the charge transfer rate. The slower the charge transfer rate, the larger the Tafel slope [195–198]. They are in inverse proportion to one another. In this thesis, Tafel slopes were obtained from the data taken from LSV results by plotting the log j graph against potential based on the Tafel equation.

5.4 Incident Photon to Current Efficiency (IPCE) Measurements

Incident Photon-Current Efficiency (IPCE) is one of the most important parameters for PEC measurements. As a function of the illumination wavelength, it expresses the gathered photocurrent per incident photon flux [199]. In other words, IPCE denotes a solar cell's spectral response to incident light in terms of current and is also called external quantum efficiency (EQE) [199,200]. IPCE is the ratio of the output flux of electrons producing hydrogen to the incident photon flux when an electrode is illuminated by monochromatic light. IPCE data, measured under zero-bias or short-circuit conditions, can be integrated across the entire solar-spectrum wavelength range to determine the highest STE efficiency possible. Although IPCE is not regarded as a valid estimate for STH under an applied bias, it is a parameter that offers researchers an idea about the properties of PEC materials. The IPCE is typically obtained from the chronoamperometry measurement technique of the potentiostat device used in a PEC measurement [199]. Moreover, IPCE defines how many incoming photons of one wavelength are converted into electrons [124,201]. In this thesis, IPCE values were calculated using the current values obtained from the LSV measurements using the equation in 5.4.

$$\mathrm{IPCE}(\%) = \frac{\mathrm{J_{ph}(mA/cm^2)}}{\mathrm{P_{mono}(mW/cm^2)}} \times \frac{1240}{\lambda(\mathrm{nm})} \qquad (\mathbf{5.4})$$

Where, P_{mono} is the monochromated illumination power intensity, J_{ph} is the photocurrent density obtained for an applied voltage, and λ is the wavelength concerning power density [67,201–203].

5.5 Applied Bias Photon to Current Efficiency (ABPE) Measurements

Applied bias photon-to-current efficiency (ABPE) is a measurement technique commonly used in efficiency evaluation in PEC measurements [124,204]. ABPE is a characterization parameter used in PEC measurements to analyze the photoresponse performance of a photoelectrode–under voltage applied to a photoelectrode using a potentiostat device [115,124,204,205]. However, the ABPE measurement is not

considered a true solar-hydrogen efficiency value because the ABPE value is measured by applying external bias, such as energy not produced from sunlight [124,199,205]. Nevertheless, the ABPE value is the efficiency assessment that provides researchers with an insight into understanding the material properties and characterization of the PEC system [115]. The ABPE of a PEC system is calculated from the J-V curve of the photoelectrode using the formula shown in equation 5.5 [67,115,188,205]

$$\mathrm{ABPE}(\%) = \frac{\mathrm{J_{ph}}(\mathrm{mA/cm^2})\ \mathrm{X}\ (1.23 - |\ \mathrm{V_b}|)}{\mathrm{P_{total}}(\mathrm{mW/cm^2})} \qquad (\mathbf{5.5})$$

In this equation, P is the power density, J_{ph} is the photocurrent density for applied voltage, and V_b is the potential applied between the working electrode and counter electrode.

5.6 Electrochemical Impedance Spectroscopy (EIS) Measurements

Electrochemical impedance spectroscopy (EIS) is a multi-purpose technique to investigate electrode materials used in energy applications such as water splitting, proton exchange membrane fuel cells (PEMFC), Li-ion batteries, corrosion rate measurement, and electro/photocatalysis [206–211]. EIS is a useful measurement technique that provides information about the electrochemical properties of the interfaces, surfaces, and coatings of the materials [211,212]. The EIS technique is an AC technique that applies a small amplitude sinusoidal potential perturbation (typically in the 5-10 mV range) to the working electrode in a galvanostatic or potentiostatic mode over a wide frequency range (typically 100 kHz to 100 MHz) in a three-electrode electrochemical cell [209–213]. The impedance could be described as a frequency-dependent resistance that inhibits the current flow, as represented in equation 5.6 [210,214].

$$\mathrm{Z_\omega} = \frac{\mathrm{E_\omega(t)}}{\mathrm{I_\omega\ (t)}} \qquad (\mathbf{5.6})$$

Where, E_ω is the frequency-dependent potential, $I_\omega$is the frequency-dependent current, and Z_ω is the electrochemical impedance.

In this thesis, EIS analysis was carried out to elucidate the effect of the interfacial charge transport behavior in the photoanodes. The EIS measurements were performed using a three-electrode configuration in 0.1 M Na_2SO_4 in the same manner described in section 5.1. The measurements were done in a potentiostatic mode at various potentials from (-1.0 V) to (+1.0 V) versus RHE in the frequency range of 0.01 to 10^5 Hz under dark and light conditions with an amplitude of 10 mV.

5.6.1 Mott-Schottky Analysis

Mott-Schottky (MS) is a technique used in PEC studies as an EIS [215]. Furthermore, MS is a beneficial measurement technique in determining the V_{fb} of the materials [216–218]. The flat band potential is an essential criterion for evaluating photoelectrode efficiency better to understand the properties of the semiconductor/electrolyte interface [215–218]. Moreover, the flat band potential value could be used to identify the semiconductor electrode's valence and conduction band edges in relation to the redox-active species present in the electrolyte [215]. In the literature, several methods have been proposed to estimate the flat band potential of materials. For example, open-circuit potential (OCP) might be one of the methods used to determine the flat band potential by applying an external bias that provides efficient charge carrier separation. However, this method is not considered an accurate estimate due to the possibility of defects such as charge carrier recombination and surface kinetics [215]. To our knowledge, MS analysis is one of the most reliable methods for determining a semiconductor's exact flat band potential. The V_{fb} value could be estimated by plotting V against $1/C^2$, using the linear part of the graph fitted with the x-intercept (Figure 5.5). In the literature, positive and negative slopes of the potential against C^{-2} indicate n-type and p-type semiconductor behavior, respectively [217,219]. The heterostructures band properties and semiconductor type were investigated using the MS equation [67,150,215,217,220]. The carrier concentration was calculated from the slope of the linear region of the MS plot [216]. Besides this, MS measurements were carried out under DC potential polarization between [(-1.0) and (+1.0) V]. EIS was performed between 0.01 and 100000 Hz in dark and light conditions.

$$\frac{1}{C^2} = \frac{2}{e\,\varepsilon\,\varepsilon_0\,N_d}\left(V - V_{fb} - \frac{k_B T}{e}\right) \qquad (\mathbf{5.7})$$

Where,

C: is the capacitance per unit area of the space charge layer (F cm^{-2}).

e: is the fundamental charge constant (1.602×10^{-19} C)

ε: is the dielectric constant of the semiconductor

ε_0:is the permittivity of vacuum (8.85×10^{-14} F/cm)

N_d: is the carrier concentration,

V: is the applied potential,

V_{fb}: is the flat-band potential,

k_B: is Boltzmann's constant (1.381×10^{-23}J K^{-1}),

T: is the absolute temperature (298 K).

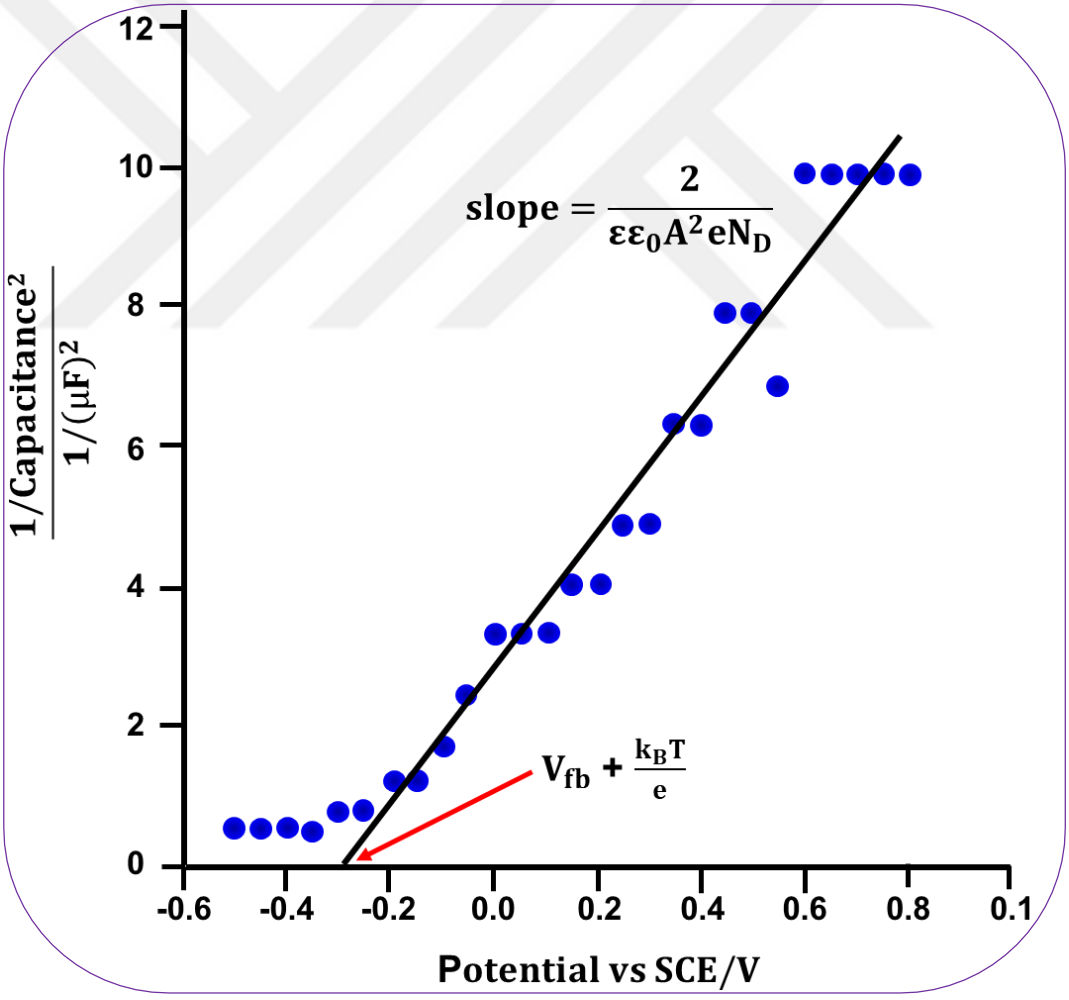

Figure 5. 5 Mott-Schottky plot of ZnO photoanode for correct V_{fb} determination

5.6.2 Nyquist Plot Analysis

Nyquist plots are one of the most commonly used EIS measurement techniques [221,222]. Electrochemical measurements are made using an electrical circuit. Since the electrodes have a circuit element, they work harmoniously to balance the potential. The working electrode, reference electrode, and counter electrode provide electrical balance in the electrode solution. The circuit configuration is constructed according to these element's curves and electrode surface properties [222]. Nyquist plots exhibit the association between the real and imaginary parts of the impedance for a range of frequencies (Figure 5.6a) [214,221,222]. Figures 5.5 (b-c) display Randles cell circuit models, which include the solution (R_s), electron transfer resistance of the electrode (R_{ct}), Warburg impedance (W), and capacitor (C). In the circuit model, the terms R_{ct}, W, and CPE represent electron transfer capability, mass transfer, and electrode surface capacitor at the electrode surface, respectively [209,214,221,222].

Tablo 5. 1 EIS data circuit elements summary

Element	Unit	Meaning
R	Ω/cm^2	Resistant of an electrode surface of the solution
C	F/cm^2	Electrical charge configuration of an electrode double layer surface
CPE	F/cm^2	The capacitor of double layer
W	Ω/s^2	Mass transport through electrode surface

In this measurement technique, the electrolyte resistance is obtained by taking the high-frequency intercept value of the real axis. In contrast, the charge transfer resistance is found in the semicircle diameter [210]. A smaller arc radius indicates a lower charge transfer resistance and an efficient electron transfer process at the electrode/electrolyte interface [210]. For Nyquist plot measurements, the circuits shown in Figure 5.6 b for ZnO@MOF-5-C NPs and Figure 5.6 c for ZnO@PDA/CeO_2 NPs were used.

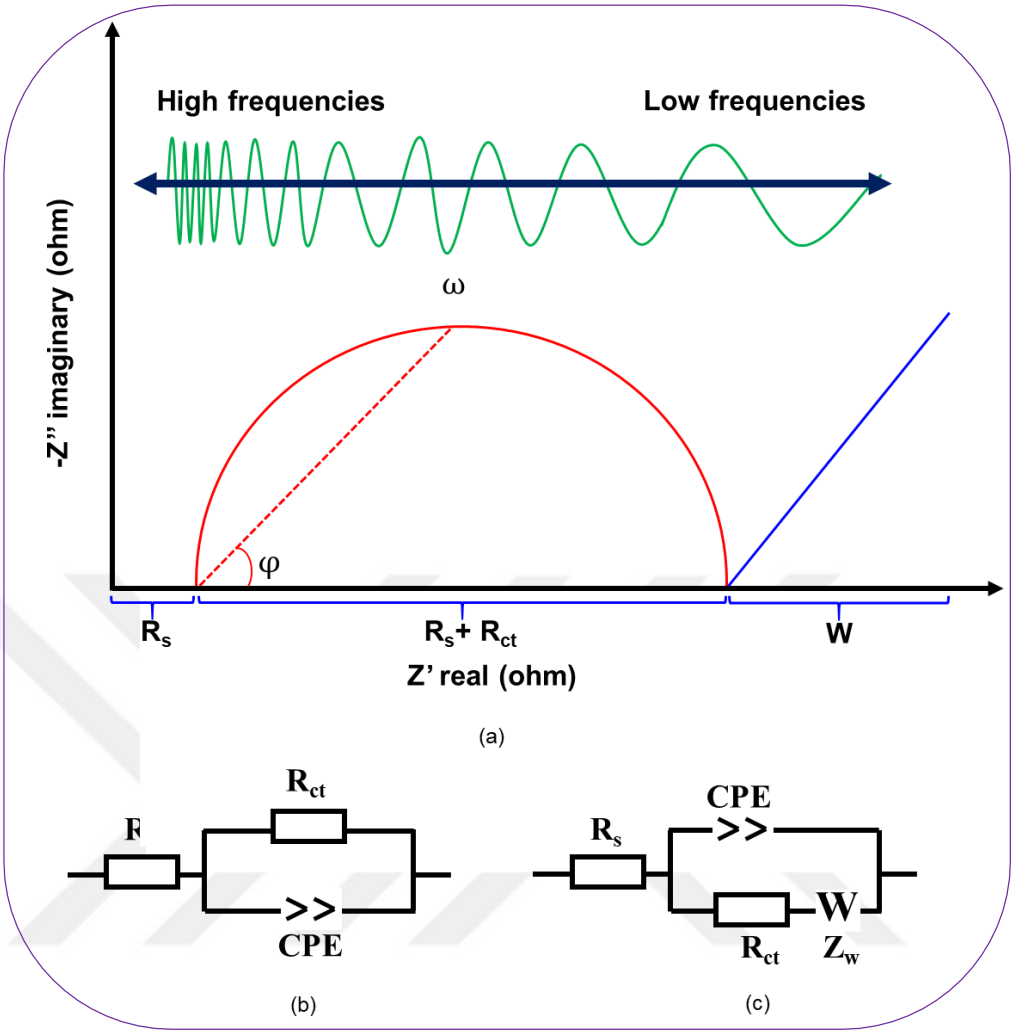

Figure 5. 6 Representation of Impedance in a Nyquist plot (a) Randles equivalent circuit (b)**,** Randles circuit with Warburg elements (c)

5.6.3 Bode Plot Analysis

The bode plot gives us information about the lifetime of an electron at the electrode and electrolyte interface transitions [53,223]. In this thesis, the electron lifetime of the photoanodes was calculated according to equation 5.8.

$$\tau_n = \frac{1}{(2\pi f_{max})} \qquad (5.8)$$

Where, τ_n is the electron lifetime, f_{max} is the maximum peak log of frequency obtained from the Bode plot [53,224].

CHAPTER 6

RESULTS and DISCUSSION

6.1 Physical and Chemical Characterization of Z-scheme ZnO@PDA/CeO_2 Photoanodes

6.6.1 XRD Pattern of ZnO and Z-scheme ZnO@PDA/CeO_2 NPs

Fig.6.1 shows XRD results of the synthesized pristine ZnO and ZnO@PDA/CeO_2 heterostructures. The XRD results of the synthesized materials were compared with the literature results (ZnO, JCPDS:01-075-1533 and CeO_2, JCPDS 00-001-0800). It is clear that ZnO has a wurtzite hexagonal phase structure. In addition, the peak at 28.5 degrees indicates the presence of the cubic phase of CeO_2 in ZnO@PDA/CeO_2 heterostructures [29,175]. Moreover, the results show that some peaks of ZnO and CeO_2 were broadened, and the intensity of some of them decreased in crystal structure, confirming the successful synthesis of ZnO@PDA/CeO_2 heterojunctions.

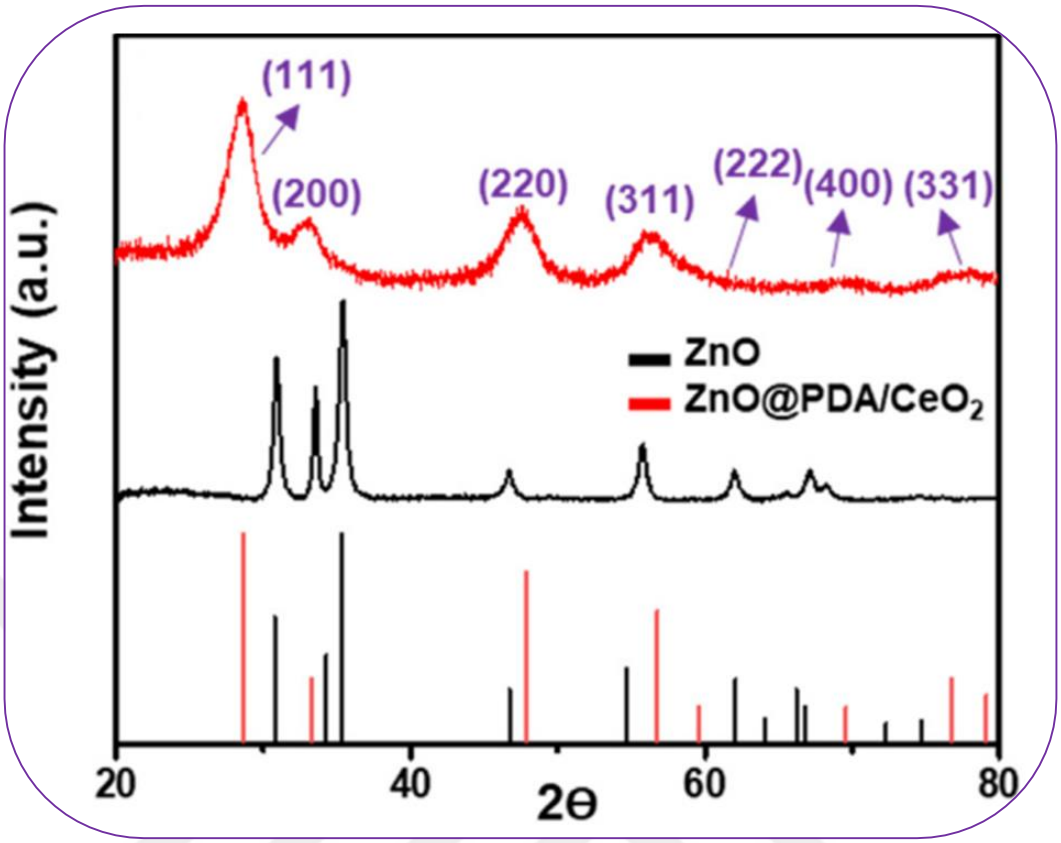

Figure 6. 1 XRD pattern of ZnO and ZnO@PDA/CeO_2 heterostructures

6.1.2 SEM Images of ZnO, ZnO@PDA and ZnO@PDA/CeO_2 NPs

Figure 6.2 shows the SEM analysis results of pristine ZnO star, ZnO@PDA, and ZnO@PDA/CeO_2 heterostructures. The SEM analysis results prove that ZnO NPs with good star-shaped morphology (400 nm in size) were successfully synthesized (Figure 6.2a). In Figure 6.2b, the mean size has changed slightly after the PDA shell layer coating onto ZnO. However, the morphology of the ZnO@PDA NPs was not changed, and agglomeration was not observed. Due to the adhesive behavior of the redox-active PDA hydroxyl groups, the synthesized ZnO@PDA/CeO_2 NPs showed well-defined core (ZnO@PDA)/shell (CeO_2) morphologies (Figure 6.2c). Moreover, the elemental mapping of the heterostructures was also used to assess the distribution of the component element (Figure 6.2d). All major elements (Ce, O, and Zn) were distributed uniformly onto ZnO@PDA/CeO_2 heterostructures [150].

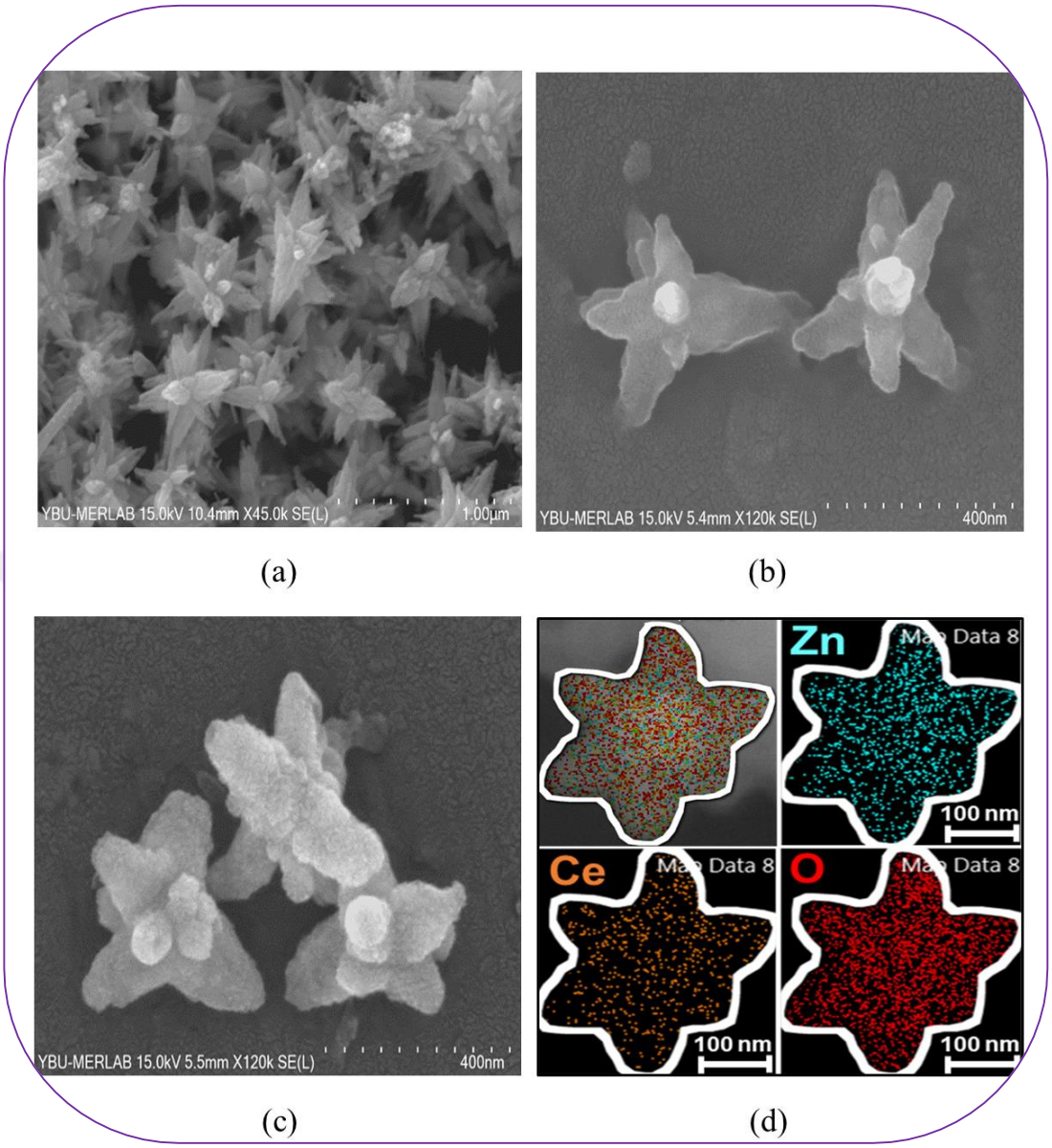

Figure 6. 2 SEM images of (a) ZnO star, (b) ZnO@PDA, and (c) ZnO@PDA/CeO_2 heterostructures, (d) corresponding SEM elemental mapping images of Zn, Ce, and O

6.1.3 TEM Images of ZnO, ZnO@PDA and ZnO@PDA/CeO_2 NPs

Figure 6.3 shows the TEM analysis of ZnO@PDA/CeO_2 heterostructures. TEM images revealed that CeO_2 was successfully deposited using a self-assembly auto-redox approach as well as the homogeneous wrapping of ZnO@PDA by CeO_2 shell layer (uniform thickness: 9 nm) achieved due to the hydrophilicity of the superficial PDA catechol groups [150].

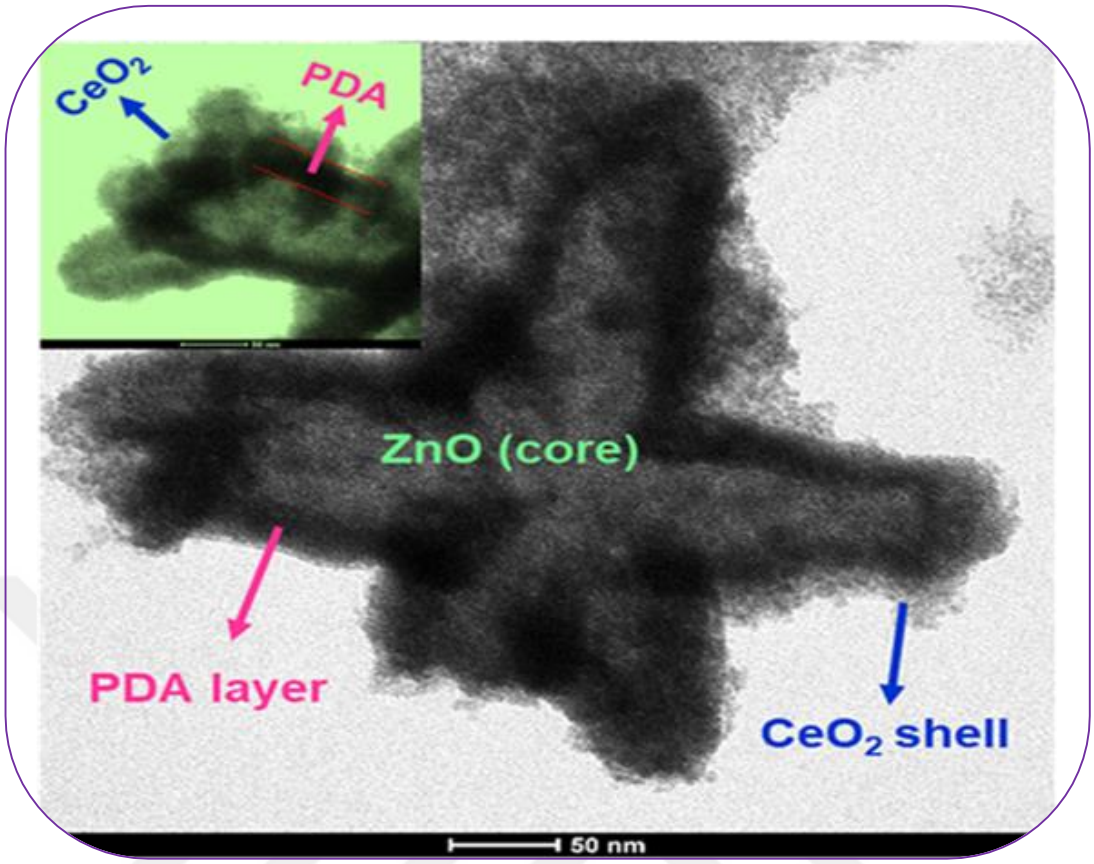

Figure 6. 3 TEM images of ZnO@PDA/CeO_2 heterostructures

6.1.4 Uv-Vis Specta of ZnO, ZnO@PDA and ZnO@PDA/CeO_2 heterostructures

Figure 6.4 (a) exhibits the UV-Vis spectra of pristine ZnO, pristine CeO_2, and ZnO@PDA/CeO_2 heterostructures. The observed peak at around 373 nm proves that hexagonal wurtzite ZnO was formed, which means the absorption peak of the ZnO is red-shifted by 8 nm compared with the literature results [225]. The broad absorption peak was observed at around 303 nm associated with Ce^{4+} of CeO_2 NPs at UV-Vis spectrum [226]. Likewise, The UV-Vis spectrum of ZnO@PDA/CeO_2 shows a broad absorption peak at around 308 nm; however, the sharp peak of ZnO at 378nm was eliminated (Figure 6.4 a). This result can be assigned to successfully covering of ZnO star nanostructures with PDA and CeO_2 coatings. In the literature, it has been reported that ZnO is a direct wide bandgap semiconductor, while CeO_2 is a rare earth metal oxide semiconductor with an indirect bandgap [227,228].

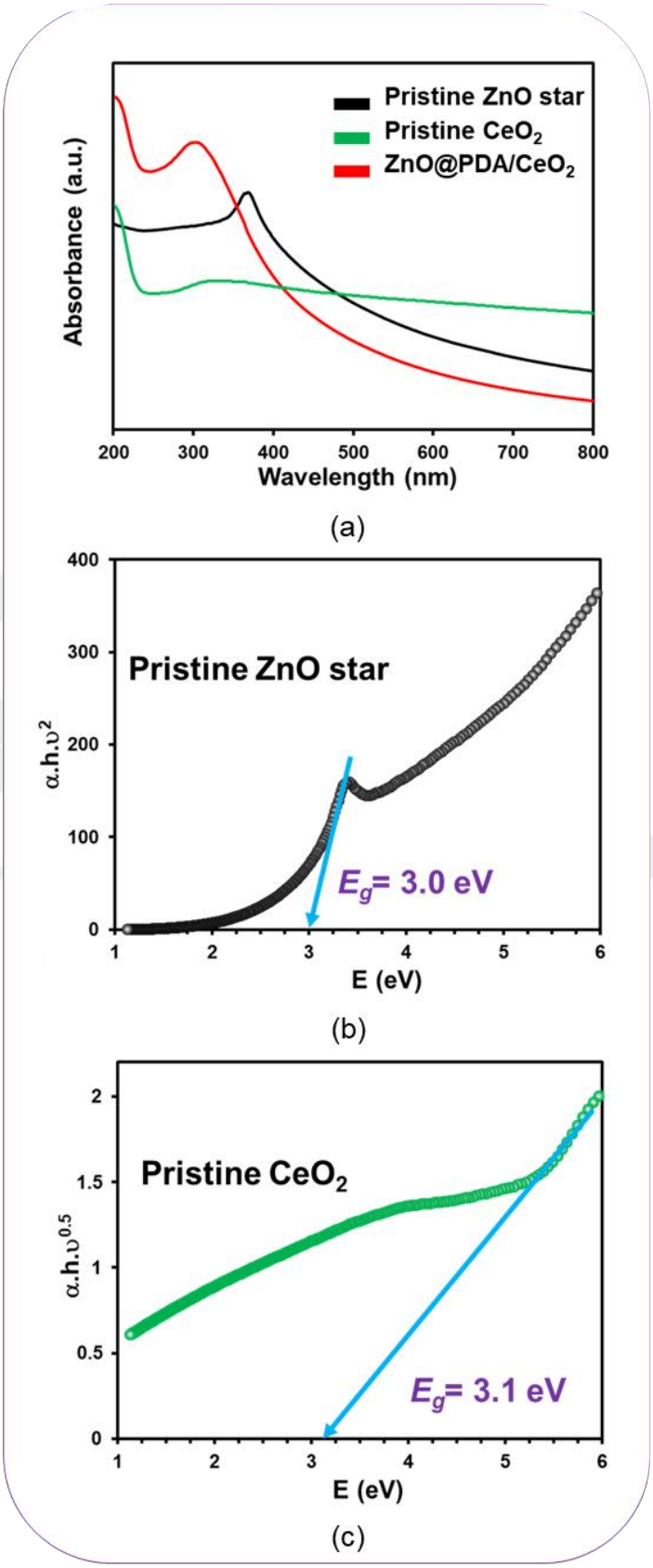

Figure 6. 4 (a) UV-Vis spectra of ZnO, CeO_2, and ZnO@PDA/CeO_2 heterostructures ; (b) Tauc plot of ZnO; (c) Tauc plot of CeO_2 NPs

Therefore, Tauc plots were used to calculate bandgap energies of ZnO star and CeO_2 according to their direct and indirect allowed transitions, respectively. Figures 6 (b) and (c) show the bandgap values of pristine ZnO star and CeO_2, respectively. As seen here, the pristine ZnO star bandgap value was found to be 3.0 eV, and the pristine CeO_2 bandgap value was 3.1 eV. Moreover, the bandgap energy of CeO_2 coincides with literature results [227,228]. However, the bandgap energy of ZnO nanoparticles (3.63eV) is remarkably narrowed by tuning the morphology. In addition, the UV–Vis absorption spectra and Tauc plots of ZnO nanostructures with different morphologies (NP, NR and NS) were reported in the literature [229,230]. The main absorption peaks at room temperature for ZnO NP (25 nm), ZnO NR (35 nm), and ZnO NS (27 nm) are approximately 362 nm, 375 nm, and 367 nm, respectively. Therefore, a blue shift was clearly seen at the characteristic absorption peaks with a decrease in the crystallite size of the nanostructures. This blue shift may be associated with reduction in size as well as changes in surface morphology. The reported energy bandgap values for ZnO NP, ZnO NR, and ZnO NS are 3.26, 3.10, and 3.24 eV, respectively. As seen from this findings, the optical confinement effect increased the energy band gap with decrease in the crystallite size for ZnO nanostructure [229,230].

6.1.5 XPS Images ZnO, and ZnO@PDA/CeO_2 NPs

XPS was used to determine the chemical composition and surface state of the ZnO and ZnO@PDA/CeO_2 heterostructures. Zn, O, and Ce elements were also marked on the XPS spectra (Figure 6.5a). Two peaks at 1021 eV and 1044.2 eV were observed on the XPS spectrum of pristine ZnO, which belongs to $Zn_{3/2}$ and $Zn_{1/2}$, respectively (Figure 6.5b). For ZnO@PDA/CeO_2 samples, the energies of $Zn_{3/2}$ and $Zn_{1/2}$ have shifted to higher energies (10.21eV and 1044.9 eV), indicating the successful deposition of the CeO_2 shell (Figure 6.5b). Furthermore, high-resolution spectra of O 1s revealed two peaks with binding energies of 529.4 eV and 532 eV, which could be attributed to lattice oxygen and non-lattice oxygen (adsorbed oxygen), respectively (Figure 6.5c). Compared with pristine ZnO, the peak corresponding to adsorbed oxygen (5.32 eV) in ZnO@PDA/CeO_2 became significantly higher, indicating more oxygen vacancies [231,232]. In Ce3d high-resolution XPS spectra, the peaks belonging to spin-orbital electrons of $Ce3d_{5/2}$ and $Ce3d_{3/2}$ were attributed to V and U

with eight binding energies regions, respectively (Figure 6.5d). The peaks corresponding to Ce^{4+} were marked as V, V^{II}, $V^{III,}$ and U, U^{II} U^{III}, whereas the peaks of Ce^{3+} were denoted as V^{I} and U^{I} [29,175,231]. These results prove that both Ce^{+4} and Ce^{+3} oxidation states co-existed in ZnO@PDA/CeO_2 heterostructures, and most cerium ions belong to Ce^{+4} chemical states [29]. The XPS results prove the formation of ZnO@PDA/CeO_2 heterostructures through interface engineering using PDA between ZnO and CeO_2 semiconductors.

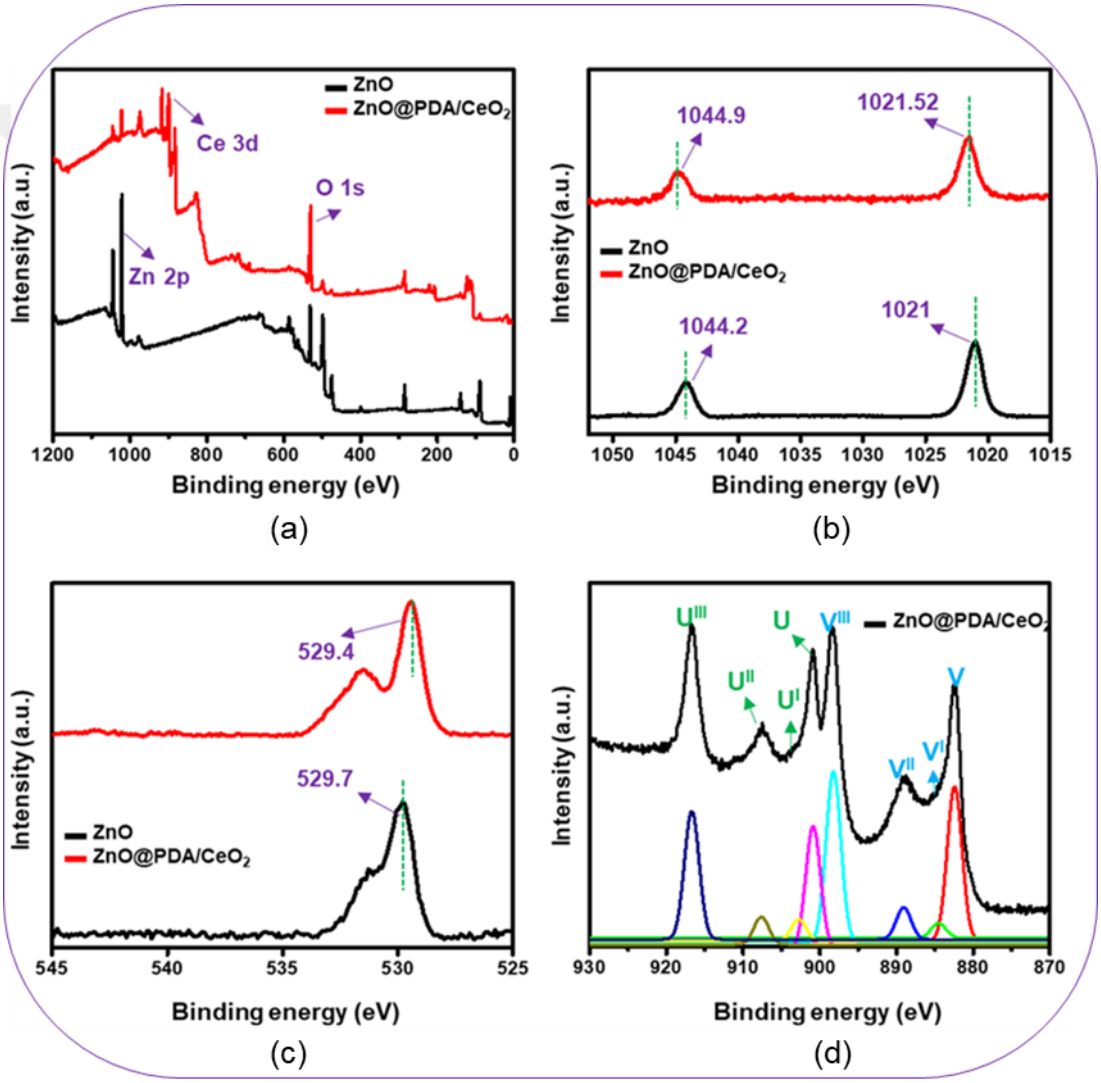

Figure 6. 5 (a) X-ray photoelectron spectroscopy survey spectra of: (a) pristine ZnO and ZnO@PDA/CeO_2 NPs ; (b) high-resolution Zn 2p core level for ZnO and ZnO@PDA/CeO_2 NPs ;(c) high-resolution O 1s core level for ZnO and ZnO@PDA/CeO_2 NPs; (d) high-resolution 3d for ZnO@PDA/CeO_2 NPs

6.1.6 Brunauer-Emmett-Teller (BET) analaysis of ZnO and ZnO@PDA/CeO_2 NPs

The BET method was used to investigate the pore size distribution and SSA of pristine ZnO and ZnO@PDA/CeO_2 heterostructures (Fig 6.6a-b and Table 6.1). The N_2 adsorption-desorption isotherms exhibited a typical IV isotherm with a hysteresis loop [185,233]. Furthermore, pore size distribution results of pristine ZnO and ZnO@PDA/CeO_2 have demonstrated significant peaks corresponding to the mesoporous compartment fractions (2-12 nm).

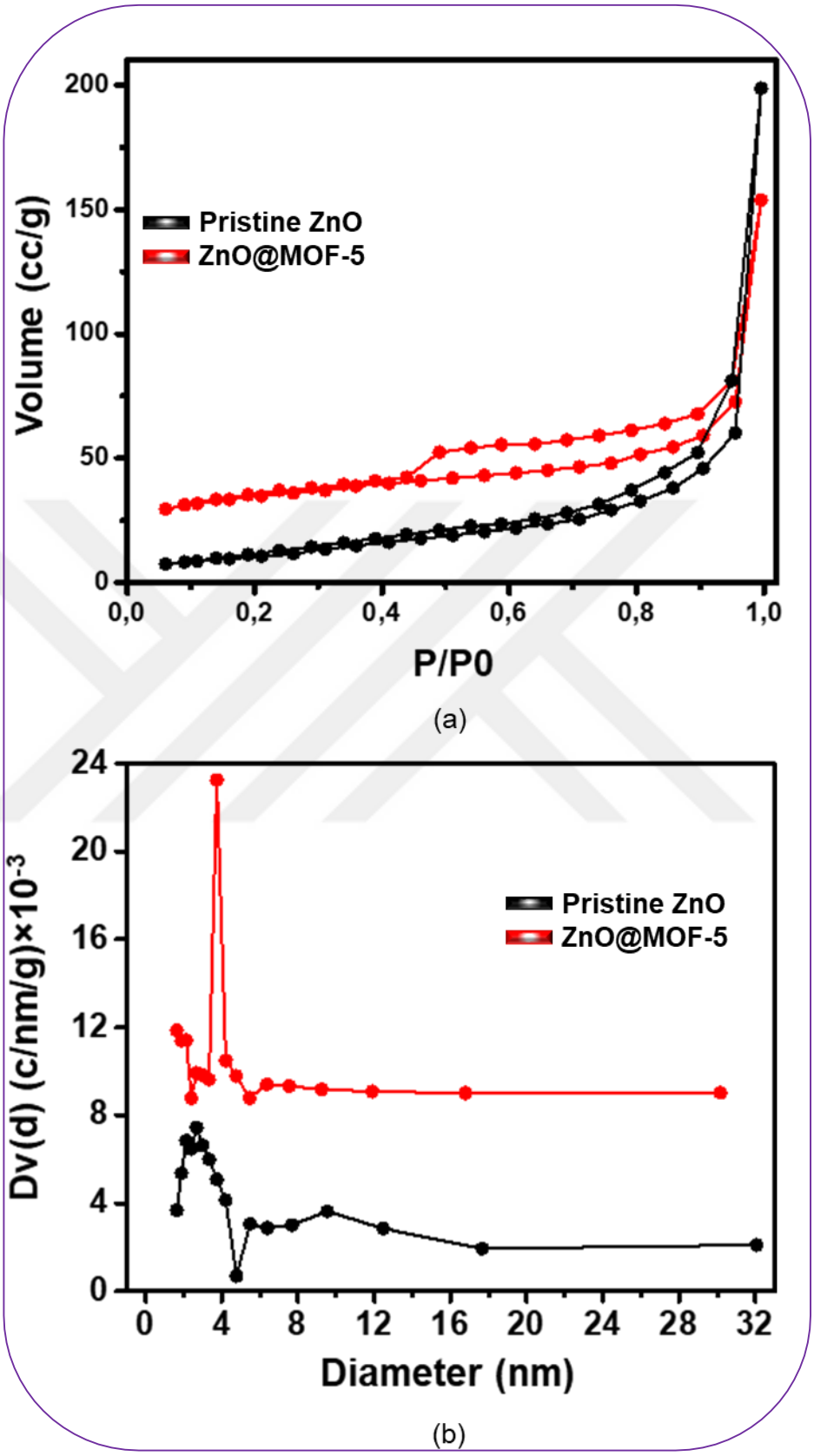

Figure 6. 6 (a) Nitrogen adsorption-desorption diagram and, (b) Pore size distribution of ZnO and Z-scheme ZnO@PDA/CeO_2 NPs

It was apparent from the comparison of surface area results of pristine ZnO ($29 m^2/g$) and (ZnO@PDA/CeO_2 (116 m^2/g) that the surface area of ZnO@PDA/CeO_2 increased because of the smaller mesoporous fraction at 4.0 nm (Figure.6.6b and Table 6.1).

Table 6. 1 Experimentally obtained specific surface area (SSA), pore volume, and mean pore size value of ZnO star and ZnO@PDA/CeO_2 NPs

Sample	**SSA (m^2/g)**	**Pore volume (cm^3/g)**	**Mean pore size (nm)**
Pristine ZnO	29	0.008	2.4
ZnO@PDA/CeO_2	116	0.05	1.5

Additionally, the increment of the pore volume of the ZnO@PDA/CeO_2 resulted in the improvement of absorption capacity/mass transfer of these nanocomposites in photocatalytic reactions [150].

6.1.7 Photoluminescence Spectroscopy (PL) Analysis of ZnO, ZnO@PDA/CeO_2 NPs

PL measurements were then performed to determine the efficiency of electron-hole separation in the photocatalytic process. As illustrated in Figure. 6.7. PL intensity was restrained for ZnO@PDA/CeO_2 compared to pristine ZnO, rendering a prolonged lifetime of charge carriers. These results indicate that using PDA facilitates charge transfer between ZnO and CeO_2 and significantly increases the electron-hole separation, which will provide high photocatalytic efficiency [150].

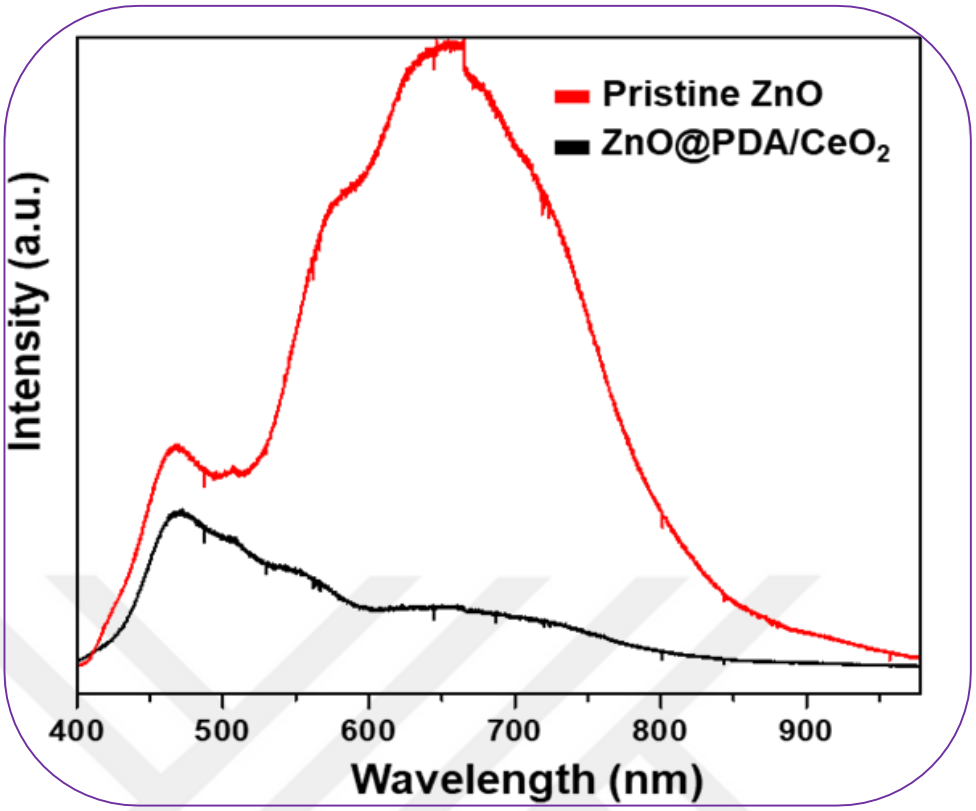

Figure 6. 7 Photoluminescence of pristine ZnO and Z-scheme ZnO@PDA/CeO_2 NPs

6.1.8 LSV Results of ZnO, and ZnO@PDA/CeO_2 NPs

Due to low charge separation in the dark, the LSV results show a low photocurrent density of 24 μA/cm^2 for ZnO@PDA/CeO_2 heterojunctions. However, under visible LED irradiation, the PEC performance of ZnO@PDA/CeO_2 heterojunctions significantly improved by enhancing rapid separation/transfer of photogenerated charge carriers. At 0.25 V vs. RHE, the maximum 251 μA/cm^2 photocurrent density was obtained for Z-scheme ZnO@PDA/CeO_2 heterojunctions.

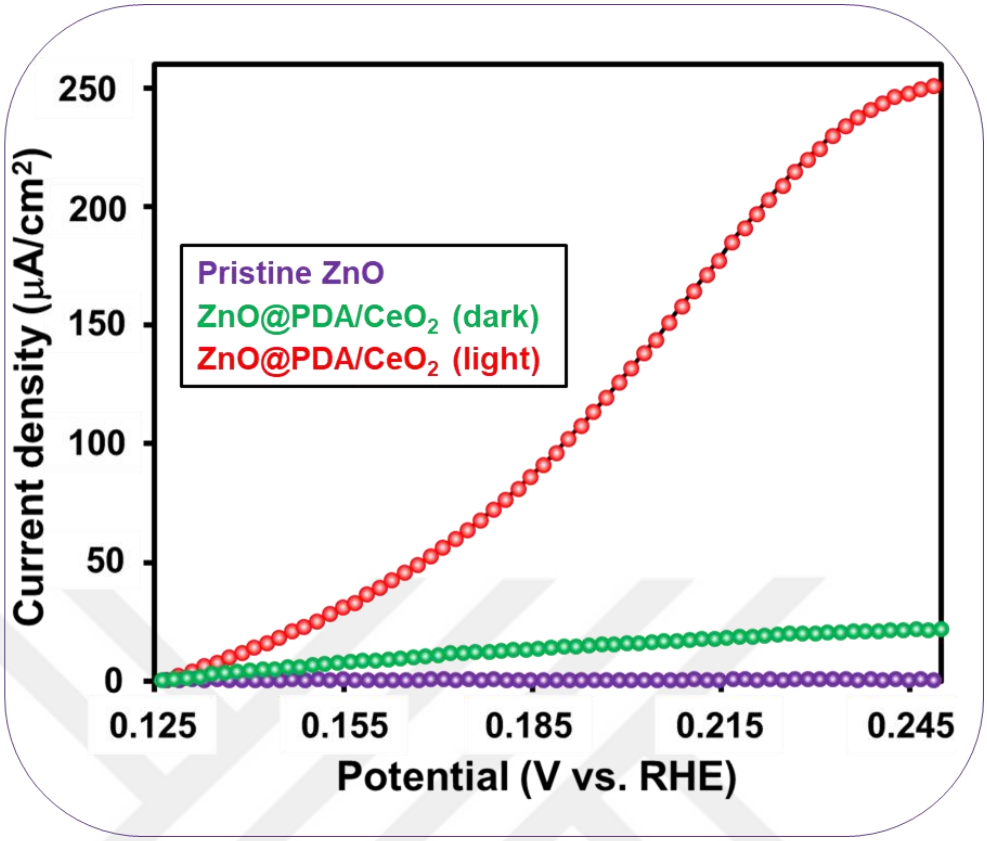

Figure 6.8 J-V results of pristine ZnO and Z-scheme ZnO@PDA/CeO_2 heterostructures (under dark and light)

Because of the rapid separation/transfer of photogenerated electrons from the CB of ZnO onto the VB of CeO_2, the J-V curves ZnO@PDA/CeO_2 heterostructures increased 10.5-fold in comparison with the dark condition. In this photoanodes, PDA plays the role of electron transfer mediator for accelerating hot electron injection and provides an efficient accumulation of electrons and holes in the CB of CeO_2 and VB of ZnO, respectively [150].

6.1.9 Tafel slope of ZnO and ZnO@PDA/CeO_2 NPs

The Tafel slopes are shown in Figure 6.9 [67,177]. In the dark condition, the Tafel slope for pristine ZnO, ZnO@PDA/CeO_2 (dark), and ZnO@PDA/CeO_2 (light) is 117 mV/dec, 90 mV/dec, and 38 mV/dec, respectively.

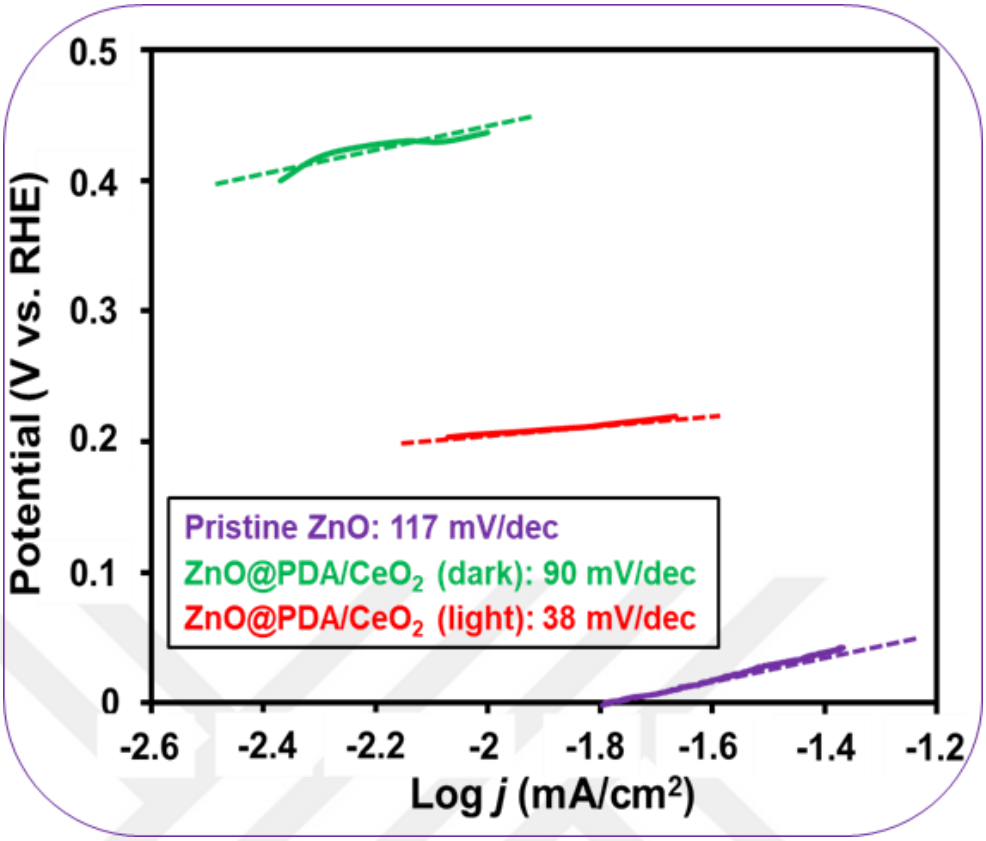

Figure 6.9 Tafel plots of ZnO, ZnO@PDA/CeO_2 heterostructures

The results show that bridging ZnO and CeO_2 semiconductors with PDA significantly reduced the Tafel slopes; this result approves the highest photocurrent density and interfacial kinetics toward water splitting. Moreover, the smaller Tafel slopes and lower overpotential value prove the enhancement of the photocatalytic activity of the Z-scheme structure in which PDA was used as an electron transfer layer for accelerating separation/transfer of photoinduced charge carrier under visible LED light.

6.1.10 IPCE Results of ZnO and ZnO@PDA/CeO_2 heterostructures

For further investigation of the light conversion efficiency of the ZnO@PDA/CeO_2 heterostructures, incident photon-to-current efficiency (IPCE) values were measured and presented in Figure 6.10 [67,177]. Because of the PDA thin layer, ZnO@PDA/CeO_2 photoanodes performed maximum IPCE% in the visible region (450-575 nm). The IPCE value of the ZnO@PDA/CeO_2 heterojunction photoanodes

was increased by 9% compared with the pristine ZnO and ZnO@PDA/CeO_2 (in dark condition) samples. The increment in IPCE results confirms that PDA bridged heterojunctions were successfully synthesized, providing efficient electron-hole separation and electron migration from CB of ZnO to VB of CeO_2.

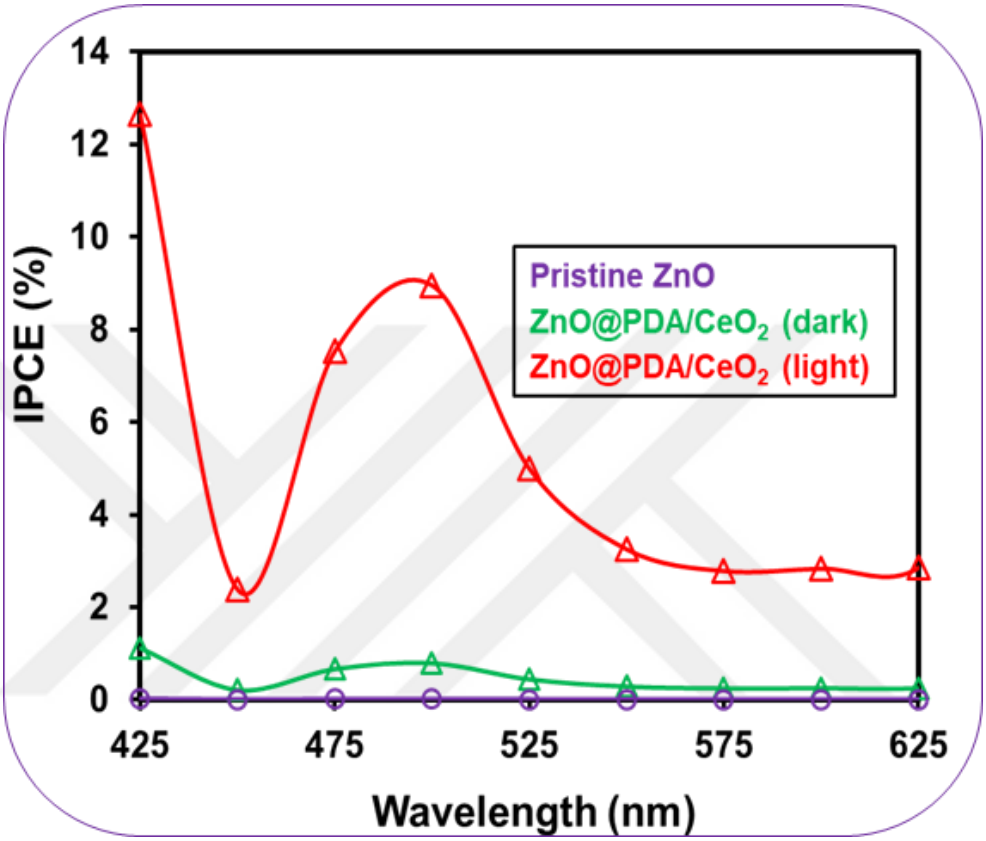

Figure 6.10 IPCE spectra of ZnO and ZnO@PDA/CeO_2 heterostructures

The light absorption in the visible area increased according to suppressing electron-hole recombination of ZnO@PDA/CeO_2 heterojunction photoanodes [150].

6.1.11 ABPE Results of ZnO and ZnO@PDA/CeO_2 NPs

The PEC performance of ZnO@PDA/CeO_2 heterojunction photoanodes also was analyzed by ABPE measurements (Figure 6.11). The highest ABPE value was achieved for ZnO@PDA/CeO_2 heterojunction under LED illumination at 0.25 V vs. RHE ~~was~~ (0.83%). Nevertheless, the highest ABPE value for pristine ZnO and ZnO@PDA/CeO_2 heterojunctions at dark was 0.085% (at 0.42 V vs. RHE) and 0.001% (at 0.35 V vs. RHE), respectively. These results once more proved that the

photon conversion efficiency of photoanodes (10-fold increase about dark conditions) was increased thanks to the PDA bridge used between ZnO and CeO_2 nanoparticles.

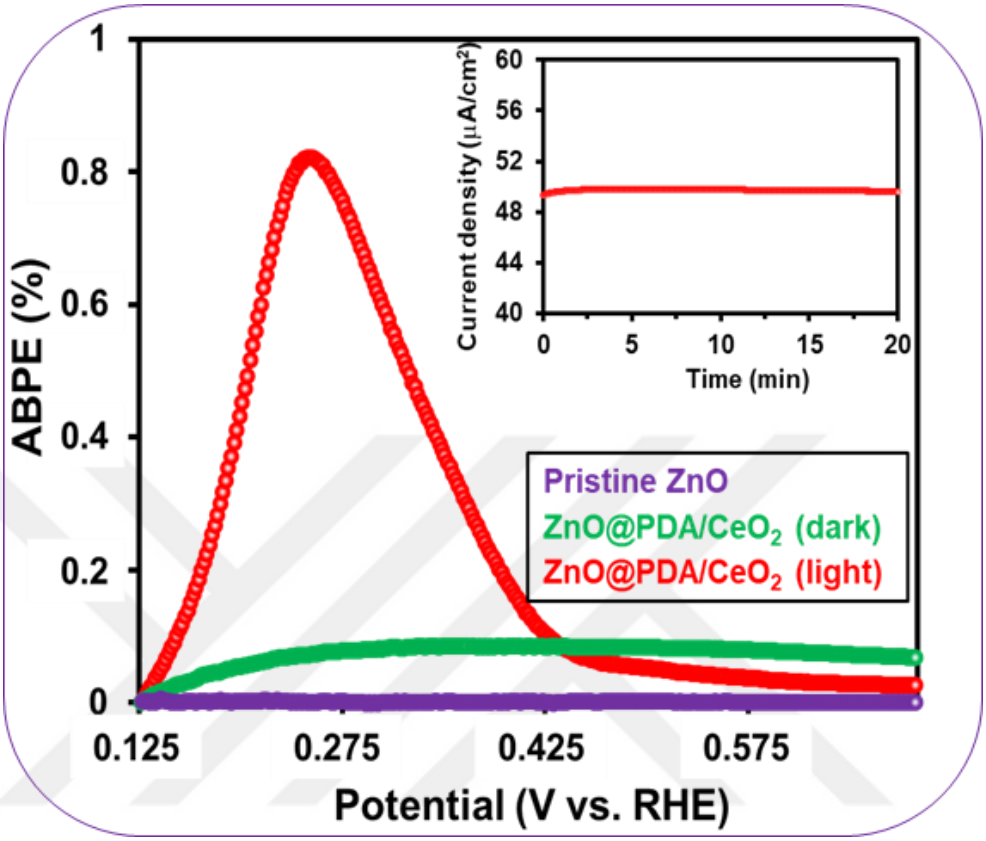

Figure 6.11 ABPE value of ZnO and ZnO@PDA/CeO_2 heterostructures (inset: PEC stability of the ZnO@PDA/CeO_2 NPs under 0.16 V (vs. reversible hydrogen electrode) for 1200 s)

Besides, the highest ABPE value with the lowest potential is proof of Z-scheme heterojunction between ZnO/CeO_2 interface using PDA. In addition, the long-term stability of the ZnO@PDA/CeO_2 photoanodes was investigated at 0.16 V (vs. RHE) for 1200 s. (Figure 6.11-inset). The novel ZnO@PDA/CeO_2 photoanodes indicated a consistently constant photocurrent density, verifying the electrodes stability as well [150].

6.1.12 Mott-Schottky Results of ZnO and CeO_2 NPs

Mainly in the literature Mott-Schottky measurement was utilized to calculate the flat band position and semiconductor type [67,234]. The Mott-Schottky measurement of ZnO star, CeO_2, and ZnO@PDA/CeO_2 are shown in Figure 6.12. As seen here, the

positive slope of the C^{-2} vs. potential indicates the n-type behavior related to the ZnO and CeO_2 NPs [25,29]. The flat band potential (V_{fb}) of the synthesized nanoparticles was calculated by extrapolation. The flat band value for ZnO nanoparticles was obtained as 0.3 V vs. RHE (Figure 6.12a). This value corresponds to 0.113 eV when converted to a normal hydrogen electrode (NHE). Moreover, the flat band value for CeO_2 was obtained as -0.1 V vs. RHE. Its value corresponds to 0.512 eV in the NHE (Figure 6.12b). The Mott Schottky plot of ZnO@PDA/CeO_2 incorporates both linear regions of ZnO star and CeO_2 as expected with identical flat-band potential values (Figure 6.12c). The Mulliken electronegativity equation was used to calculate the conduction and valence band potentials (E_{CB} and E_{VB}, respectively) of ZnO stars and CeO_2 [235].

$$E_{CB} = \chi - E_e - 0.5E_g \quad \textbf{(6.1)}$$

$$E_{VB} = \chi - E_e + 0.5E_g \quad \textbf{(6.2)}$$

Where, χ represents the electronegativity, E_e denotes the free electrons energy (vs. NHE, 4.5 eV), and E_g is the bandgap energy. According to the literaure, the electronegativity values for CeO_2 and ZnO were 5.56 and 5.79, respectively [235,236].

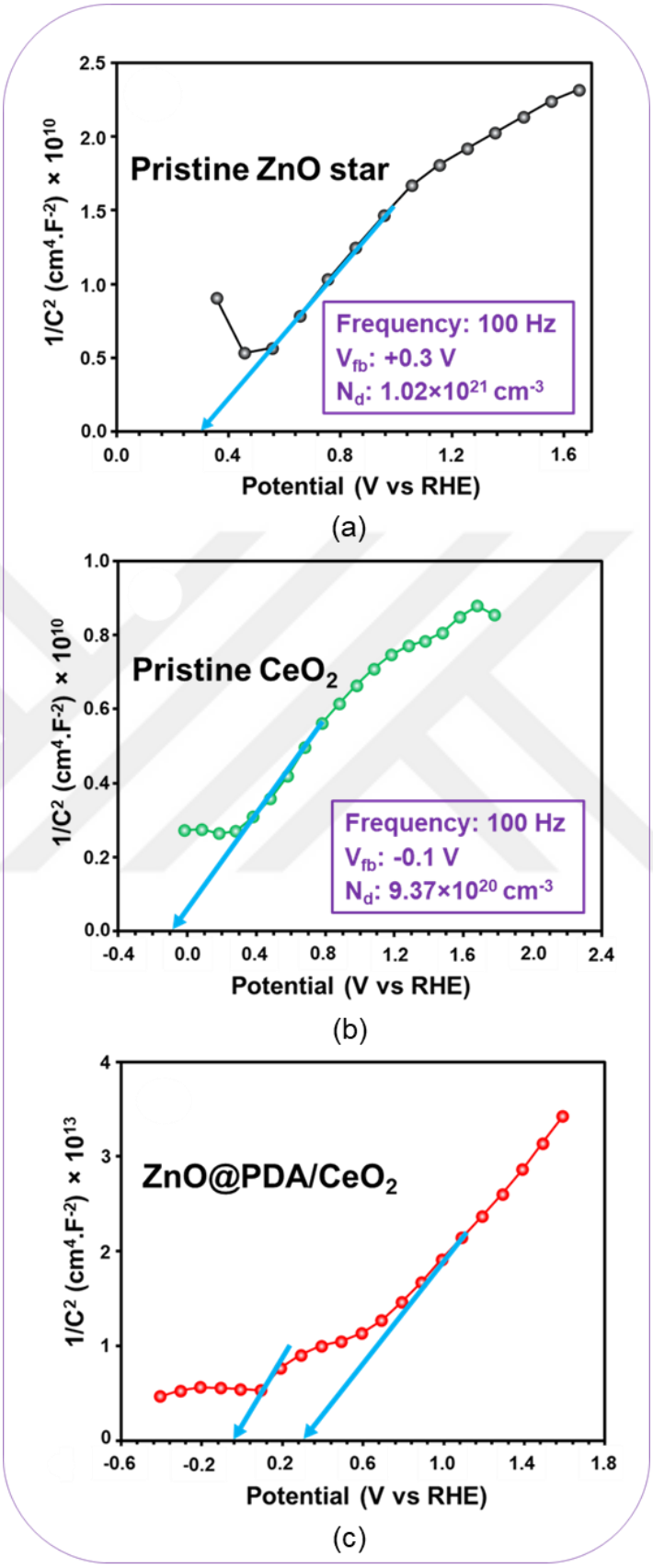

Figure 6. 12 Mott-Schottky plots for (a) ZnO, (b) CeO_2, and (c) ZnO@PDA/CeO_2 heterostructures

Using the band gap energy values from equations 6.1 and 6.2, the CB and VB are found to be -0.49 eV and 2.61 eV for CeO_2 and -0.2 eV and 2.8 eV for ZnO star, respectively (Figure 6.13). Mott-Schottky plots were utilized to calculate the carrier concentration of ZnO and CeO_2 nanostructures [220]. The dielectric constants of CeO_2 and ZnO were found to be 24 and 6.1, respectively [237,238]. With the equation in (5.7), the carrier concentrations of ZnO and CeO_2 were determined to be 1.02×10^{21} and 9.37×10^{20} cm^3, respectively [173].

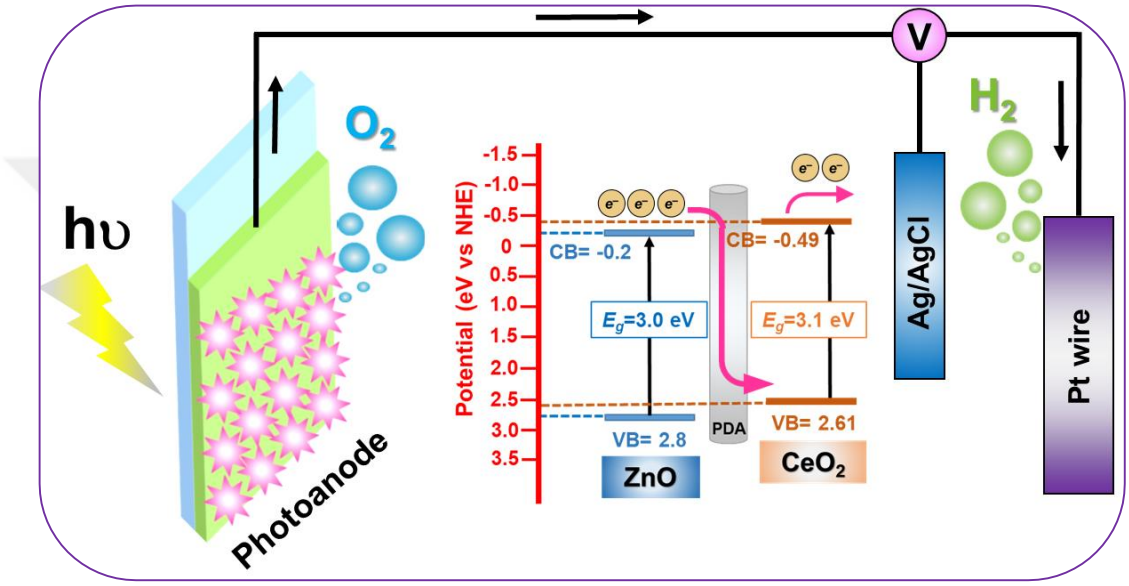

Figure 6.13 Schematic representation of the PEC reaction mechanism of Z-scheme ZnO@PDA/CeO_2 heterojunctions

6.1.13 Nyquist Plot Results of ZnO and ZnO@PDA/CeO_2 heterostructures

The EIS measured the resistance properties of ZnO@PDA/CeO_2 photocatalysts, and the results are shown in Figures 6.14 and Table 6.2. Figure 6.14 shows the resistivity of Z-scheme ZnO@PDA/CeO_2 photoanodes in dark and light conditions. Their resistivity is 21.73 and 21.24 Ω, respectively (Table 6.2). Besides, The R_{ct} values of the prepared photoanodes were also found to be 304.5 and 229.3 Ω under dark and light conditions, respectively. Under visible LED irradiation, the charge transfer resistance is reduced by 1.3, indicating that electron-hole recombination is inhibited, and photo-induced charge carrier migration is facilitated, which is consistent with PL results (Figure 6.7).

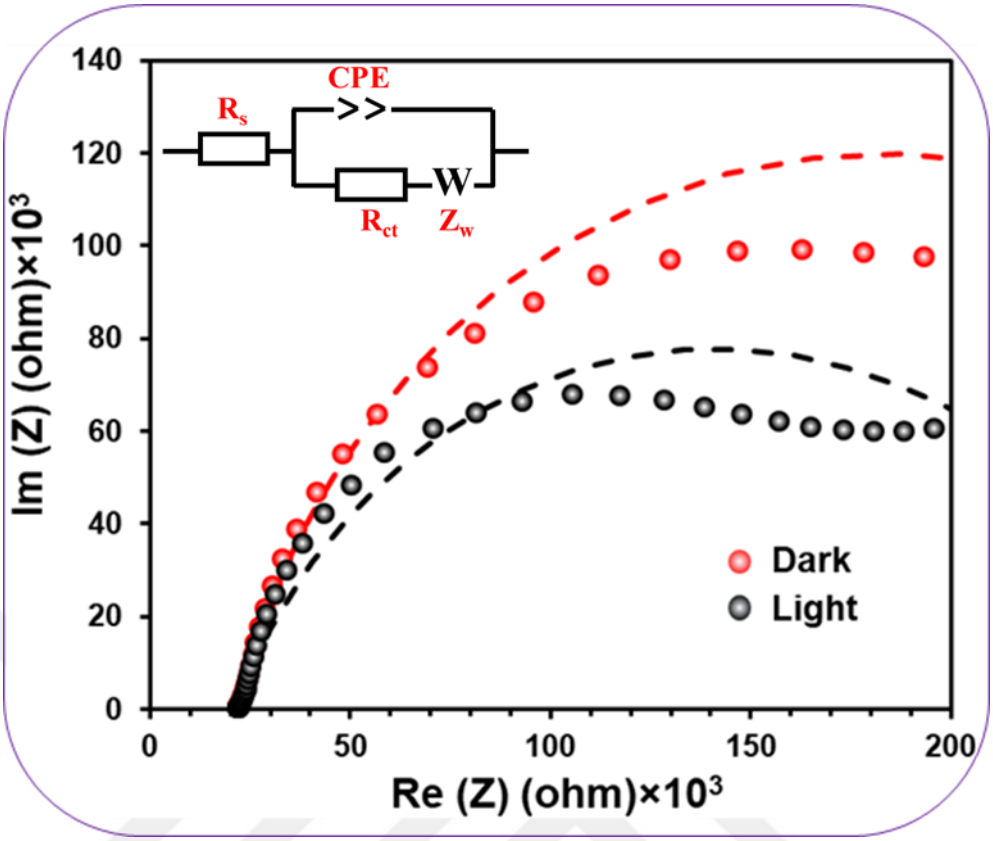

Figure 6.14 Nyquist plots of Z-scheme ZnO@PDA/CeO_2 heterostructures in dark and light

Table 6. 2 Values of circuit elements for Z-scheme ZnO@PDA/CeO_2 heterostructures calculated from Nyquist plots.

Conditions	R_S (Ω)	R_{CT} (Ω)	CPE	W
Dark	21.73	304.5	113.5×10^{-6}	11.29×10^{-3}
Light	21.24	229.3	205.2×10^{-6}	11.29×10^{-3}

6.1.14 Z-Scheme Charge Transfer Mechanism for ZnO@PDA/CeO_2 NPs

The photocatalytic performance of ZnO@PDA/CeO_2 photocatalyst was further evaluated using a homemade photoreactor under visible LED light illumination [67,177] (Figure 6.15c). As seen here, 95% of decolorization was obtained in 90 minutes using the ZnO@PDA/CeO_2 photocatalyst, which was much higher than that of pristine ZnO (40%). This result showed that PDA was essential as an electron transfer mediator for high photocatalytic performance by facilitating electron transfer and efficient electron-hole separation [36]. Furthermore, the PEC water splitting and organic dye degradation mechanism of ZnO@PDA/CeO_2 under visible LED light

irradiation were determined with trapping experiments performed to detect the predominant active oxidants, namely h^+,$^{\cdot}O_2^-$ and $^{\cdot}OH$ for photocatalytic experiments. Consequently, ethylenediaminetetra acetic acid (EDTA), benzoquinone (BQ), and isopropanol (IPA) were utilized to assign h^+,$^{\cdot}O_2^-$ and $^{\cdot}OH$, respectively. As shown in Figure 6.14c, introducing IPA and BQ into the reaction medium decreases photocatalytic efficiency obviously, representing$^{\cdot}O_2^-$ and $^{\cdot}OH$ are the main reactive species. However, after the addition of EDTA, degradation efficiency remains the same, which implies that h^+ is not an active species. Thermodynamically, it is favorable to produce $^{\cdot}O_2^-$ and $^{\cdot}OH$ radicals for pristine CeO_2 because CB reduction capacity is more negative than the redox potential of $O_2^{\cdot-}/O_2$ and VB oxidation potential is more positive than the redox potential of $^{\cdot}OH$ /OH^-. However, in the case of pristine ZnO, only $^{\cdot}OH$ could be produced owing to the suitable VB position, having more positive redox potential than the redox potential of $^{\cdot}OH$ /OH^-. Corresponding to the CB of ZnO, $O_2^{\cdot-}$ could not be generated due to a more positive CB potential value compared to the redox potential of $O_2^{\cdot-}/O_2$. The suitable and relative band positions of heterojunction photocatalyst with respect to each other are crucial because it determines the direction of charge carriers, affecting the recombination of electron-hole and photocatalytic performance. If the charge migration behaviour of the ZnO@PDA/CeO_2 agrees with the conventional Type II heterojunction mechanism (Figure 6.15a), the photoinduced electrons in the CB of CeO_2 would move to the CB of ZnO along with the PDA layer meanwhile holes would migrate from VB of ZnO to CeO_2. Therefore, electrons were accumulated on CB of ZnO while holes were accumulated on VB of CeO_2. Holes on CeO_2 could produce $^{\cdot}OH$ owing to more positive VB potential than the redox potential of $^{\cdot}OH$ /OH^- (2.27 eV) $^{\cdot}OH$ /H_2O (1.99 eV), but electrons on the CB of ZnO was unable to generate $O_2^{\cdot-}$ due to the more positive CB potential (-0.2 eV) than the redox potential of $O_2^{\cdot-}/O_2$ (-0.33 eV). However, both $^{\cdot}OH$ and of $O_2^{\cdot-}$ were determined as the main active species from PL measurements and scavenger experiments, representing both radicals were responsible for photocatalytic degradation and water splitting using ZnO@PDA/CeO_2 catalyst. These results contradict with Type II mechanism in which it was only possible to produce $^{\cdot}OH$ radicals for ZnO@PDA/CeO_2 catalytic system (Figure 6.15a), so it was expected low photocatalytic performance. According to the abovementioned trapping

results, a Z-scheme mechanism for ZnO@PDA/CeO_2 heterojunctions could be announced for the first time in the literature. Upon LED illumination, photoinduced electrons on CB of ZnO were transferred through PDA to VB of CeO_2. Subsequently, electrons on the less negative CB potential of ZnO move to the less positive VB potential of CeO_2, bringing about the accumulation of electrons in more negative CB and holes in more positive VB potentials. As seen in Figure 6.15b, CeO_2 has more negative CB potential than $O_2^{\cdot-}/O_2$ (-0.33 eV), confirming the generation of $O_2^{\cdot-}$ by CeO_2. Even holes were accumulated on ZnO semiconductors (i.e., having more positive VB potential than CeO_2 VB). In this case, the reduction occurred on CB of CeO_2, having stronger reducibility than that of ZnO, resulting in a more radical formation and an enhancement in photocatalyst performance. In addition, the Z-scheme mechanism for ZnO@PDA/CeO_2 photocatalyst was further verified by PL measurements (Figure 6.15e and f). For this purpose, TPA and BQ were used as probe molecules for the detection of hydroxyl and peroxide radicals, respectively. Fluorescent 2-hydroxyterephthalic acid (TAOH) was generated by a terephthalic reaction with ·OH radicals [239]. In the case of BQ, $O_2^{\cdot-}$ radicals were consumed with BQ, and reduction occurred, thus yielding hydroquinone in the reaction medium [240]. Therefore, the production of hydroquinone led to the increase in the time-dependent PL intensity while the PL quenching effect of BQ was reduced (Figure 6.15c) [241]. As seen in Figure 6.15f, no PL signal was observed before LED light illumination, but PL intensities increased with time, suggesting photocatalysts were activated under visible LED illumination, thus generating ·OH radicals, which were one of the main radicals for the catalytic process. These results clearly implied that the $O_2^{\cdot-}$ and ·OH, radicals played a crucial role in the photocatalytic performance of ZnO@PDA/CeO_2. As previously declared, ZnO semiconductor was unable to produce $O_2^{\cdot-}$ radical due to more positive CB potential compared with $O_2^{\cdot-}/O_2$ (-0.33 eV) and wrapping by PDA. Consequently, $O_2^{\cdot-}$ radicals could only be generated from CeO_2 having more negative CB potential. This result strongly supported the Z-scheme mechanism in which $O_2^{\cdot-}$ radicals, for heterojunction photocatalyst, were obtained from semiconductor with more negative CB potential value, which was also consistent with trapping experiments as well as XPS results.

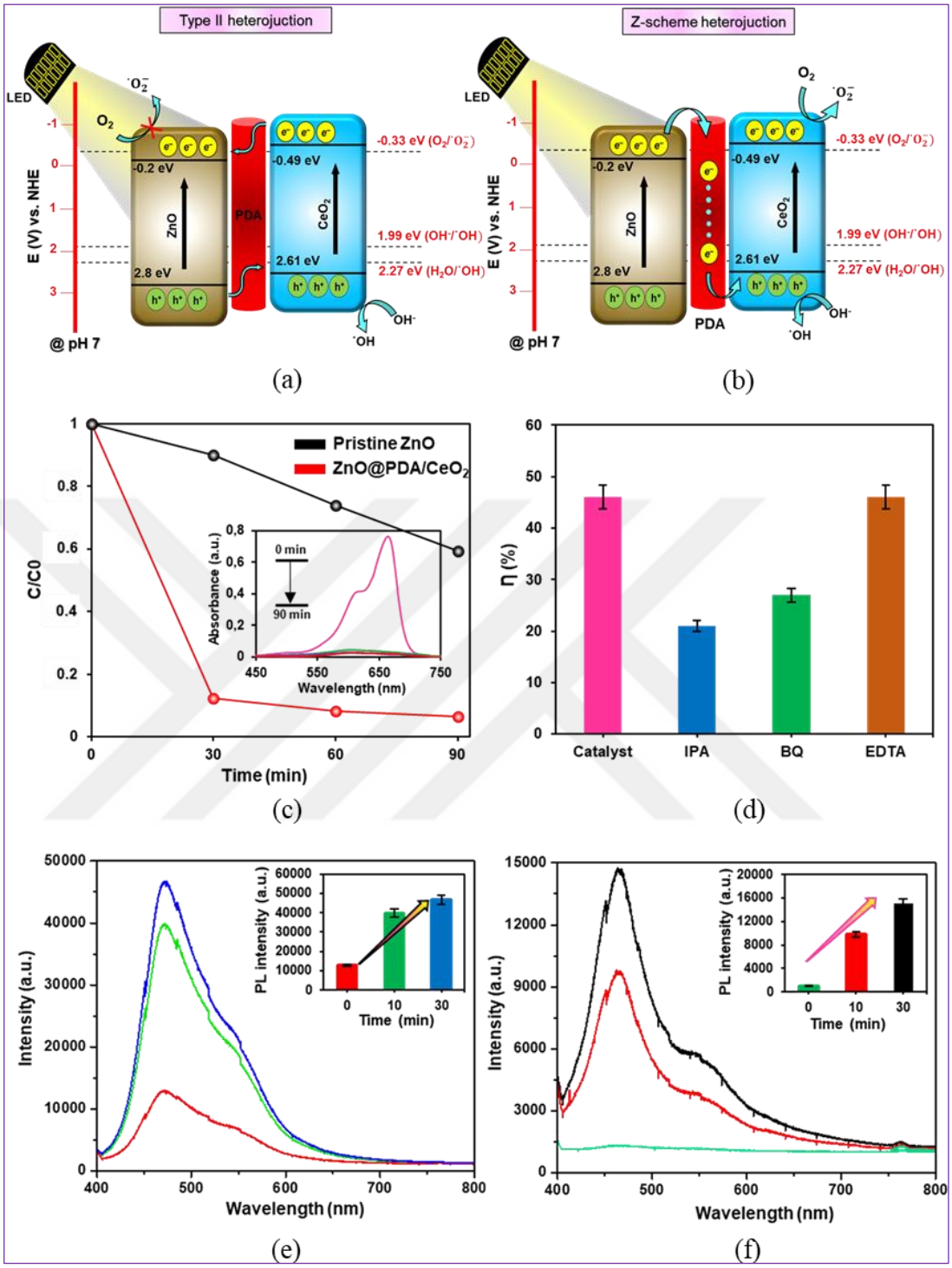

Figure 6. 15 Schematic representation of photoinduced charge transfer prosses for ZnO@PDA/CeO_2 NPs: (a) Type II heterojunction and (b) Z-scheme heterojunctions, (c) The change of MB concentration with time using pristine ZnO and Z-scheme ZnO@PDA/CeO_2 NPs (reaction conditions: concentration of MB: 3.125×10^{-5} M; photocatalyst amount: 10 mg); (d) Photocatalytic performance of Z-scheme ZnO@PDA/CeO_2 NPs using IPA, BQ, and Na-EDTA scavengers (the error bars were calculated according to three replicate experiments); PL spectra belong to (e) the $\cdot O_2^-$ and (f) the $^{\bullet}$OH trapping experiments using Z-scheme ZnO@PDA/CeO_2 NPs (reaction conditions: photocatalyst amount: 10 mg; the concentration of BQ and TPA: 0.5 mM) (the error bars were calculated according to three replicate experiments).

The Z-scheme mechanism over ZnO@PDA/CeO_2 heterojunctions was extended using XPS results by considering the changes in the electron density of semiconductors. As seen in Figures 6.5b and c, the O 1s peak of ZnO@PDA/CeO_2 shifted to a lower energy region, whereas Zn 2p XPS peak of ZnO@PDA/CeO_2 displayed an obvious peak shift toward higher energy regions, compared with pristine ZnO. Therefore, the negative and positive shifting of the binding energies could be ascribed to the decrease and increase in the electron density, respectively. Thereby, the electron transfer pathway within ZnO@PDA/CeO_2 heterojunctions could be predicted from ZnO (CB) to CeO_2 (VB). Therefore, the presence of PDA provided a solid-solid interfacial interaction that facilitated the pumping and separation of photogenerated charge carriers for enhanced PEC water splitting.

6.2 Physical and Chemical Characterization of Z-scheme ZnO@MOF-5 NPs

6.2.1 XRD Pattern of ZnO, ZnO@MOF-5 and ZnO@MOF-5-C heterostructures

Figure 6.16a (dark, blue, and green line) and 6.16b (red line) display the XRD patterns of the ZnO, ZnO@MOF-5, ZnO@MOF-5-C, and bare MOF-5. Figure 6.16a (dark line) shows the peaks of the ZnO nanoparticle between 2 θ = 10^0-80^0 degrees. Moreover, (100), (002), (101), (102), (103), (110), and (112) are the peaks corresponding to the hexagonal wurtzite plane of the ZnO structure. These sharp and strong peaks are related to 2θ~31.4°, 34.2°, 36.1°, 47.3°, 56.4°, 62.5°, and 67.8°, respectively, with good agreement with literature (JCPDS card #36-145) [242]. After the MOF-5 structure was coated on ZnO using the solvothermal synthesis method, new peaks appeared between 2 θ = 10-30 (Figure 6.16a blue line). Figure 6.16b shows that these peaks belong to the MOF-5 structure. After the ZnO (core) and MOF-5 (shell) composite structure is formed the crystal structure ZnO has not changed. In addition, the X-ray diffraction patterns of bare MOF-5 are given in Figure 6.16b. MOF-5's nine main characteristic peaks were observed at 2θ of 6.26^0, 8.79^0, 13.77^0, 15.34^0, 20.50^0, 22.46^0, 24.73^0, 30.05^0, and 32.18^0 corresponding to the (200), (220), (400), (420), (531), (533), (551), (751), and (911) planes, respectively [65,163,243,244]. Moreover, these main diffraction peaks confirm the successful synthesis of MOF-5 crystalline

phase. Besides, this indicates that the MOF-5 was successfully coated onto the ZnO surface. Finally, the XRD pattern of ZnO@MOF-5-C (after calcination process) is shown in Figure. 6.16a (green line). Here, we can say that the peak at 27.07^0 belongs to MOF-5 structures and is compatible with the literature [244–246]. In addition, even after this calcination process, the peaks of the wurtzite hexagonal crystal structure of ZnO and the peaks of the crystal structure of MOF-5 are observed. These results mainly showed the successful formation of N-doped carbon layer onto ZnO@MOF-5 core-shell heterostructures.

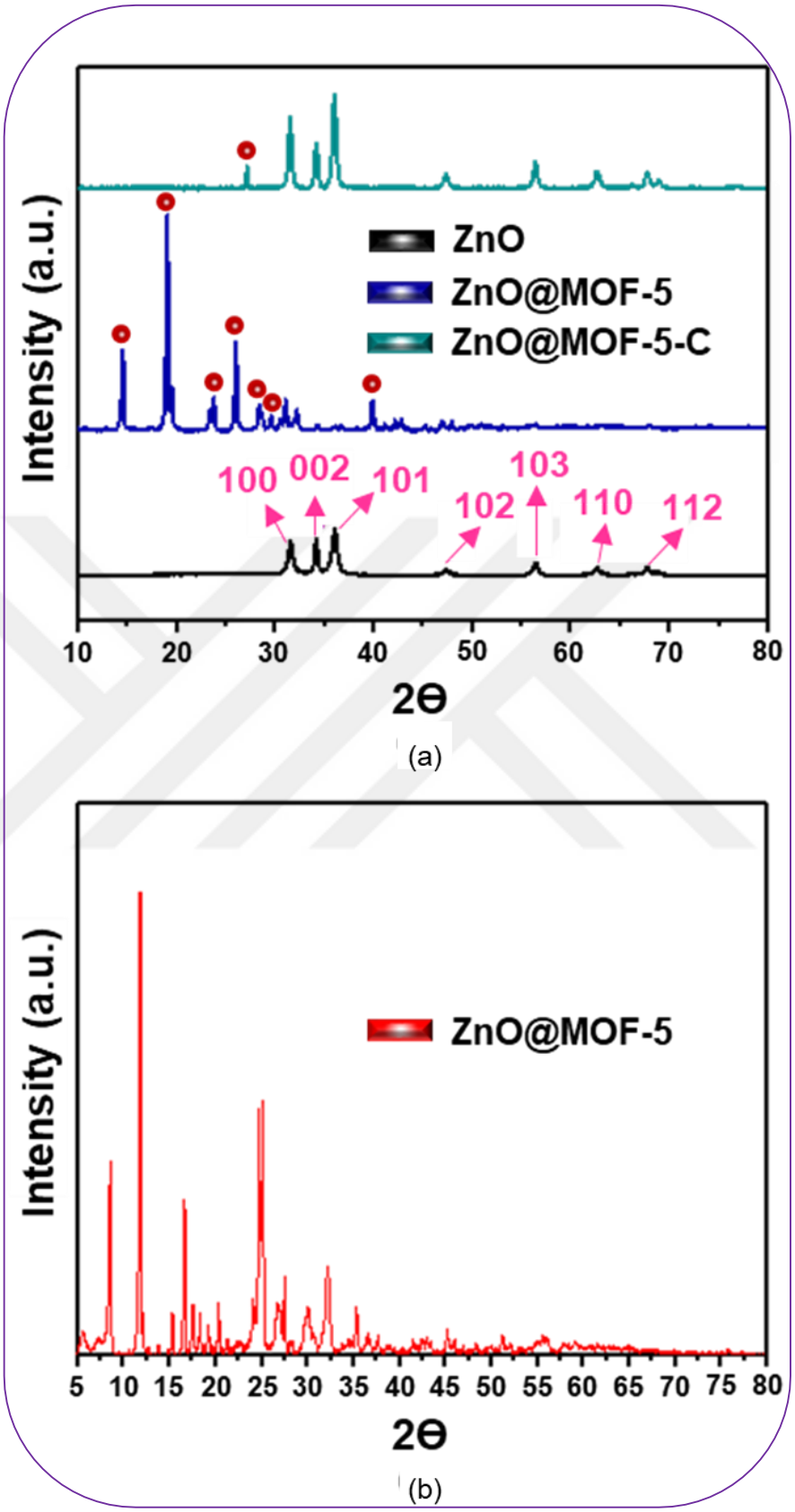

Figure 6. 16 XRD pattern of (a) ZnO, ZnO@MOF-5 , and ZnO@MOF-5-C NPs (b) Bare MOF-5 NPs

6.2.2 SEM Images of ZnO, ZnO@MOF-5, and ZnO@MOF-5-C heterostructures

The SEM of bare ZnO star, ZnO@MOF-5, and ZnO@MOF-5-C nanoparticles were shown in Figure 6.17. Fig.6.17a demonstrates the SEM images of the ZnO star NPs, with quite narrow and monodisperse size distributions. Moreover, the average diameter of the ZnO star was found to be approximately 800 nm. SEM images of ZnO@MOF-5 core-shell heterostructures are given in Figure 6.17b. As seen here, the average diameter of the ZnO star decreased after the MOF-5 coating. The average diameter of the ZnO@MOF-5 core-shell structure was found to be approximately 556 nm, with no change in the star shape of ZnO nanoparticles. These decrease is due to the etching of the surface of ZnO in ethanol as well as formation of Zn^{2+} onto the surface. Then, addition of terephthalic acid to the raction medium led to the formation of metal-affinity between Zn^{2+} and –COOH groups that initialized the synthesis of ZnO@MOF-5 core-shell at 51°C [247]. In the last stage, the PDA layer was coated onto ZnO@MOF-5 core-shell nanoparticles and subsequently the calcination was performed under the nitrogen environment. Following the calcination process, a thin layer of N-doped carbon was formed onto the surface of the ZnO@MOF-5 composites. Furthermore, ZnO@MOF-5-C ternary structure with preserved star-shaped morphology and uniform monodispersibility was achieved (Figure 6.17c). Moreover, elemental mapping (EDX) of heterostructures was also investigated to evaluate the distribution of component elements. All main elements (Zn, O, C, N) have been proven to exist in ZnO@MOF-5-C NPs (Figure 6.17d). Besides this, the N element is detected in EDX mapping, indicating the particles were coated by an N-doped carbon layer, which agrees with XPS results as well.

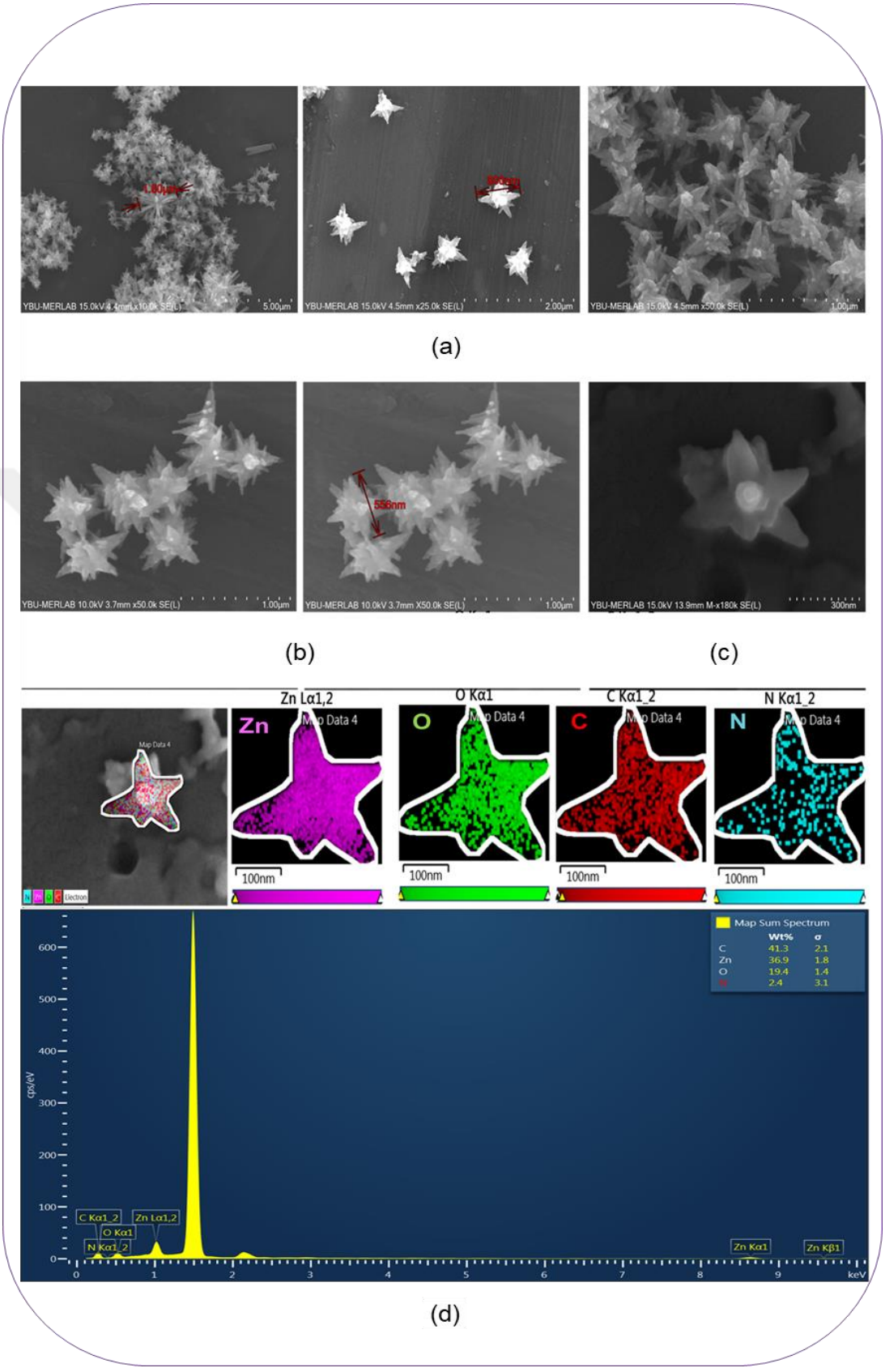

Figure 6. 17 SEM images of (a) ZnO star, (b) ZnO@MOF-5, and (c) ZnO@MOF-5-C heterostructures; (d) corresponding SEM elemental mapping images of Zn, O, C, and N

6.2.3 UV-Vis Spectra Images of ZnO, ZnO@MOF-5 and, ZnO@MOF-5-C heterostructures

Figures 6.18a show UV-Vis spectra of ZnO star, MOF-5, ZnO@MOF-5 and ZnO@MOF-5-C. As seen here, the ZnO absorption peak was observed at around 369 nm, which is the characteristic peak for hexagonal wurtzite of ZnO; besides this, a red-shift of 4 nm was exhibited according to the absorption peak of bulk ZnO at 365 nm [225]. In addition, the bare MOF-5 shows a characteristic peak at 329 nm with no absorption spectra in the visible region, which is in agreement with the literature (310.2 - 364.9 nm) [243,248]. After formation of ZnO@MOF-5 core-shell structure, a broad absorption peak ranging from 330 nm to 600 nm was obtained that outstandingly demonstrated an enhancement toward visible-light absorption as well.

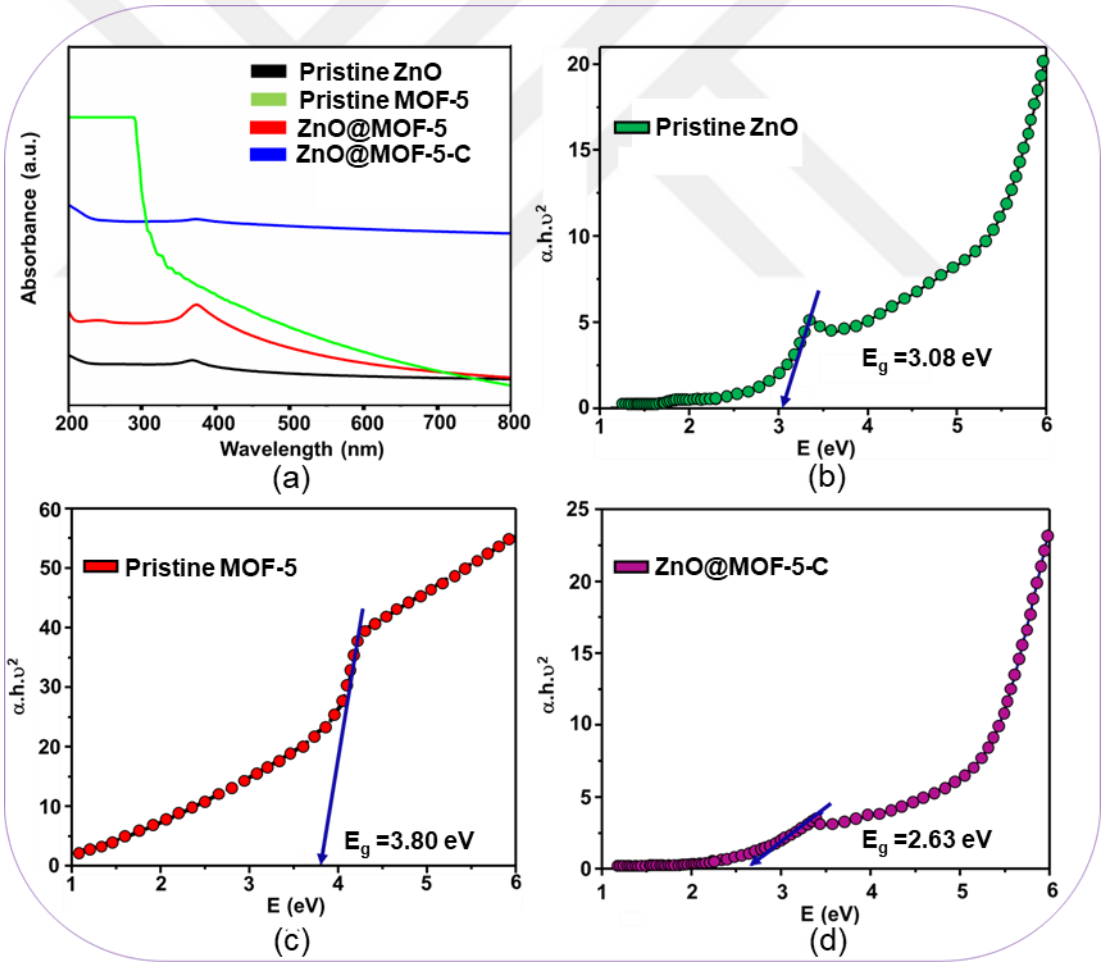

Figure 6. 18 (a) UV-Vis spectra of ZnO, MOF-5, ZnO@MOF-5 and ZnO@MOF-5-C heterostructures; (b) Tauc plot of ZnO; (c) Tauc plot of MOF-5 and (d) Tauc plot of ZnO@MOF-5-C heterostructures

Tauc plots of pristine ZnO, bare MOF-5, and ZnO@MOF-5-C heterostructures are shown in Figures 6.18 b, c, and d, respectively. The same with literature findings, bare ZnO nanoparticle demonstrated a direct band gap of approximately 3.37 eV [142,150,249,250]. Additionally, the MOF-5 NPs showed a bandgap ranging between 3.4 eV and 4.0 eV which depends on the synthesis conditions (crystal size, concentration, temperature, preparation method, and sample processing) [248]. In our case, the synthesized MOF-5 NPs demonstrated 3.80 eV band gap in good agreement with the literature [243,251].

6.2.4 XPS Results of ZnO, ZnO@MOF-5-C heterostructures

XPS was used to determine the chemical composition and valance state of the bare ZnO and ZnO@MOF-5-C heterostructures. Zn, O, and C elements were also marked on the XPS spectra (Figure 6.19a) [53,252]. In Figure 6.19b, the two peaks at 1021.4 and 1044.5 eV were assigned to the Zn 2p high-resolution core levels (Zn $2p_{3/2}$ and Zn $2p_{1/2}$, respectively) [150]. These two peaks were shifted to higher energies after fabrication of ZnO@MOF-5-C heterostructures (1021.6 and 1044.7 eV, respectively) [252]. This result shows the successful formation of the N-doped carbon layer onto the core-shell ZnO@MOF-5 heterostructures. Additionally, in the O 1s high-resolution core levels, two peaks with binding energies of 529.4 eV and 532 eV were assigned. These peaks can be attributed to lattice oxygen and non-lattice oxygen (adsorbed oxygen), respectively (Figure 6.19c). The peak corresponding to adsorbed oxygen (532 eV) in ZnO@MOF-5-C became more apparent, and the peak area increased compared to pristine ZnO. These findings clearly proved the ternary heterostructure with more oxygen vacancies [53]. In Figure 6.19d, the high resolution of core level of N 1s were deconvoluted into three peaks (400.9, 399.6, and 398.2 eV), which are attributed to graphitic N, pyrrolic N, and pyridinic N, respectively [253,254]. The nitrogen state and content are crucial in terms of PEC activity; however, the influence of nitrogen chemical states on ORR has yet to be discovered. In the literature it is believed that pyridinic N plays the most important role in ORR activity, while in some studies the graphitic nitrogen is accepted as most active centre. Still, it is generally argued that both may contribute equally to catalytic activity as well [255]. Moreover, the presence of functional groups of N atom (graphitic, pyrrolic, and pyridinic) in N1s core level

proves that the ZnO@MOF-5 core-shell heterostructure is successfully deposited with an N-doped carbon layer. Figure 6.19e shows the deconvoluted high-resolution XPS C1s core level related to ZnO@MOF-5 core-shell heterostructure.

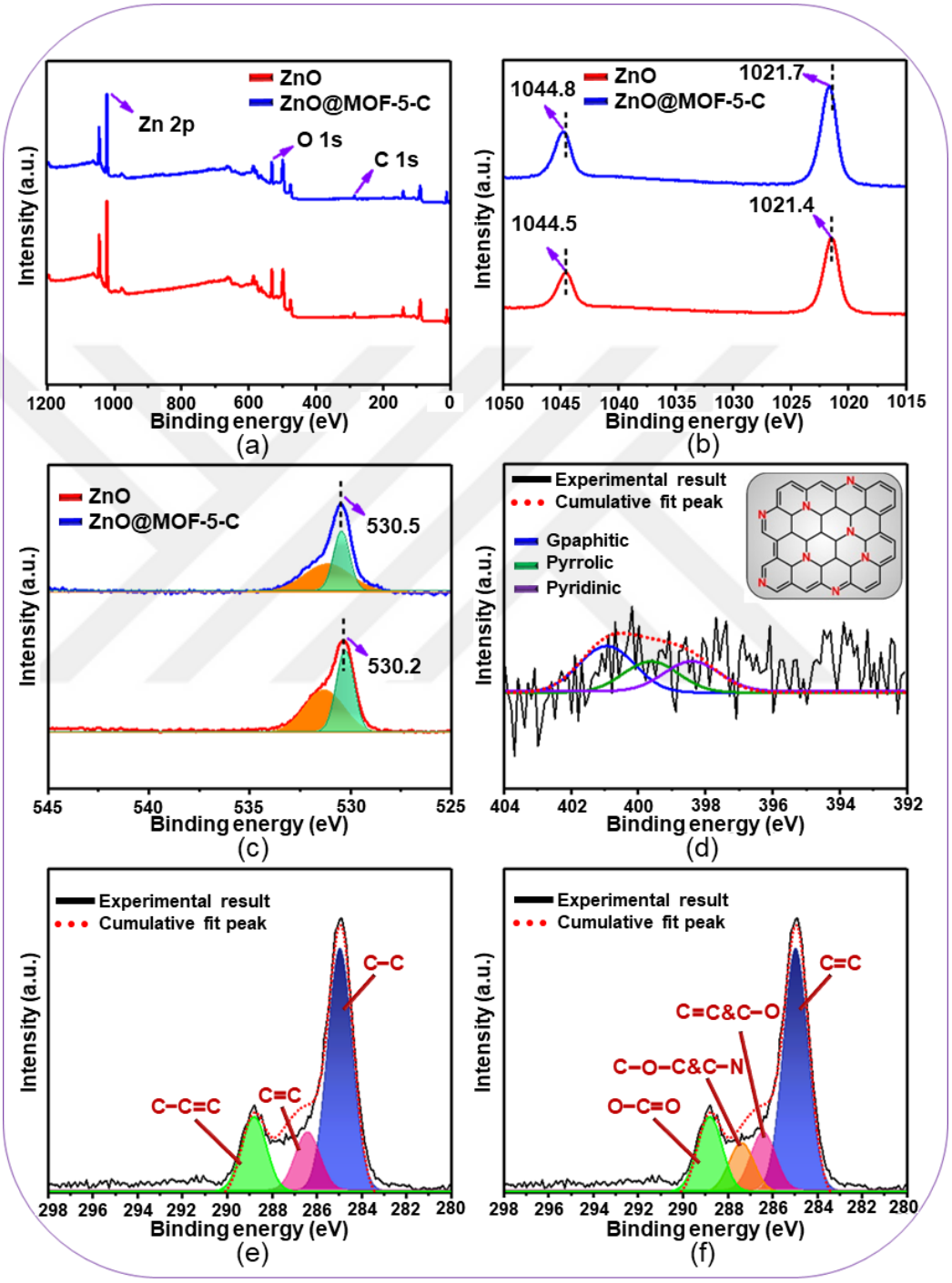

Figure 6. 19 XPS survey spectra of (a) bare ZnO and ZnO@MOF-5-C heterostructures; (b) high-resolution Zn 2p core level for ZnO and ZnO@MOF-5-C NPs; (c) high-resolution O 1s core level for ZnO and ZnO@MOF-5-C heterostructures; (d) high-resolution N 1s for ZnO@MOF-5-C heterostructures (e) C1s of ZnO@MOF-5 sample (f) C1s of ZnO@MOF-5-C heterostructures.

As seen here, the peaks at 284.4, 285.1, 286.8, and 289.1 eV belong to C-C, C=C, and O-C−O bonds, respectively. The peak at 284.6 is attributed to the C-C or C=C of aromatic rings. Additionally, the peak at 284.6 eV is ascribed to the COO species in the network of MOF-5 phase as well [65]. The C1s core level specta of ZnO@MOF-5-C ternary heterostructure was deconvoluted into four diffraction peaks (284.3 eV, 285.1 eV, 286.2 eV, and 288.6 eV) attributed to C–C/C=C, C–N, C–O, and O–C=O groups, respectively (Figure 6.19f) [253,256]. In the literature, the N-doped carbon layer with more than one nitrogen species provides high electrical conductivity and electrochemical activity which helps carrier transport at the interface due to defects caused by N doping [257].

6.2.5 Brunauer-Emmett-Teller (BET) analysis of ZnO and ZnO@MOF-5-C heterostructures

The surface areas and porosity of the obtained materials were analyzed by the adsorption-desorption isotherm according to Brunauer-Emmett-Teller (BET) method (Figure 6.20). As seen here a typical IV isotherm with a hysteresis loop was obtained (Figure 6.20a) [185,258]. Furthermore, the pore size distributions obviously revealed the mesoporous characteristics of the ZnO@MOF-5-C ternary nanoparticle at approximately (2-10 nm) (Figure 6.20b). In conclusion, the formation of sharp peaks in the mesoporous fraction of ZnO@MOF-5-C ternary heterostructures clearly showed an increase in specific surface area, pore-volume, and average pore size compared to bare ZnO NPs (Table 6.3). This phenomenon directly impacts the mass absorption capacity of ZnO@MOF-5-C ternary heterostructures, thereby improving the PEC water splitting efficiency.

Table 6. 3 Experimentally obtained specific surface area (SSA), pore-volume, and mean pore size value of ZnO star and ZnO@MOF-5-C heterostructures

Sample	SSA (m^2/g)	Pore volume (cm^3/g)	Mean pore size (nm)
Pristine ZnO	21	0.006	2.3
ZnO@MOF-5-C	26	0.008	2.3

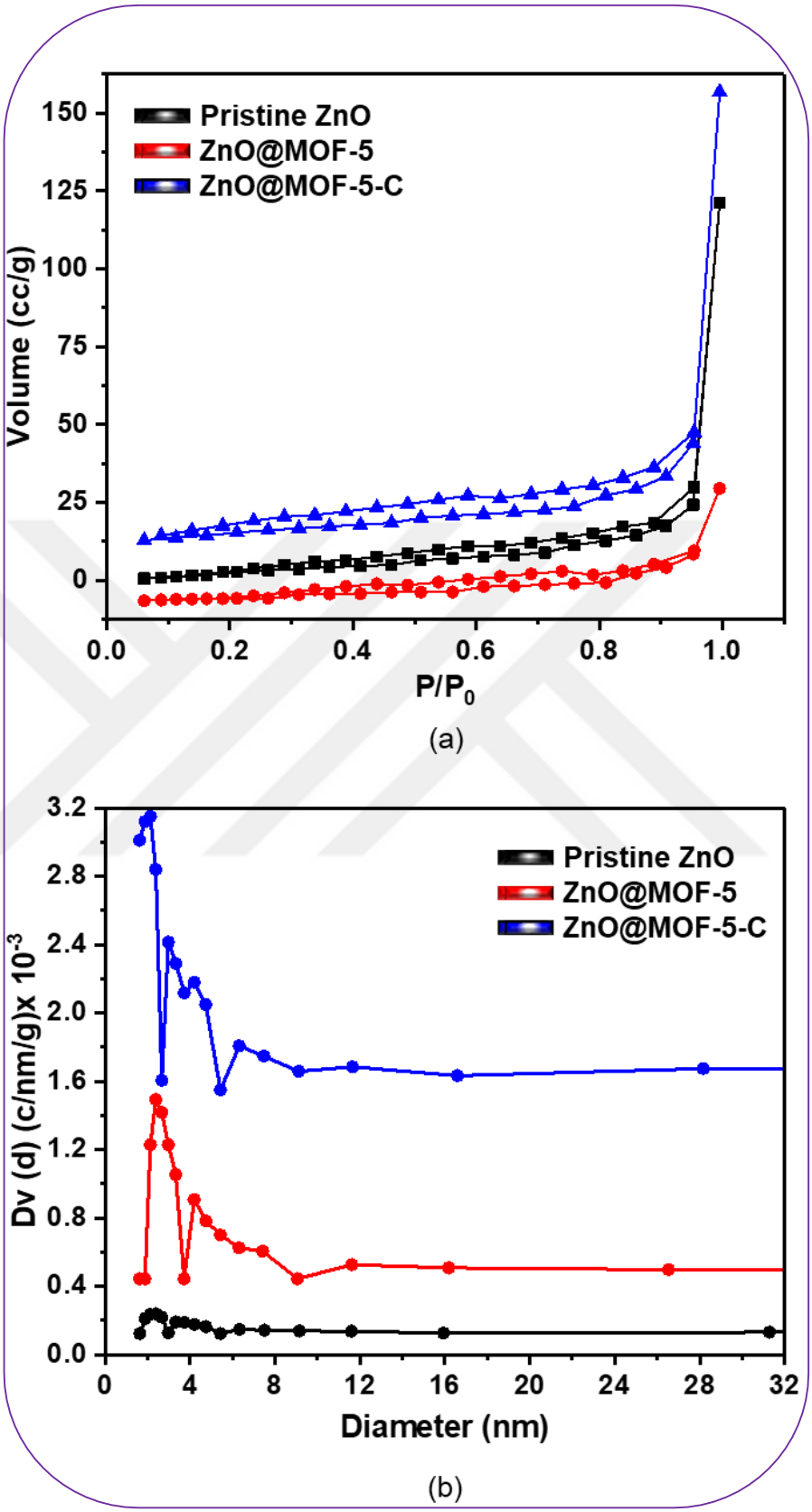

Figure 6. 20 (a) Nitrogen adsorption-desorption diagram ZnO, ZnO@MOF-5, and ZnO@MOF-5-C heterostructures, and (b) pore size distribution of ZnO, ZnO@MOF-5, and ZnO@MOF-5-C heterostructures

6.2.6 Photoluminescence Spectroscopy (PL) Analysis of ZnO and ZnO@MOF-5-C heterostructures

Photoluminescence (PL) experiments were carried out to better understand the efficiency of charge trapping and e^-/h^+ recombination (Figure 6.21). The PL intensity was significantly suppressed for ZnO@MOF-5-C compared to pristine ZnO, rendering a prolonged lifetime of charge carriers. These results revealed that using the N-doped carbon layer facilitated charge transfer onto core-shell ZnO@MOF-5, resulting in enhancement of electron-hole separation, which would provide high photocatalytic performance.

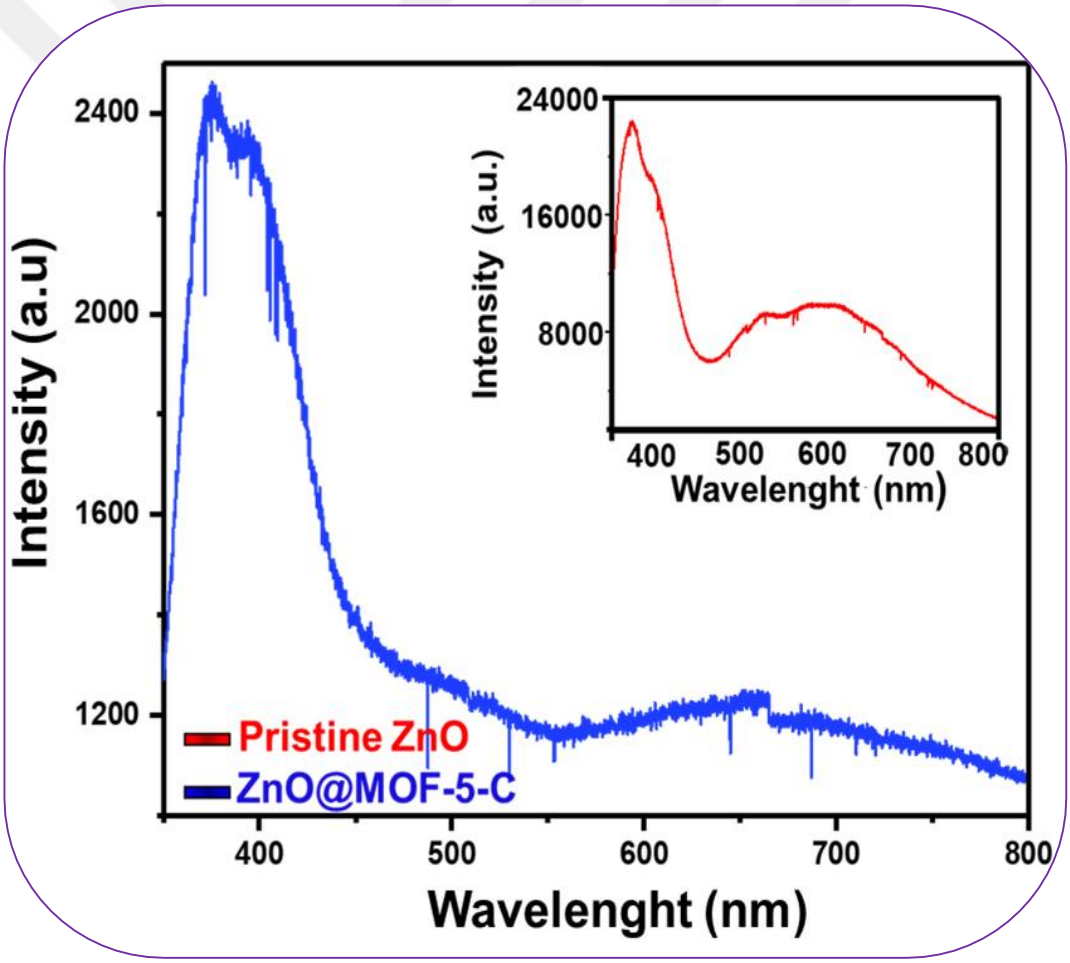

Figure 6. 21 Photoluminescence of pristine ZnO and ZnO@MOF-5-C heterostructures

6.2.7 LSV Images of ZnO, ZnO@MOF-5 and ZnO@MOF-5-C heterostructures

The PEC water splitting performance of the ZnO, ZnO@MOF-5, and ZnO@MOF-5-C heterostructures was investigated under dark and Xe (300W lamp) light irradiation (Figure 6.22). In dark condition, the maximum photocurrent density for ZnO, ZnO@MOF-5, and ZnO@MOF-5-C heterostructures were obtained as 0.49 mA/cm^2, 0.21 mA/cm^2, and 0.27 mA/cm^2 at 2.50 V vs. RHE, respectively. The same results were reported in the literature [259,260]. After completely wrapping of ZnO NPS with MOF-5 layer, the maximum photocurrent density was increased to 2.49 mA/cm^2 at 2.50 V vs. RHE under Xe (lamp) light conditions. In the case of ZnO@MOF-5 core-shell heterostructures, the light response dramatically increased the highest photocurrent density which is 11.8 times higher than dark conditions.

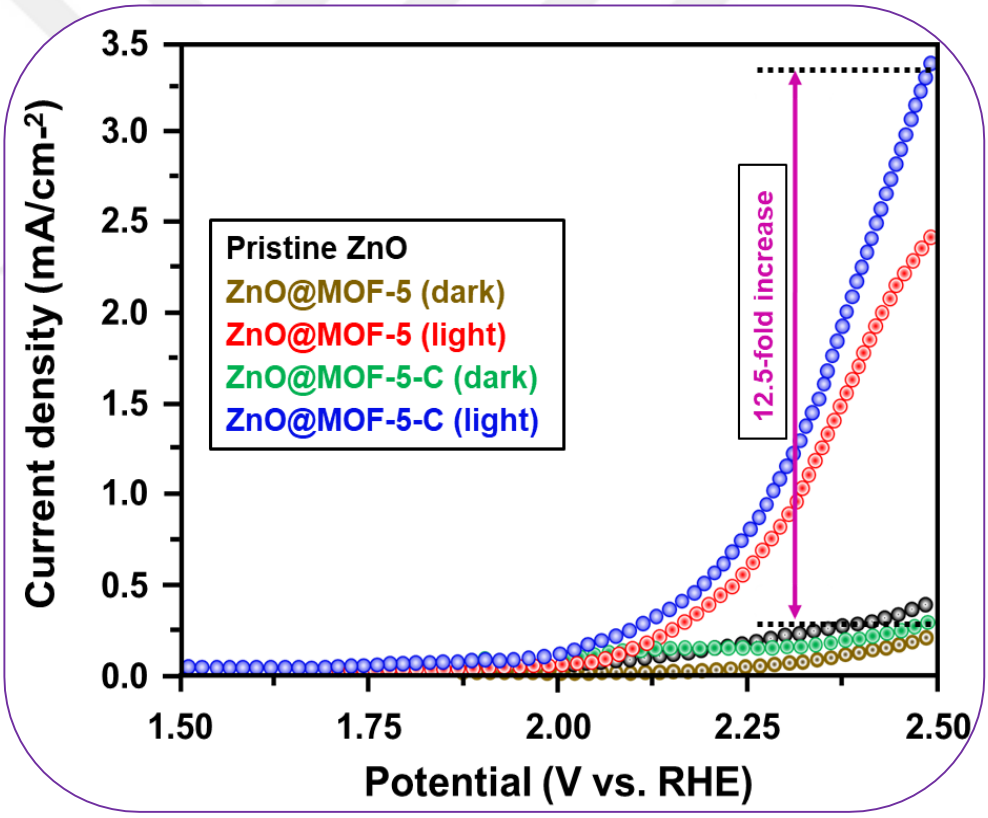

Figure 6. 22 J-V results of pristine ZnO, ZnO@MOF-5, and Z-scheme ZnO@MOF-5-C NPs (under dark and light)

This increase can be explained due to the rapid separation and transfer of a photo-generated electron from the CB of ZnO to the VB of MOF-5. In addition, efficiency

increased due to a reduction in electron-hole recombination. Moreover, in the case of ZnO@MOF-5–C ternary heterostructures, an enhancement was observed for under Xe light which is 12.5-fold times higher than dark condition. This enhancement can be explained due to the rapid separation and transfer of a photogenerated electron from the CB of ZnO to the VB of MOF-5.

6.2.8 Tafel slope of ZnO, ZnO@MOF-5 and ZnO@MOF-5-C NPs

Tafel slopes were measured for photoanodes in order to assess the electrode-catalytic kinetics process. From the literature, the small Tafel slope demonstrates quick kinetic charge transfer and low polarization resistance [261]. Figure 6.23 shows Tafel plots of bare ZnO star, ZnO-MOF-5, and ZnO@MOF-5-C heterostructures, which were found to be 286 mV/dec, 60mV/dec, and 48 mV/dec, respectively. The smallest Tafel slope was obtained for ZnO@MOF-5-C ternary heterostructure. Furthermore, these Tafel slope values were consistent with the LSV results. These results were obtained due to good electronic coupling, higher catalytic activity, high conductivity, and low charge transfer resistance.

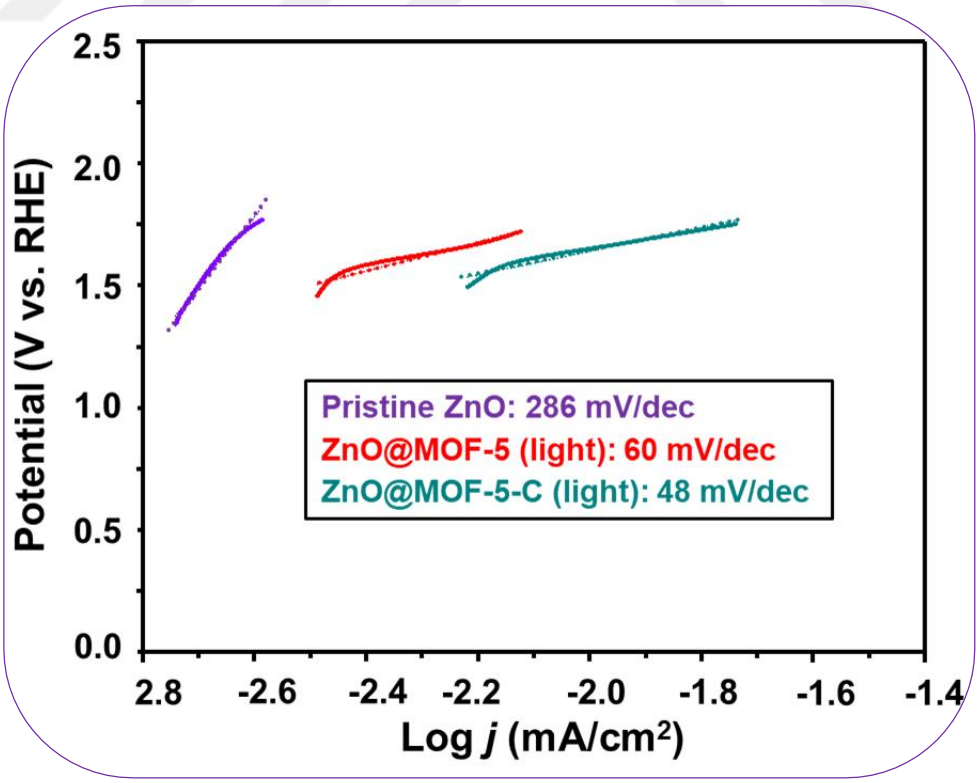

Figure 6. 23 Tafel plots of ZnO, ZnO@MOF-5 and ZnO@MOF-5-C heterostructures

6.2.9 IPCE Results of ZnO, ZnO@MOF-5, and ZnO@MOF-5-C heterostructures

The IPCE calculations were carried out to determine the maximum possible efficiency. Figure 6.24 represents the IPCE for ZnO, ZnO@MOF-5, and ZnO@MOF-5-C heterostructures under dark and Xe light illumination. The IPCE value for ZnO (light), ZnO@MOF-5 (dark and light), and ZnO@MOF-5-C (dark and light) are 2.89 %, 1.92 % and 17.64 % and 2.08 % and 24.5%, respectively.

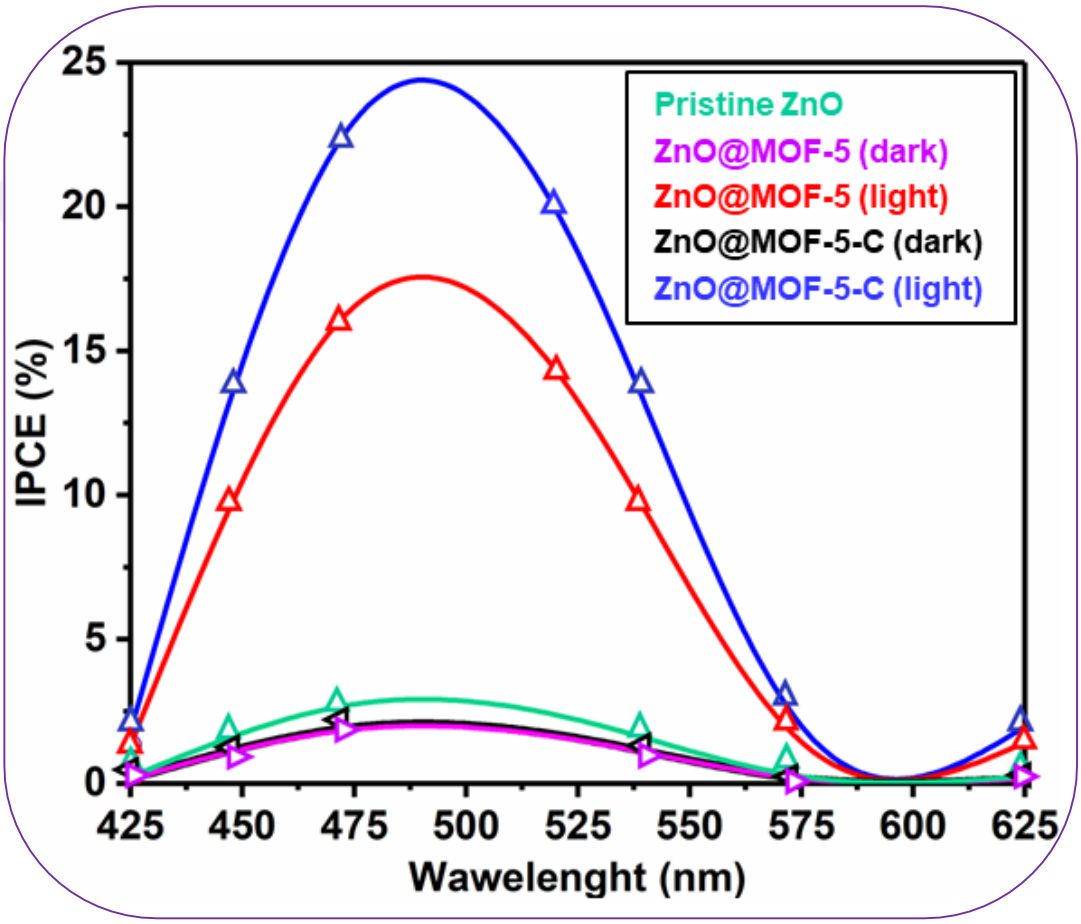

Figure 6. 24 IPCE spectra of ZnO, ZnO@MOF-5, and ZnO@MOF-5-C heterostructures

Moreover, IPCE values of ZnO@MOF-5 under Xenon light conditions are increased approximately 6.1 and 9 times compared with ZnO (under light conditions) and ZnO@MOF-5 (under dark conditions) photoanodes. These results indicated that the ZnO@MOF-5 heterostructures increase the absorption range of visible as well as high photoelectric conversion efficiency because of the effective separation of charge carriers. Also, after the coating of N-doped carbon layer onto ZnO@MOF-5

heterostructures, IPCE values are increased 8.5-fold times than pure ZnO nanoparticles. This increase could be attributed to the N-doped carbon layer onto the ZnO@MOF-5 core-shell photoanodes due to an enhancement in the electrical conductivity, rapid charge transfer, and low electron-hole recombination [53,257]. In conclusion, the increased IPCE values are in agreement with LSV results as well.

6.2.10 ABPE Results of ZnO, ZnO@MOF-5 and ZnO@MOF-5-C heterostructures

The ABPE values are calculated using LSV curves to understand better the PEC performance efficiency of the photoanodes [262]. Figure 6.25 shows the results of applied bias of the photon to current efficiency (i.e., photon to hydrogen) as a function of external bias towards RHE for pristine ZnO under the light condition as well as ZnO@MOF-5 and ZnO@MOF-5-C nanoparticles under dark and light conditions, respectively. As seen here, the maximum ABPE value for pure ZnO was achieved as 0.014 % at 0.45 V vs. RHE under Xe light conditions. Furthermore, after the MOF-5 coating onto ZnO, the ABPE value increased which is 1.8-fold higher than pure ZnO (0.025 % at 0.45 V vs. RHE under light conditions). Moreover, after PDA covering and calcination treatment on ZnO@MOF-5 heterostructures, the highest ABPE value was obtained at approximately 0.10 % at 0.40 V vs. RHE under light conditions. Also, the maximum ABPE value of ZnO@MOF-5-C photoanode was 7.1 and 4-fold higher than pristine ZnO and ZnO@MOF-5 photoanodes, respectively. The maximum ABPE value of ZnO@MOF-5-C was obtained as the highest among all these photoanodes, and this higher ABPE value was obtained at a lower voltage. Obviously, the N-doped carbon layer has an essential role in the improvement of ABPE values. This improvement is due to the enhanced electron conductivity, adsorption capacity, and charge transport, as well as inhibition in the recombination of electron-hole under light irradiation [61,263].

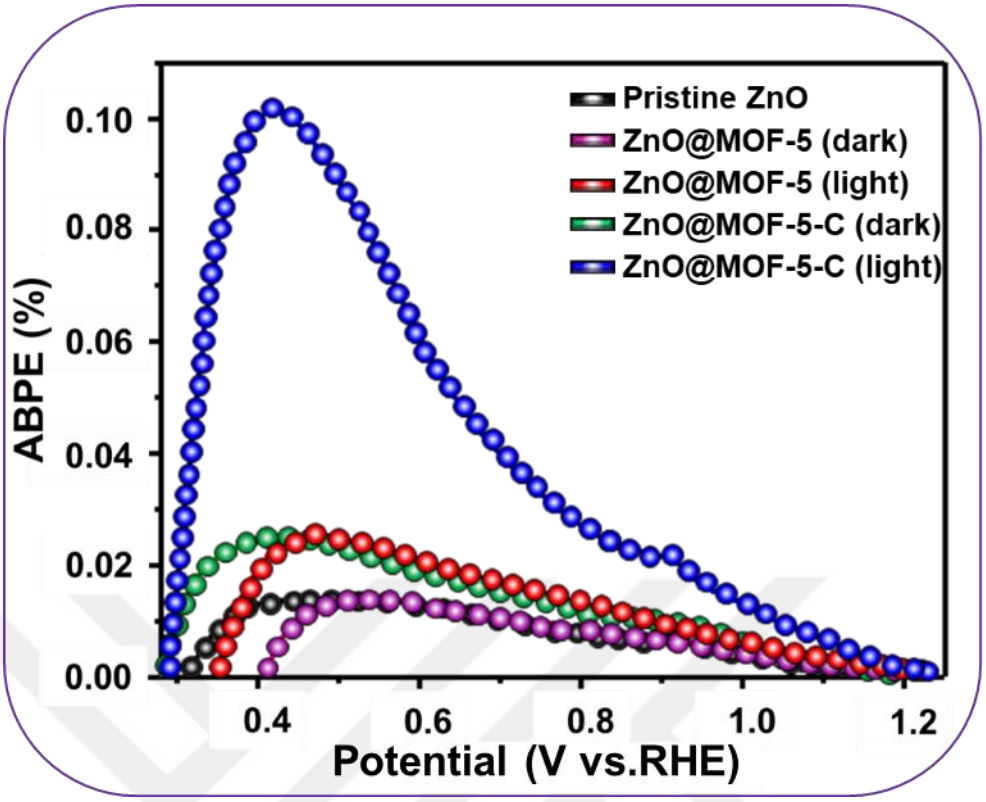

Figure 6. 25 ABPE value of ZnO, ZnO@MOF-5, and ZnO@MOF-5-C heterostructures

6.2.11 Mott-Schottky Results of ZnO and MOF-5 heterostructures

Figure 6.26a and b show the Mott-Schottky plots of pristine ZnO and MOF-5 NPs. The positive curve of the synthesized NPs indicated that ZnO and MOF-5 were n-type semiconductors. The flat band position of ZnO and MOF-5 nanoparticles was calculated by extrapolating of the Mott-Schottky plot. Mott-Schottky plot for pristine ZnO and MOF-5 were obtained as -0.30V vs. NHE (-0.497 V vs. Ag/AgCl and 0.713 V vs. RHE) and as -1.3 V vs NHE (-1.497 V vs. Ag/AgCl and 0.88 V vs. RHE), respectively, which are in good agreement with literature [264,265]. The valence band potential (HOMO) was calculated using the band gap energy and conduction band values from the following equation [67].

$$E_g = E_{VB} - E_{CB} \quad \textbf{(6.3)}$$

The CB and VB are found to be -0.4 eV and 2.68 eV for ZnO star and -1.40 eV and 2.40 eV for MOF-5, respectively (Figure 6.27).

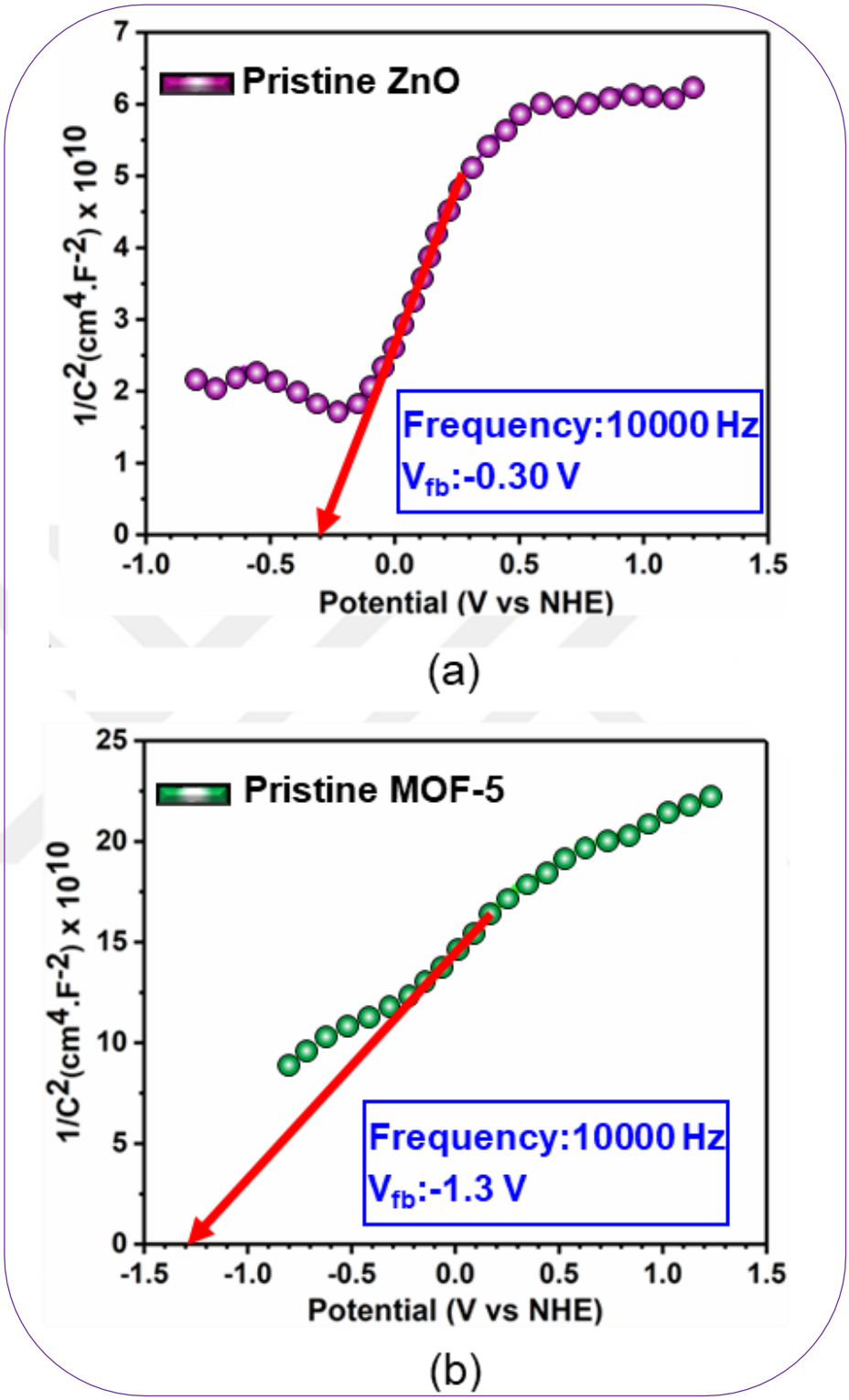

Figure 6. 26 Mott-Schottky plots for (a) Pristine ZnO, (b) Pristine MOF-5 NPs

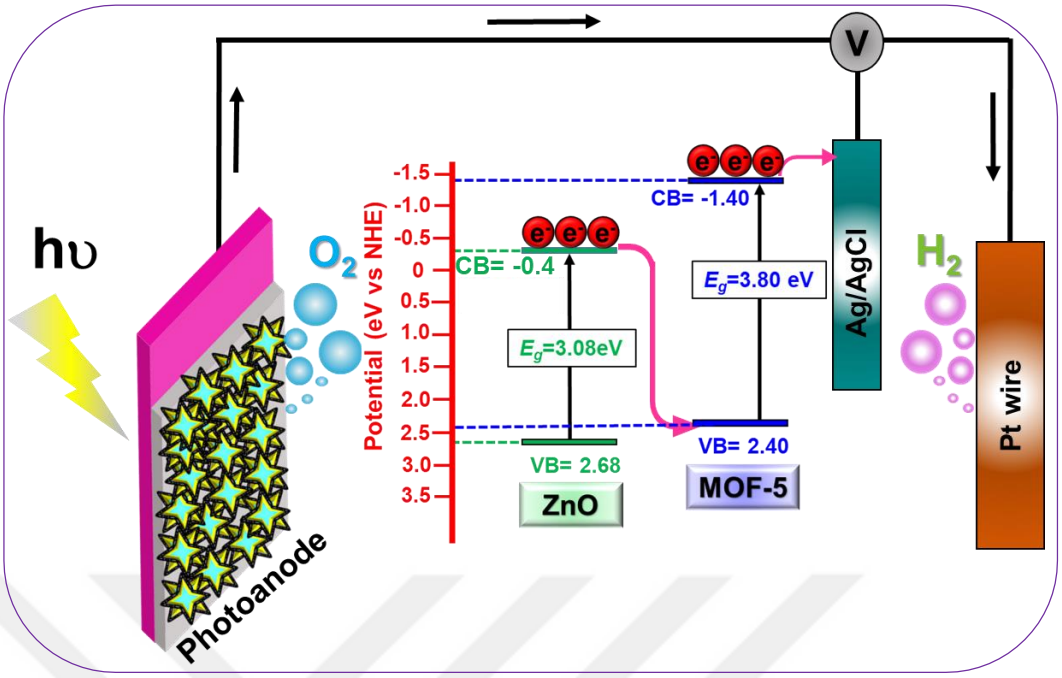

Figure 6. 27 Schematic representation of the PEC reaction mechanism of Z-scheme ZnO@MOF-5-C heterojunctions

6.2.12 Nyquist Plot Results of ZnO, ZnO@MOF-5, and ZnO@MOF-5-C heterostructures

The charge transfers resistance properties of pristine ZnO, ZnO@MOF-5, and ZnO@MOF-5-C photocatalysts were measured based on EIS method. The scattered points and solid lines in the Nyquist plot represent the experiment and resultant fitting data as well. The randless circuit model was used for fitting the obtained values. The relevant circuit model is shown in (Figure 6.28a-inset). The Nyquist plot results obtained by EIS measurements are shown in Figure 6.28 a-b and Table 6.4 under light and dark conditions, respectively. As reported in the literature, it is well known that arc radii in the mid and high-frequency regions of the Nyquist plot are correlated with the electron transport resistance of the electrochemical surface. If the arc has a smaller radius, it has a lower conduction resistance but a higher charge transfer efficiency [266,267]. Nyquist plot for pristine ZnO, ZnO@MOF-5, and ZnO@MOF-5-C heterostructures demonstrated charge transfer resistance values of (R_{ct}:1990000-314000 Ω), (R_{ct}:111000-79651 Ω) and, (R_{ct}:175000-32450 Ω) under dark and light conditions, respectively.

Table 6. 4 Values of circuit elements for ZnO, ZnO@MOF-5, and ZnO-MOF-5-C heterostructures calculated from Nyquist plots

Conditions	**R_S (Ω)**	**R_{CT} (Ω)**	**CPE**
ZnO Dark	24.85	1990000	1.23×10^{-5}
ZnO Light	24.75	314000	1.93×10^{-5}
ZnO@MOF-5 Dark	24.95	111000	1.70×10^{-5}
ZnO@MOF-5 Light	24.65	79651	1.69×10^{-5}
ZnO@MOF-5-C Dark	24.97	175000	1.95×10^{-5}
ZnO@MOF-5-C Light	24.08	32450	4.43×10^{-5}

These results showed that the carbonized PDA (N-doped carbon layer) coating on the ZnO@MOF-5 core-shell increased the EIS conductivity due to charge carrier separation and fast charge transfer.

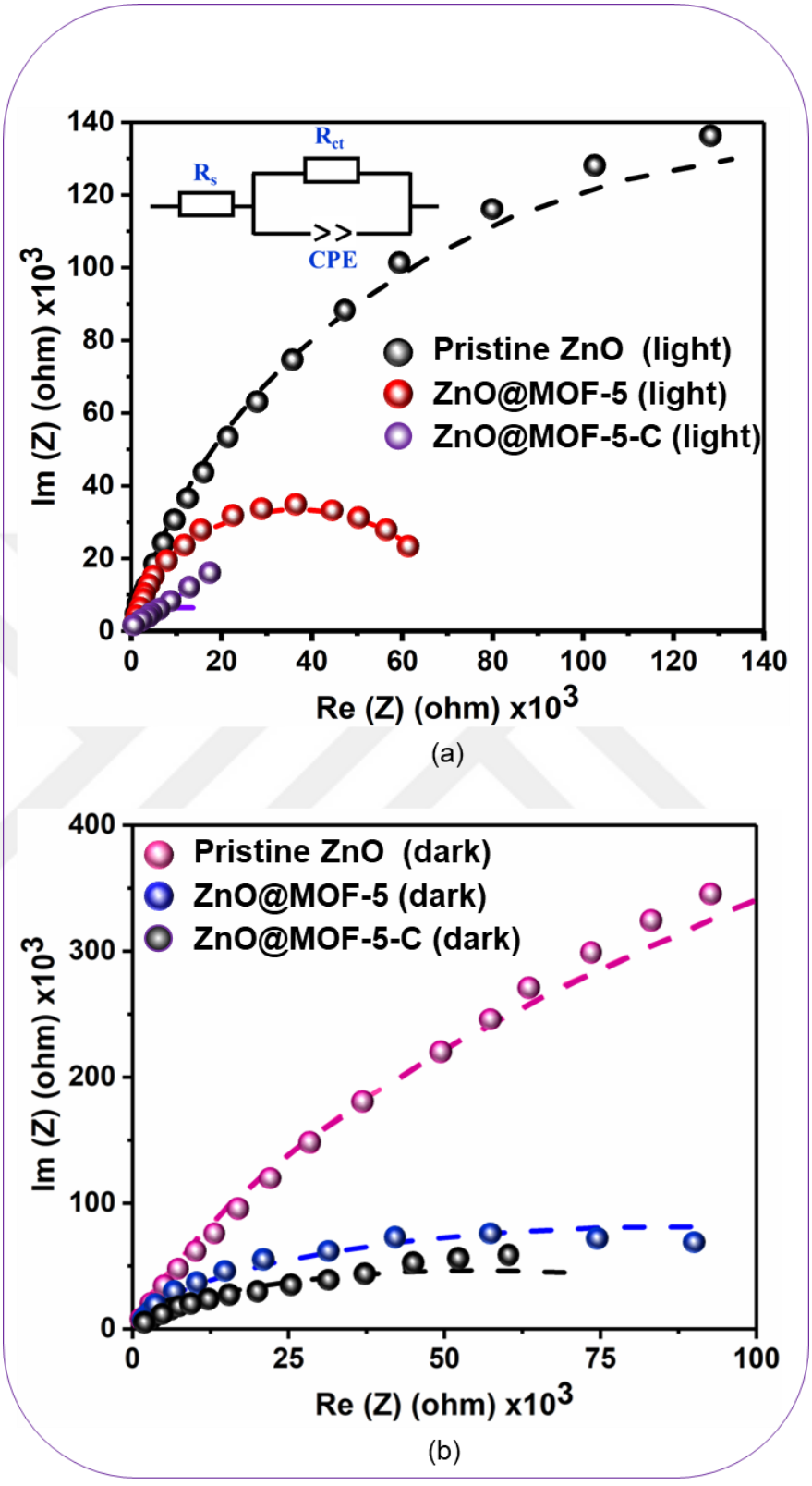

Figure 6. 28 Nyquist plots of ZnO, ZnO@MOF-5, and ZnO-MOF-5-C heterostructures (a) light, (b) dark

6.2.13 Bode Plot Results of ZnO, ZnO@MOF-5, and ZnO@MOF-5-C heterostructures

The Bode plot of pristine ZnO star, ZnO@MOF-5, and ZnO@MOF-5-C heterostructures is shown in Figure 6.29.

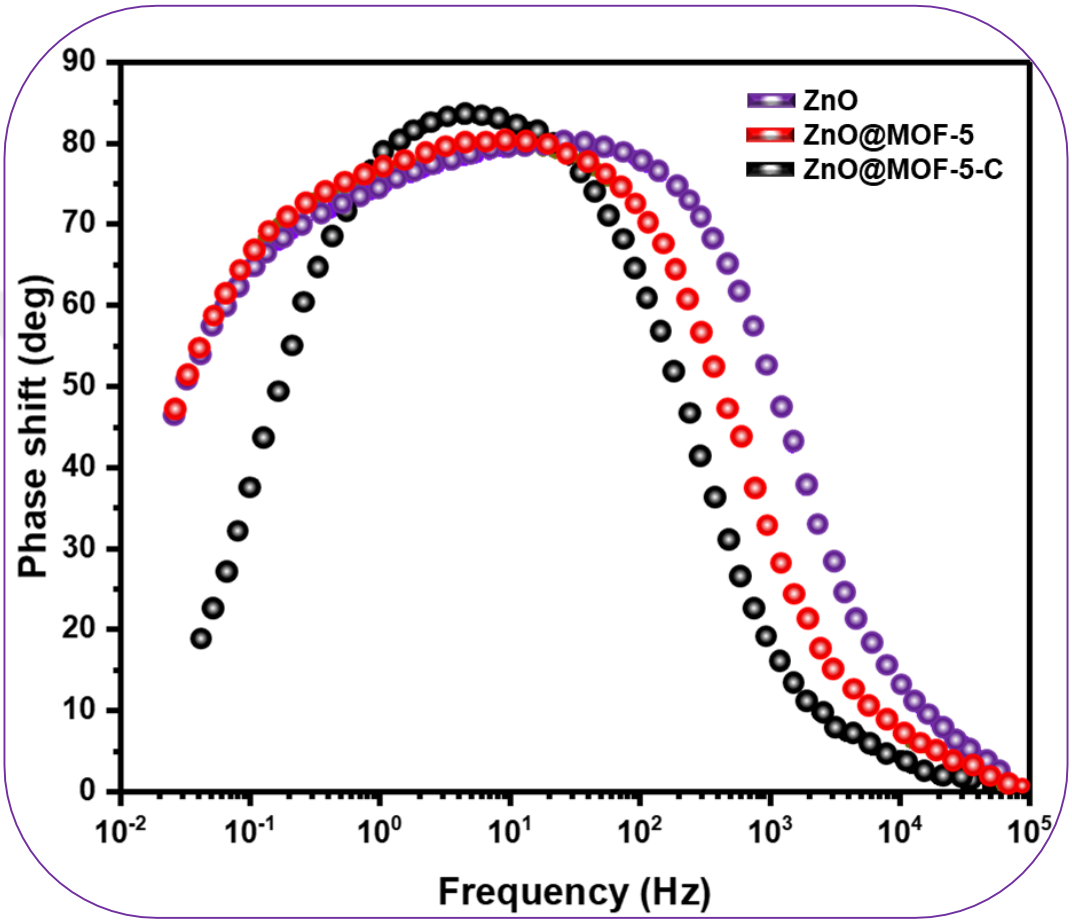

Figure 6. 29 Nyquist plots of ZnO, ZnO@MOF-5, and ZnO-MOF-5-C heterostructures in dark

The electron lifetime of the synthesized nanoparticles was calculated using the Bode plot and the equation 5.11. Shifting the characteristic frequency peak (f_{max}) to a lower value indicates reduced charge recombination. Therefore, the lifetime of electrons also increases because of inhibited recombination. Electron lifetimes from the Bode plot were found for pristine ZnO star, ZnO@MOF-5, and ZnO@MOF-5-C heterostructures (31.1 ms, 36.6 ms, and 42.9 ms), respectively (Table 6.5). The value obtained for the pristine ZnO shows that the lifetime is low due to the high recombination.

Table 6. 5 Electron lifetimes and corresponding frequencies, obtained by EIS

Condition	f_{max} **[Hz]**	$\tau(ms)$
ZnO Light	5.10	31.1
ZnO@MOF-5 Light	4.35	36.6
ZnO@MOF-5-C Light	3.71	42.9

However, after the PDA coating and calcination process (N-doped carbon layer), the charge transfer accelerated and led to the suppression of the recombination. In conclusion, this study demonstrates that ZnO@MOF-5 and ZnO@MOF-5-C photoanode effectively suppress charge-transfer recombination thanks to fast charge transport and a prolonged lifetime of photogenerated charge carriers.

6.2.14 Z-Scheme charger transfer mechanism for ZnO@MOF-5-C heterostructures

Figures 6.30 (a-b) schematically illustrate the possible mechanisms for hydrogen production using ZnO@MOF-5-C photoanodes. For this purpose, the PL densities of the reactive radical species over time ($O_2^{\cdot-}$ and $\cdot OH$ on CB and VB, respectively) were investigated (Figure 6.30 c and d). The type II mechanism is given in Figure 6.30 a. In this mechanism, while peroxide radicals are produced on CB with a lower reduction potential (ZnO), hydroxyl radicals are generated on VB (MOF-5) with a lower oxidation potential. In particular, this mechanism reduced the redox capacity of photocatalysis due to the reduction in $O_2^{\cdot-}$ and $\cdot OH$ numbers, which led to a decrease in photocatalyst efficiency. If a conventional type II mechanism were constructed between ZnO and MOF-5, photogenerated electrons would transfer from the more negative energy level CB of MOF-5 to the less negative energy level CB of ZnO. Suppose a conventional type II mechanism is built between ZnO and MOF-5. In that case, photogenerated electrons transferred from the CB of MOF-5 with a more negative energy level to the CB of ZnO with a less negative energy level will move towards the less positive energy level VB of MOF-5. Due to the Coulomb repulsion between the electrons, the migration of electrons through the CB was challenging [53]. Furthermore, regarding the CB position of ZnO (-0.4 eV), it cannot form peroxide radicals $O_2^{\cdot-}$ since the reduction potential of CB is more positive than O_2 /$O_2^{\cdot-}$ (-0.33

eV). Moreover, it has been demonstrated that peroxide can be obtained from PL experiments for ZnO@MOF-5-C heterostructures (Figure 6.30 c and d).

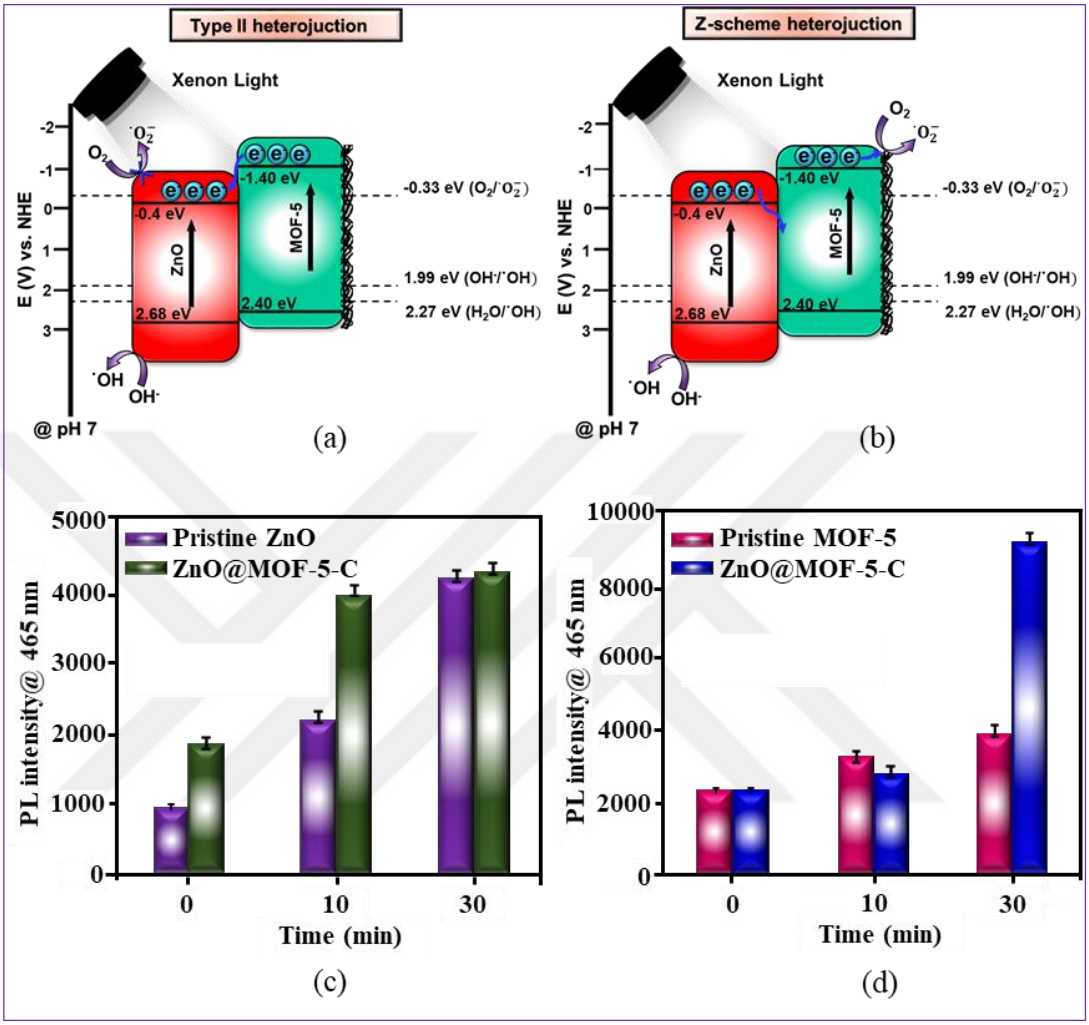

Figure 6. 30 Schematic representation of photoinduced charge transfer prosses for ZnO@PDA/CeO_2 NPs: (a) Type II heterojunction and (b) Z-scheme heterojunctions, (c) the ·OH (d) $O_2^{\cdot-}$ the trapping experiments using Z-scheme ZnO@MOF-5-C heterostructures (reaction conditions: photocatalyst amount:4 mg; the concentration of TPA and BQ: 0.5 mM) (the error bars were added based on three replicate experiments)

For the pure MOF-5, a PL signal was observed representing the production of O_2 in its CB due to the lower negative energy level of the MOF-5 compared to its reduction potential of O_2 /$O_2^{\cdot-}$. The PL density for the ZnO@MOF-5-C photoanodes was significantly increased compared to the pristine MOF-5. The increase in PL density in this ZnO@MOF-5-C nanocomposite suggested that it could produce more O_2 in CB. Similar PL results were acquired for the ·OH active species. For pristine ZnO, PL

intensities were attained due to the VB potential, which was higher than the oxidation potential of the OH generation reaction. However, higher PL density was obtained for ZnO@MOF-5-C photoanodes, representing more ·OH formation, compared with pristine ZnO (Figure 6.30c). Consequently, when we compare the PL signals, ZnO@MOF-5-C photoanodes have a better PL signal than pure ZnO and pure MOF-5. This situation demonstrates that the electron-hole pairs of the produced heterostructure are well separated, and the charge carriers are inhibited. According to these results, it contradicts the type II mechanism. Therefore, it is strongly recommended to establish the Z-scheme mechanism directly between ZnO and MOF-5 since more efficient electrons and holes can generate more peroxide and hydroxyl radicals, thereby increasing its photocatalytic performance under visible light illumination [53,100].

CHAPTER 7

CONCLUSIONS

In this Ph.D. thesis, two different photoanodes based on ZnO were fabricated, and their PEC water splitting performance were studied. The morphology, crystallinity, specific surface area, surface composition, optical and band properties of Z-scheme ZnO@PDA/CeO_2 and ZnO@MOF-5-C heterostructures photoanodes were investigated using scanning electron microscope (SEM-EDX), X-ray diffractometer (XRD), Bernauer-Emmet-Teller (BET), X-ray spectroscopy (XPS), and UV-Vis spectroscopy. For this purpose, the PEC measurements were performed at room temperature utilizing a conventional three-electrode system (CorrTest Electrochemical Workstation Potentiostat/Galvanostat, China). The PEC performance of photoanodes was analyzed using linear sweep voltammetry (LSV), applied bias photon to current efficiency (ABPE), incident photon to current efficiency (IPCE), and Tafel slope measurements. The Mott-Schottky, Nyquist plots and bode plots analyses of the photoanodes were carried out using the electrochemical impedance spectroscopy (EIS) measurement methods. In the first study, Z-scheme ZnO@PDA/CeO_2 photoanodes were fabricated by the nucleation-growth method, thanks to the automatic redox properties and dual functions of the selected PDA layer. Note that the PDA bridging of ZnO and CeO_2 semiconductors directly influenced the photocatalyst efficiency of the Z-scheme ZnO@PDA/CeO_2 ternary heterostructure. The highest photocurrent was obtained for Z-scheme ZnO@PDA/CeO_2 NPs at 251 $\mu A/cm^2$ at 0.25 V vs. RHE (a 10-fold increase compared with under dark conditions) (Table 7.1). Besides this, the Tafel slopes for pure ZnO, ZnO@PDA/CeO_2 in the dark, and ZnO@PDA/CeO_2 under LED irradiation were 117, 90, and 38 mV/dec, respectively. The decrease in Tafel measurements demonstrates an effective electron transfer mechanism of the PDA layer as well as an increase in photocatalytic performance under LED illumination. Furthermore, the comparison of current density values at specific potentials, IPCE, ABPE, Tafel slope, light source, and power values of various Z-scheme and Type II heterojunction catalysts with ZnO@PDA/CeO_2 photoanodes were provided (Table 7.1) [14,30,52,54]. As seen here, the photocurrent density of the Z-scheme

ZnO@PDA/CeO_2 heterojunction (0.25 mA/cm^2 at 0.25 V vs. RHE) is a satisfactory value compared to those Type II heterojunctions.

Table 7. 1 Comparison of current density values at specific potentials, IPCE, ABPE,Tafel plot, light source, and power values of various Z-scheme and Type II heterojunction with ZnO@PDA/CeO_2 photoanodes

Catalyst	**Junction type/ application area**	**Current density @ potential**	**IPCE/ ABPE/ Tafel plot**	**Light source**	**Ref.**
Ce doped ZnO	Not reported /WS	2μA/cm^2 @ 1.2 V vs Ag/AgCl	Not reported	Xenon/ 0.1 W/cm^2 visible	[54]
CeO_2/ZnO	Type II heterojunction /WS	0.3 mA/cm^2 @ 0.5 V	Not reported	Xenon/ 200 mW/cm^2	[30]
Ag-ZnO-CeO_2	Z-scheme heterojunction /WS	16 μA/cm^2 @ not reported	Not reported	300 W Xenon (AM 1.5 G)/ 100 mW/cm^2	[52]
ZnO-CeO_2-rGO	Type II heterojunction /WS	0.69 mA/cm^2 @ 1.5 V vs. RHE	Not reported	Xenon/100 mW/cm^2 (AM 1.5 G)	[14]
ZnO-PDA-CeO_2	Z-scheme heterojunction /WS	0.25 mA/cm^2 @ 0.25 V vs RHE	9.0 %/ 38mV/dec/ 0.83% 0.25V vs RHE	LED/ 30 mW/cm^2	Our study

Moreover, radical trapping, radical scavenger experiments, and XPS measurements were conducted as verification tests to determine the Z-scheme charge transfer pathway within ZnO@PDA/CeO_2 heterojunctions from traditional type II heterojunctions. Thus, the photo-induced electrons from the CB of ZnO (0.2 eV) were transferred to the VB of CeO_2 (2.61 eV) via PDA. According to these findings, both $O_2^{\cdot-}$ and ·OH radicals were generated in the CeO_2 semiconductor through Z-scheme ZnO@PDA/CeO_2 heterojunctions under visible LED irradiation, resulting in electron accumulation at the more negative CB (CeO_2: 0.49 eV) potential. Also, nyquist measurements were performed for Z-scheme ZnO@PDA/CeO_2 photoanodes. It was found to be 304.5 and 229.3 Ω in the dark and light, respectively. The charge transfer

resistance suppressed electron-hole recombination and facilitated photo-induced charge carrier migration, which was consistent with the PL results. This novel study resulted in enhanced electron-hole separation through PDA facilitated charge transfer between ZnO and CeO_2, providing high photocatalytic performance and more effective separation/transfer of photoinduced electron-hole pairs, paving the way for the design of Z-scheme heterojunctions for improved PEC H_2 generation. In the second study, ZnO star, ZnO@MOF-5 NPs, and carbon incorporated Z-scheme ZnO@MOF-5-C heterostructures were fabricated, and the photoresponsive properties and PEC water splitting performance were investigated under dark and Xenon light illumination. The maximum photocurrent density, representing H_2 generation, was measured as 0.40 mA/cm^2, 2.43 mA/cm^2, and 3.40 mA/cm^2 for ZnO, ZnO@MOF-5, and ZnO@MOF-5-C at (2.50 V vs. RHE) under light conditions, respectively. In addition, photocurrent density as 0.23 mA/cm^2 and 0.27 mA/cm^2 were obtained for ZnO@MOF-5 and ZnO@MOF-5-C under dark conditions at 2.50 V vs. RHE, respectively. When we compared with the photoanodes under dark and light conditions, ZnO@MOF-5 showed 10.5-fold, and ZnO@MOF-5-C demonstrated 12.5-fold higher value than dark conditions. Furthermore, LSV measurements were also utilized to calculate photoanode Tafel slopes. The slopes of ZnO@MOF-5 and ZnO@MOF-5-C under Xenon illumination and pristine ZnO star under dark conditions were 60.48, and 286 mV/dec, respectively. The slope of ZnO@MOF-5 and ZnO@MOF-5-C under light was significantly lower than that of pristine ZnO and dark conditions, indicating effective charge transfer and photoresponsivity of the synthesized photoanode, which is also consistent with LSV measurements. Also, ABPE and IPCE results of the photoanodes were investigated. The highest ABPE value was obtained at a lower voltage than other photoanodes as 0.40 V vs. RHE at 0.10 % for Z-scheme ZnO@MOF-5-C photoanodes. The maximum ABPE value of the ZnO@MOF-5-C photoanode compared with pristine ZnO was 0.014 % at 0.45 V vs. RHE and ZnO@MOF-5 at 0.025 % at 0.45 V vs. RHE photoanodes increased 7.1 and 4-fold, respectively. Besides this, ZnO@MOF-5-C demonstrated a significant IPCE value of 24.5% at 489 nm in the visible region under Xenon light conditions. This value was calculated as 2.89% and 2.08% for pristine ZnO under light and ZnO@MOF-5-C under dark conditions, respectively. Furthermore, the comparison of

current density values at specific potentials, IPCE, ABPE, Tafel slope, light source, and power values of various Z-scheme and Type II heterojunction catalysts with ZnO@MOF-5-C photoanodes were provided (Table 7.2) [66,245,268,269].

Table 7. 2 Comparison of current density values at specific potentials, IPCE, ABPE,Tafel plot, light source, and power values of various Z-scheme and Type II heterojunction with ZnO@MOF-5-C photoanodes

Catalyst	Junction type/ application area	Current density @ potential	IPCE/ ABPE/ Tafel plot	Light source	Ref.
MOF-5 -gCN	Not reported/ WS	0.042 mA/cm^2 @ 1.40 V vs SCE	Not reported	Xenon/ 150 W (AM 1.5 G)	[245]
ZnNi MOF@ ZnO	Not reported/ WS	1.40 mA/cm^2 @ 1.20 V vs RHE	Not reported	300 W Xenon (AM 1.5 G)/ 100 mW/cm^2	[268]
Cu@ MOF-5 -ZnO	Not reported/ WS	6 mA/cm^2 @ 1.20 V vs RHE	Not reported	300 W Xenon	[66]
ZnO@Z IF-8/67	Not reported/ WS	0.11 mA/cm^2 @ 1.45 V vs RHE	1.1 %/ Not reported	300 W Xenon (AM 1.5 G)/ 100 mW/cm^2	[269]
ZnO-MOF-5 -C	Z-scheme heterojunction /WS	3.40 mA/cm^2 @ 2.50 V vs RHE	24.5 %/ 48mV/dec/ 0.10 % 0.40 V vs RHE	300 W Xenon (AM 1.5 G)/ 100 mW/cm^2	Our study

As seen here, the photocurrent density of the Z-scheme ZnO@MOF-5-C heterojunction (3.40 mA/cm^2 at 2.50 V vs. RHE) is a satisfactory value compared to those other heterojunctions. Finally, solar water splitting (PC and PEC) indicates promise as a forward-looking solution to energy and environmental problems. Recently, Z-scheme photoanodes have been produced, attracting the researchers attention. However, the desired level of performance has not been reached yet. Therefore, developing new and superior photocatalyst materials is still a significant issue.

REFERENCES

[1] Li X, Yu J, Low J, Fang Y, Xiao J, Chen X. Engineering heterogeneous semiconductors for solar water splitting. J Mater Chem A 2015;3:2485–534. https://doi.org/10.1039/c4ta04461d.

[2] Maggio G, Nicita A, Squadrito G. How the hydrogen production from RES could change energy and fuel markets: A review of recent literature. Int J Hydrogen Energy 2019;44:11371–84. https://doi.org/10.1016/j.ijhydene.2019.03.121.

[3] Singla S, Sharma S, Basu S, Shetti NP, Aminabhavi TM. Photocatalytic water splitting hydrogen production via environmental benign carbon based nanomaterials. Int J Hydrogen Energy 2021;46:33696–717. https://doi.org/10.1016/j.ijhydene.2021.07.187.

[4] Song H, Luo S, Huang H, Deng B, Ye J. Solar-Driven Hydrogen Production: Recent Advances, Challenges, and Future Perspectives. ACS Energy Lett 2022;7:1043–65. https://doi.org/10.1021/acsenergylett.1c02591.

[5] Ji M, Wang J. Review and comparison of various hydrogen production methods based on costs and life cycle impact assessment indicators. Int J Hydrogen Energy 2021;46:38612–35. https://doi.org/10.1016/j.ijhydene.2021.09.142.

[6] Acar C, Dincer I. The potential role of hydrogen as a sustainable transportation fuel to combat global warming. Int J Hydrogen Energy 2020;45:3396–406. https://doi.org/10.1016/j.ijhydene.2018.10.149.

[7] Quarton CJ, Samsatli S. How to incentivise hydrogen energy technologies for net zero: Whole-system value chain optimisation of policy scenarios. Sustain Prod Consum 2021;27:1215–38. https://doi.org/10.1016/j.spc.2021.02.007.

[8] Pervaiz E, Ali M, Adil M. ScienceDirect Unfolding essence of nanoscience for improved water splitting hydrogen generation in the light of newly

emergent nanocatalysts 2022.

[9] Yue M, Lambert H, Pahon E, Roche R, Jemei S, Hissel D. Hydrogen energy systems: A critical review of technologies, applications, trends and challenges. Renew Sustain Energy Rev 2021;146:111180. https://doi.org/10.1016/j.rser.2021.111180.

[10] Hanley ES, Deane JP, Gallachóir BPÓ. The role of hydrogen in low carbon energy futures–A review of existing perspectives. Renew Sustain Energy Rev 2018;82:3027–45. https://doi.org/10.1016/j.rser.2017.10.034.

[11] Gong Y, Yao J, Wang P, Li Z, Zhou H, Xu C. Perspective of hydrogen energy and recent progress in electrocatalytic water splitting. Chinese J Chem Eng 2022;43:282–96. https://doi.org/10.1016/j.cjche.2022.02.010.

[12] Koumi Ngoh S, Njomo D. An overview of hydrogen gas production from solar energy. Renew Sustain Energy Rev 2012;16:6782–92. https://doi.org/10.1016/j.rser.2012.07.027.

[13] Vishwakarma AK, Tripathi P, Srivastava A, Sinha ASK, Srivastava ON. Band gap engineering of Gd and Co doped BiFeO3 and their application in hydrogen production through photoelectrochemical route. Int J Hydrogen Energy 2017;42:22677–86. https://doi.org/10.1016/j.ijhydene.2017.07.153.

[14] Murali A, Sarswat PK, Free ML. Minimizing electron-hole pair recombination through band-gap engineering in novel ZnO-CeO2-rGO ternary nanocomposite for photoelectrochemical and photocatalytic applications. Environ Sci Pollut Res 2020;27:25042–56. https://doi.org/10.1007/s11356-020-08990-z.

[15] Lv Z, Zhong Q, Ou M. Utilizing peroxide as precursor for the synthesis of CeO 2 /ZnO composite oxide with enhanced photocatalytic activity. Appl Surf Sci 2016;376:91–6. https://doi.org/10.1016/j.apsusc.2016.01.280.

[16] Lamba R, Umar A, Mehta SK, Kansal SK. CeO2ZnO hexagonal nanodisks: Efficient material for the degradation of direct blue 15 dye and its simulated

dye bath effluent under solar light. J Alloys Compd 2015;620:67–73. https://doi.org/10.1016/j.jallcom.2014.09.101.

[17] Shen H, Liu G, Yan X, Jiang J, Hong Y, Yan M, et al. All-solid-state Z-scheme system of RGO-Cu2O/Fe2O3 for simultaneous hydrogen production and tetracycline degradation. Mater Today Energy 2017;5:312–9. https://doi.org/10.1016/j.mtener.2017.07.008.

[18] Ai L, Zhang C, Li L, Jiang J. Iron terephthalate metal-organic framework: Revealing the effective activation of hydrogen peroxide for the degradation of organic dye under visible light irradiation. Appl Catal B Environ 2014;148–149:191–200. https://doi.org/10.1016/j.apcatb.2013.10.056.

[19] Saravanan R, Agarwal S, Gupta VK, Khan MM, Gracia F, Mosquera E, et al. Line defect Ce3+ induced Ag/CeO2/ZnO nanostructure for visible-light photocatalytic activity. J Photochem Photobiol A Chem 2018;353:499–506. https://doi.org/10.1016/j.jphotochem.2017.12.011.

[20] Wang J, Wang Z, Huang B, Ma Y, Liu Y, Qin X, et al. Oxygen vacancy induced band-gap narrowing and enhanced visible light photocatalytic activity of ZnO. ACS Appl Mater Interfaces 2012;4:4024–30. https://doi.org/10.1021/am300835p.

[21] Han J, Liu Z, Guo K, Wang B, Zhang X, Hong T. High-efficiency photoelectrochemical electrodes based on ZnIn2S4 sensitized ZnO nanotube arrays. Appl Catal B Environ 2015;163:179–88. https://doi.org/10.1016/j.apcatb.2014.07.040.

[22] Liu IT, Hon MH, Teoh LG. The preparation, characterization and photocatalytic activity of radical-shaped CeO2/ZnO microstructures. Ceram Int 2014;40:4019–24. https://doi.org/10.1016/j.ceramint.2013.08.053.

[23] Han J, Liu Z. Optimization and Modulation Strategies of Zinc Oxide-based Photoanodes for Highly Efficient Photoelectrochemical Water Splitting. ACS Appl Energy Mater 2021;4:1004–13. https://doi.org/10.1021/acsaem.0c02985.

[24] Zhang S, Liu Z, Ruan M, Guo Z, E L, Zhao W, et al. Enhanced piezoelectric-effect-assisted photoelectrochemical performance in ZnO modified with dual cocatalysts. Appl Catal B Environ 2020;262:118279. https://doi.org/10.1016/j.apcatb.2019.118279.

[25] Ahn KS, Deutsch T, Yan Y, Jiang CS, Perkins CL, Turner J, et al. Synthesis of band-gap-reduced p -type ZnO films by Cu incorporation. J Appl Phys 2007;102:023517. https://doi.org/10.1063/1.2756517.

[26] Ma C, Liu Z, Cai Q, Han C, Tong Z. ZnO photoelectrode simultaneously modified with Cu2O and Co-Pi based on broader light absorption and efficiently photogenerated carrier separation. Inorg Chem Front 2018;5:2571–8. https://doi.org/10.1039/c8qi00596f.

[27] Lan Y, Liu Z, Guo Z, Li X, Zhao L, Zhan L, et al. A ZnO/ZnFe2O4 uniform core-shell heterojunction with a tubular structure modified by NiOOH for efficient photoelectrochemical water splitting. Dalt Trans 2018;47:12181–7. https://doi.org/10.1039/c8dt02581a.

[28] Liang X, Wang P, Gao Y, Huang H, Tong F, Zhang Q, et al. Design and synthesis of porous M-ZnO/CeO2 microspheres as efficient plasmonic photocatalysts for nonpolar gaseous molecules oxidation: Insight into the role of oxygen vacancy defects and M=Ag, Au nanoparticles. Appl Catal B Environ 2020;260. https://doi.org/10.1016/j.apcatb.2019.118151.

[29] Zhu L, Li H, Xia P, Liu Z, Xiong D. Hierarchical ZnO Decorated with CeO2 Nanoparticles as the Direct Z-Scheme Heterojunction for Enhanced Photocatalytic Activity. ACS Appl Mater Interfaces 2018;10:39679–87. https://doi.org/10.1021/acsami.8b13782.

[30] Xiao Y, Yu H, Dong X ting. Ordered mesoporous CeO2/ZnO composite with photodegradation concomitant photocatalytic hydrogen production performance. J Solid State Chem 2019;278:120893. https://doi.org/10.1016/j.jssc.2019.120893.

[31] Kumar D, Bai R, Chaudhary S, Pandya DK. Enhanced photoelectrochemical response for hydrogen generation in self-assembled aligned ZnO/PbS core/shell nanorod arrays grown by chemical bath deposition. Mater Today Energy 2017;6:105–14. https://doi.org/10.1016/j.mtener.2017.09.004.

[32] Zhang B, Wang Z, Zhang X, Qin X, Wang P, Liu Y, et al. Fabrication of In2O3/ZnO hetero-epitaxial-junctions with enhanced PEC performances. Mater Today Energy 2017;6:65–71. https://doi.org/10.1016/j.mtener.2017.07.011.

[33] Zhang Q, Zhao X, Duan L, Shen H, Liu R. Controlling oxygen vacancies and enhanced visible light photocatalysis of CeO2/ZnO nanocomposites. J Photochem Photobiol A Chem 2020;392. https://doi.org/10.1016/j.jphotochem.2019.112156.

[34] Khan MS, Zhang F, Osada M, Mao SS, Shen S. Graphitic Carbon Nitride-Based Low-Dimensional Heterostructures for Photocatalytic Applications. Sol RRL 2020;4. https://doi.org/10.1002/solr.201900435.

[35] Zhou P, Yu J, Jaroniec M. All-solid-state Z-scheme photocatalytic systems. Adv Mater 2014;26:4920–35. https://doi.org/10.1002/adma.201400288.

[36] Guo F, Chen J, Zhao J, Chen Z, Xia D, Zhan Z, et al. Z-scheme heterojunction g-C3N4@PDA/BiOBr with biomimetic polydopamine as electron transfer mediators for enhanced visible-light driven degradation of sulfamethoxazole. Chem Eng J 2020;386. https://doi.org/10.1016/j.cej.2020.124014.

[37] Meng Q, Lv H, Yuan M, Cheng Z, Chen Z, Wang X. In Situ Hydrothermal Construction of Direct Solid-State Nano-Z-Scheme BiVO4/Pyridine-Doped g-C3N4 Photocatalyst with Efficient Visible-Light-Induced Photocatalytic Degradation of Phenol and Dyes. ACS Omega 2017;2:2728–39. https://doi.org/10.1021/acsomega.7b00338.

[38] Chen S, Hu Y, Ji L, Jiang X, Fu X. Preparation and characterization of direct Z-scheme photocatalyst Bi 2 O 3 /NaNbO 3 and its reaction mechanism. Appl

Surf Sci 2014;292:357–66. https://doi.org/10.1016/j.apsusc.2013.11.144.

[39] Tian N, Huang H, He Y, Guo Y, Zhang T, Zhang Y. Mediator-free direct Z-scheme photocatalytic system: BiVO4/g-C3N4 organic-inorganic hybrid photocatalyst with highly efficient visible-light-induced photocatalytic activity. Dalt Trans 2015;44:4297–307. https://doi.org/10.1039/c4dt03905j.

[40] Li Q, Guan Z, Wu D, Zhao X, Bao S, Tian B, et al. Z-Scheme BiOCl-Au-CdS Heterostructure with Enhanced Sunlight-Driven Photocatalytic Activity in Degrading Water Dyes and Antibiotics. ACS Sustain Chem Eng 2017;5:6958–68. https://doi.org/10.1021/acssuschemeng.7b01157.

[41] Zhang G, Ao J, Guo Y, Zhang Z, Shao M, Wang L, et al. Green synthesis and catalytic performance of nanoscale CeO2 sheets. RSC Adv 2014;4:20131–5. https://doi.org/10.1039/c4ra01004c.

[42] Keshvadi N, Haghighatzadeh A, Mazinani B. Improvement in visible-light-induced photocatalytic activity of Ag–CeO2 Schottky-type contact heterostructures. Appl Phys A Mater Sci Process 2020;126. https://doi.org/10.1007/s00339-020-3429-4.

[43] Qiu C, Wang S, Gao R, Qin J, Li W, Wang X, et al. Low-temperature synthesis of PdO-CeO2/C toward efficient oxygen reduction reaction. Mater Today Energy 2020;18:100557. https://doi.org/10.1016/j.mtener.2020.100557.

[44] Ma X, Jiang Q, Guo W, Zheng M, Xu W, Ma F, et al. Fabrication of g-C3N4/Au/CdZnS Z-scheme photocatalyst to enhance photocatalysis performance. RSC Adv 2016;6:28263–9. https://doi.org/10.1039/c5ra27429j.

[45] Xie K, Wu Q, Wang Y, Guo W, Wang M, Sun L, et al. Electrochemical construction of Z-scheme type CdS-Ag-TiO2 nanotube arrays with enhanced photocatalytic activity. Electrochem Commun 2011;13:1469–72. https://doi.org/10.1016/j.elecom.2011.09.023.

[46] Zhu H, Yang B, Xu J, Fu Z, Wen M, Guo T, et al. Construction of Z-scheme type CdS-Au-TiO2 hollow nanorod arrays with enhanced photocatalytic

activity. Appl Catal B Environ 2009;90:463–9. https://doi.org/10.1016/j.apcatb.2009.04.006.

[47] Zheng D, Pang C, Wang X. The function-led design of Z-scheme photocatalytic systems based on hollow carbon nitride semiconductors. Chem Commun 2015;51:17467–70. https://doi.org/10.1039/c5cc07867a.

[48] Fu J, Yu J, Jiang C, Cheng B. g-C3N4-Based Heterostructured Photocatalysts. Adv Energy Mater 2018;8. https://doi.org/10.1002/aenm.201701503.

[49] Li W, Zhang G, Sheng W, Dong C, Dai Y, Li C, et al. Engineering plasmonic Ag/AgCl-polydopamine-carbon nitride composites for enhanced photocatalytic activity based on mussel chemistry. RSC Adv 2016;6:106697–704. https://doi.org/10.1039/c6ra24637k.

[50] Huo R, Yang XL, Yang JY, Yang SY, Xu YH. Self-assembly synthesis of BiVO4/Polydopamine/g-C3N4 with enhanced visible light photocatalytic performance. Mater Res Bull 2018;98:225–30. https://doi.org/10.1016/j.materresbull.2017.10.016.

[51] Wu Y, Zhou Y, Xu H, Liu Q, Li Y, Zhang L, et al. Highly Active, Superstable, and Biocompatible Ag/Polydopamine/g-C3N4 Bactericidal Photocatalyst: Synthesis, Characterization, and Mechanism. ACS Sustain Chem Eng 2018;6:14082–94. https://doi.org/10.1021/acssuschemeng.8b02620.

[52] Hezam A, Wang J, Drmosh QA, Karthik P, Abdullah Bajiri M, Namratha K, et al. Rational construction of plasmonic Z-scheme Ag-ZnO-CeO2 heterostructures for highly enhanced solar photocatalytic H2 evolution. Appl Surf Sci 2021;541. https://doi.org/10.1016/j.apsusc.2020.148457.

[53] Celebi N, Salimi K. Yolk-shell ZnO@C-CeO2 ternary heterostructures with conductive N-doped carbon mediated electron transfer for highly efficient water splitting. J Colloid Interface Sci 2022;605:23–32. https://doi.org/10.1016/j.jcis.2021.07.052.

[54] Yousefi M, Amiri M, Azimirad R, Moshfegh AZ. Enhanced photoelectrochemical activity of Ce doped ZnO nanocomposite thin films under visible light. J Electroanal Chem 2011;661:106–12. https://doi.org/10.1016/j.jelechem.2011.07.022.

[55] Dutta R, Shrivastav R, Srivastava M, Verma A, Saxena S, Biswas NK, et al. MOFs in photoelectrochemical water splitting: New horizons and challenges. Int J Hydrogen Energy 2022;47:5192–210. https://doi.org/10.1016/j.ijhydene.2021.11.185.

[56] Falcaro P, Ricco R, Yazdi A, Imaz I, Furukawa S, Maspoch D, et al. Application of metal and metal oxide nanoparticles at MOFs. Coord Chem Rev 2016;307:237–54. https://doi.org/10.1016/j.ccr.2015.08.002.

[57] Wang W, Xu X, Zhou W, Shao Z. Recent Progress in Metal-Organic Frameworks for Applications in Electrocatalytic and Photocatalytic Water Splitting. Adv Sci 2017;4. https://doi.org/10.1002/advs.201600371.

[58] Chen J, Abazari R, Adegoke KA, Maxakato NW, Bello OS, Tahir M, et al. Metal–organic frameworks and derived materials as photocatalysts for water splitting and carbon dioxide reduction. Coord Chem Rev 2022;469:214664. https://doi.org/10.1016/j.ccr.2022.214664.

[59] Çelebi N, Soysal F, Salimi K. Well-defined core/shell pDA@Ni-MOF heterostructures with photostable polydopamine as electron-transfer-template for efficient photoelectrochemical H2 evolution. Int J Hydrogen Energy 2022;47:13828–37. https://doi.org/10.1016/j.ijhydene.2022.02.111.

[60] Cardenas-Morcoso D, Ifraemov R, García-Tecedor M, Liberman I, Gimenez S, Hod I. A metal-organic framework converted catalyst that boosts photo-electrochemical water splitting. J Mater Chem A 2019;7:11143–9. https://doi.org/10.1039/c9ta01559k.

[61] Çelebi N, Soysal F, Salimi K. Spherical shape-defined hollow UiO-66 metal-organic frameworks with superior incident photon scattering for enhanced

photoelectrochemical H2 evolution. J Colloid Interface Sci 2022;608:1238–46. https://doi.org/10.1016/j.jcis.2021.10.145.

[62] Ali M, Pervaiz E, Noor T, Rabi O, Zahra R, Yang M. Recent advancements in MOF-based catalysts for applications in electrochemical and photoelectrochemical water splitting: A review. Int J Energy Res 2021;45:1190–226. https://doi.org/10.1002/er.5807.

[63] Afzali N, Keshavarzi R, Tangestaninejad S, Gimenez S, Mirkhani V, Moghadam M, et al. Multifunctional approach to improve water oxidation performance with MOF-based photoelectrodes. Appl Mater Today 2021;24:101159. https://doi.org/10.1016/j.apmt.2021.101159.

[64] Zhou S, Chen K, Huang J, Wang L, Zhang M, Bai B, et al. Preparation of heterometallic CoNi-MOFs-modified BiVO4: a steady photoanode for improved performance in photoelectrochemical water splitting. Appl Catal B Environ 2020;266. https://doi.org/10.1016/j.apcatb.2019.118513.

[65] Hao X, Cui Z, Zhou J, Wang Y, Hu Y, Wang Y, et al. Architecture of high efficient zinc vacancy mediated Z-scheme photocatalyst from metal-organic frameworks. Nano Energy 2018;52:105–16. https://doi.org/10.1016/j.nanoen.2018.07.043.

[66] Xiao Y, Wang XL, Yu H, Yang Y, Dong X ting. MOF-5 derived C-doped ZnO decorated with Cu cocatalyst for enhancing visible-light driven photocatalytic hydrogen evolution. J Phys Chem Solids 2021;149:5192–247. https://doi.org/10.1016/j.jpcs.2020.109793.

[67] Celebi N, Aydin MY, Soysal F, Ylldlz N, Salimi K. Core/Shell PDA@UiO-66 Metal-Organic Framework Nanoparticles for Efficient Visible-Light Photodegradation of Organic Dyes. ACS Appl Nano Mater 2020;3:11543–54. https://doi.org/10.1021/acsanm.0c02636.

[68] Bai H, Wang F, You Z, Sun D, Cui J, Fan W. Fabrication of Zn-MOF decorated BiVO4 photoanode for water splitting. Colloids Surfaces A

Physicochem Eng Asp 2022;640:128412. https://doi.org/10.1016/j.colsurfa.2022.128412.

[69] Qi J, Zhang W, Cao R. Solar-to-Hydrogen Energy Conversion Based on Water Splitting. Adv Energy Mater 2018;8:1–16. https://doi.org/10.1002/aenm.201701620.

[70] Maeda K. Photocatalytic water splitting using semiconductor particles: History and recent developments. J Photochem Photobiol C Photochem Rev 2011;12:237–68. https://doi.org/10.1016/j.jphotochemrev.2011.07.001.

[71] Bhatt MD, Lee JS. Recent theoretical progress in the development of photoanode materials for solar water splitting photoelectrochemical cells. J Mater Chem A 2015;3:10632–59. https://doi.org/10.1039/c5ta00257e.

[72] Ahmad H, Kamarudin SK, Minggu LJ, Kassim M. Hydrogen from photo-catalytic water splitting process: A review. Renew Sustain Energy Rev 2015;43:599–610. https://doi.org/10.1016/j.rser.2014.10.101.

[73] Fajrina N, Tahir M. A critical review in strategies to improve photocatalytic water splitting towards hydrogen production. Int J Hydrogen Energy 2019;44:540–77. https://doi.org/10.1016/j.ijhydene.2018.10.200.

[74] Shi N, Li X, Fan T, Zhou H, Zhang D, Zhu H. Artificial chloroplast: Au/chloroplast-morph-TiO2 with fast electron transfer and enhanced photocatalytic activity. Int J Hydrogen Energy 2014;39:5617–24. https://doi.org/10.1016/j.ijhydene.2014.01.187.

[75] Wang YY, Chen YX, Barakat T, Zeng YJ, Liu J, Siffert S, et al. Recent advances in non-metal doped titania for solar-driven photocatalytic/photoelectrochemical water-splitting. J Energy Chem 2022;66:529–59. https://doi.org/10.1016/j.jechem.2021.08.038.

[76] Tong H, Ouyang S, Bi Y, Umezawa N, Oshikiri M, Ye J. Nano-photocatalytic materials: Possibilities and challenges. Adv Mater 2012;24:229–51. https://doi.org/10.1002/adma.201102752.

[77] Li X, Wang Z, Wang L. Metal–Organic Framework-Based Materials for Solar Water Splitting. Small Sci 2021;1:2000074. https://doi.org/10.1002/smsc.202000074.

[78] Ishaq T, Yousaf M, Bhatti IA, Batool A, Asghar MA, Mohsin M, et al. A perspective on possible amendments in semiconductors for enhanced photocatalytic hydrogen generation by water splitting. Int J Hydrogen Energy 2021;46:39036–57. https://doi.org/10.1016/j.ijhydene.2021.09.165.

[79] Chen S, Takata T, Domen K. Particulate photocatalysts for overall water splitting. Nat Rev Mater 2017;2:1–17. https://doi.org/10.1038/natrevmats.2017.50.

[80] Pokrant S, Dilger S, Landsmann S, Trottmann M. Size effects of cocatalysts in photoelectrochemical and photocatalytic water splitting. Mater Today Energy 2017;5:158–63. https://doi.org/10.1016/j.mtener.2017.06.005.

[81] Hisatomi T, Kubota J, Domen K. Recent advances in semiconductors for photocatalytic and photoelectrochemical water splitting. Chem Soc Rev 2014;43:7520–35. https://doi.org/10.1039/c3cs60378d.

[82] Osterloh FE. Inorganic nanostructures for photoelectrochemical and photocatalytic water splitting. Chem Soc Rev 2013;42:2294–320. https://doi.org/10.1039/c2cs35266d.

[83] Wang Z, Li C, Domen K. Recent developments in heterogeneous photocatalysts for solar-driven overall water splitting. Chem Soc Rev 2019;48:2109–25. https://doi.org/10.1039/c8cs00542g.

[84] Xiao N, Li S, Li X, Ge L, Gao Y, Li N. The roles and mechanism of cocatalysts in photocatalytic water splitting to produce hydrogen. Chinese J Catal 2020;41:642–71. https://doi.org/10.1016/S1872-2067(19)63469-8.

[85] Ding C, Shi J, Wang Z, Li C. Photoelectrocatalytic Water Splitting: Significance of Cocatalysts, Electrolyte, and Interfaces. ACS Catal 2017;7:675–88. https://doi.org/10.1021/acscatal.6b03107.

[86] Chou HL, Hwang BJ, Sun CL. Catalysis in Fuel Cells and Hydrogen Production. Elsevier B.V.; 2013. https://doi.org/10.1016/B978-0-444-53880-2.00014-4.

[87] Saruyama M, Pelicano CM, Teranishi T. Bridging electrocatalyst and cocatalyst studies for solar hydrogen production via water splitting. Chem Sci 2022;13:2824–40. https://doi.org/10.1039/d1sc06015e.

[88] Puangpetch T, Chavadej S, Sreethawong T. Hydrogen production over Au-loaded mesoporous-assembled SrTiO3 nanocrystal photocatalyst: Effects of molecular structure and chemical properties of hole scavengers. Energy Convers Manag 2011;52:2256–61. https://doi.org/10.1016/j.enconman.2010.12.026.

[89] Ismail AA, Bahnemann DW. Photochemical splitting of water for hydrogen production by photocatalysis: A review. Sol Energy Mater Sol Cells 2014;128:85–101. https://doi.org/10.1016/j.solmat.2014.04.037.

[90] Osterloh FE. Inorganic materials as catalysts for photochemical splitting of water. Chem Mater 2008;20:35–54. https://doi.org/10.1021/cm7024203.

[91] Ran J, Zhang J, Yu J, Jaroniec M, Qiao SZ. Earth-abundant cocatalysts for semiconductor-based photocatalytic water splitting. Chem Soc Rev 2014;43:7787–812. https://doi.org/10.1039/c3cs60425j.

[92] Cheng C, Zhang W, Chen X, Peng S, Li Y. Strategies for improving photoelectrochemical water splitting performance of Si-based electrodes. Energy Sci Eng 2022;10:1526–43. https://doi.org/10.1002/ese3.1087.

[93] Nadeem MA, Khan MA, Ziani AA, Idriss H. An overview of the photocatalytic water splitting over suspended particles. Catalysts 2021;11:1–25. https://doi.org/10.3390/catal11010060.

[94] Maeda K, Domen K. Photocatalytic water splitting: Recent progress and future challenges. J Phys Chem Lett 2010;1:2655–61. https://doi.org/10.1021/jz1007966.

[95] Li J, Yuan H, Zhang W, Jin B, Feng Q, Huang J, et al. Advances in Z-scheme semiconductor photocatalysts for the photoelectrochemical applications: A review. Carbon Energy 2022;4:294–331. https://doi.org/10.1002/cey2.179.

[96] Ng BJ, Putri LK, Kong XY, Teh YW, Pasbakhsh P, Chai SP. Z-Scheme Photocatalytic Systems for Solar Water Splitting. Adv Sci 2020;7. https://doi.org/10.1002/advs.201903171.

[97] Zhang G, Wang Z, Wu J. Construction of a Z-scheme heterojunction for high-efficiency visible-light-driven photocatalytic CO2reduction. Nanoscale 2021;13:4359–89. https://doi.org/10.1039/d0nr08442e.

[98] Li X, Garlisi C, Guan Q, Anwer S, Al-Ali K, Palmisano G, et al. A review of material aspects in developing direct Z-scheme photocatalysts. Mater Today 2021;47:75–107. https://doi.org/10.1016/j.mattod.2021.02.017.

[99] Ng BJ, Putri LK, Kong XY, Teh YW, Pasbakhsh P, Chai SP. Z-Scheme Photocatalytic Systems for Solar Water Splitting. Adv Sci 2020;7. https://doi.org/10.1002/advs.201903171.

[100] Zhang X, Chen Z, Luo Y, Han X, Jiang Q, Zhou T, et al. Construction of NH2-MIL-125(Ti)/CdS Z-scheme heterojunction for efficient photocatalytic H2 evolution. J Hazard Mater 2021;405:124128. https://doi.org/10.1016/j.jhazmat.2020.124128.

[101] Lee DK, Lee D, Lumley MA, Choi KS. Progress on ternary oxide-based photoanodes for use in photoelectrochemical cells for solar water splitting. Chem Soc Rev 2019;48:2126–57. https://doi.org/10.1039/c8cs00761f.

[102] Yang W, Prabhakar RR, Tan J, Tilley SD, Moon J. Strategies for enhancing the photocurrent, photovoltage, and stability of photoelectrodes for photoelectrochemical water splitting. Chem Soc Rev 2019;48:4979–5015. https://doi.org/10.1039/c8cs00997j.

[103] Joy J, Mathew J, George SC. ScienceDirect Nanomaterials for photoelectrochemical water splitting e review. Int J Hydrogen Energy 2018:1–

14. https://doi.org/10.1016/j.ijhydene.2018.01.099.

[104] Belver C, Bedia J, Gómez-Avilés A, Peñas-Garzón M, Rodriguez JJ. Semiconductor Photocatalysis for Water Purification. 2018. https://doi.org/10.1016/B978-0-12-813926-4.00028-8.

[105] Lee SY, Park SJ. TiO2 photocatalyst for water treatment applications. J Ind Eng Chem 2013;19:1761–9. https://doi.org/10.1016/j.jiec.2013.07.012.

[106] Fu Y-S, Li J, Li J. Metal/Semiconductor Nanocomposites for Photocatalysis: Fundamentals, Structures, Applications and Properties n.d. https://doi.org/10.3390/nano9030359.

[107] Boyjoo Y, Sun H, Liu J, Pareek VK, Wang S. A review on photocatalysis for air treatment: From catalyst development to reactor design. Chem Eng J 2017;310:537–59. https://doi.org/10.1016/j.cej.2016.06.090.

[108] Zhang L, Ran J, Qiao SZ, Jaroniec M. Characterization of semiconductor photocatalysts. Chem Soc Rev 2019;48:5184–206. https://doi.org/10.1039/c9cs00172g.

[109] Fine GF, Cavanagh LM, Afonja A, Binions R. Metal oxide semi-conductor gas sensors in environmental monitoring. Sensors 2010;10:5469–502. https://doi.org/10.3390/s100605469.

[110] Tamirat AG, Rick J, Dubale AA, Su WN, Hwang BJ. Using hematite for photoelectrochemical water splitting: A review of current progress and challenges. Nanoscale Horizons 2016;1:243–67. https://doi.org/10.1039/c5nh00098j.

[111] Chen X, Li Y, Shen S. Surface- and interface-engineered heterostructures for solar hydrogen generation. J Phys D Appl Phys 2018;51:163002. https://doi.org/10.1088/1361-6463/aab318.

[112] Kudo A, Miseki Y. Heterogeneous photocatalyst materials for water splitting. Chem Soc Rev 2009;38:253–78. https://doi.org/10.1039/b800489g.

[113] Jiang Y, Tian B. Inorganic semiconductor biointerfaces. Nat Rev Mater 2018;3:473–90. https://doi.org/10.1038/s41578-018-0062-3.

[114] Wang Q, Domen K. Particulate Photocatalysts for Light-Driven Water Splitting: Mechanisms, Challenges, and Design Strategies. Chem Rev 2020;120:919–85. https://doi.org/10.1021/acs.chemrev.9b00201.

[115] Hamdani IR, Bhaskarwar AN. Recent progress in material selection and device designs for photoelectrochemical water-splitting. Renew Sustain Energy Rev 2021;138. https://doi.org/10.1016/j.rser.2020.110503.

[116] Jiang C, Moniz SJA, Wang A, Zhang T, Tang J. Photoelectrochemical devices for solar water splitting-materials and challenges. Chem Soc Rev 2017;46:4645–60. https://doi.org/10.1039/c6cs00306k.

[117] Alfaifi BY, Ullah H, Alfaifi S, Tahir AA, Mallick TK. Photoelectrochemical solar water splitting: From basic principles to advanced devices. Veruscript Funct Nanomater 2018;2:BDJOC3. https://doi.org/10.22261/fnan.bdjoc3.

[118] Phuan YW, Ong WJ, Chong MN, Ocon JD. Prospects of electrochemically synthesized hematite photoanodes for photoelectrochemical water splitting: A review. J Photochem Photobiol C Photochem Rev 2017;33:54–82. https://doi.org/10.1016/j.jphotochemrev.2017.10.001.

[119] Ahmed AY, Ahmed MG, Kandiel TA. Hematite photoanodes with size-controlled nanoparticles for enhanced photoelectrochemical water oxidation. Appl Catal B Environ 2018;236:117–24. https://doi.org/10.1016/j.apcatb.2018.04.073.

[120] Singh R, Dutta S. A review on H2 production through photocatalytic reactions using TiO2/TiO2-assisted catalysts. Fuel 2018;220:607–20. https://doi.org/10.1016/j.fuel.2018.02.068.

[121] Sha C, Danlian H, Piao X, Wenjing X, Lei L, Min C, et al. Semiconductor-based photocatalysts for photocatalytic and photoelectrochemical water splitting: will we stop with photocorrosion? 2015.

https://doi.org/10.1039/C9TA12799B.Volume.

[122] Wang G, Wang H, Ling Y, Tang Y, Yang X, Fitzmorris RC, et al. Hydrogen-treated TiO2 nanowire arrays for photoelectrochemical water splitting. Nano Lett 2011;11:3026–33. https://doi.org/10.1021/nl201766h.

[123] Zhao Y, Hoivik N, Wang K. Recent advance on engineering titanium dioxide nanotubes for photochemical and photoelectrochemical water splitting. Nano Energy 2016;30:728–44. https://doi.org/10.1016/j.nanoen.2016.09.027.

[124] Arifin K, Yunus RM, Minggu LJ, Kassim MB. Improvement of TiO2 nanotubes for photoelectrochemical water splitting: Review. Int J Hydrogen Energy 2021;46:4998–5024. https://doi.org/10.1016/j.ijhydene.2020.11.063.

[125] Shakeel Ahmad M, Pandey AK, Abd Rahim N. Advancements in the development of TiO2 photoanodes and its fabrication methods for dye sensitized solar cell (DSSC) applications. A review. Renew Sustain Energy Rev 2017;77:89–108. https://doi.org/10.1016/j.rser.2017.03.129.

[126] Zhou D, Fan K. Recent strategies to enhance the efficiency of hematite photoanodes in photoelectrochemical water splitting. Chinese J Catal 2021;42:904–19. https://doi.org/10.1016/S1872-2067(20)63712-3.

[127] Park Y, Mc Donald KJ, Choi KS. Progress in bismuth vanadate photoanodes for use in solar water oxidation. Chem Soc Rev 2013;42:2321–37. https://doi.org/10.1039/c2cs35260e.

[128] Tayebi M, Lee BK. Recent advances in BiVO4 semiconductor materials for hydrogen production using photoelectrochemical water splitting. Renew Sustain Energy Rev 2019;111:332–43. https://doi.org/10.1016/j.rser.2019.05.030.

[129] Wang Q, He J, Shi Y, Zhang S, Niu T, She H, et al. Designing non-noble/semiconductor Bi/BiVO4 photoelectrode for the enhanced photoelectrochemical performance. Chem Eng J 2017;326:411–8. https://doi.org/10.1016/j.cej.2017.05.171.

[130] Quiñonero J, Lana-Villarreal T, Gómez R. Improving the photoactivity of bismuth vanadate thin film photoanodes through doping and surface modification strategies. Appl Catal B Environ 2016;194:141–9. https://doi.org/10.1016/j.apcatb.2016.04.057.

[131] Huang ZF, Pan L, Zou JJ, Zhang X, Wang L. Nanostructured bismuth vanadate-based materials for solar-energy-driven water oxidation: A review on recent progress. Nanoscale 2014;6:14044–63. https://doi.org/10.1039/c4nr05245e.

[132] Xia L, Bai J, Li J, Zeng Q, Li L, Zhou B. High-performance BiVO4 photoanodes cocatalyzed with an ultrathin α-Fe2O3 layer for photoelectrochemical application. Appl Catal B Environ 2017;204:127–33. https://doi.org/10.1016/j.apcatb.2016.11.015.

[133] Moniz SJA, Shevlin SA, Martin DJ, Guo ZX, Tang J. Visible-light driven heterojunction photocatalysts for water splitting-a critical review. Energy Environ Sci 2015;8:731–59. https://doi.org/10.1039/c4ee03271c.

[134] Patil SS, Mali MG, Hassan MA, Patil DR, Kolekar SS, Ryu S-W. One-Pot in Situ Hydrothermal Growth of BiVO 4 /Ag/rGO Hybrid Architectures for Solar Water Splitting and Environmental Remediation OPEN n.d. https://doi.org/10.1038/s41598-017-08912-z.

[135] Tian T, Dong C, Liang X, Yue M, Ding Y. Enhanced photoelectrochemical water oxidation activity of BiVO4 by coating of Co-phenolic networks as hole-transfer and co-catalyst. J Catal 2019;377:684–91. https://doi.org/10.1016/j.jcat.2019.08.012.

[136] Rohloff M, Anke B, Zhang S, Gernert U, Scheu C, Lerch M, et al. Mo-doped BiVO4 thin films-high photoelectrochemical water splitting performance achieved by a tailored structure and morphology. Sustain Energy Fuels 2017;1:1830–46. https://doi.org/10.1039/c7se00301c.

[137] Zhong DK, Choi S, Gamelin DR. Near-complete suppression of surface

recombination in solar photoelectrolysis by “co-Pi” catalyst-modified W:BiVO4. J Am Chem Soc 2011;133:18370–7. https://doi.org/10.1021/ja207348x.

[138] Kegel J, Povey IM, Pemble ME. Zinc oxide for solar water splitting: A brief review of the material’s challenges and associated opportunities. Nano Energy 2018;54:409–28. https://doi.org/10.1016/j.nanoen.2018.10.043.

[139] Lee KM, Lai CW, Ngai KS, Juan JC. Recent developments of zinc oxide based photocatalyst in water treatment technology: A review. vol. 88. Elsevier Ltd; 2016. https://doi.org/10.1016/j.watres.2015.09.045.

[140] Ma M, Huang Y, Liu J, Liu K, Wang Z, Zhao C, et al. Engineering the photoelectrochemical behaviors of ZnO for efficient solar water splitting. J Semicond 2020;41. https://doi.org/10.1088/1674-4926/41/9/091702.

[141] Ikram M, Rashid M, Haider A, Naz S, Haider J, Raza A, et al. A review of photocatalytic characterization, and environmental cleaning, of metal oxide nanostructured materials. Sustain Mater Technol 2021;30:e00343. https://doi.org/10.1016/j.susmat.2021.e00343.

[142] Kang Z, Si H, Zhang S, Wu J, Sun Y, Liao Q, et al. Interface Engineering for Modulation of Charge Carrier Behavior in ZnO Photoelectrochemical Water Splitting. Adv Funct Mater 2019;29. https://doi.org/10.1002/adfm.201808032.

[143] Han J, Liu Z, Yadian B, Huang Y, Guo K, Liu Z, et al. Synthesis of metal sulfide sensitized zinc oxide-based core/shell/shell nanorods and their photoelectrochemical properties. J Power Sources 2014;268:388–96. https://doi.org/10.1016/j.jpowsour.2014.06.060.

[144] Tai M, Zhao X, Shen H, Guo Y, Zhang M, Zhou Y, et al. Ultrathin Zn2SnO4 (ZTO) passivated ZnO nanocone arrays for efficient and stable perovskite solar cells. Chem Eng J 2019;361:60–6. https://doi.org/10.1016/j.cej.2018.12.056.

[145] Wibowo A, Maradhana A, Marsudi A, Amal MI, Ananda MB, Stephanie R, et

al. ZnO nanostructured materials for emerging solar cell applications 2020. https://doi.org/10.1039/d0ra07689a.

[146] Liu CF, Lu YJ, Hu CC. Effects of Anions and pH on the Stability of ZnO Nanorods for Photoelectrochemical Water Splitting. ACS Omega 2018;3:3429–39. https://doi.org/10.1021/acsomega.8b00214.

[147] Mahala C, Sharma MD, Basu M. ZnO@CdS heterostructures: An efficient photoanode for photoelectrochemical water splitting. New J Chem 2019;43:7001–10. https://doi.org/10.1039/c9nj01373c.

[148] Bai Z, Yan X, Kang Z, Hu Y, Zhang X, Zhang Y. Photoelectrochemical performance enhancement of ZnO photoanodes from ZnIn2S4 nanosheets coating. Nano Energy 2015;14:392–400. https://doi.org/10.1016/j.nanoen.2014.09.005.

[149] Kusmierek E. A CeO2 semiconductor as a photocatalytic and photoelectrocatalytic material for the remediation of pollutants in industrial wastewater: A review. Catalysts 2020;10:1–54. https://doi.org/10.3390/catal10121435.

[150] Celebi N, Arlı F, Soysal F, Salimi K. Z-scheme ZnO@PDA/CeO2 heterojunctions using polydopamine as electron transfer layer for enhanced photoelectrochemical H2 generation. Mater Today Energy 2021;21:100765. https://doi.org/10.1016/j.mtener.2021.100765.

[151] Fauzi AA, Jalil AA, Hassan NS, Aziz FFA, Azami MS, Hussain I, et al. A critical review on relationship of CeO2-based photocatalyst towards mechanistic degradation of organic pollutant. Chemosphere 2022;286. https://doi.org/10.1016/j.chemosphere.2021.131651.

[152] Jing M, Song W, Li Y, Zhao Z, Liu J, Henkelman G. Theoretical study of structure sensitivity on Au doped CeO2 surfaces for formaldehyde oxidation: The effect of crystal planes and Au doping. Chem Eng J 2022;433:133599. https://doi.org/10.1016/j.cej.2021.133599.

[153] Xie S, Wang Z, Cheng F, Zhang P, Mai W, Tong Y. Ceria and ceria-based nanostructured materials for photoenergy applications. Nano Energy 2017;34:313–37. https://doi.org/10.1016/j.nanoen.2017.02.029.

[154] Luo H, Zeng Z, Zeng G, Zhang C, Xiao R, Huang D, et al. Recent progress on metal-organic frameworks based- and derived-photocatalysts for water splitting. Chem Eng J 2020;383:123196. https://doi.org/10.1016/j.cej.2019.123196.

[155] Wang Q, Astruc D. State of the Art and Prospects in Metal-Organic Framework (MOF)-Based and MOF-Derived Nanocatalysis. Chem Rev 2020;120:1438–511. https://doi.org/10.1021/acs.chemrev.9b00223.

[156] Behera P, Subudhi S, Tripathy SP, Parida K. MOF derived nano-materials: A recent progress in strategic fabrication, characterization and mechanistic insight towards divergent photocatalytic applications. Coord Chem Rev 2022;456:214392. https://doi.org/10.1016/j.ccr.2021.214392.

[157] Baumann AE, Burns DA, Liu B, Thoi VS. Metal-organic framework functionalization and design strategies for advanced electrochemical energy storage devices. Commun Chem 2019;2. https://doi.org/10.1038/s42004-019-0184-6.

[158] Meyer K, Ranocchiari M, Van Bokhoven JA. Metal organic frameworks for photo-catalytic water splitting. Energy Environ Sci 2015;8:1923–37. https://doi.org/10.1039/c5ee00161g.

[159] Li R, Zhang W, Zhou K. Metal–Organic-Framework-Based Catalysts for Photoreduction of CO2. Adv Mater 2018;30:1–31. https://doi.org/10.1002/adma.201705512.

[160] Ali M, Pervaiz E, Noor T, Rabi O, Zahra R, Yang M. Recent advancements in MOF-based catalysts for applications in electrochemical and photoelectrochemical water splitting: A review 2020. https://doi.org/10.1002/er.5807.

[161] Xiong W, Zeng Z, Li X, Zeng G, Xiao R, Yang Z, et al. Multi-walled carbon nanotube/amino-functionalized MIL-53(Fe) composites: Remarkable adsorptive removal of antibiotics from aqueous solutions. Chemosphere 2018;210:1061–9. https://doi.org/10.1016/j.chemosphere.2018.07.084.

[162] Cheng M, Lai C, Liu Y, Zeng G, Huang D, Zhang C, et al. Metal-organic frameworks for highly efficient heterogeneous Fenton-like catalysis. Coord Chem Rev 2018;368:80–92. https://doi.org/10.1016/j.ccr.2018.04.012.

[163] Kumar G, Masram DT. Sustainable Synthesis of MOF-5@GO Nanocomposites for Efficient Removal of Rhodamine B from Water. ACS Omega 2021;6:9587–99. https://doi.org/10.1021/acsomega.1c00143.

[164] Campbell MG, Dincă M. Metal–organic frameworks as active materials in electronic sensor devices. Sensors (Switzerland) 2017;17:1–11. https://doi.org/10.3390/s17051108.

[165] Fang Y, Wen J, Zeng G, Jia F, Zhang S, Peng Z, et al. Effect of mineralizing agents on the adsorption performance of metal–organic framework MIL-100(Fe) towards chromium(VI). Chem Eng J 2018;337:532–40. https://doi.org/10.1016/j.cej.2017.12.136.

[166] Sun Y, Zhou HC. Recent progress in the synthesis of metal-organic frameworks. Sci Technol Adv Mater 2015;16:54202. https://doi.org/10.1088/1468-6996/16/5/054202.

[167] Volanti M, Cespi D, Passarini F, Neri E, Cavani F, Mizsey P, et al. Terephthalic acid from renewable sources: Early-stage sustainability analysis of a bio-PET precursor. Green Chem 2019;21:885–96. https://doi.org/10.1039/c8gc03666g.

[168] Gangu KK, Maddila S, Jonnalagadda SB. The pioneering role of metal-organic framework-5 in ever-growing contemporary applications - a review. RSC Adv 2022;12:14282–98. https://doi.org/10.1039/d2ra01505f.

[169] McKinstry C, Cussen EJ, Fletcher AJ, Patwardhan S V., Sefcik J. Effect of

synthesis conditions on formation pathways of metal organic framework (MOF-5) crystals. Cryst Growth Des 2013;13:5481–6. https://doi.org/10.1021/cg4014619.

[170] Bennabi S, Belbachir M. Synthesis and characterization of a new hybrid material (MOF-5/Mag-H+) based on a metal-organic framework and a proton exchanged montmorillonite clay (Maghnite-H+) as catalytic support. J Mater Environ Sci 2017;8:4391–8. https://doi.org/10.26872/jmes.2017.8.12.463.

[171] Silva P, Vilela SMF, Tomé JPC, Almeida Paz FA. Multifunctional metal-organic frameworks: From academia to industrial applications. Chem Soc Rev 2015;44:6774–803. https://doi.org/10.1039/c5cs00307e.

[172] Bao Z, Yuan Y, Leng C, Li L, Zhao K, Sun Z. One-Pot Synthesis of Noble Metal/Zinc Oxide Composites with Controllable Morphology and High Catalytic Performance. ACS Appl Mater Interfaces 2017;9:16417–25. https://doi.org/10.1021/acsami.7b02667.

[173] Salimi K, Usta DD, Çelikbıçak Ö, Pinar A, Salih B, Tuncel A. Ti(IV) carrying polydopamine-coated, monodisperse-porous SiO2 microspheres with stable magnetic properties for highly selective enrichment of phosphopeptides. Colloids Surfaces B Biointerfaces 2017;153:280–90. https://doi.org/10.1016/j.colsurfb.2017.02.028.

[174] Usta DD, Celebi N, Soysal F, Saglam ASY, Yildiz N, Salimi K. Bio-inspired NIR responsive Au-pDA@pDA sandwich nanostructures with excellent photo-thermal performance and stability. Colloids Surfaces A Physicochem Eng Asp 2021;611:125758. https://doi.org/10.1016/j.colsurfa.2020.125758.

[175] Salimi K. Self-assembled bio-inspired Au/CeO2 nano-composites for visible white LED light irradiated photocatalysis. Colloids Surfaces A Physicochem Eng Asp 2020;599. https://doi.org/10.1016/j.colsurfa.2020.124908.

[176] Yoon KR, Lee KA, Jo S, Yook SH, Lee KY, Kim ID, et al. Mussel-Inspired Polydopamine-Treated Reinforced Composite Membranes with Self-

Supported CeOx Radical Scavengers for Highly Stable PEM Fuel Cells. Adv Funct Mater 2019;29:1806929. https://doi.org/10.1002/adfm.201806929.

[177] Celebi N, Aydin MY, Soysal F, Ciftci YO, Salimi K. Ligand-free fabrication of Au/TiO2 nanostructures for plasmonic hot-electron-driven photocatalysis: Photoelectrochemical water splitting and organic-dye degredation. J Alloys Compd 2021;860:157908. https://doi.org/10.1016/j.jallcom.2020.157908.

[178] Makuła P, Pacia M, Macyk W. How To Correctly Determine the Band Gap Energy of Modified Semiconductor Photocatalysts Based on UV-Vis Spectra. J Phys Chem Lett 2018;9:6814–7. https://doi.org/10.1021/acs.jpclett.8b02892.

[179] Raval N, Maheshwari R, Kalyane D, Youngren-Ortiz SR, Chougule MB, Tekade RK. Importance of physicochemical characterization of nanoparticles in pharmaceutical product development. Elsevier Inc.; 2018. https://doi.org/10.1016/B978-0-12-817909-3.00010-8.

[180] Pope CG. X-ray diffraction and the bragg equation. J Chem Educ 1997;74:129–31. https://doi.org/10.1021/ed074p129.

[181] Modena MM, Rühle B, Burg TP, Wuttke S. Nanoparticle Characterization: What to Measure? Adv Mater 2019;31:1–26. https://doi.org/10.1002/adma.201901556.

[182] Guy OJ, Walker KAD. Graphene Functionalization for Biosensor Applications. Second Edi. Elsevier Inc.; 2016. https://doi.org/10.1016/B978-0-12-802993-0.00004-6.

[183] Khan I, Saeed K, Khan I. Nanoparticles: Properties, applications and toxicities. Arab J Chem 2019;12:908–31. https://doi.org/10.1016/j.arabjc.2017.05.011.

[184] Palchoudhury S, Baalousha M, Lead JR. Methods for Measuring Concentration (Mass, Surface Area and Number) of Nanomaterials. vol. 8. Elsevier; 2015. https://doi.org/10.1016/B978-0-08-099948-7.00005-1.

[185] Ambroz F, Macdonald TJ, Martis V, Parkin IP. Evaluation of the BET theory for the characterization of meso and microporous MOFs. Small Methods 2018;2. https://doi.org/10.1002/smtd.201800173.

[186] Ye KH, Li H, Huang D, Xiao S, Qiu W, Li M, et al. Enhancing photoelectrochemical water splitting by combining work function tuning and heterojunction engineering. Nat Commun 2019;10. https://doi.org/10.1038/s41467-019-11586-y.

[187] Ding Q, Gou L, Wei D, Xu D, Fan W, Shi W. Metal-organic framework derived Co3O4/TiO2 heterostructure nanoarrays for promote photoelectrochemical water splitting. Int J Hydrogen Energy 2021;46:24965–76. https://doi.org/10.1016/j.ijhydene.2021.05.065.

[188] Qiu Y, Pan Z, Chen H, Ye D, Guo L, Fan Z, et al. Current progress in developing metal oxide nanoarrays-based photoanodes for photoelectrochemical water splitting. Sci Bull 2019;64:1348–80. https://doi.org/10.1016/j.scib.2019.07.017.

[189] Pavlenko M, Siuzdak K, Coy E, Załęski K, Jancelewicz M, Iatsunskyi I. Enhanced solar-driven water splitting of 1D core-shell Si/TiO2/ZnO nanopillars. Int J Hydrogen Energy 2020;45:26426–33. https://doi.org/10.1016/j.ijhydene.2019.11.231.

[190] Chai H, Koo B, Son S, Jung SP. Validity and Reproducibility of Various Linear Sweep Voltammetry Tests of Anode and Cathode Electrodes in Microbial Electrolysis Cells 2020:1–17. https://doi.org/10.20944/preprints202008.0664.v1.

[191] Lv Y, Zhang X, Zhang P, Wang H, Ma Q, Tao X. Comparison between voltammetric detection methods for abalone-flavoring liquid. Open Life Sci 2021;16:354–61. https://doi.org/10.1515/biol-2021-0035.

[192] Murthy AP, Theerthagiri J, Madhavan J. Insights on Tafel Constant in the Analysis of Hydrogen Evolution Reaction. J Phys Chem C 2018;122:23943–9.

https://doi.org/10.1021/acs.jpcc.8b07763.

[193] Li D, Shi J, Li C. Transition-Metal-Based Electrocatalysts as Cocatalysts for Photoelectrochemical Water Splitting: A Mini Review. Small 2018;14:1–22. https://doi.org/10.1002/smll.201704179.

[194] Li J, Zheng G. One-dimensional earth-abundant nanomaterials for water-splitting electrocatalysts. Adv Sci 2017;4. https://doi.org/10.1002/advs.201600380.

[195] Seeber R, Zanardi C, Inzelt G. Links between electrochemical thermodynamics and kinetics. ChemTexts 2015;1. https://doi.org/10.1007/s40828-015-0018-9.

[196] Zeng M, Li Y. Recent advances in heterogeneous electrocatalysts for the hydrogen evolution reaction. J Mater Chem A 2015;3:14942–62. https://doi.org/10.1039/C5TA02974K.

[197] Devi Munusamy T, Rahman Khan M, Chin SY. Photoelectrochemical performance of P@MoS2for hydrogen evolution reaction. Mater Today Proc 2021;48:766–70. https://doi.org/10.1016/j.matpr.2021.02.249.

[198] Hou Y, Qiu M, Zhang T, Zhuang X, Kim CS, Yuan C, et al. Ternary Porous Cobalt Phosphoselenide Nanosheets: An Efficient Electrocatalyst for Electrocatalytic and Photoelectrochemical Water Splitting. Adv Mater 2017;29. https://doi.org/10.1002/adma.201701589.

[199] Chen Z, Dinh HN, Miller E. Photoelectrochemical Water Splitting. New York, NY: Springer New York; 2013. https://doi.org/10.1007/978-1-4614-8298-7.

[200] Devadiga D, Selvakumar M, Shetty P, Santosh MS. The integration of flexible dye-sensitized solar cells and storage devices towards wearable self-charging power systems: A review. Renew Sustain Energy Rev 2022;159. https://doi.org/10.1016/j.rser.2022.112252.

[201] Gibson EA. Dye-sensitized photocathodes for H2 evolution. Chem Soc Rev

2017;46:6194–209. https://doi.org/10.1039/c7cs00322f.

[202] Bedoya-Lora FE, Holmes-Gentle I, Hankin A. Electrochemical techniques for photoelectrode characterisation. Curr Opin Green Sustain Chem 2021;29:100463. https://doi.org/10.1016/j.cogsc.2021.100463.

[203] Guo CX, Xie J, Yang H, Li CM. Au@CdS Core–Shell Nanoparticles-Modified ZnO Nanowires Photoanode for Efficient Photoelectrochemical Water Splitting. Adv Sci 2015;2:1–6. https://doi.org/10.1002/advs.201500135.

[204] Li R. Latest progress in hydrogen production from solar water splitting via photocatalysis, photoelectrochemical, and photovoltaic-photoelectrochemical solutions. Cuihua Xuebao/Chinese J Catal 2017;38:5–12. https://doi.org/10.1016/S1872-2067(16)62552-4.

[205] Choudhary S, Upadhyay S, Kumar P, Singh N, Satsangi VR, Shrivastav R, et al. Nanostructured bilayered thin films in photoelectrochemical water splitting - A review. Int J Hydrogen Energy 2012;37:18713–30. https://doi.org/10.1016/j.ijhydene.2012.10.028.

[206] Feliu S. Electrochemical impedance spectroscopy for the measurement of the corrosion rate of magnesium alloys: Brief review and challenges. Metals (Basel) 2020;10:1–23. https://doi.org/10.3390/met10060775.

[207] Rezaei Niya SM, Hoorfar M. Study of proton exchange membrane fuel cells using electrochemical impedance spectroscopy technique - A review. J Power Sources 2013;240:281–93. https://doi.org/10.1016/j.jpowsour.2013.04.011.

[208] Zhang S, Chen D, Liu Z, Ruan M, Guo Z. Novel strategy for efficient water splitting through pyro-electric and pyro-photo-electric catalysis of BaTiO3 by using thermal resource and solar energy. Appl Catal B Environ 2021;284:119686. https://doi.org/10.1016/j.apcatb.2020.119686.

[209] Bredar ARC, Chown AL, Burton AR, Farnum BH. Electrochemical Impedance Spectroscopy of Metal Oxide Electrodes for Energy Applications. ACS Appl Energy Mater 2020;3:66–98.

https://doi.org/10.1021/acsaem.9b01965.

[210] Mei BA, Lau J, Lin T, Tolbert SH, Dunn BS, Pilon L. Physical Interpretations of Electrochemical Impedance Spectroscopy of Redox Active Electrodes for Electrical Energy Storage. J Phys Chem C 2018;122:24499–511. https://doi.org/10.1021/acs.jpcc.8b05241.

[211] Sacco A. Electrochemical impedance spectroscopy: Fundamentals and application in dye-sensitized solar cells. Renew Sustain Energy Rev 2017;79:814–29. https://doi.org/10.1016/j.rser.2017.05.159.

[212] Anantharaj S, Noda S. Appropriate Use of Electrochemical Impedance Spectroscopy in Water Splitting Electrocatalysis. ChemElectroChem 2020;7:2297–308. https://doi.org/10.1002/celc.202000515.

[213] Yu ZY, Duan Y, Feng XY, Yu X, Gao MR, Yu SH. Clean and Affordable Hydrogen Fuel from Alkaline Water Splitting: Past, Recent Progress, and Future Prospects. Adv Mater 2021;33. https://doi.org/10.1002/adma.202007100.

[214] Dai Y, Yu J, Cheng C, Tan P, Ni M. Engineering the interfaces in water-splitting photoelectrodes-an overview of the technique development. J Mater Chem A 2020;8:6984–7002. https://doi.org/10.1039/d0ta01670e.

[215] Hankin A, Bedoya-Lora FE, Alexander JC, Regoutz A, Kelsall GH. Flat band potential determination: Avoiding the pitfalls. J Mater Chem A 2019;7:26162–76. https://doi.org/10.1039/c9ta09569a.

[216] Gelderman K, Lee L, Donne SW. Flat-band potential of a semiconductor: Using the Mott-Schottky equation. J Chem Educ 2007;84:685–8. https://doi.org/10.1021/ed084p685.

[217] Sivula K. Mott-schottky analysis of photoelectrodes: Sanity checks are needed. ACS Energy Lett 2021;6:2549–51. https://doi.org/10.1021/acsenergylett.1c01245.

[218] Shi X, Cai L, Ma M, Zheng X, Park JH. General Characterization Methods for Photoelectrochemical Cells for Solar Water Splitting. ChemSusChem 2015;8:3192–203. https://doi.org/10.1002/cssc.201500075.

[219] Zhang K, Kim W, Ma M, Shi X, Park JH. Tuning the charge transfer route by p-n junction catalysts embedded with CdS nanorods for simultaneous efficient hydrogen and oxygen evolution. J Mater Chem A 2015;3:4803–10. https://doi.org/10.1039/c4ta05571c.

[220] Yang X, Lian X, Liu S, Tian J, Jiang C, Wang G, et al. Investigation of enhanced photoelectrochemical property of cerium doped hematite film prepared by sol-gel route. vol. 8. 2013.

[221] Leva-Bueno J, Peyman SA, Millner PA. A review on impedimetric immunosensors for pathogen and biomarker detection. Med Microbiol Immunol 2020;209:343–62. https://doi.org/10.1007/s00430-020-00668-0.

[222] Uygun ZO, Ertuğrul Uygun HD. A short footnote: Circuit design for faradaic impedimetric sensors and biosensors. Sensors Actuators, B Chem 2014;202:448–53. https://doi.org/10.1016/j.snb.2014.05.029.

[223] Ali A, Li X, Song J, Yang S, Zhang W, Zhang Z, et al. Nature-mimic ZnO nanoflowers architecture: Chalcogenide quantum dots coupling with ZnO/ZnTiO3 Nanoheterostructures for efficient photoelectrochemical water splitting. J Phys Chem C 2017;121:21096–104. https://doi.org/10.1021/acs.jpcc.7b04701.

[224] Sitara E, Nasir H, Mumtaz A, Ehsan MF, Sohail M, Iram S, et al. Enhanced photoelectrochemical water splitting using zinc selenide/graphitic carbon nitride type-II heterojunction interface. Int J Hydrogen Energy 2021;46:25424–35. https://doi.org/10.1016/j.ijhydene.2021.05.054.

[225] Pudukudy M, Yaakob Z. Facile Synthesis of Quasi Spherical ZnO Nanoparticles with Excellent Photocatalytic Activity. J Clust Sci 2015;26:1187–201. https://doi.org/10.1007/s10876-014-0806-1.

[226] Nurhasanah I, Safitri W, Arifin Z, Subagio A, Windarti T. Antioxidant activity and dose enhancement factor of CeO2 nanoparticles synthesized by precipitation method. IOP Conf. Ser. Mater. Sci. Eng., vol. 432, Institute of Physics Publishing; 2018. https://doi.org/10.1088/1757-899X/432/1/012031.

[227] Al-Kuhaili MF, Durrani SMA, Bakhtiari IA. Carbon monoxide gas-sensing properties of CeO 2 -ZnO thin films. Appl Surf Sci 2008;255:3033–9. https://doi.org/10.1016/j.apsusc.2008.08.058.

[228] He G, Fan H, Wang Z. Enhanced optical properties of heterostructured ZnO/CeO2 nanocomposite fabricated by one-pot hydrothermal method: Fluorescence and ultraviolet absorption and visible light transparency. Opt Mater (Amst) 2014;38:145–53. https://doi.org/10.1016/j.optmat.2014.09.037.

[229] Agarwal S, Jangir LK, Rathore KS, Kumar M, Awasthi K. Morphology-dependent structural and optical properties of ZnO nanostructures. Appl Phys A Mater Sci Process 2019;125. https://doi.org/10.1007/s00339-019-2852-x.

[230] Neshchimenko V, Li C, Mikhailov M, Lv J. Optical radiation stability of ZnO hollow particles. Nanoscale 2018;10:22335–47. https://doi.org/10.1039/c8nr04455d.

[231] Li B, Zhang B, Nie S, Shao L, Hu L. Optimization of plasmon-induced photocatalysis in electrospun Au/CeO2 hybrid nanofibers for selective oxidation of benzyl alcohol. J Catal 2017;348:256–64. https://doi.org/10.1016/j.jcat.2016.12.025.

[232] Kumar V, Bhawna, Yadav SK, Gupta A, Dwivedi B, Kumar A, et al. Facile Synthesis of Ce–Doped SnO 2 Nanoparticles: A Promising Photocatalyst for Hydrogen Evolution and Dyes Degradation. ChemistrySelect 2019;4:3722–9. https://doi.org/10.1002/slct.201900032.

[233] Bardestani R, Patience GS, Kaliaguine S. Experimental methods in chemical engineering: specific surface area and pore size distribution measurements—BET, BJH, and DFT. Can J Chem Eng 2019;97:2781–91.

https://doi.org/10.1002/cjce.23632.

[234] Sun L, Sun J, Sun X, Bai S, Zhao Y, Luo R, et al. rGO decorated ZnO/CdO heterojunction as a photoanode for photoelectrochemical water splitting. J Colloid Interface Sci 2022;608:2377–86. https://doi.org/10.1016/j.jcis.2021.10.140.

[235] Uddin MT, Hoque ME, Chandra Bhoumick M. Facile one-pot synthesis of heterostructure SnO2/ZnO photocatalyst for enhanced photocatalytic degradation of organic dye. RSC Adv 2020;10:23554–65. https://doi.org/10.1039/d0ra03233f.

[236] Elaziouti A, Laouedj N, Bekka A, Vannier RN. Preparation and characterization of p-n heterojunction CuBi2O4/CeO2 and its photocatalytic activities under UVA light irradiation. J King Saud Univ - Sci 2015;27:120–35. https://doi.org/10.1016/j.jksus.2014.08.002.

[237] Ghosh CK, Chattopadhyay KK, Mitra MK. Effect of Co doping on the static dielectric constant of ZnO nanoparticles. J Appl Phys 2007;101:124911. https://doi.org/10.1063/1.2749481.

[238] Kim DH, Lim SK, An C. The microwave dielectric properties of xTiO2(1-x)CeO2 ceramics. Mater Lett 2002;52:240–3. https://doi.org/10.1016/S0167-577X(01)00434-7.

[239] Žerjav G, Albreht A, Vovk I, Pintar A. Revisiting terephthalic acid and coumarin as probes for photoluminescent determination of hydroxyl radical formation rate in heterogeneous photocatalysis. Appl Catal A Gen 2020;598. https://doi.org/10.1016/j.apcata.2020.117566.

[240] Samoilova RI, Crofts AR, Dikanov SA. Reaction of superoxide radical with quinone molecules. J Phys Chem A 2011;115:11589–93. https://doi.org/10.1021/jp204891n.

[241] Li Z, Sun R, Ni Y, Kokot S. A novel fluorescent probe involving a graphene quantum dot-enzyme hybrid system for the analysis of hydroquinone in the

presence of toxic resorcinol and catechol. Anal Methods 2014;6:7420–5. https://doi.org/10.1039/c4ay01222d.

[242] Sulciute A, Nishimura K, Gilshtein E, Cesano F, Viscardi G, Nasibulin AG, et al. ZnO Nanostructures Application in Electrochemistry: Influence of Morphology. J Phys Chem C 2021;125:1472–82. https://doi.org/10.1021/acs.jpcc.0c08459.

[243] Cui L, Zou X, Liu Y, Li X, Jiang L, Li C, et al. Dramatic enhancement of photocatalytic H2 evolution over hydrolyzed MOF-5 coupled Zn0.2Cd0.8S heterojunction. J Colloid Interface Sci 2020;577:233–41. https://doi.org/10.1016/j.jcis.2020.05.023.

[244] Tong YY, Li YF, Sun L, Yang R, Zhang S, Fu Y, et al. The prominent photocatalytic activity with the charge transfer in the organic ligand for [Zn4O(BDC)3] MOF-5 decorated Ag3PO4 hybrids. Sep Purif Technol 2020;250:117142. https://doi.org/10.1016/j.seppur.2020.117142.

[245] Aleksandrzak M, Sielicki K, Mijowska E. Enhancement of photocatalytic hydrogen evolution with catalysts based on carbonized mof-5 and g-C3N4. RSC Adv 2020;10:4032–9. https://doi.org/10.1039/c9ra08388j.

[246] Hussain MZ, Pawar GS, Huang Z, Tahir AA, Fischer RA, Zhu Y, et al. Porous ZnO/Carbon nanocomposites derived from metal organic frameworks for highly efficient photocatalytic applications - A correlational study. Carbon N Y 2019;146:348–63. https://doi.org/10.1016/j.carbon.2019.02.013.

[247] Lin L, Zhang T, Liu H, Qiu J, Zhang X. In situ fabrication of a perfect Pd/ZnO@ZIF-8 core–shell microsphere as an efficient catalyst by a ZnO support-induced ZIF-8 growth strategy. Nanoscale 2015;7:7615–23. https://doi.org/10.1039/C5NR00257E.

[248] Yang LM, Fang GY, Ma J, Ganz E, Han SS. Band gap engineering of paradigm MOF-5. Cryst Growth Des 2014;14:2532–41. https://doi.org/10.1021/cg500243s.

[249] Cantwell G, Harsch WC, Jogai B. Valence-band ordering in zno. Phys Rev B - Condens Matter Mater Phys 1999;60:2340–4. https://doi.org/10.1103/PhysRevB.60.2340.

[250] Wang BS, Li RY, Zhang ZY, Xing-Wang, Wu XL, Cheng GA, et al. An overlapping ZnO nanowire photoanode for photoelectrochemical water splitting. Catal Today 2019;321–322:100–6. https://doi.org/10.1016/j.cattod.2018.02.028.

[251] Fiaz M, Hussain D, Athar M. Synthesis of transition metal oxide incorporated MOF-5 and NH2-MOF-5 as efficient photoanode for oxygen evolution reaction. Ionics (Kiel) 2021;27:759–70. https://doi.org/10.1007/s11581-020-03866-1.

[252] Asadevi H, Prasannakumaran Nair Chandrika Kumari P, Padmavati Amma R, Khadar SA, Charivumvasathu Sasi S, Raghunandan R. ZnO@MOF-5 as a Fluorescence “Turn-Off” Sensor for Ultrasensitive Detection as well as Probing of Copper(II) Ions. ACS Omega 2022;7:13031–41. https://doi.org/10.1021/acsomega.2c00416.

[253] Nie Z, Huang Y, Ma B, Qiu X, Zhang N, Xie X, et al. Nitrogen-doped Carbon with Modulated Surface Chemistry and Porous Structure by a Stepwise Biomass Activation Process towards Enhanced Electrochemical Lithium-Ion Storage. Sci Rep 2019;9. https://doi.org/10.1038/s41598-019-50330-w.

[254] Li F, Xu R, Li Y, Liang F, Zhang D, Fu WF, et al. N-doped carbon coated NiCo 2 S 4 hollow nanotube as bifunctional electrocatalyst for overall water splitting. Carbon N Y 2019;145:521–8. https://doi.org/10.1016/j.carbon.2019.01.065.

[255] Cong K, Radtke M, Stumpf S, Schröter B, McMillan DGG, Rettenmayr M, et al. Electrochemical stability of the polymer-derived nitrogen-doped carbon: An elusive goal? Mater Renew Sustain Energy 2015;4. https://doi.org/10.1007/s40243-015-0046-9.

[256] Liu P, Gao S, Wang Y, Huang Y, He W, Huang W, et al. Carbon nanocages with N-doped carbon inner shell and Co/N-doped carbon outer shell as electromagnetic wave absorption materials. Chem Eng J 2020;381. https://doi.org/10.1016/j.cej.2019.122653.

[257] Zhou R, Guo H, Yang Y, Wang Z, Li X, Zhou Y. N-doped carbon layer derived from polydopamine to improve the electrochemical performance of spray-dried Si/graphite composite anode material for lithium ion batteries. J Alloys Compd 2016;689:130–7. https://doi.org/10.1016/j.jallcom.2016.07.315.

[258] Tian Y, Wu J. A comprehensive analysis of the BET area for nanoporous materials. AIChE J 2018;64:286–93. https://doi.org/10.1002/aic.15880.

[259] Jaihindh DP, Manikandan A, Chueh Y, Fu Y. Deep Eutectic Solvent-Assisted Synthesis of Ternary Heterojunctions for the Oxygen Evolution Reaction and Photocatalysis. ChemSusChem 2020;13:2726–38. https://doi.org/10.1002/cssc.202000177.

[260] Hung W-H, Teng Y-J, Tseng C-M, Nguyen HTT. Enhanced Patterned Cocatalyst TiO2/Fe2O3 Photoanodes for Water-Splitting. Nanoscale Res Lett 2021;16:76. https://doi.org/10.1186/s11671-021-03529-8.

[261] Zhao F, Li W, Song Y, Fu Y, Liu X, Ma C, et al. Constructing S-scheme Co3O4-C3N4 catalyst with superior photoelectrocatalytic efficiency for water purification. Appl Mater Today 2022;26. https://doi.org/10.1016/j.apmt.2022.101390.

[262] Fan K, Chen H, He B, Yu J. Cobalt polyoxometalate on N-doped carbon layer to boost photoelectrochemical water oxidation of BiVO4. Chem Eng J 2020;392. https://doi.org/10.1016/j.cej.2019.123744.

[263] Lv CN, Zhang L, Huang XH, Zhu YX, Zhang X, Hu JS, et al. Double functionalization of N-doped carbon carved hollow nanocubes with mixed metal phosphides as efficient bifunctional catalysts for electrochemical overall

water splitting. Nano Energy 2019;65. https://doi.org/10.1016/j.nanoen.2019.103995.

[264] Dom R, Kim HG, Borse PH. Efficient hydrogen generation over (100)-oriented ZnO nanostructured photoanodes under solar light. CrystEngComm 2014;16:2432–9. https://doi.org/10.1039/c3ce42058b.

[265] Dual Metal–Organic Framework Heterointerface _ Enhanced Reader mtt tooky-atıf.pdf n.d.

[266] Guo L, Li J, Lei N, Song Q, Liang Z. Morphological evolution and enhanced photoelectrochemical performance of V4+ self-doped, [010] oriented BiVO4 for water splitting. J Alloys Compd 2019;771:914–23. https://doi.org/10.1016/j.jallcom.2018.09.037.

[267] Gopalakrishnan S, Bhalerao GM, Jeganathan K. SrTiO3 NPs/g-C3N4 NSs Coupled Si NWs based Hybrid Photocathode for Visible Light Driven Photoelectrochemical Water Reduction. ACS Sustain Chem Eng 2019;7:13911–9. https://doi.org/10.1021/acssuschemeng.9b02093.

[268] Peng Z, Abbas SC, Lv J, Yang R, Wu M, Wang Y. Mixed-metal organic framework-coated ZnO nanowires array for efficient photoelectrochemical water oxidation. Int J Hydrogen Energy 2019;44:2446–53. https://doi.org/10.1016/j.ijhydene.2018.12.064.

[269] Jia G, Liu L, Zhang L, Zhang D, Wang Y, Cui X, et al. 1D alignment of ZnO@ZIF-8/67 nanorod arrays for visible-light-driven photoelectrochemical water splitting. Appl Surf Sci 2018;448:254–60. https://doi.org/10.1016/j.apsusc.2018.04.102.

CURRICULUM VITAE

PERSONAL INFORMATION

Name Surname : Fatih ARLI

Date of Birth

Phone

E-mail

EDUCATION

High School : Selcuk High School

Bachelor : Kahramanmaras Sutcu Imam University

Master Degree : Selcuk University

WORK EXPERIENCE

Sırnak University- Research Assistant-Department of Energy Systems Engineering (2011-2017)

Ankara Yıldırım Beyazıt University-Research Assistant-Department of Energy Systems Engineering (2017-)

TOPICS OF INTEREST

- Hydrogen generation
- Nanomaterials
- Energy systems

PUBLICATIONS

- Celebi N, Arlı F, Soysal F, Salimi K. Z-scheme ZnO@PDA/CeO2 heterojunctions using polydopamine as electron transfer layer for enhanced photoelectrochemical H2 generation. Mater Today Energy 2021;21. https://doi.org/10.1016/j.mtener.2021.100765.
- Simsek S, Uslu S, Sahin M, Arlı F & Bilgic G. Impact of a novel fuel additive containing boron and hydrogen on diesel engine performance and emissions,

Energy Sources, Part A: Recovery, Utilization, and Environmental Effects(2021). https: DOI: 10.1080/15567036.2021.1946621

- Taşkesen, E., Acar, Ş., Ertuğrul, G., Arlı, F., Dumrul, H. & Bulbul, S. (2021). Şırnak-Uludere Bölgesinde Yaygın Olarak Bulunan Asfaltitlerden Doğal Hümik Asit Elde Edilebilirliğinin İncelenmesi. Politeknik Dergisi, 1-1. DOI: 10.2339/politeknik.766461
- Bulbul, S., Ertugrul, G. & Arli, F. (2018). Investigation of usage potentials of global energy systems. International Advanced Researches and Engineering Journal,2(1),58-67. https://dergipark.org.tr/en/pub/iarej/issue/34178/398277

INTERNATIONAL CONFERENCES

- Celebi N, Arlı F, Soysal F, Salimi K. “Star-shaped ZnO-CeO2 Z-scheme heterostructures for photoelectrochemical water splitting” PV-CON 30 kasım 2 Aralık

- Sahin, M., Bulbul, S. , Ertugrul, G. & Arli, F. “Yeraltı Maden İşletmelerinde Açığa Çıkan Yeraltı Sularının Hidrokimyasal Özelliklerinin İncelenmesi.” The International Alumınıum-Themed Engineering and Natural Sciences Conference in Seydişehir/TURKEY (IATENS’19) October 4-6(1)1163-1166